The University Of Sheffield.

Department of Civil and Structural Engineering

Development of a Mechanically Correct Fire Resistance Design Process for Composite Floor systems in Buildings

By Ali Alskeif

A thesis submitted for the degree of Master of Philosophy

August 2015

Abstract

In this study, an alternative simplified method of tensile membrane action (TMA) of thin-flat concrete slabs at ambient temperature was extended to consider composite slabs in fire. The existing simplified method (Bailey-BRE) of estimating the influence of tensile membrane action on the slab strength in fire has some shortcomings in its assumptions and results. The alternative simplified method showed reasonable results, avoiding inherent flaws in the existing method that cause large differences in the results when a marginal change in reinforcement ratio is made.

This thesis takes into consideration the presence of a secondary downstand steel beam which was left unprotected against elevated temperatures. The main objectives of this study were: 1. to examine the mechanics of tensile membrane action of composite slabs in the presence of an unprotected secondary beam; 2. to examine the similarity of the structural behaviour of composite slabs with the results of the alternative method of flat slabs in terms of the benefits of large deflections; 3. to compare the extended method in this study against the existing Bailey-BRE simplified method.

The mechanics behind this study was divided into two main parts: 1. small-deflection analysis; 2. large-deflection analysis. The small-deflection analysis is based on the yield-line theory, where the slab was heated from the bottom side, affecting the unprotected secondary steel beam, until the yield-lines formed in what is known as the "optimum yield-line pattern". The second part of the study took this yield-line pattern configuration. With further deflection, tensile membrane action started to mobilize, and the slab gained further capacity. The method accounts for the internal work dissipation by the reinforcement and the steel beam as they extend, which contributes to the total internal work of the slab. The small-deflection analysis was coded in Visual Basic in a Microsoft Excel spreadsheet, increasing the temperature to obtain the optimum yield-line pattern. The large-deflection analysis was coded in Matlab in order to conduct a deflection-controlled loop, increasing the temperature until the failure of the slab, giving the temperature enhancement for every deflection level through the analysis.

The study allows the stress pattern around the yield-lines to be monitored. It also monitors the formation of the cracks on the slab, reinforcement fracture in different phases as the temperature increases and the slab deflects, until the structural failure. Comparisons against the Bailey-BRE method confirmed that the latter is conservative when small size reinforcement is used, as previous studies showed.

Page Intentionally Left Blank

Acknowledgements

Firstly, I would like to express my sincere gratitude to my supervisors, Dr Shan-Shan Huang and Prof Ian Burgess for providing me with the opportunity to study such an interesting area and for their constant help and support. I would also like to thank all the technicians in the Heavy Structures laboratory at the University of Sheffield for their effort and time they dedicated to me during the tests I conducted in the lab.

I also thank my research group and office colleagues for their support and the friendly atmosphere during my full-time research period.

Finally, I would like to thank my dear wife for every support she gave me from the beginning of this research, for her love and patience until this work was done. I give me sincere thanks to my family for every support they offered.

Declaration

This thesis is a presentation of my original research work, except where specific reference has been made to the work of others. Wherever contributions of others are involved in this thesis, every effort is made to indicate these contributions clearly.

Ali Alskeif

Contents

List of Figures

Glossary of Terms

All symbols are initially defined within the text as it first appears. A glossary of term was dedicated to each method in order to retain the original symbols as presented by its author. In some cases, two methods shared the same glossary of terms when different authors used the same notations. In certain instances, the same term may be defined by different symbols in order to keep the original notations as presented by the original authors.

Symbols

Chapter 2

l	short span of slab
l_i	projected length of yield-line on corresponding axis of support
M	moment of resistance of slab at hinge lines per length unit
n	yield-lines intersection point distance from short edge of the slab
p	external load acting on slab
δ	maximum deflection of slab
θ	angle of rotation of slab element about short span
ϕ	angle of rotation of slab element about large span

Sawczuk & Winnicki Method

a	larger span of slab
A	area of slab
b	short span of slab
d	energy dissipation of slab
F_z	reinforcement area per unit width
H	reinforcement distance from plate middle plane
l_i	length of hinge line on slab
M	bending moment of slab at hinge line
$M_{\alpha\beta}$	bending stress on slab
N	axial force at hinge line
$N_{\alpha\beta}$	membrane forces in slab
p	transverse loading
R_c	concrete compressive strength
W	deflection at yield hinge
W_0	maximum deflection of central yield-line of slab

W_{min}	minimum deflection required for membrane action
β_0	parameter defining bending response range in y direction
β_1	parameter defining membrane response range in y direction
η	parameter defining collapse mode of slab
θ	angle of rotation of slab element about its support
$\kappa_{\alpha\beta}$	curvature rate of middle surface of slab
$\lambda_{\alpha\beta}$	extension rate of middle surface of slab
$\bar{\xi}$	average of neutral layer distance from middle plane
$\bar{\xi}_0$	neutral layer distance at stress state at bending collapse
σ_0	reinforcement yield stress
Ψ_0	parameter defining bending response range in *x* direction
Ψ_1	parameter defining membrane response range in *x* direction

Kemp's Method

d	overall depth of slab
d_1	effective depth of slab
dx, dy	differential distances on axes *x, y* respectively
e	plastic axial elongation at mid-depth of slab
k_1, k_3	coefficients related to average compressive stress on concrete at yield
k_2	coefficient related to depth of resultant compressive force in concrete at yield
l	extension of pure tensile membrane
L	span of square slab
M	yield bending moment
M_o	yield bending moment with zero axial force
N	yield axial force at mid-depth of slab
p	uniformly distributed load
p_y	yield-line theory collapse load
t	reinforcement percentage of slab
T_o	reinforcement yield force per unit width
u	concrete cube strength
w_o	deflection in central region of slab
w_o'	deflection limit to keep neutral axis depth inside slab section
x, y, z	global axes, or denote distances and positions on *x,y,z* axes respectively
α, β	coefficients related to yield criterion in non dimensional form
Δ	horizontal movement of slab element
θ	rotation of triangular middle surface element about free edge
μ	height of neutral axis from mid-depth of slab
μ_o	height of neutral axis from mid-depth of slab at origin

Hayes & Bailey's Methods

a	aspect ratio of slab *(L/l)*
A, A'	parameters in yield criterion
b	parameter defining in-plane stress distribution
B, B'	parameters in yield criterion
C	total compressive membrane force
d_1, d_2	reinforcement effective depth in x and y directions.
d_n	concrete compression depth at zero deflection analysis
e	Total enhancement factor of slab
e_1, e_2	enhancements due to both bending action and membrane forces in slab elements 1 and 2, respectively
e_{1b}, e_{2b}	enhancements due to bending action in slab elements 1 and 2, respectively
e_{1m}, e_{2m}	enhancements due to membrane forces in slab elements 1 and, 2 respectively
e_{sys}	enhancement of slab-beam system due to membrane action
E	elastic modulus of reinforcement
f_u	steel ultimate stress
f_y	steel yield stress
g_o, g_o'	parameters fixing depth of compressive stress block when membrane forces are absent
h	depth of slab
k	parameter defining in-plane stress distribution
K	parameter related to steel forces per unit width
k'	lever arm/slab thickness for tensile membrane analysis
k_1	lever arm/slab thickness for zero deflection analysis
l	short span of slab
L	larger span of slab
M	bending capacity of slab
M_0	resistance moment when membrane force is absent
M_{1m}, M_{2m}	moments about slab supports due to membrane forces in slab elements 1 and 2, respectively
M_{fi}	moment capacity of steel beam at elevated temperatures
n	parameter fixing yield-line pattern
S	in-plane shear force at yield-line
T_o	steel forces per unit width
T_1, T_2	net tensile membrane forces along yield-lines
T_b	tensile capacity of steel beam at elevated temperatures
T_{bot}	temperature at slab bottom surface

T_{top}	temperature at slab top surface
v	parameter fixing extent of central membrane
w,W	yield-line deflection
w_{lim}	vertical deflection limit
w_p	load-carrying capacity of slab
α, β	coefficients related to enhancements due to bending action
α_T	coefficient of thermal expansion of concrete
γ	parameter fixing proportion of reinforcement which does not attain yield stress
δ	parameter fixing maximum reduction in reinforcement stress
μ	coefficient of orthotropy
φ , ϕ	parameters fixing yield-line pattern

The Alternative Method (Chapters 4 to 8, including the appendices)

A	area of steel beam cross-section
A_{1x}	compression area in diagonal yield-lines at slab edge
A_{2x}	compression area in central yield-lines at slab central region
A_c	concrete area around bolts in pull-out specimens
A_{nc}	cross section area of concrete notch
As	cross section area of reinforcement bar
C	concrete compression force in diagonal yield-lines
C_r	number of continuous long edges of slab
C_s	number of continuous short edges of slab
C_{x2}	concrete compression force in central yield-line
d	distance between two reinforcement bars in any direction
d_s	diameter of reinforcement bar
e	enhancement factor of slab
E	external work done by loads on slab
E_a	modulus of elasticity of steel for normal temperature design
$E_{a,\theta}$	slope of linear elastic range for steel at elevated temperature
f_c	concrete characteristic strength
f_{ctm}	mean axial tensile strength of concrete
$f_{ctm}(t_i)$	mean axial tensile strength of concrete after t_i days
$f_{p,\theta}$	proportional limit for steel at elevated temperature
f_{px}	reinforcement yield stress in x direction

f_{py}	reinforcement yield stress of *y* direction
f_y	yield stress of beam at ambient temperature
$f_{y,\theta}$	effective yield strength of steel at elevated temperature
h_a	total depth of beam
h_e	height of concrete frustum around pulled-out bolt
I_B	internal work dissipated by steel beam
I_S	internal work of slab
I_{tot}	total internal work of slab
K	value of double sagging moment of slab
$k_{E,\theta}$	reduction factor for slope of linear elastic range at steel temperature
$k_{p,\theta}$	reduction factor relative to steel yield stress for proportional limit
k_y, $k_{y,\theta}$	thermal reduction factor of steel due to current temperature
l	short span of slab
L	larger span of slab
L_a	lateral surface area of concrete pull-out cone
m_p	sagging moment of slab
$\overline{m_p}$	hogging moment of slab
M_{pl}	moment of resistance of steel beam
n	yield-lines intersection point distance from short edge of slab
N	yield-lines intersection point distance from larger edge of slab
P	load carrying capacity of slab
P_a	applied load on slab
P_o	initial yield-line load capacity
r	aspect ratio of slab *(L/l)*
r_1, r_2	small and big bases of concrete frustum around pulled-out bolt, respectively
S	shear force between slab elements
S_r	distance between reinforcement bar in tension and edge of slab
S_s	coefficient depends on type of cement
t	depth of concrete part of slab
T_b	tension force of steel beam
T_{cr}	critical temperature of composite slab
T_{x1}, T_{x2}	reinforcement tension forces in *x* direction across diagonal and central yield-lines, respectively
T_{y1}	reinforcement tension force in *y* direction across diagonal yield-lines
u	movement in *x* direction
v	movement in *y* -direction
V_p	pull-out loading rate
x, y, z	global axes, or denote distances and positions on *x*,*y*,*z* axes respectively
x_c	neutral axis depth

X_{CA}	distance in *x* direction from origin to centroid of concrete compression area
X_{Lim}	distance covers intact reinforcement in *x* direction, for *x* or *y* bars
$X_{Lim,2}$	distance covers intact reinforcement across central yield-line crack in *x* direction
X_T	distance covers reinforcement bars in compression in *x* direction
Y_1	length of triangular concrete compression block in *y* direction
Y_{CA}	distance in *y* direction from origin to centroid of concrete compression area
Y_{Lim}	distance covers intact reinforcement bar in *y* direction, for *x* or *y* bars
$Y_{Lim,2}$	distance covers intact reinforcement across central yield-line crack in *y* direction
Y_T	distance that covers reinforcement bars in compression in *y* direction
z_1	compression depth at slab edge
z_2	compression depth at central region of slab
α	angle of diagonal yield-lines cracks
$\beta_{cc}(t_i)$	coefficient depends on age (t_i) of concrete
γ	angle between diagonal yield lines and slab support
δ	maximum deflection of slab
Δ	extension of reinforcement
Δ_A	displacement in *x* direction between edges of slab elements 1 and 2
Δ'_A	displacement in *y* direction between edges of slabs elements 1 and 2
Δ_{Lim}	maximum extension of reinforcement in *x* or *y* direction
Δx	deformation or movement of slab elements in *x* direction
Δy	deformation or movement of slab elements in *y* direction
ε_u	fracture ductility strain of reinforcement
η	angle of rotation between slab elements across cracks
θ	angle of rotation of slab about short span
μ	reinforcement depth ratio
ξ	rotation angle between two slab elements
ϕ	angle of rotation of slab about large span

1 Background of the Study

1.1 Introduction

Over the last couple of decades, attention to structural fire engineering increased and huge efforts were made to study the behaviour of structures in fire, especially composite-floor structures. Life safety is the main concern in the event of fire. Thus the Building Regulations in England and Wales changed from prescriptive requirements to performance-based approach in 1991, emphasising the safety of occupants so that fire can be resisted and the building stability is maintained during evacuation (Foster 2006; Vassart & Zhao 2011). The regulations in Scotland and Northern Ireland followed suite, allowing the implementation of the performance-based approach for fire safety.

However, fire incidents during the last two decades brought more attention to fire safety and fire engineering. Fire incidents, like the collapse of the World Trade Center buildings in 2001, the Windsor Tower fire in Madrid 2005 and the Olympus Hotel Tower fire in Grozny 2013 are amongst the most famous fire events since 2000.

Evacuation can sometimes be possible and casualties can be avoided or minimized. However, some other cases can be tragic and result in a huge number of casualties as it was the case in the WTC towers in 11 September events 2001. Nevertheless, the evacuation of WTC towers is considered a successful story, thanks to the tower's ability to stand long enough before collapse.

Before the 1990s, the main practice that was used in structures in fire conditions depended on an element-based approach. Such principles were reliable to some extent, and still they are being used since they showed efficiency in preventing extensive structural damage in fire. However, the collapse of WTC buildings in September 2011 showed that the element-based approach may not be sufficient to be implemented for structural safety in fire (Wang et al. 2012). Wang et al. argue that the collapse of WTC building 7 demonstrated a good example of the shortcomings of the element-based approach. For example, in WTC building 7, it is believed that the main girder detached

from one of the columns by the effect of fire. This caused the whole structure to collapse, although the rest of the structural elements remained within their strength capacity at the moment of the building collapse. Therefore, Wang et al. suggest that the prescriptive approach, based on element-based behaviour, may not be sufficient. Therefore, the performance-based approach, which considers the structure as a whole, should be implemented in order to understand the structural behaviour in fire conditions.

1.2 Element-based approach and prescriptive fire safety design

The element-based approach considers the structure as a group of elements comprises the whole structure independently. Hence, the fire resistance of the structure is determined by the design of the individual elements of the structure to resist fire (Purkiss 2007). Thus, the interaction of the elements is not considered. Fire resistance may be defined by any of the time, strength or temperature criteria. Using the time criterion implies that the required fire resistance time should be more than the factual fire period imposed on the structure. The strength criterion is similar to the normal structural design procedure at ambient temperature, taking into consideration the effect of the elevated temperatures. Finally, the temperature criterion assumed that the critical temperature in the structure should be lower than the actual temperature experienced in the structure in fire conditions (Wang et al. 2012). However, the element-based approach does not take the effects of thermal deformations at elevated temperature into consideration. Therefore, the application of this approach is allowed when such effects are negligible or favourable.

Purkiss (2007) and Wang et al. (2012) argue that the element-based approach is simple, quick, however not economic. Nonetheless, this method is still adopted by codes of practice including the Eurocodes. Similar to the structural design procedures at ambient temperature, mechanical and fire loads are calculated; material and loading safety factors are considered and then standards are applied depending on the used construction materials (i.e. concrete, steel, timber and masonry).

The prescriptive approach provides good instructions and prerequisites for safety and minimizing losses. However, such potential loss for a specific situation is vague. For instance, the prescriptive approach specifies the number and spacing of sprinklers and

fire detectors even though the designers do not know the extent of the possible damage before these sprinklers are activated, or the extent of fire spread before evacuation is complete (Meacham & Custer 1995).

In the UK, a prescriptive fire guide was published by the Association for Specialist Fire Protection (ASFP) under the name "Fire protection for structural steel in buildings", also known as the "Yellow Book". This guide presents fire testing and protection methods of structural elements to achieve certain fire resistance time. A variety of materials can be used to protect the structural elements from excessive heat in fire conditions. These materials can be applied in different ways to achieve the required fire resistance periods. Sprayed materials can be applied to section profiles; boards can be used to envelope elements' sections by forming a box all around the structural element; and special insulating concrete can be used to surround the section and form solid protection around it (ASFP 2010). Examples of section profile protection are shown in Figure 1.

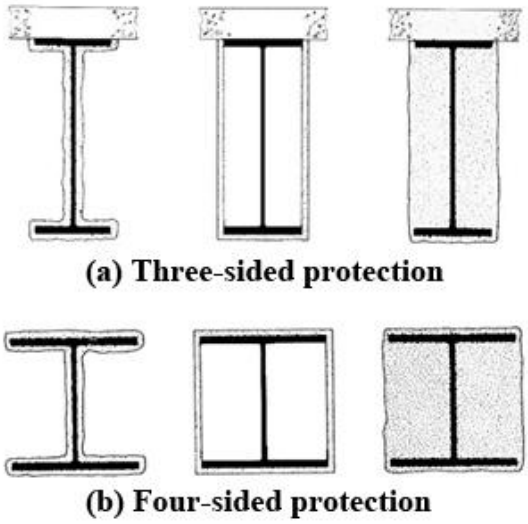

Figure 1: Sprayed, board and solid insulating concrete protection (ASFP 2010)

According to the Yellow Book, the thickness of fire protection materials is specified so that columns and beams temperatures do not exceed 550ºC and 620ºC, respectively. This assumes that these elements are heavily loaded during the fire. This is now known to be conservative in most cases, and unconservative in few others. However, according to the Eurocodes (EC 3-1.2 and EC 4-1.2) the designers are required to determine the failing temperature. If this is not possible, the limit temperatures are used.

1.3 Performance-based approach

The Cardington fire tests in mid 1990s showed that in continuous frames the effects of restraint to thermal expansion make the element-based approach inapplicable in fire conditions (Wang et al. 2012). Therefore, it is not appropriate to consider a structure as an assemblage of individual-isolated members. Then in 2001 the collapse of the World Trade Center buildings led the designers to question the fire safety procedures and the prescriptive approach. Although the prescriptive approach is still adopted in many codes of practice, it is often inadequate for large buildings, inflexible and leads to conservative designs. On the other hand, despite the fact that the performance-based approach is not new, it is not used on a wide scale yet, because of a lack of understanding of this approach by the designers (Green et al. 2003). New techniques are being developed to enable a wide use of such an approach and make it more flexible, economical and safely implemented.

While in the prescriptive approach the structural system as a whole and the interaction of the individual elements are not considered, the performance-based approach considers these factors. This provides more flexible and cost-effective designs. It also allows the internal secondary steel beams to be used with no fire protection, without compromising the safety level (Hamilton 2011). Performance-based fire engineering is a systematic engineering approach which considers fire as part of the structure, and its [fire] growth is viewed as a design objective. Hence, this approach includes fire modelling and dynamics, and risk assessment which is eventually subjected to engineering judgment (Meacham & Custer 1995).

1.4 World Trade Center collapse, 11 September 2001

The collapse of World Trade Center (WTC) buildings 1, 2 and 7 was one of the main reasons to questioning the element-based design approach. Therefore, the analysis of the collapse of the twin towers (buildings 1, 2) and building 7 is discussed briefly in this section.

The twin towers collapsed following the impact of the planes (one plane hit each tower). However, the collapse of the twin towers occurred due to the exacerbation of the situation by the fire. This fire was ignited and fed by the huge amount of jet fuel after

the attack. A report issued by the Structural Engineering Institute of the American Society of Civil Engineers (SEI/ASCE) and the Federal Emergency Management Agency (FEMA) in May 2002 stated that despite the tremendous localised damage made by the direct impact, both the towers remained standing and did not collapse immediately (Corley et al. 2002). Corley et al. argue that the jet fuel which flowed down the elevators and through the damaged floors caused huge fires by igniting most of the furniture and contents of the buildings. This in turn weakened the steel-framed structure, leading to progressive collapse. WTC building 7, however, was not directly hit by any plane. It was hit by debris from the planes collision with the twin towers which ignited the building. Few parts of building 7 were probably damaged to some extent, leading to its global collapse after fire was ignited by the debris (NIST NCSTAR 1A 2008).

Alexander (2002) argues that the huge amount of jet fuel carried by the planes (about 38,000 litres by the plane that hit the WTC-1), along with the furniture, burned up in few minutes, allowing the temperature to rise to 1000ºC. This overwhelmed the sprinkler system although it was reported to have been in a good state prior to the event. However, according to the 1968 New York City Building Code, WTC buildings were classified as Class 1B, contrary to what the early stages of the design indicated as 1A (Gross & McAllister 2005). To comply with this classification, columns, girders and trusses should have 3-hour fire-resistance. Yet, as Gross and McAllister mention in their report, WTC-1 collapsed 102 minutes after the plane impact, while it took only 56 minutes for WTC-2 to collapse after the impact. This probably happened because of the deteriorated insulation materials of the trusses which was detected in a survey prior to the September event. The deteriorated insulation materials increased the trusses temperature beyond the critical temperature. Figure 2 shows dislodged fire insulation in one of the WTC buildings.

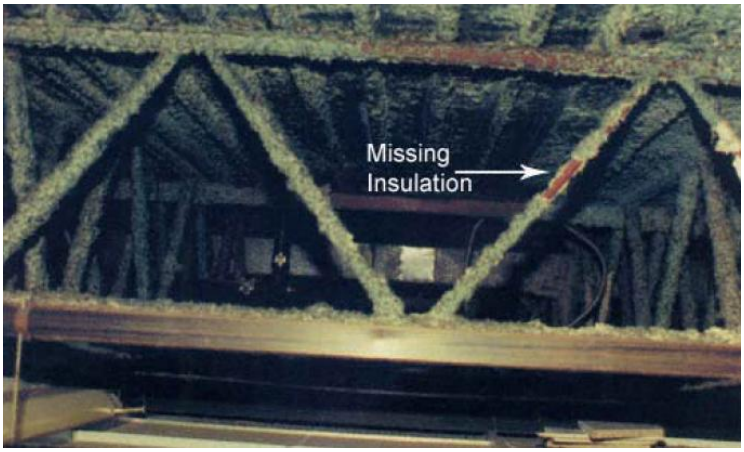

Figure 2: Dislodged sprayed fire insulation in WTC buildings (Gross & McAllister 2005)

As Wang et al. (2012) argue, the excessive temperature caused the floor trusses to develop catenary mechanism, applying horizontal pull forces on the columns. Furthermore, the floor trusses stopped providing lateral restraint to the columns. Therefore, the buckling length of the columns increased, reaching few floors height which exceeds these columns capacity.

WTC Building 7 was not hit directly by a plane. Fires were ignited by debris from WTC-1 when the latter was hit. Since there was no jet fuel over building 7, the fire developed slowly and unnoticed; spreading between offices and floors uninterrupted by the sprinkler system as a result of the loss and damage of the city water pipes due to WTC 1 & 2 collapse (Gann 2008). Gann argues that regardless of the lack of photos of WTC-7 fires, there was enough information to establish an assessment of fire development. Gann (2008) and Wang et al. (2012) argue that the collapse of WTC-7 was due to connection failure that caused buckling of key column 79, as shown in Figure 3. Due to the elevated temperature, lateral forces in beams existed due to their [beams] expansion. Restraint by the primary beams led to axial compression which was large due to the large sizes of the beams, leading to shear failure of the connections. This failure led to the collapse of floor 13 which triggered a series of successive floor collapse, leaving columns 79, 80 and 81 with insufficient lateral support, therefore initiating a global building collapse.

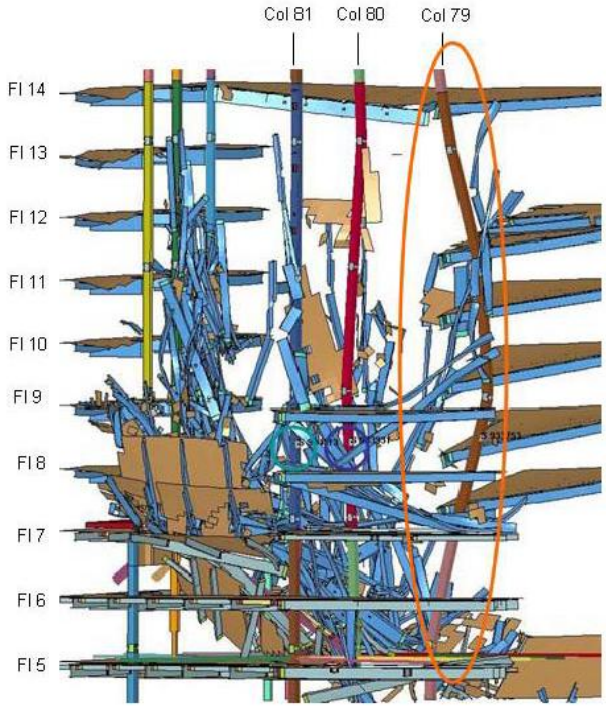

Figure 3: Column 79 buckling in WTC-7 (Gann 2008)

However, Alexander (2002) argues that the fact that the twin towers remained standing long enough for the evacuation of everyone who had an unblocked route, makes the incident a success story. After all, only 2923 out of 58,000 people who were in the buildings died. In a study of the evacuation of the World Trade Center buildings, Gershon et al. (2011) argue that about 87% of all occupants in the WTC were evacuated, making this evacuation largely successful.

Although the loss of 2923 is tragic, WTC incident is considered a successful fire safety story. It could have been far worse if the buildings did not stand long enough after the impact. Alexander (2002) argues that in general it is not practical to design structures to withstand impacts from planes. However, buildings need to show more robust and be redundant enough to further decrease the numbers of casualties as much as possible.

1.5 Windsor Tower fire, Madrid 2005

In 2005, fire caused partial collapse of the Windsor Tower in Madrid. The Windsor Tower was a 32-storey building that consisted of a reinforced concrete core supporting two-way deep waffle flooring system (Wang et al. 2012). At the time of its construction, Spanish building codes did not require the steelwork to be fire-protected and did not require sprinkler systems to be installed in buildings. Hence, in accordance to the Spanish building codes, the perimeter columns and the internal steel beams were not fire-protected (Parker 2005; Wang et al. 2012). The fire started in floor 21 and spread downwards quickly. It is believed that fire spread by dropping flamed materials through service openings and the incomplete vertical compartmentation which lacked fire-stopping system, especially since the building was in the process of refurbishment at the time of the incident (Wang et al. 2012).

Fletcher et al. (2006) argue that the concrete structure, floors and columns, performed very well and remained intact. However, the steel part above floor 21 collapsed. Fletcher, et al. present an interesting notice that although floor 9 experienced a full fire flashover, and although the steel members in that floor were not fire-protected, the overall stability was maintained. No significant collapse occurred despite the fact that the steel columns suffered from extensive buckling as shown in Figure 4.

Figure 4: Columns buckling of the 9th floor, Windsor Tower (Pope 2006)

The columns of the floors above and below the 9th floor were fire-protected. This provided alternative load paths through these floors. This alternative load path, in turn, provided support to floor 9, preventing it from total collapse despite the severe buckling of its columns (Pope 2006; Fletcher et al. 2006).

Although the tower was severely damaged and needed to be demolished and replaced, it should be given credits for remaining standing after the extensive 20-hour fire.

1.6 Cardington full-scale fire tests

Before the Broadgate fire in 1990, codes of practice for structural behaviour in fire conditions, including the British Standards and the Eurocodes, were based on structural element performance as isolated members. Hence, allowing the failure of some steel members in fire and using the alternative load-carrying mechanism was not considered. However, this started to change after the Broadgate fire incident, initiating a new understanding of the structural behaviour of buildings at elevated temperatures. This new behaviour was possible to be examined and researched by the Cardington structural fire research programme in the 1990s (Wang et al. 2012).

In the 1990s, a series of large-scale fire tests was conducted by the Building Research Establishment (BRE), in collaboration with Tata Steel (British Steel that time) within the BRE Large Building Test facility at Cardington (Lennon 2014). These tests were conducted in order to examine the behaviour of a composite building in fire conditions.

The building at which the tests were conducted was an 8-storey steel framed structure with composite slab flooring system which was designed according to the UK national design codes and complied with the Eurocode provisions of steel structures design. The total floor area was 945m^2 which consists of five 9-meter-bays along the elevation and 6m, 9m, 6m bays successively across the building. For construction cost and time reduction and for standardization purpose, only four beam sections and three column sections were used. The peripheral edge beams were protected using double glazed units while the secondary beams were left unprotected. All the columns were either protected or located behind walls that were used to fire-protect compartments (Lennon 2014). The composite floor slab was light-weight concrete comprised trapezoidal steel deck and

reinforced by anti-cracking A142 steel mesh (i.e. 6mm- bars spacing 200mm) (Bailey 2001).

1.6.1 BRE corner fire test

Lennon (2014) explains that in order to minimise the effect of the high temperatures on the hangar itself, at which the BRE corner test in 1995 was conducted, the fire was ignited on the second floor, heating the third floor which was to be tested. Furthermore, this facilitated the observations during the test. The compartment was formed using fire-resistant boards, made of British gypsum fireline. The peripheral walls were made by full height concrete walls, while the boundary was formed using a one-meter high concrete wall with double glazing units on its top (Huang et al. 2001)

Lennon (2014) argues that in order to simulate a realistic compartment, representing a corner office which resides in commercial buildings, no additional boundary wall restraint was provided. Huang et al. (2001) and Lennon (2014) state that a fire load of 40kg/m^2 was provided by 12 timber cribs, distributed on the second floor over 54m^2 area, resulting in an overall fire load of 2160kg. According to Huang et al., the maximum atmosphere temperature recorded in the centre of the compartment during the test was 1051ºC at 102 minutes. The maximum recorded temperature of the bottom of the unprotected-secondary beams was 842ºC, and for the protected edge beams the temperature was 590ºC at 114 minutes. The maximum average recorded temperature of the bottom of the concrete slab was 285ºC at 114 minutes.

Huang et al. (2001) argue that it was observed in this test that the tension in the central region of the slab was totally balanced by the peripheral compression in the beams. The importance of this observation lies in the fact that the slab was almost horizontally unrestrained. This balance was mainly achieved taking into account that the four peripheral beams provided vertical support to the slab. This mechanism, which balances the central tension and the peripheral compression, is essential to supporting the whole slab at large deflections, as shown in Chapter 3. Since large deflections are acceptable in fire conditions, this point is the basis of the mechanism which is derived in this study and is presented in Chapter 6.

1.6.2 BRE large compartment fire test

The large compartment fire test in Cardington was carried out on the third floor. The fire was ignited on the second floor, heating and testing the third floor. The test took place in a large compartment representing a modern wide office which has an area of 18m x 21m (Lennon 2014). Uniformly distributed timber cribs gave a fire load of 40kg/m^2. The fire load was distributed differently from the corner fire test, with more timber in each crib and larger distance between them. Lennon argues that this different fire-load distribution, along with the ventilation conditions, had a significant effect on the fire development in the compartment.

All the secondary steel beams were left unprotected. The columns, and their connections, were fire protected. The maximum atmosphere temperature reached 763ºC; steelwork temperature reached 691ºC and the maximum average temperature of the bottom of the slab reached 260ºC (Huang et al. 2001). Table 1 shows the summery of Cardington fire tests results:

Table 1: Building Research Establishment (BRE), United Kingdon; BS, British Steel (now Tata Steel), United Kingdom; SCI, Steep Construction Institute, United Kingdom; CTU, E.U. collaborative research led by Czech Technical University in Prague.
(Wang et al., 2012)

No.	Organization	Level	Time to max temperature [Minutes]	Reached temperature [ºC]		Measured deformations [mm]	
				Gas	Steel	Max	permanent
1	BS	7	170	913	875	232	113
2	BS	4	125	820	800	445	265
3	BS	2	75	1020	950	325	425
4	BRE + SCI	3	114	1000	903	269	160
5	BRE	3	70	---	691	557	481
6	BS	2	40	1150	1060	610	---
7	CTU	4	55	1108	1088	>1000	925

Table 1 shows the temperatures that the steelwork and the structure in general were subjected to. Since the steel was left unprotected, temperature differences between the gas and the steel did not exceed 90ºC at most. This illustrates that the unprotected steel

can become extremely heated in fire conditions. In levels 2 and 7, this temperature difference was only 20ºC. Nevertheless, with the maximum temperatures to which the steel was subjected, reaching 1150ºC and 1108ºC in levels 2 and 4 respectively, the maximum measured deformations were 610mm in level 2 and over 1000mm in level 4, as illustrated in Table 1. Based on the predictions of the element-based approach, runaway collapse should have been witnessed in tests with such high temperatures. However, observations from the Cardington fire tests showed no runaway collapse in the composite beams. This was interesting since the downstand steel beams were subjected to excessively high temperatures beyond their critical limits. These beams would have failed and collapsed if they were tested on an individual basis, (Burgess et al. 2014). At temperatures exceeded 1000ºC, the composite slab had undergone large deflection of (L/20), as shown in Figure 5. Signs of local buckling on the beams and signs of connection fracture due to high tensile forces appeared, as shown in Figure 6. However, no structural collapse occurred (Lim 2003).

Figure 5: Composite slab in large deflection after Cardington fire tests (Kirby 1998)

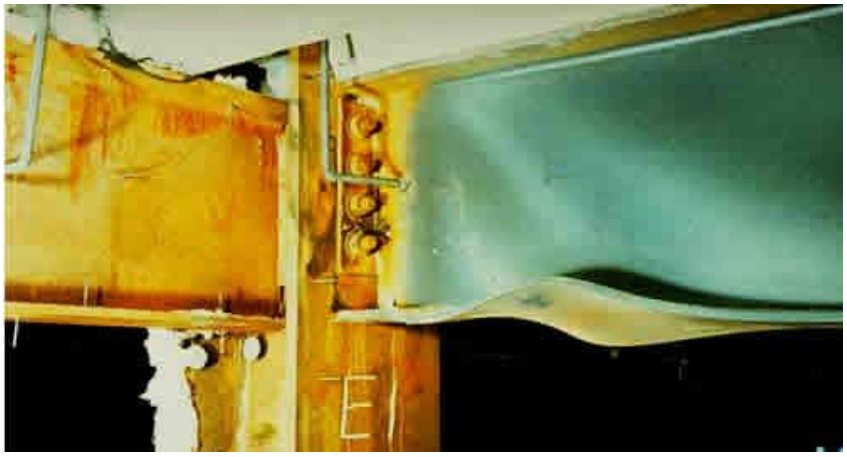

Figure 6: Beam buckling in Cardington (Newman et al. 2000)

Bailey (2001) argues that these results show that the composite slab which experienced large deflections had larger fire resistance than what was thought according to the conventional design methods, which were then mainly based on flexural behaviour.

Burgess et al. (2014) argue that the mechanism which caused the capacity enhancement of the slab is somewhat a two-dimensional catenary action. In a cable, catenary action resists the pull-in and the vertical forces, providing that support is available on the both ends of the cable. A similar mechanism takes place in highly-deflected slabs by horizontal reaction which is provided by compressive membrane stresses on the perimeter of the slab. However, if two-way continuity of the concrete slab panels is provided, the heated parts of the slab, which are vertically supported by their cool surrounding structure, generate high biaxial curvatures. This leads to the creation of a tensile membrane stress area in the central zone of the slab.

Today, this mechanism of membrane stresses is known as the Tensile Membrane Action (TMA). Burgess et al. (2014) argue that TMA depends on two factors: 1. good degree of vertical support around the edge of the slab; 2. the extent of the deflection of the central zone of the slab. In fire conditions, the secondary steel beams which are left unprotected lose significant degree of their strength, leading to large deflections. Under such large deflections, TMA carries the loads, leading to enhancement in load-carrying capacity of the slab beyond the capacity predicted by conventional flexural-behaviour methods.

Hayes (1968a) explains TMA by considering a one-way spanning strip. At large deflections, the ends of the strip moves inward. If this movement is resisted, the so-called “catenary action” is generated and the loads on the slab are supported by catenary mechanism. However, in case of a two-way spanning slab, a similar mechanism in both ways is generated even without restraining the edges of the slab. Thus, this tensile membrane action mechanism can be generated at large deflections even for isolated slabs with no restraint. Bailey (2001) argues that the application of TMA is limited since the required large deflections to initiate this behaviour are not usually encountered in normal conditions. However, such large deflections are acceptable in fire conditions. Therefore, this behaviour is important when it is about studying slabs behaviour at elevated temperatures. The behaviour of composite slabs at large deflections is further discussed in Chapter 3. The TMA mechanism, which was behind the survival of the slab in the BRE large compartment fire test, was developed in this study as is discussed in Chapter 6.

1.6.3 BRE ambient temperature test

This test was conducted at ambient temperature to investigate the tensile membrane action in slabs. Although the test was conducted at ambient temperature, the intention was to examine TMA in slabs in fire conditions (Lim 2003). The slab was built on trapezoidal steel deck, which was removed later to study the slab while reinforced only with A142 anti-cracking steel mesh. The removal of the steel deck was necessary due to the fact that the steel sheeting has only nominal strength, especially since BRE tests showed that temperatures can go beyond 1100ºC. Furthermore, it was observed that steel decks in composite slabs detach from the concrete part of the slab due to the steam released at high temperatures (Bailey 2001).

The slab was simply supported around its edges. No horizontal restraint was provided. The test showed that the composite slab failed when the load was about double that expected by the normal yield-line theory. Failure occurred by the formation of a full-depth crack at the central zone of the slab. This failure mode is essential to studying the behaviour of the composite slabs when they undergo large deflections. Examining this failure mode is the key to this research, as is further discussed in Chapters 5 and 6.

In the 1960s, attempts were made to establish simplified methods to predict slabs' load-carrying capacity in compliance with test observations. These methods are briefly presented in Chapter 3. An existing simplified method to calculate the slab load enhancement is presented in Section 3.4. However, the enhancement according to the existing method has been found to be conservative for flat concrete slabs (Burgess et al. 2014). The alternative simplified method that was established by Burgess et al. (2014) has been extended in this study in order to calculate the enhancement factors for composite slabs at elevated temperatures and predict the extent of the load that composite slabs can withstand beyond the predictions of conventional methods.

It should be noted that all previous methods, in addition to this study, used the same coordinate system with its origin at the corner of the slab. The exception to this was Kemp (1967), who restricted attention to a bisymmetric problem of square slabs. Therefore, Kemp used the centre of the slab as the origin of the coordinate system. The original coordinate system of each method is used when presented in this thesis.

2 Yield Line Method

2.1 Introduction

Structural analysis based on the elastic theory of structures gives good estimation of deformations and stresses for structures obeying the Hooke's law at small deformations. However, at structural failure, the assumptions of the elastic theory are not valid; and its estimation of the real load-carrying capacity is not accurate. This leads to an inaccurate safety factors against collapse, mostly conservative. On the other hand, there are some cases at which the theory of elasticity might give unsafe results (Szilard 2004). The yield line analysis, based on the plastic theory, eliminates the shortcomings and the limitations of the theory of elasticity. Since this study is based on the yield line theory, its principles are briefly presented in this chapter.

2.2 Principles of the yield-line method

2.2.1 A brief on plasticity

The method proposed in this study is based on plastic yield-line analysis. A yield-line is a linear plasticized hinge on a slab. Therefore, the concept of plasticity and plastic hinges is discussed in this section, prior to introducing the concept of the yield-lines in Section 2.2.2.

When a beam, for example, is loaded, the stress distribution takes the usual triangular pattern according to the elastic theory. However, if the load is progressively increased further, the outer fiber of the beam yields (i.e. reaches the yield stress as shown in Figure 7(a)). With further load increase, yielding takes place in the adjacent fibers towards the neutral axis of the beam as shown in Figure 7 (b) & (c). With the yield stress penetrating the cross-section fibers and reaching the neutral axis, the stress distribution of the beam becomes nearly rectangular as shown in Figure 7(d). This fully plasticized section forms a plastic hinge in the structural element. The plastic hinge rotates under a constant moment which does not increase further in case of adding

additional loads. The collapse of the structural element, however, is dependent on the number of the plastic hinges that the element can take (i.e. determinacy).

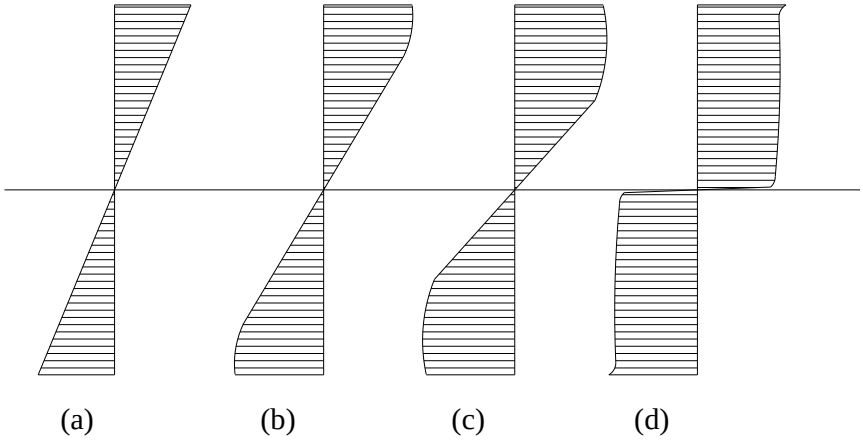

Figure 7: Stress distribution of a plastically bending beam; (a) elastic stress distribution; (b & c) yielding towards the neutral axis; (d) fully plasticized section (i.e. plastic hinge)

2.2.2 The concept of yield-lines

The concept of the plastic analysis of beams and frames was extended to include slabs in what is called the yield line analysis. A yield line is a two-dimension plastic hinge, which is observed in particular patterns on slabs when plasticized. While the conventional design methods attempt to work out the elastic deformation shape of slabs, the yield-line analysis defines all the possible failure patterns (Szilard 2004). The optimum yield-line mechanism is the mechanism which corresponds to the smallest load that causes the collapse. This load is called the optimum yield-line capacity, or the ultimate load. In this study, the optimum yield-line capacity is used as the basic capacity of the slab in order to determining the load enhancement (i.e. the extra load that the slab can carry beyond its basic capacity). Therefore, conducting yield-line analysis is the key to determine the efficiency of the tensile membrane action at large deflections.

When a slab is loaded to the verge of failure, yield-lines form along the most stressed areas of the slab by the formation of continuous plastic hinges. These yield-lines together form what is known as the yield-line pattern (Kennedy & Goodchild 2004). It is important to determine the correct yield-line pattern in order to conduct the yield-line

analysis and to calculate the optimum yield-line capacity correctly, as is discussed in Chapter 6. The yield-lines divide the slab into parts which are called slab elements. When the slab deflects, these slab elements rotate about the yield lines as rigid bodies (Szilard 2004). A typical yield-line pattern is demonstrated in Figures 8 and 9.

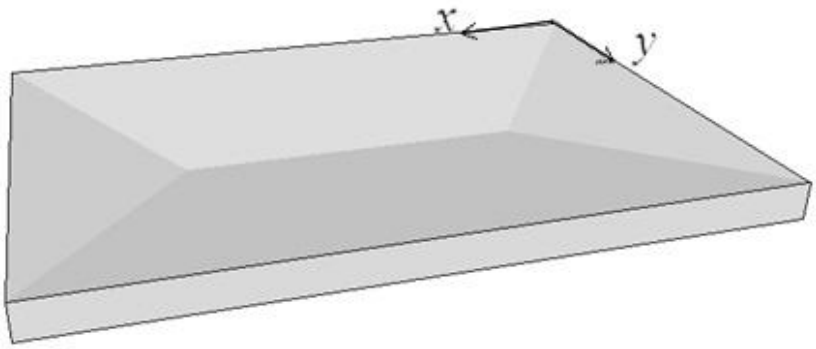

Figure 8: Yield line pattern of a rectangular slab

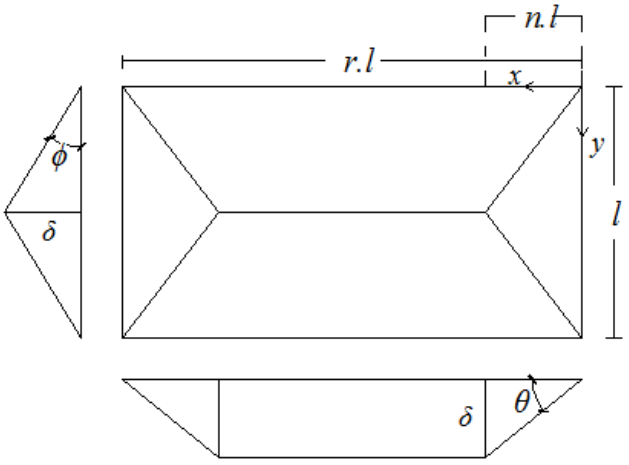

Figure 9: Typical yield-line pattern on a rectangular slab

l is the short span of the slab.
n is the yield-lines intersection point distance from the short edge of the slab.
θ is the angle of rotation of slab element about it the short span of the slab.
ϕ is the angle of rotation of slab element about it the larger span of the slab.
δ is the maximum deflection of the slab

This study considers a few of the yield-line method's assumptions. These are:

1. The yield lines are straight lines.
2. The yield lines pass through the intersection points of the axis of rotation of two adjacent elements (i.e. the slab corners).
3. The yield lines end at the boundary of the slab.
4. The yield lines develop along the lines of maximum moments. These moments develop to the ultimate moment and then remain constant.
5. The slab elements, which are defined by the formation of the yield lines, are rigid bodies; and the elastic deformations within these elements are negligible.
6. When the yield-line pattern is optimum, no twisting moments exist.

The first three of these assumptions are apparent in Figure 9. Although these assumptions are used in this study, they are over-simplified, as is further discussed in Section 8.2. Nonetheless, this is justifiable in simplified methods. This study presents an alternative simplified method intended to replace the Bailey-BRE method, and the effects of such simplification is not significant. The last four assumptions are key to the calculation of the optimum yield-line capacity. When calculating this optimum capacity, only the sagging moments at the yield-lines are considered, and no twisting moments are considered within the slab elements, as is discussed in Section 6.2.

2.3 The work method

The work method, also known as the virtual work or energy method, is the simplest method of implementing the yield line theory in order to calculate the critical load, thus the resisting moment, at which the slab fails (Kennedy & Goodchild 2004). The main principle of the method is that the work done externally and the work dissipated internally on the slab must be in balance. That is, the external work done by the loads on the slab equals the internal work dissipated by the slab along the yield lines. This balance principle is mathematically expressed by:

$$\sum_{all\ regions} (p.\delta) = \sum_{all\ regions} (M.l_i.\theta) \quad (1)$$

p is the external load acting on the slab
M is the moment of resistance of the slab at the hinge lines per length unit
l_i is the projected length of the yield-line on the corresponding axis of support

The left-hand term of Equation 1 represents the external work done by the loads on the slab. The right-hand term represents the internal work dissipated by the slab. The application of the work method in this study is discussed in detail in Section 6.2.

The yield line theory and the work method give upper-bound kinematic solutions to the ultimate load. The upper-bound theorem is based on plastic failure mechanisms. When such a plastic failure mechanism takes place, the structure fails. Hence, the minimum upper-bound solution expresses the failure load; while in lower-bound solutions the resultant failure load is either equal to or smaller than the actual failure load (Chen & El-Metwally 2011). This is the reason of describing the upper-bound theorem as either exactly correct or critically wrong. However, the key is to get the correct failure pattern in order to get the correct solution. Once this is satisfied, it is highly unlikely that the yield line analysis is seriously wrong (Kennedy & Goodchild 2004). For the case of this study, this is not a key issue. The failure patterns of rectangular slabs are easy to define, whether the slab is composite or a concrete flat slab, as is discussed in Section 6.1. Figure 10 demonstrates a comparison between the upper and lower bound solutions.

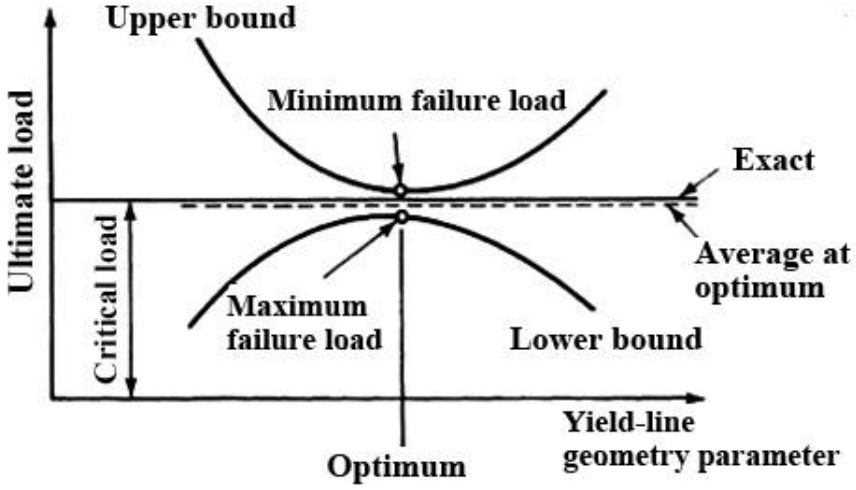

Figure 10: Comparison between upper and lower bound solutions (Szilard 2004)

3 Previous Work on Tensile Membrane Action

3.1 Sawczuk & Winnicki, 1965

Sawczuk & Winnicki (1965) examined the behaviour of simply supported concrete slabs at large deflections. Their paper came after the analysis of post-yield behaviour of circular reinforced concrete plates by R. H. Wood in 1961. Following previous studies, it was noticed that beyond the plastic collapse stage, two factors influence the behaviour of structures: 1. the material strain-hardening; 2. the change in the geometry of the structure during plastic deformations. The assumptions which were considered for Sawczuk and Winnicki's method include the following:

1. The model is based on an energy method.

2. The slab which is considered in this method is a rectangular reinforced concrete slab.

3. The slab is assumed to be simply supported along its four edges.

4. Two failure modes of the slab are considered. The main mode of failure included tension cracks starting at the intersection points of the yield-lines. This mode of failure is adopted in the calculations. The second failure mode included a crack starting at the centre of the slab.

Sawczuk & Winnicki (1965) argue that according to observations, slabs' load-carrying capacity is larger than those estimated by the limit analysis theory, even after modifying for the material strain-hardening. It is observed from experiments that in rectangular reinforced concrete slabs the post yield membrane action is either localized in bending yield hinges zones, or additional membrane hinges form. To balance the membrane action, compressive forces are carried by the supporting edges of the slab, forming what is known as the compressive ring. As deflection increases, membrane forces $N_{\alpha\beta}$ appear. Thus, the yield condition is dependent on bending stresses $M_{\alpha\beta}$ and membrane forces $N_{\alpha\beta}$. Since deflection is accompanied with energy dissipation, Sawczuk and Winnicki express this dissipation d by two components; bending and stretching as follows:

$$d = M_{\alpha\beta}.\kappa_{\alpha\beta} + N_{\alpha\beta}.\lambda_{\alpha\beta} \quad (2)$$

Where $\kappa_{\alpha\beta}$ and $\lambda_{\alpha\beta}$ express the curvature and the extension rates respectively.

According to the energy theory, the work done by the external forces must not be smaller than the energy dissipated by the internal work. Following arrangements, the load-deflection relationship is written as:

$$\int_A p.W\, dA \geq \sum_1^n (N.W + M).\theta.l_i \quad (3)$$

p	is the transverse loading
W	is the deflection
M	is the bending moment
N	is the axial force
θ	is the angle of rotation of the slab element about its support
l_i	is the length of the hinge line
A	is the area of the slab

Sawczuk and Winnicki consider a cross section of unit width, with reinforcement lies at the bottom of the section at distance H from the section's middle plane as shown in Figure 11.

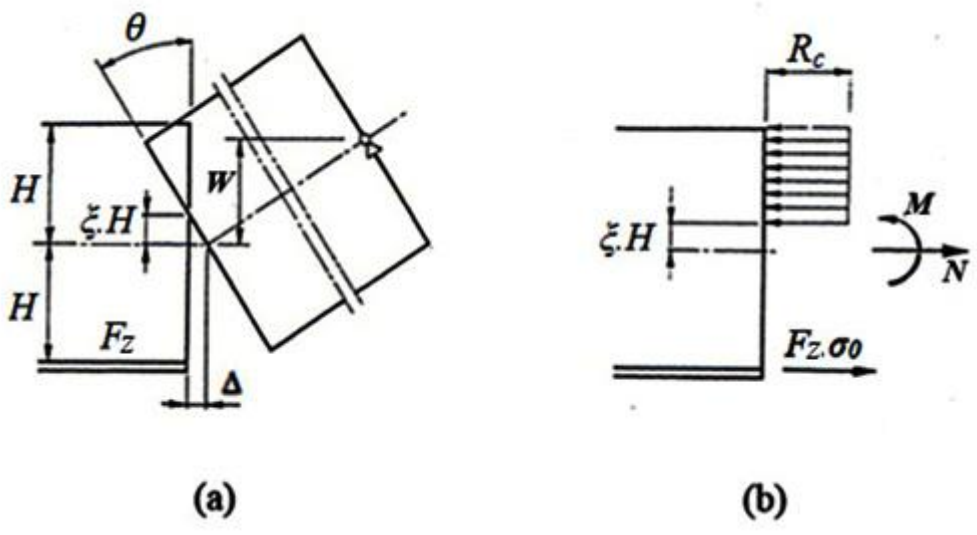

Figure 11: (a) geometry of deformation; (b) stress distribution at failure (Sawczuk & Winnicki 1965)

F_z is the reinforcement area per unit width.
ξ is the average of the neutral layer distance from the middle plane.
R_c is the concrete compressive strength.

From the equilibrium and cross-section analysis, Sawczuk and Winnicki concluded that the minimum deflection required for membrane action is given by:

$$W_{min} = 2H \,.\, \xi_0 \tag{4}$$

Where ξ_0 is the neutral layer distance at stress state at the bending collapse (i.e. $N=0$) and it is dependent on the reinforcement percentage and the materials properties.

Considering a plate which is free to rotate but horizontally restrained, a kinematic collapse mode could be depicted as shown in Figure 12 across the points A, K, L, C", C', C, D, D" and E.

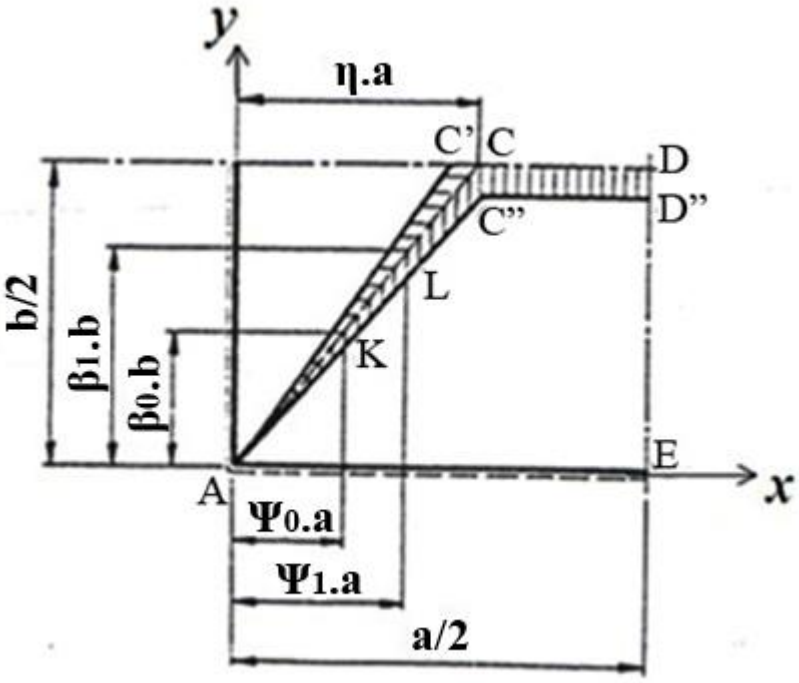

Figure 12: Kinematic collapse mode (Sawczuk & Winnicki 1965)

a is the larger span of the slab.
b is the short span of the slab.
β_0 is a parameter defining the bending response range in the *y*-direction.
β_1 is a parameter defining the membrane response range in the *y*-direction.

Ψ_0 is a parameter defining the bending response range in the *x*-direction.
Ψ_1 is a parameter defining the membrane response range in the *x*-direction.
η is a parameter defining the collapse mode of the slab.

The process goes through many stages, depending on the magnitude of the deflection W as follows:

- Pure bending moment work: within the range $0 \leq W \leq 2\xi_0.H$.
- Combined bending moment and membrane action: within the range $2\xi_0 \leq W \leq 2H$.
- Pure membrane action: when $W \geq 2H$.

Taking other cases into account, in consistence with Wood (1961), Sawczuk & Winnicki (1965) argue that if a rectangular slab is horizontally unrestrained, then as the deflection increases, a full-depth crack appears perpendicularly to the slab's long edge with no rotation of its adjacent parts relatively to the crack is observed. This is illustrated in Figure 13 across the slab points A, F_0, F_1, C", C', C, D, D", E" and E . The difference between this collapse mode and the mode presented in Figure 12 is the rotation of the element ACDE around its perpendicular-to-plane axis when the slab is horizontally unrestrained. The authors observe that the extent of the bending zone depends on the deflection magnitude. Furthermore, it appears that the compression in the slab is carried without any energy dissipation.

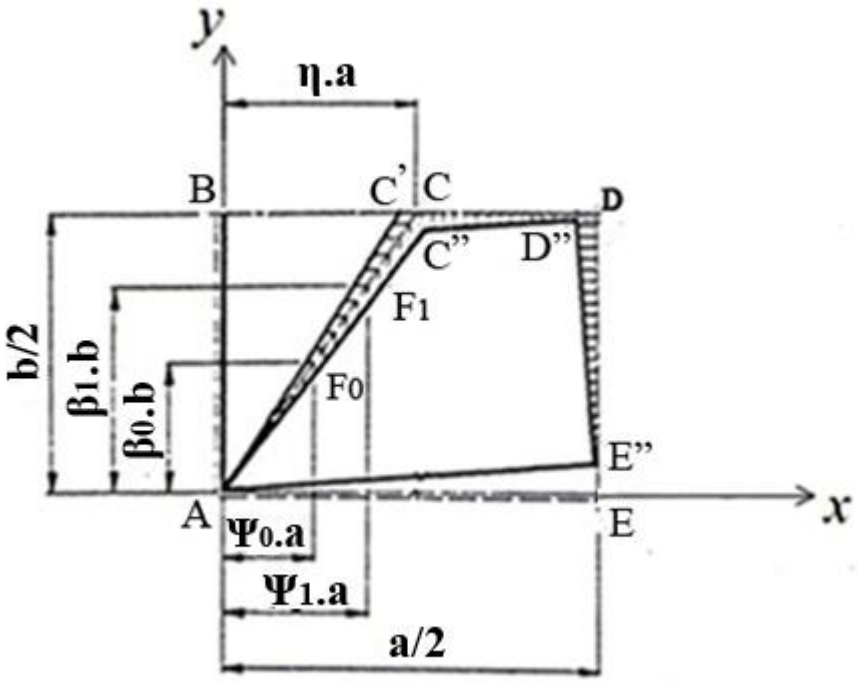

Figure 13: Collapse mode for horizontally unrestrained rectangular plates (Sawczuk & Winnicki 1965)

Sawczuk and Winnicki argue that the collapse mode, shown in Figure 13, occurs with small values of limit loads accompanied by deflection of the order of magnitude of the slab thickness. However, with larger deflections, transverse cracks form with a lower load value.

Figure 14 shows a collapse mode with tension cracks involved. Bending moments act along the hinge ACD, while the line FC is subjected to concentrated axial extension.

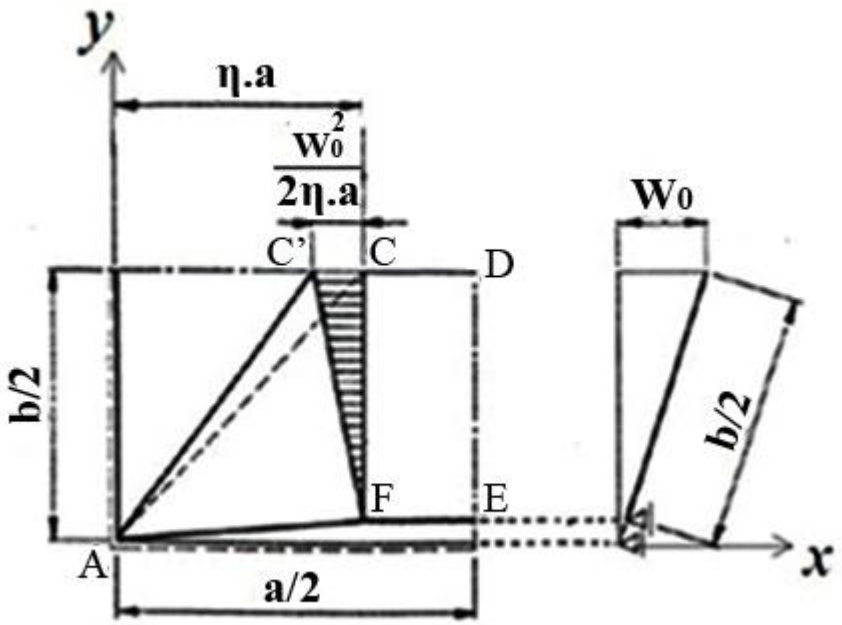

Figure 14: Failure mode involving tension cracks (Sawczuk & Winnicki 1965)

W_0 is the maximum deflection of the central yield-line of the slab.

Sawczuk & Winnicki (1965) argue that tests conducted on reinforced concrete slabs showed agreement with the predictions of the theoretical method of post-yield analysis for reinforced concrete slabs. The authors also argue that their study demonstrates the significant influence of geometry changes on slabs' load-carrying capacity, especially in the case of restrained edges.

The method that was established by Sawczuk & Winnicki (1965) had certain benefits and shortcomings as follows:

Benefits:

- The method includes the formation of cracks across the short span of the slab in the failure modes. Although the adopted failure mode itself is not correct, at least the model includes slab tension cracking.

Shortcomings:

- The mode of failure which is adopted for the method contradicts Wood's (1961) test observations.

- The method shows slab boundary forces, even for simply supported slabs. This is illogical (Hayes 1967b).
- The moments along the yield-lines are equal to the moments given by the simple yield-line theory. Therefore, taking the transverse moment equilibrium of rigid slab portions does not lead to load-enhancement (Hayes 1967b).

Although Sawczuk's method includes one of the probable modes of failure (i.e. cracks across the short span of the slab) a new model that includes the correct mode of failure was necessary to be developed. A superior model which took the cracking failure mode into account was established later by Hayes (1968 a&b), changing the method from energy based to equilibrium based method, as is further discussed in Section 3.3.

3.2 K. O. Kemp, 1967

Kemp (1967) developed a solution for a yield load of a square reinforced concrete slab. The solution had the following list of assumptions:

1. Upper bound solution for square reinforced concrete slabs is assumed.
2. Slabs in this method are simply supported.
3. Rigid-perfectly plastic behaviour is assumed for this model.
4. The slab fails in a diagonal yield-line pattern.
5. The method is limited to isotropic reinforcement, located at the bottom of the slab.

Kemp (1967) argues that when a slab is loaded, a yield line mechanism forms according to the simple yield-line theory. Only after this formation of the yield line mechanism, membrane forces can be significant. Kemp assumes normal diagonal yield line pattern forming four triangular portions, as illustrated in Figure 15.

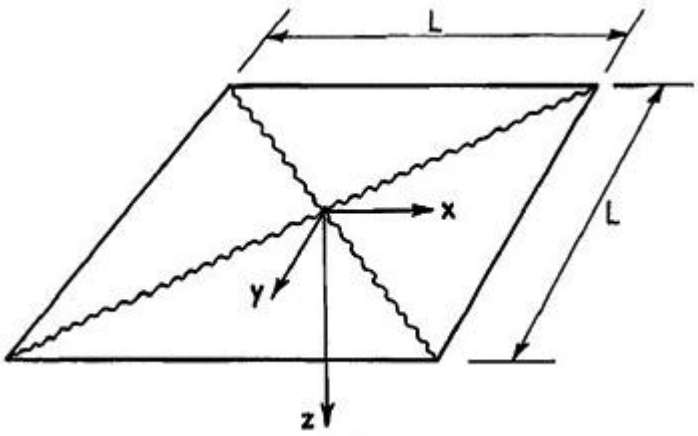

Figure 15: Diagonal yield-line pattern of a square slab (Kemp 1967)

The four triangular portions of the slab, which are defined by the yield-lines, are assumed to be rigid. Kemp argues that plastic deformations, whether axial or bending, can only occur along the yield lines. The axial-plastic strains in the mid-plane surfaces of the portions depend on the two possible movements of these surfaces, which are: 1- the rotation of the rigid body about the simply supported edges; 2- the horizontal rigid-body movement perpendicularly on the slab's edges. In order to determine the axial forces at the slab's mid-depth, Kemp determines the axial strains at that depth. Kemp uses the geometry equilibrium. At a particular deflection $w_{o,}$ the rotation and horizontal movement of each element can be obtained. Taking the rigidity of each triangular element, the plastic axial elongation e at any point on the yield line can be determined. Kemp gives the relationship between the rotation θ, horizontal movement Δ and the elongation e by:

$$\Delta + \left(\frac{L}{2} - x\right)\cos(\theta) + \frac{e}{\sqrt{2}} = \left(\frac{L}{2} - x\right) \tag{5}$$

x is the distance of the studied point on the yield line from the origin in the x-direction.

L is the span of the square slab.

θ is the rotation of the triangular middle surface element about the free edge

With rearrangement and substitution, the height of the neutral axis from the mid-depth of the slab μ in relation to the deflection w_o is given by:

$$\mu = \mu_o - \frac{w_o}{L} . x \tag{6}$$

μ_o is the height of the neutral axis from the mid-depth at the origin.

To determine the value of μ_o for a given deflection w_o, the horizontal equilibrium for each triangular element should be considered. The triangular element, shown in Figure 16, should be in horizontal equilibrium when subjected to the axial force *N* along the yield lines.

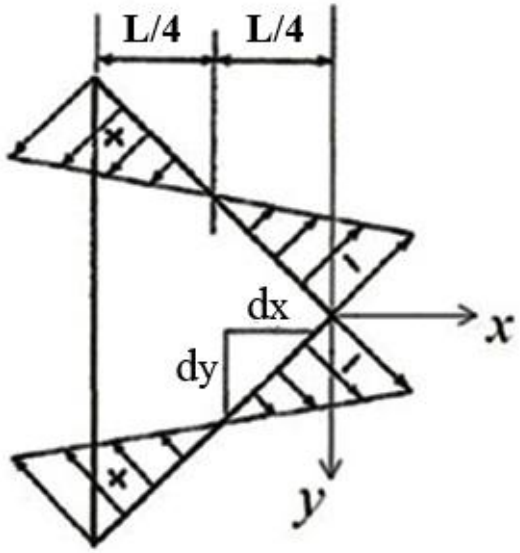

Figure 16: Horizontal forces on the triangular element before the pure membrane action occurs (Kemp 1967)

The full derivation is not presented in this study. The calculations done by Kemp (1967) give the value of μ_o as:

$$\mu_o = \frac{w_o}{4} + \alpha \frac{M_o}{T_o} \tag{7}$$

Where $\alpha \frac{M_o}{T_o} = \left(\frac{d}{2} - \frac{2k_2 T_o}{k_1 u}\right)$ and it represents the height of the neutral axis above mid-depth when *N*=0

d is the overall depth of the slab

T_o is the reinforcement yield force per unit width
u is concrete cube strength
M_o is the yield bending moment with zero axial force
k_1 is a coefficient related to average compressive stress on concrete at yield.
k_2 is a coefficient related to the depth of the resultant compressive force in concrete at yield.
α is a coefficient related to the yield criterion in a non dimensional form.

Equation 7 is valid for a particular range of deflection (i.e. $w_o' = 2d - 4\alpha \frac{M_o}{T_0}$.)

Where w_o' is the deflection limit to keep the neutral axis depth inside the slab section. When the central deflection exceeds the limit w_o', the neutral axis lies outside of the slab section, and the slab cracks at its central zone. The axial force then is $N = -T_o$ (i.e. tensile membrane action is mobilized). As the deflection increases, the pure membrane action spreads outwards from the central zone of the slab. Kemp assumes that the yield line pattern remains unchanged, and plasticity still applies to the diagonal yield lines and thus the equilibrium persists. However, Kemp argues that if the outwards-extension of the pure membrane action reached a position $x=l/2$, a discontinuity in the forces at that position takes place, as shown in Figure 17.

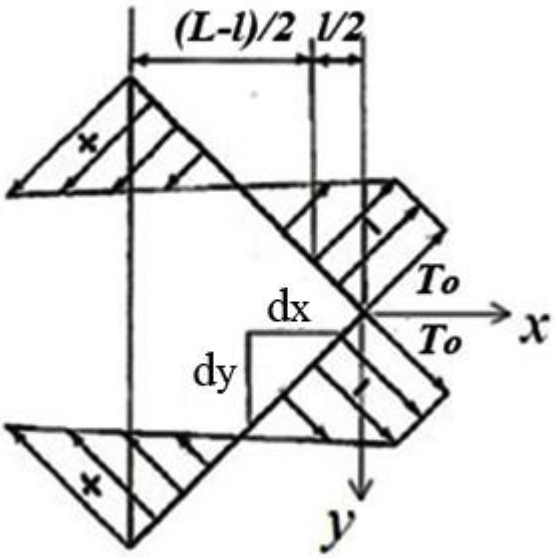

Figure 17: Horizontal forces on a triangular element after the formation of pure membrane action (Kemp 1967)

l is the extension of the pure tensile membrane.

dx and *dy* represent differential distances in the *x* and *y* directions, respectively.

Kemp's calculations give the relationship between the deflection in the central region w_o and the extension of the pure tensile membrane l as the follows:

$$w_o = \frac{8\beta L^2}{(L-l)^2}\frac{M_o}{T_o} \tag{8}$$

β is a coefficient related to the yield criterion in a non dimensional form. It is given by:

$$\beta = \frac{\frac{k_2 T_o}{k_1 k_3 u d_1}}{\left(1 - \frac{k_2 T_o}{k_1 k_3 u d_1}\right)} \tag{9}$$

k_3 is a coefficient related to the average compressive force in the concrete at yield.

The extension of the pure tensile membrane l is given by:

$$l = L\left[1 - \sqrt{\frac{w_o'}{w_o}}\right] \tag{10}$$

The axial force *N* can be determined by the relation:

$$\frac{N}{T_o} = \frac{w_o}{w_o'}\left[\frac{4x}{L} - 1\right] \tag{11}$$

x in Equation 11 represent an arbitrary distance on *x* axis.

As Equation 11 shows, for deflections lower than w_o', the axial force changes linearly along the yield line and equals zero when *x=L/4*. Thus, the membrane force is tensile at the inner half of the slab, and compressive at the outer half of it (Kemp 1967).

Since the yield membrane forces $\frac{N}{T_o}$ and the yield moments $\frac{M}{M_o}$ (where *M* is the yield bending moment) were determined as a function of the slab deflection w_o, Kemp determined the yield loads corresponding to any magnitude of the deflection w_o by taking the equilibrium of the slab. Due to the symmetry, vertical shear and torsional moments along the yield lines are zero. Thus, yield-load calculations can be done for

one of the triangular elements of the slab. Kemp takes the moment equilibrium about the mid-depth of a simply supported slab edge, as shown in Figure 18.

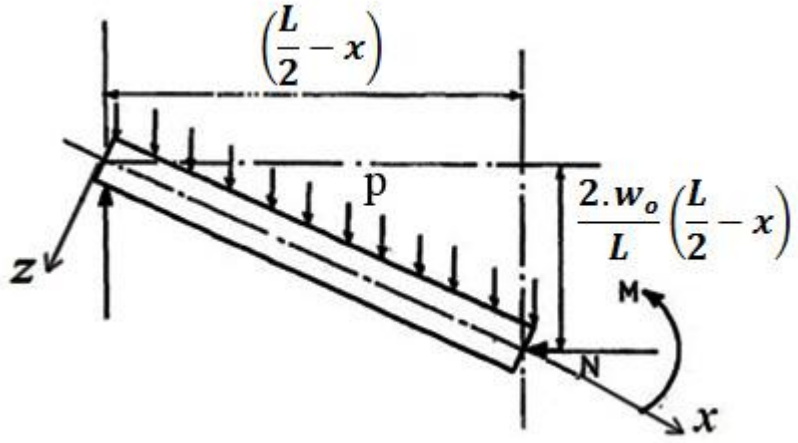

Figure 18: Moment equilibrium of a triangular rigid-element (Kemp 1967)

The whole derivation is not presented in this thesis. Thus the equations of the two cases are presented directly.

For deflections less than the critical deflection of w'_o (i.e. $w_o \leq w'_o$):

$$\frac{p}{p_y} = 1 + \frac{{w_o}^2}{64\beta}\left(\frac{T_o}{M_o}\right)^2 \tag{12}$$

p is the uniformly distributed load
p_y is the yield-line theory collapse load

For deflections larger than the critical deflection of w_o (i.e. $w_o \geq w'_o$):

$$\frac{p}{p_y} = 1 + \beta\left[\sqrt{\frac{w_o}{2\beta}\frac{T_o}{M_o} - 1}\right]^2 \tag{13}$$

Kemp (1967) argues that the yield load due to membrane action stays pretty small until full-depth cracks occur in the slab. The magnitude of this yield load becomes significantly larger as deflections exceed this stage, and noticeable for slabs with low reinforcement percentage. The effect of the reinforcement ratio on the increase of the yield load, due to membrane action, beyond the yield line theory collapse load is illustrated in Figure 19.

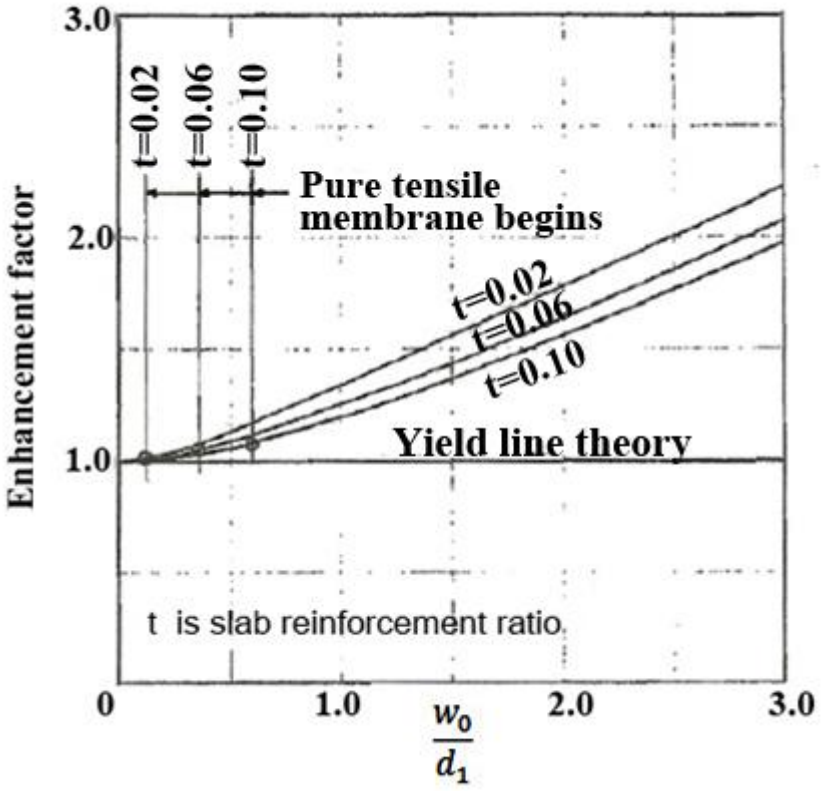

Figure 19: The effect of membrane action of yield load due to deflections and steel ratio (Kemp 1967)

t is the slab reinforcement ratio.

Figure 19 shows no deflection before reaching the simple yield line theory collapse load. The reason for this is the assumed rigid perfectly plastic behaviour of the slab. However, such deflections before this stage appear in the experimental results. Kemp argues that these theoretical yield loads are obtained as upper bound solutions. Therefore, these theoretical values are conservative, where in reality the yield loads are estimated to be larger than what is shown. This is due to the strain-hardening in the reinforcement, until reaching a deflection value of w_o/d_1 =1, where d_1 is the effective

depth of the slab. In practice, a collapse load is reached as the reinforcement in the central region of the slab fractures, or when the concrete on the perimeter of the slab crushes (Kemp 1967).

The benefits and shortcomings of Kemp's model are summaries as the following:

Benefits:

- Kemp's method presents the relationship between the slab deflection and the load-enhancement. This relationship is key for the mechanics of tensile membrane action at large deflection for future studies, including this thesis, as is further discussed in Section 6.3.

Shortcomings:

- Hayes (1968b) shows that the neutral axis depth of the slab affects the load enhancement by only 2%. This means that the method is almost insensitive to neutral axis depth.
- Bailey (2001) shows that Kemp ignored the development of a large crack across the short span of the slab, which leads to overestimating the enhancement factor.

Because of such shortcomings, especially ignoring the formation of full-depth cracks, a new model was necessary as a replacement for Kemp's model of square slabs, in addition to addressing rectangular slabs. Hayes (1968 a&b), Bailey (2001) and Burgess et al. (2014) corrected this and took the formation of full-depth cracks into consideration. As an extension of the method that was established by Burgess et al. (2014), this study also takes the full-depth cracks into consideration, as is further discussed in Chapter 6.

3.3 Brian Hayes, 1968

3.3.1 TMA for square slabs

Hayes (1968a) presents an equilibrium based method to examine the tensile membrane action, TMA, for concrete slabs. The assumptions that are considered in Hayes' method include the following:

1. Square and rectangular reinforced concrete slabs are considered.

2. The slab is considered simply-supported along its four edges.
3. Reinforcement is considered at yield stress in this model.
4. The equilibrium method is assumed for this model, based on yield-line theory.
5. Plastic analysis at large deflections is assumed.
6. Cracks across the short span of the slab at the intersections of the yield-lines are assumed as the main failure mode of the slab.
7. Compression is confined to a peripheral ring around the central region of the slab with triangular compressive stress blocks at large deflections.

The collapse pattern that of the slab that was considered by Hayes (1968a) is shown in Figure 20.

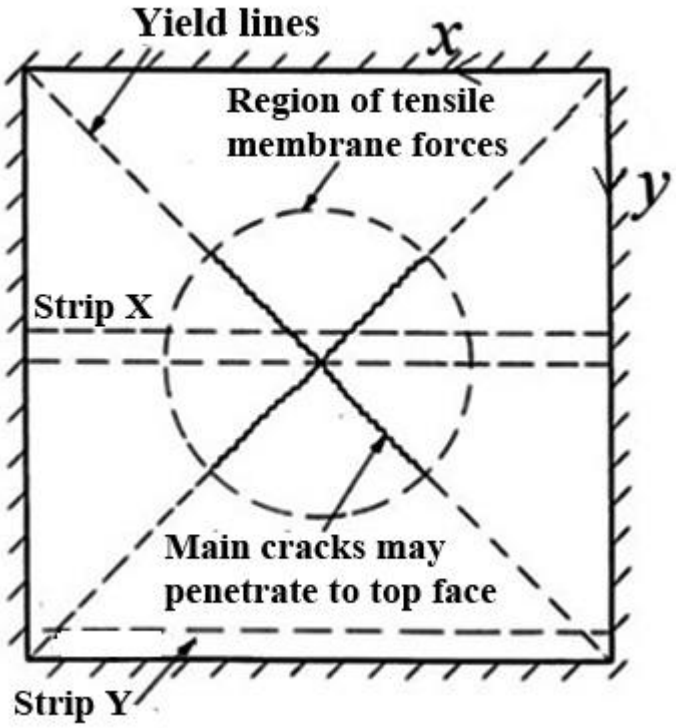

Figure 20: Diagonal collapse pattern of a simply supported slab (Hayes 1968a)

At large deflections, internal slab strips, as the strip X as illustrated in Figure 20, tend to move inward. However, the strips on the edge of the slab, like the strip Y, do not deflect due to their being supported. Therefore, these supported strips do not move inward. Within reinforced concrete slabs, the adjacent strips of the two kinds (i.e. X and Y

strips) interact as the slab deflects; leading to tensile stresses in the internal strips, and compression stresses in the edge strips. Eventually, tensile net is generated at the centre of the slab, and a compression ring appears around it. This membrane action is added to the flexural stresses. However, at large deflections pure tension is generated across the depth of the slab at its central region.

Hayes (1968a) argues that this mechanism can be developed in both square and rectangular slabs. Hayes argues that the triangular part (i.e. the triangular slab element) of a square slab which is collapsing in a diagonal yield-line pattern acts as a deep beam which is relatively strong in resisting the in-plane bending. However, in isolated rectangular slabs, the bigger the aspect ratio is (i.e. the longer the rigid part) the weaker its resistance to the in-plane bending action. This is illustrated in Figure 21.

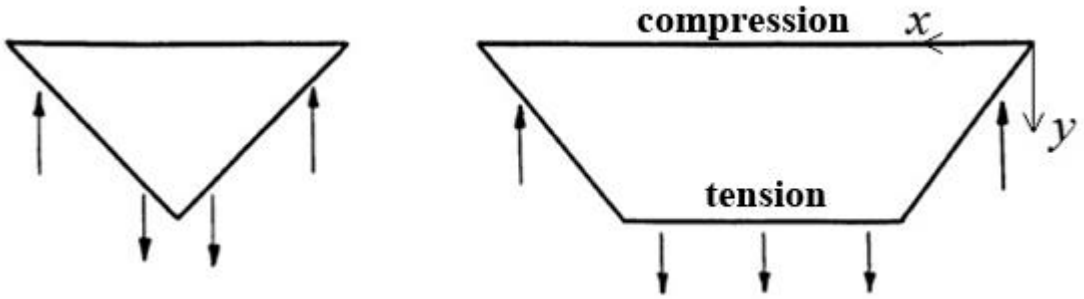

Figure 21: TMA in square and rectangular slabs (Hayes 1968a)

Hayes (1968a) observed from previous tests on slabs that excessive loads which go beyond the predictions of the simple yield-line theory can be supported. Hayes' study is based on a proposition made by Taylor (1965), that the load carrying capacity could be determined by allowing the increase in the reinforcement effective depth which results from the redistribution of the compression zone. This is illustrated in Figure 22.

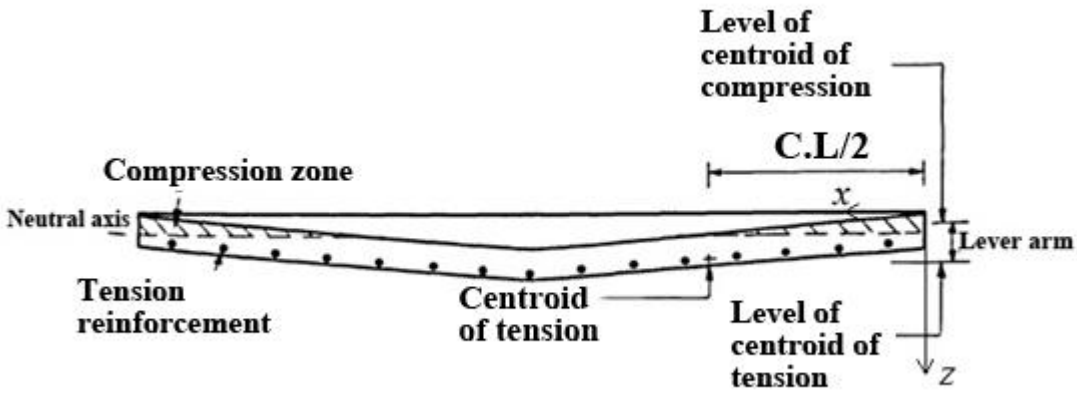

Figure 22: Development of TMA at large deflections (Hayes, 1968)

C is the total compressive membrane force.

L is the larger span of the slab

Figure 22 shows that the problem is based on the analysis of triangular compression zones at the slab's edges at large deflections. Hayes took Mattock & Kriz (1961) approach to address this problem. Mattock & Kriz came up with two methods to analyse sections with irregular compression zones. The first method used the same normal assumptions of the ultimate load analysis of reinforced concrete sections. It was programmed in computer software which calculated the ultimate strength of reinforced sections with irregular compression zones. The second method used rectangular stress zones for the analysis. By comparing both methods, Mattock and Kriz found that for under-reinforced sections the difference between a rectangular stress zone and linear approximations did not exceed 2% as a maximum. Hayes (1968a) argues that slab sections are usually under-reinforced, so little difference is expected between the methods that were presented by Mattock & Kriz (1961). Hayes also argues that comparisons show that the British Standard Code of Practice (CP 114) parameters are very similar and close to Mattock and Kriz's rectangular stress zones parameters.

Hayes' analysis of the development of TMA in square simply-supported reinforced concrete slabs is based on the development of the compression zone through successive stages as deflection increases. In the first stage, rectangular compression zones exist during the zero-deflection state. The analysis then depend on the simple yield-line

theory and complied with the calculation of the ultimate moment of the section. In the second stage, according to Hayes (1968a), the compression zone becomes triangular at large deflections. Therefore, the whole reinforcement is at its yield stress. Hayes argues that this is due to small strength-deflection characteristic at this stage. At the third stage, the compression zone goes deeper until the reinforcement at the corner of the slab is subjected to compression, hence it is prevented from reaching its yield stress. With the compression zone reaching the soffit of the slab, the analysis ends. It is worth noting that the intermediate stage between the first and the second stages, where the compression zone is trapezoidal, is not considered in Hayes' analysis. Figure 23 demonstrates the development of TMA through the three stages.

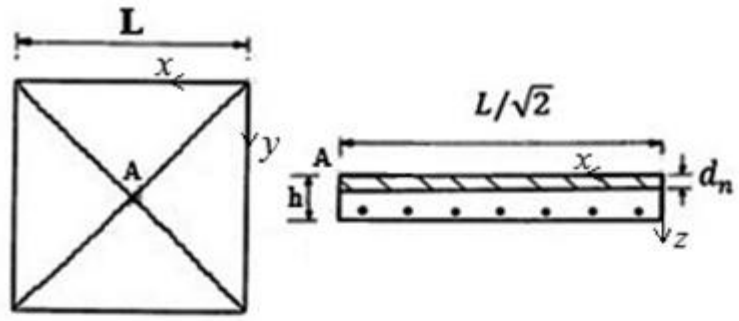

Tensile membrane analysis - stage 1

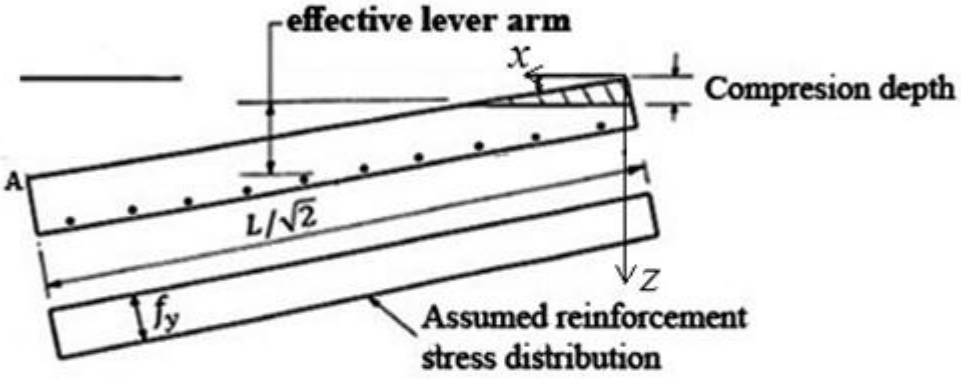

Tensile membrane analysis - stage 2

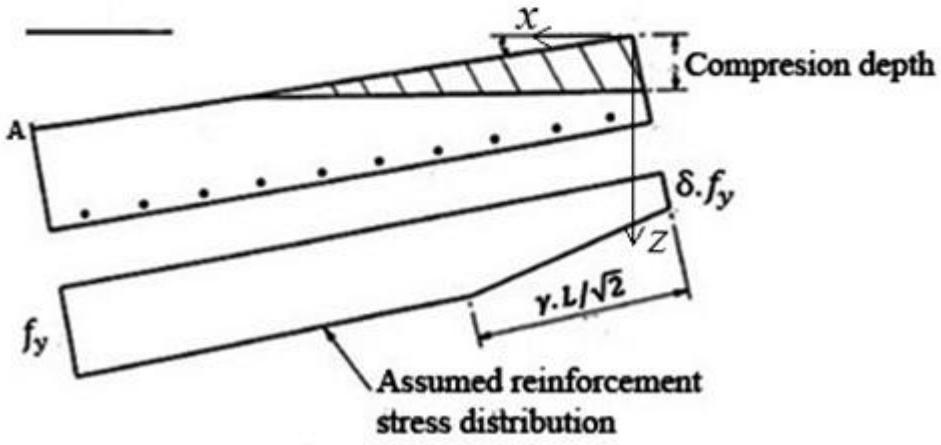

Tensile membrane analysis - stage 3

Figure 23: Tensile membrane stages (Hayes 1968a)

A here is merely a reference point.

d_n is the concrete compression depth at zero deflection analysis.

h is the depth of the slab.

f_y is the steel yield stress.

δ is a parameter fixing maximum reduction in the reinforcement stress.

γ is a parameter fixing the proportion of the reinforcement which does not attain yield stress.

Hayes argues that at the third stage, the depth of the compression zone causes reduction in the reinforcement force. This reduction, in turn, affects the area of the compression zone. The enhancement of the load-carrying capacity is given by the ratio of k'/k_1.

Where: $k_1 = \frac{the\ lever\ arm}{slab\ thickness}$, for zero deflection analysis

$k' = \frac{the\ lever\ arm}{slab\ thickness}$, for tensile membrane analysis

This analysis was coded in computer software for the strength-deflection characteristic purpose. This was carried out for simply-supported slabs. A deflection increase, in increments of one tenth of the slab thickness was loaded to the program up to three times the slab thickness in order to calculate the enhancements in load carrying capacity, compared to the simple yield-line theory prediction. Presentation of the analysis results is shown in Figure 24.

As Figure24 shows, the greatest enhancement corresponds to slabs with lightest reinforcement. However, as Hayes explains, it should be noticed that for such lightly reinforced concrete slabs, the steel force reduction does not occur. Hayes argues that the enhancement due to membrane action is increased when the reinforcement is concentrated towards the centre of the slab, compared to uniform reinforcement spacing. The degree of such reinforcement concentration depends on the design method.

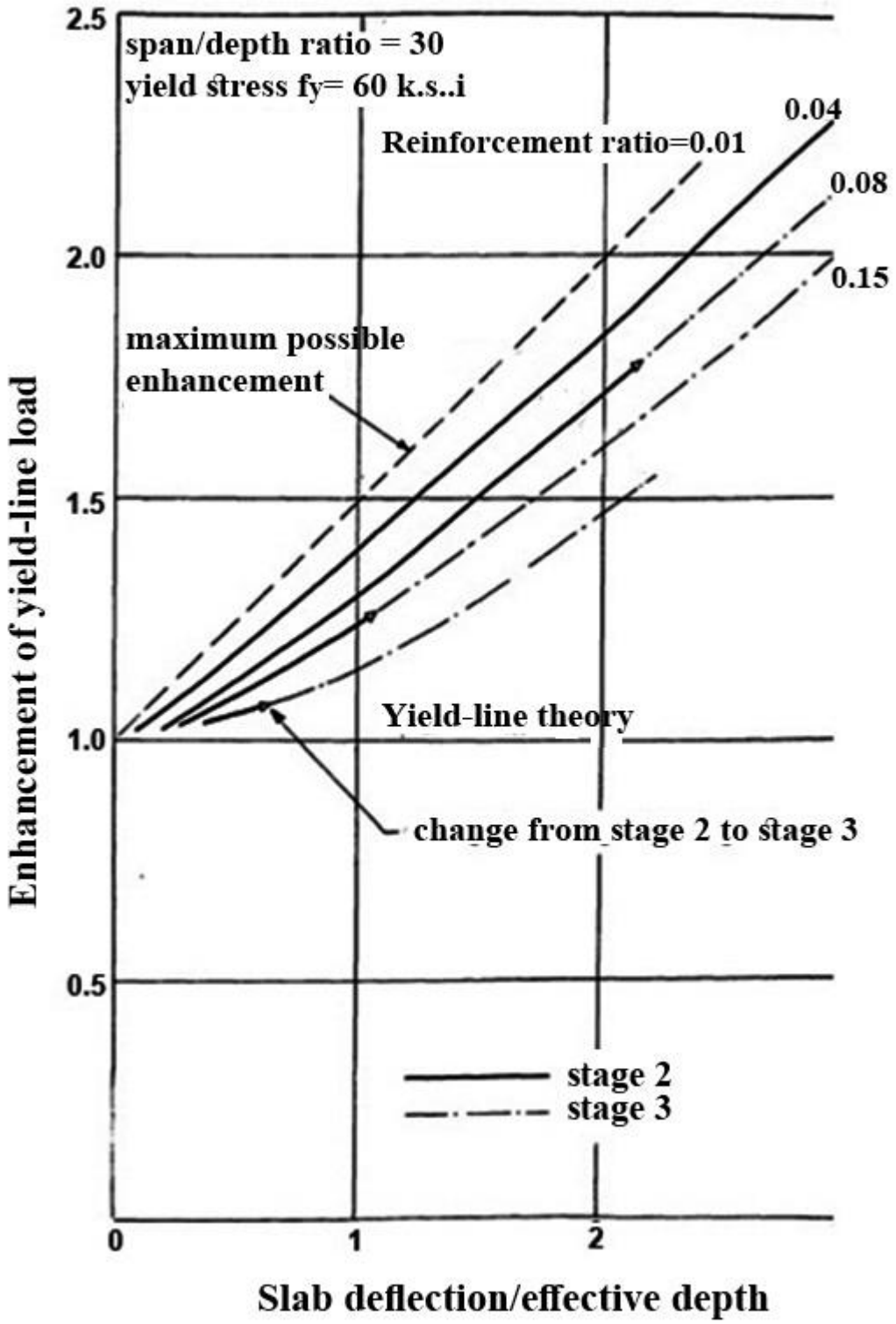

Figure 24: Predicted strength-deflection characteristics allowing for TMA for square slab (Hayes 1968a)

3.3.2 TMA for rectangular slabs

Hayes (1968a) argues that, according to Kemp (1967), if the forces in a square slab which are acting on the triangular elements of the slab are considered, then the triangular elements are subjected to in-plane bending action. While this was occasionally observed in square slabs, it could be generally realized in tests on rectangular slabs. This in-plane bending action was discovered by Sawczuk & Winnicki (1965), allowing the mobilization of tensile membrane action only due to the boundary conditions. Sawczuk considers the isotropic reinforcement case only. This was extended to cover orthotropic reinforcement in rectangular slabs by Hayes. Hayes argues that the increase of strength compared to the yield line theory is proportional to deflection. However, this increase becomes smaller as the coefficient of orthotropy and the aspect ratio (i.e. the rectangularity) increase. Thus, Hayes (1968b) argues that in order to invest in membrane action, high orthotropy coefficients are not desirable.

Hayes (1968a) established a new equilibrium method, considering a rectangular simply-supported slab subjected to uniformly distributed loads. Rigid-plastic behaviour with rigid rotations and translations are assumed. Whether the cracks are full-depth cracks penetrating the upper surface of the slab, or not, is dependent on the stress distribution. Figure 25 shows the stress distribution when there are no tension cracks penetrating the upper surface of the slab.

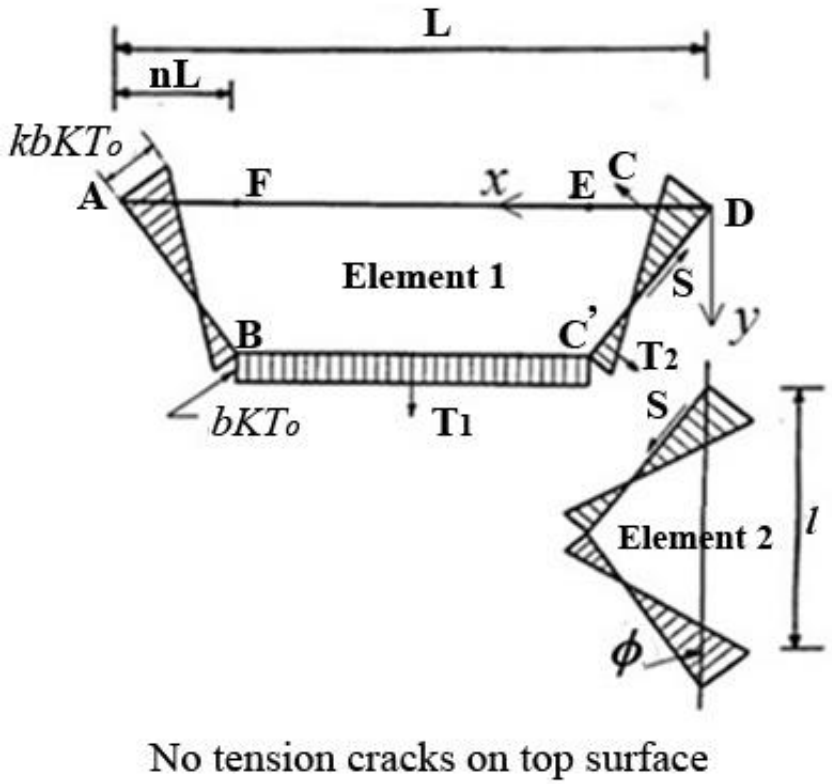

Figure 25: Stress distribution - no cracks penetrate the slab's upper surface (Hayes 1968a)

Points A, B, C', D, E and F mark the slab element 1 boundary and special points to calculate the in-plane stress equilibrium.

k and b are parameters defining the in-plane stress distribution.

K is a parameter related to the steel forces per unit width.

T_o is the steel forces per unit width

T_1 and T_2 are the net tensile membrane forces along the yield-lines.

l is the short span of the slab.

C is the compressive membrane force.

ϕ is a parameter fixing the yield-line pattern.

S is the in-plane shear force at the yield-lines.

After substitution and arrangements, Hayes gives the equation of the parameter defining the in-plane stress distribution k as follows:

$$k = 1 + \frac{4n^2a^2(1-2n)}{1+4n^2a^2} \tag{14}$$

Where: n is a parameter fixing the yield-line parameter
a is the slab aspect ratio (L/l)

By calculating the moments of the sections BF and C'E, shown in Figure 25, considering that the reinforcement along these sections yielded, the second parameter defining the in-plane stress distribution b is given by:

$$b = \frac{3}{K(1+4n^2a^2)(2k-1)} \tag{15}$$

K is a parameter related to the steel forces per unit width.

Hayes gives the slab's load carrying capacity by calculating the moment equilibrium of the slab elements 1 and 2 around their axes of rotation. The contribution of the moment equilibrium due to membrane forces and the moment equilibrium due to bending moments are defined separately.

3.3.2.1 Contribution due to membrane forces:

Hayes presents the equations to determine the enhancement due to membrane forces compared to the case of pure moment (i.e. when membrane forces do not exist). Hayes argues that if the moment about the support due to the membrane forces is divided by the coefficient of orthotropy μ, the resistance moment when membrane force is absent M_0 and the larger span of the slab L, then the enhancement due to the membrane forces e_{1m} is given by:

$$e_{1m} = \frac{4b}{(3+g_o')}\left[1 - \frac{n(4+k)}{3}\right]W \tag{16}$$

g_o' is a parameter fixing the depth of the compressive stress block when membrane forces are absent.

W is the yield-line deflection.

For the slab element 2, the enhancement due to membrane forces e_{2m} is given by:

$$e_{2m} = \frac{2bK(2-k)}{3(3+g_o)}\,W \tag{17}$$

$g_o$is a parameter fixing the depth of the compressive stress block when membrane forces are absent.

3.3.2.2 Contribution due to bending moments:

Hayes presents an approach similarly to what was presented by Wood (1961). The full derivation is not presented here. For the slab element 1, the enhancement due to bending moments e_{1b} is given by:

$$e_{1b} = 2n\left[1 + \frac{A'\,b}{2}\,(k-1) - \frac{B'\,b^2}{3}\,(k^2 - k + 1)\right] + (1-2n)(1 - A'b - B'\,b^2) \qquad (18)$$

A' and B' are parameters in the yield-line criterion. They are given by:

$$A' = \frac{2g'_o}{3 + g'_o};$$
$$B' = \frac{1 - g'_o}{3 + g'_o}$$

For the slab element 2, the enhancement due to bending moments e_{2b} is given by:

$$e_{2b} = 1 + \frac{AKb}{2}(k-1) - \frac{Bb^2}{3}(k^2 - k + 1) \qquad (19)$$

A and B are parameters in the yield-line criterion. They are given by:

$$A = \frac{2g_o}{3 + g_o};$$
$$B = \frac{1 - g_o}{3 + g_o}$$

Thus, the ultimate enhancements of combined membrane forces and bending moments e_1 , for the slab element 1, and e_2 for the slab element 2, are given by:

$$e_1 = e_{1m} + e_{1b} \qquad (20)$$

$$e_2 = e_{2m} + e_{2b} \qquad (21)$$

In the case of cracks penetrating the upper surface of the slab (i.e. full-depth cracks) a similar approach is taken in order to determine the in-plane stress distribution. Hayes gives the relations for the full-depth cracks case as follows:

$$e_{1m} = \frac{4}{(3+g_o')}\left[1 - \frac{n}{3}\,(4 - 2v + v^2 + k + kv^2 - 2kv)\right] W \qquad (22)$$

v is a parameter fixing the extent of the central membrane.

$$e_{2m} = \frac{2K}{(3+g_o)}\left[2v - v^2 + 2 - k(1-v)^2\right] W \qquad (23)$$

$$e_{1b} = 2(1-v)\,n\left[1 + \frac{A'}{2}(k-1) + \frac{B'}{3}(k^2 - k + 1)\right] + (1 - 2n + 2vn)(1 - A' - B') \qquad (24)$$

$$e_{2b} = (1-v)\left[1 + \frac{KA}{2}(k-1) - \frac{K^2 B}{3}(k^2 - k + 1)\right] + v(1 - A - B) \qquad (25)$$

Figure 26 shows the stress distribution when cracks penetrate the upper face of the slab.

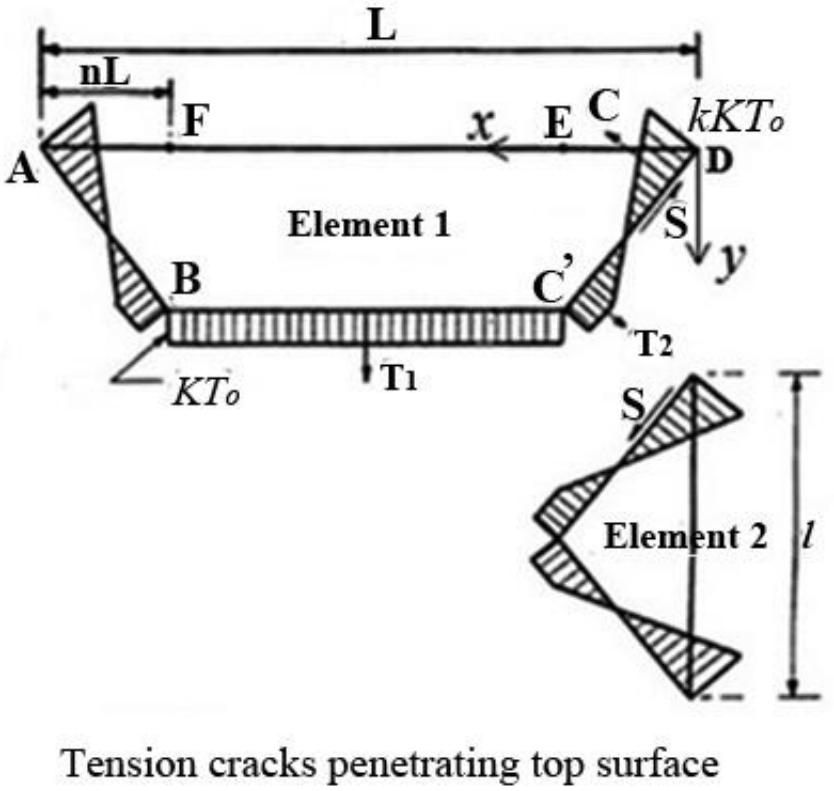

Figure 26: Stress distribution – cracks penetrate the slab's upper surface (Hayes 1968a)

The benefits and shortcomings of the method that was established by Hayes (1968a) can be summarised as follows:

Benefits:

- Hayes presented an equilibrium method which takes into account the formation of cracks across the short span of the slab in the central region. This was an improvement of Kemp's model by taking into account the formation of the cracks through the surface of the slab.

Shortcomings:

- The failure mode which is adopted as the main mode by Hayes contradicts test observations. This is evident when compared to the BRE ambient-temperature test. This is based on the same wrong assumption that was made by Sawczuk.

- The rectangular slab model is handled as a deep beam, assuming that any slab cross-section is in equilibrium in the same way as a beam. This is wrong since a slab is in equilibrium as a whole, not at every arbitrary slice taken from the slab.
- The tension force along the diagonal yield-lines varies linearly with distance as it appeared in the equilibrium figures. This contradicts the assumed plasticity of this model. It also implies that the slab does not crack along the diagonal yield-lines, in contrast to what Hayes assumed in the analysis.
- The orthotropic reinforcement solution is wrong at large deflections. At large deflections, the orthotropy results in two different neutral axis depths for the same section of the slab in the *x* and *y* directions. This means that the same section has two different concrete contact zones in the *x* and *y* directions. This is intuitively wrong.
- Two incompatible enhancement components (i.e. bending and membrane actions) are irrationally added in a single final enhancement factor without justifying the process.
- The enhancement which results from slab element 1 is not equal to the enhancement from slab element 2. This is due to the wrong equilibrium assumption which was taken from the beginning of the calculations.

Hayes' model was a development of the load enhancement calculations of square and rectangular slabs. However, since Hayes' method adopts the wrong mode of failure, and wrong equilibrium assumptions (i.e. the wrong in-plane stress distribution) a new model which corrects these shortcomings was necessary. A correction of Hayes' model was presented by Bailey & Moore (2000a). The method is known as the Bailey-BRE method which is widely used today.

3.4 The Bailey-BRE method

3.4.1 Initial method by Bailey & Moore

Based on a similar equilibrium to the one that Hayes (1968b) took, Bailey & Moore (2000 a&b) presents a new simplified method to calculate the resistance of lightly composite slabs in fire. The simplified method is based on the membrane action to calculate the load enhancement of slabs at high deflections. The method is currently

used in the fire design guides in the UK, Europe (Vassart & Zhao 2011) and New Zealand. Bailey developed the method through follow-up publications. The method is briefly discussed in this chapter through the original and the follow-up papers.

The assumptions that are considered for this method include the following:

1. Equilibrium method based on the yield-line theory is assumed.
2. Reinforcement is at ultimate stress which is 1.1fy instead of the yield stress fy as Hayes assumed.
3. Unlike Hayes and Sawczuk, Bailey considers a failure mode of the slab which includes a crack at the centre of the slab across the short span.
4. Rigid plastic behaviour is assumed in the analysis.
5. The slab is divided into panels; each of which are bounded by protected steel beams, while the internal secondary beams were left unprotected.
6. Slab panels are horizontally unrestrained.
7. Perfect vertical support along the primary beams is assumed.
8. Full connection between the beam and the slab through shear studs is assumed.
9. In elevated-temperature analysis, the slab is heated across its cross-section with a linear temperature gradient.

The design method presented by Bailey & Moore (2000a) divides the slab into multiple panels. Each panel is bounded by protected steel beams on the perimeter, while the other steel beams within the panel were left unprotected, as shown in Figure 27. Each slab panel utilises membrane action, taking into consideration the elevated temperatures of the slab. The contribution of the steel deck under the slab is ignored. This is justified since the deck detaches from the bottom of the slab in fire conditions because of the steam released as the temperature increases. The method assumes that each panel is horizontally unrestrained. This assumption is based on observations from the Cardington fire tests, where it was found that the reinforcement at the protected-peripheral beams fractures at early stages because of the high hogging moments at the perimeter of each panel.

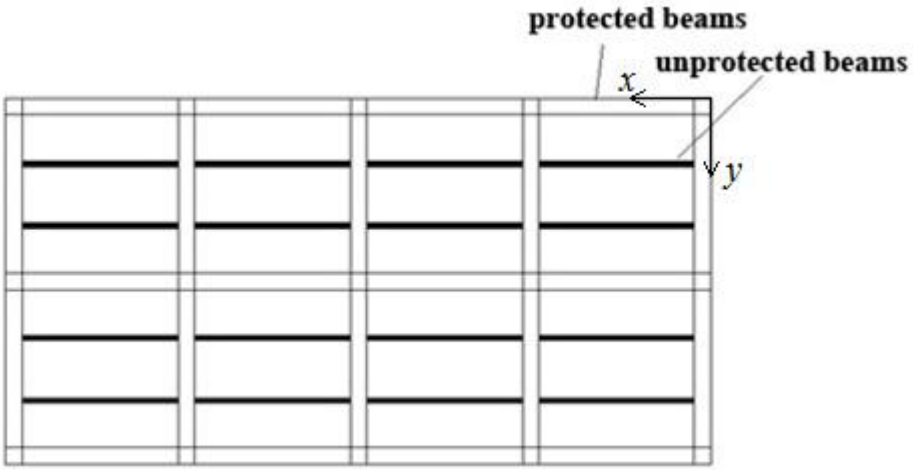

Figure 27: Division of the floor into slab panels

Bailey (2001) argues that both the energy method developed by Sawczuk & Winnicki (1965) and the equilibrium method presented by Hayes (1968b) were based on the assumption that the critical failure mode was caused by the formation of full-depth cracks across the short span of the slab at the intersection of the yield lines. According to Bailey, this assumption contradicts test observations, especially the BRE ambient temperature test. Therefore, Bailey & Moore (2000a) developed a new method to estimate the membrane behaviour of a simply supported concrete slab.

Assuming a rigid plastic behaviour, with a crack forming across the short span of the slab, the distribution of the in-plane stress is shown in Figure 28.

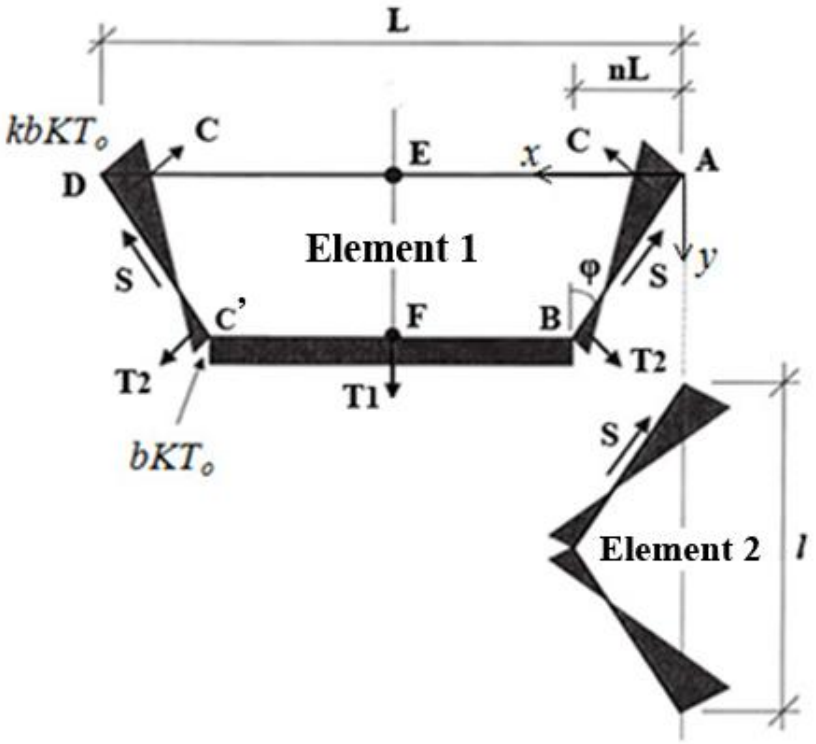

Figure 28: In-plane stress distribution of elements 1 & 2 (Bailey 2001)

Points A, B, C', D, E and F mark the slab element 1 boundary and special points for the in-plane stress calculations.

φ is a parameter fixing the yield-line pattern.

Taking the equilibrium of element 1 gives:

$$\frac{T_1}{2} sin\varphi = C - T_2 \tag{26}$$

Where

$$T_1 = bKT_o(L - 2nL)$$

$$T_2 = \frac{bKT_o}{2}\left(\frac{1}{1+k}\right)\sqrt{(nL)^2 + \frac{l^2}{4}}$$

$$C = \frac{kbKT_o}{2}\left(\frac{k}{1+k}\right)\sqrt{(nL)^2 + \frac{l^2}{4}}$$

Bailey (2001) calculates the in-plane moment of resistance along the line EF at the centre of the slab, shown in Figure 28, assuming that the full-depth crack appears at the centre. This is different than Hayes (1968a) who estimates the moment of resistance along the intersection of the yield-lines. Furthermore, while Hayes (1968a) assumes that the reinforcement at the sections passing through the yield-lines intersection points yielded, Bailey considers that the reinforcement along the line EF is at ultimate stress with a value of $f_u = 1.1.f_y$. Bailey (2001) argues that this assumption is reasonable since the mode of failure here was the fracture of the reinforcement.

By estimating the moments, Bailey's calculations give the value of *b*. Bailey (2001) calculates the enhancement of the slab as a combination of enhancement factors due to the membrane forces and bending resistance. The rationality behind combining these dependent components is further discussed in Section 3.5. By dividing the contribution of each of the membrane forces and bending in the total enhancement, on the yield-line load-carrying capacity, the enhancement of the slab is obtained. Thus, the enhancement factor due to membrane forces for element 1 e_{1m} is given by:

$$e_{1m} = \frac{M_{1m}}{M_0 L} = \frac{4b}{3+g_0}\left(\frac{w}{d_1}\right)\left((1-2n) + \frac{n(3k+2)}{3(1+k)^2} - \frac{nk^3}{3(1+k)^2}\right) \qquad (27)$$

M_{1m} is the moment about the slab supports due to membrane forces in element 1. It is given by:

$$M_{1m} = KT_o Lbw\left((1-2n) + \frac{n(3k+2)}{3(1+k)^2} - \frac{nk^3}{3(1+k)^2}\right) \qquad (28)$$

The resistance moment when membrane force is absent M_0 is given by:

$$M_0 = KT_o d_1\left(\frac{3+g_o}{4}\right) \qquad (29)$$

The moment about the slab supports due to membrane forces in element 2 M_{2m} is given by:

$$M_{2m} = KT_o lbw\left(\frac{2+3k}{6(1+k)^2} - \frac{k^3}{6(1+k)^2}\right) \tag{30}$$

w is the yield-line deflection.

Thus the enhancement factors due to membrane forces for element 2 e_{2m} is given by:

$$e_{2m} = \frac{M_{2m}}{M_0 l} = \frac{4b}{3+g_o}\left(\frac{w}{d_1}\right)\left(\frac{2+3k}{6(1+k)^2} - \frac{k^3}{6(1+k)^2}\right) \tag{31}$$

The effect of membrane forces due to the bending resistance is determined separately for each yield line. The enhancements of the bending capacity due to the membrane forces for elements 1 and 2, e_{1b} and e_{2b}, respectively, are given by:

$$e_{1b} = \frac{M}{M_0 l} = 2n\left[1 + \frac{\alpha b}{2}(k-1) - \frac{\beta b^2}{3}(k^2-k+1) + (1-2n)(1-\alpha b - \beta b^2)\right] \tag{32}$$

M is the bending capacity of the slab

α and β are coefficients related to the enhancements due to bending action. They are given by:

$$\alpha = \frac{2g_o}{3+g_o}, \quad \beta = \frac{1-g_o}{3+g_o}$$

$$e_{2b} = \frac{M}{M_0 l} = 1 + \frac{\alpha b}{2}(k-1) - \frac{\beta b^2}{3}(k^2-k+1) \tag{33}$$

The total enhancement factors *e1* and *e2*, for both slab elements 1 and 2, respectively, are given by:

$$e_1 = e_{1m} + e_{1b} \tag{34}$$

$$e_2 = e_{2m} + e_{2b} \tag{35}$$

The total enhancements of elements 1 and 2, taking into consideration both the membrane forces and bending capacity, are not the same. As Hayes (1968b) explains, this difference between the enhancements of both elements is due to the shear effect whether it is the vertical or in-plane shear. Thus, Bailey (2001) takes an averaging enhancement which represented the total enhancement of the slab as follows:

$$e = e_1 - \frac{e_1 - e_2}{1 + 2a^2} \tag{36}$$

Figures 29-32 show comparisons between the enhancement factors given by Bailey's, Sawczuk's and Hayes' methods against the displacement/effective depth of the slab for different aspect ratios. Both of Sawczuk's failure modes (crack at centre of the slab and crack at intersection of yield lines) are considered in this comparison. Note that the parameter fixing the depth of the compressive stress block when no membrane action exists g_o is the same for all the comparisons here.

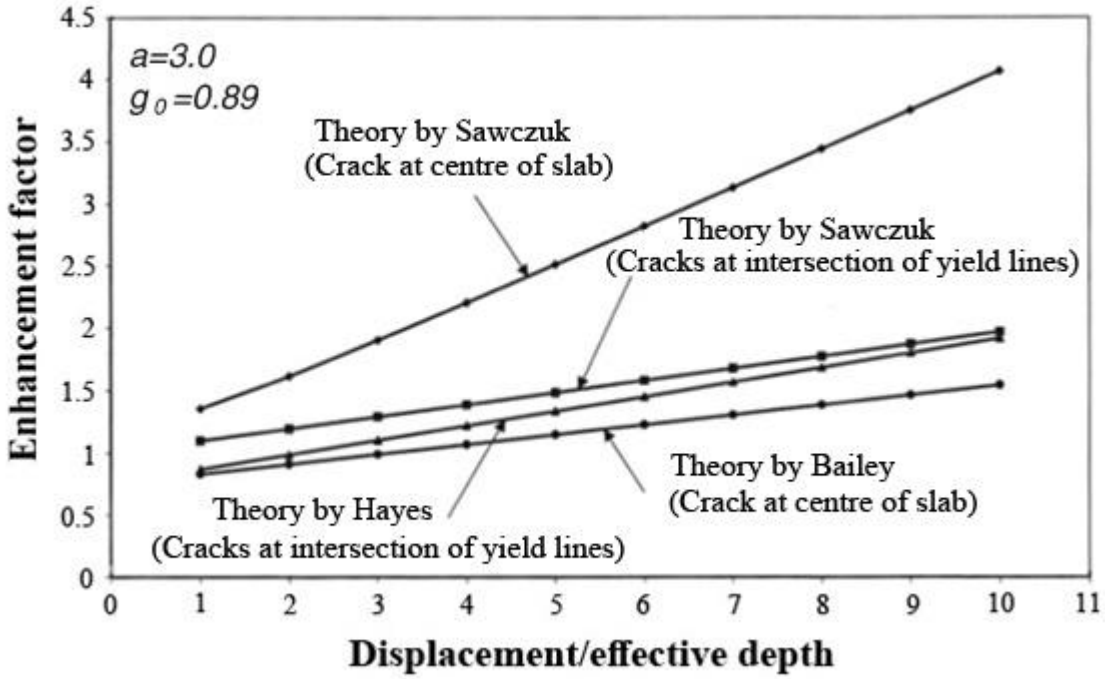

Figure 29: Comparison between Sawczuk's, Hayes' and Bailey's methods with slab's aspect ratio of 3.0 (Bailey 2001)

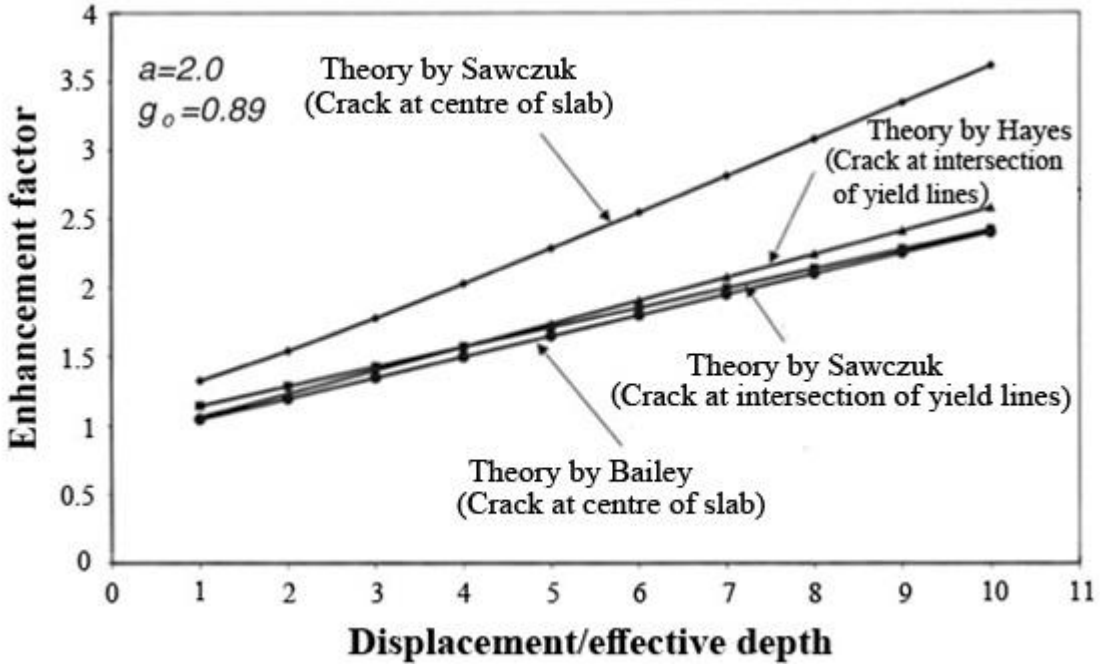

Figure 30: Comparison between Sawczuk's, Hayes' and Bailey's methods with slab's aspect ratio of 2.0 (Bailey 2001)

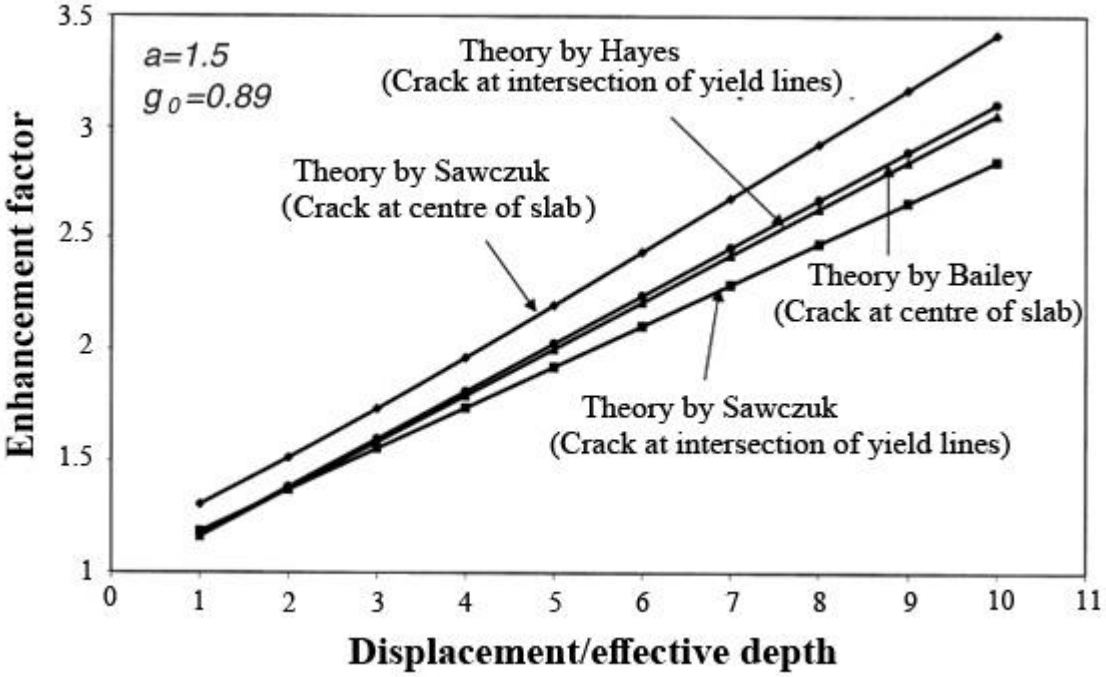

Figure 31: Comparison between Sawczuk's, Hayes' and Bailey's methods with slab's aspect ratio of 1.5 (Bailey 2001)

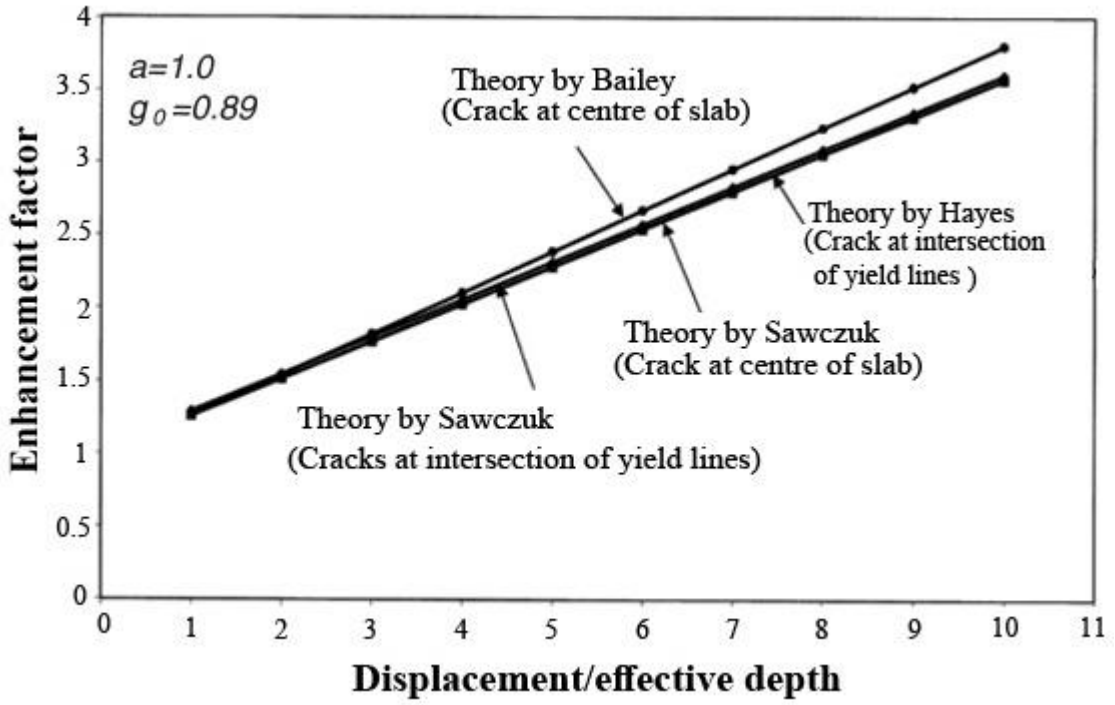

Figure 32: Comparison between Sawczuk's, Hayes' and Bailey's methods with slab's aspect ratio of 1.0 (Bailey 2001)

It is obvious from Figures 29-32 that for slab aspect ratios of 3.0 and 2.0, Sawczuk's method, which assumes the central full-depth crack, gives larger enhancements than Hayes' and Bailey's methods. Sawczuk's mode of failure leads to unconservative results. As the aspect ratio gets closer to 1.0, Sawczuk and Hayes predict the enhancement within a close range. However, Bailey's assumption of the ultimate stress of the reinforcement along the crack instead of using the yielding stress results in a slightly higher enhancement.

However, a comparison between BRE large-scale test and Bailey's method shows that the displacement-load curve as is calculated by Bailey goes below the test results until the reinforcement fractures, as shown in Figure 33. The comparison shows the UDL load capacity against the displacement.

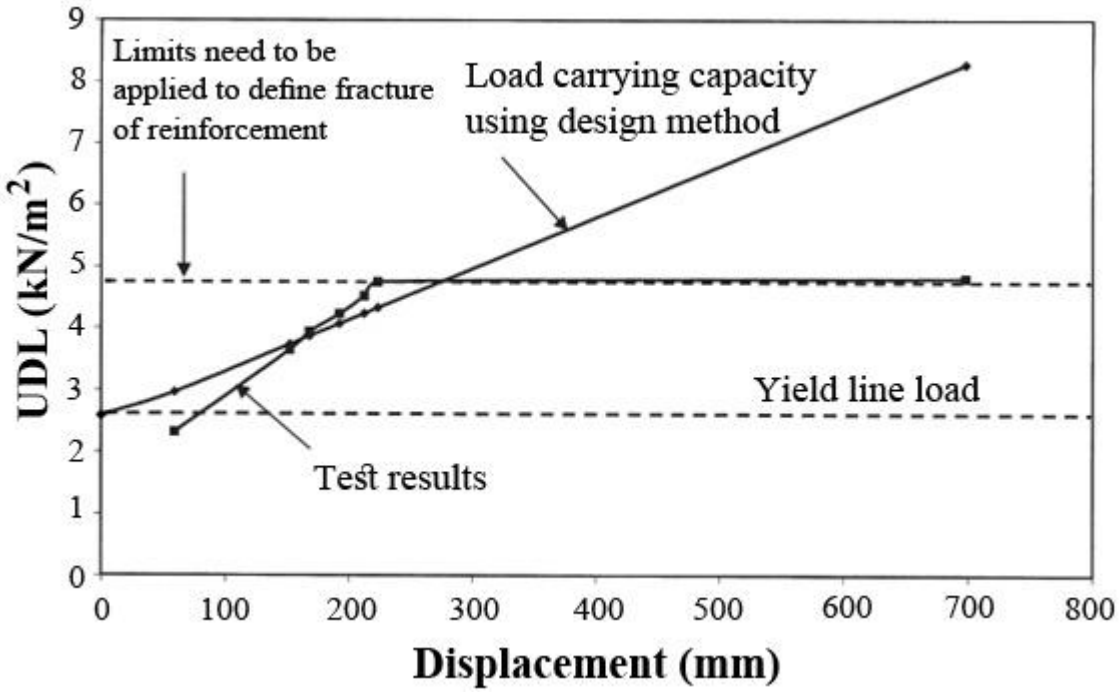

Figure 33: Comparison between BRE large-scale test and Bailey's method (Bailey 2001)

3.4.2 Tensile membrane action of orthotropic reinforced slabs

Bailey (2003) extended the simplified method in order to consider both isotropic and orthotropic reinforcement, since the previous version of the method considered isotropic reinforcement only.

The full derivation of Bailey's extended method is not presented in this thesis since it is mostly identical to the previous derivation presented in Section 3.4.1, with few modifications to take the orthotropy into account. In Equations 27 & 31, determining the enhancement factors presented in Section 3.4.1, g_o takes two values (i.e. $(g_o)_1$ and $(g_o)_2$ for e_{1m} and e_{1m}, respectively), to account for the different reinforcement ratio in the x and y directions. The effective depth of the reinforcement takes two values: d_1 and d_2, representing the different depths of the reinforcement meshes in each direction. The moment resistance M_0 when no axial force exists is multiplied by the coefficient of orthotropy μ in one direction, depending on the reinforcement distribution and arrangement in each direction.

Bailey (2003) compares his method against tests conducted by Hayes & Taylor (1969). In these tests, the reinforcement ratio was increased in the short span, but decreased in

the long span. From the tests results, Bailey observed the reduction of the maximum load due to membrane action as the coefficient of orthotropy μ increased. This implies that increasing the reinforcement on the short span, relatively to the reinforcement on the long span, reduces the effect of the membrane action. Bailey considers this observation consistent with his analytical method which emphasizes the influence of increasing the reinforcement along the longer span on the membrane action effect, and in turn, on the overall load capacity of the slab. Bailey checked this point on slabs with different aspect ratios. The comparison shows that this is true for rectangular slabs with an aspect ratio up to 3.0. The comparison shows that for aspect ratios of 2.0 or 3.0, the load carrying capacity due to the flexural behaviour decreases with lower orthotropy coefficient μ, while the load carrying capacity due to membrane action increases as μ decreases and therefore dominates the overall load-carrying capacity of the slab. However, for slabs with aspect ratios of 4.0 or 5.0, the reduction of the load-carrying capacity due to the flexural behaviour overrides as μ decreases; therefore, the total load-carrying capacity of the slab due to both membrane action & flexural behaviour decreases as μ decreases. The comparison is shown in Figure 34. The most effective orthotropy coefficient for slabs is highlighted in bold black for each aspect-ratio case. Note that when μ=1, the reinforcement is isotropic. μ >1 means that more reinforcement was placed in the shorted span of the slab. Finally, μ <1 means that more reinforcement was placed in the longer span of the slab.

Yield-line load and membrane load capacity for a given displacement and different values of coefficient of reinforcement orthotropy

μ	Load-carrying capacity using yield-line analysis (flexural behaviour) (kN/m²)			Enhancement factor due to membrane action at displacement/effective depth = 10	Total load-carrying capacity including membrane action (kN/m²)		
1.0	1.57			2.41	3.78		
0.75	1.47	↓	Decrease	2.84	4.17	↓	Increase
0.50	1.31	↓	in capacity	3.62	4.74	↓	in capacity
0.25	1.07			5.42	5.80		

Total load-carrying capacity for a rectangular slab with an aspect ratio of 5

μ	Load capacity using yield-line analysis (flexural behaviour) (kN/m²)	Enhancement factor due to membrane action at displacement/effective depth = 10	Total load-carrying capacity including membrane action (kN/m²)
1.0	1.12	1.0	1.12
2.0	**1.40**	**1.0**	**1.40**
0.5	0.82	1.17	0.97

Total load-carrying capacity for a rectangular slab with an aspect ratio of 4

μ	Load capacity using yield-line analysis (flexural behaviour) (kN/m²)	Enhancement factor due to membrane action at displacement/effective depth = 10	Total load-carrying capacity including membrane action (kN/m²)
1.0	1.19	1.11	1.26
2.0	**1.45**	**1.0**	**1.45**
0.5	0.89	1.58	1.39

Total load-carrying capacity for a rectangular slab with an aspect ratio of 3

μ	Load capacity using yield-line analysis (flexural behaviour) (kN/m²)	Enhancement factor due to membrane action at displacement/effective depth = 10	Total load-carrying capacity including membrane action (kN/m²)
1.0	1.30	1.55	2.02
2.0	1.56	1.15	1.79
0.5	**1.01**	**2.28**	**2.31**

Figure 34: The effect of orthotropy μ on total the load-carrying capacity of rectangular slabs (Bailey 2003)

3.4.3 Membrane action of composite slab/beam system

Bailey (2004) extended the simplified method in order to include the composite action of the beams in composite slabs acting compositely. Bailey argues that the assumption of ignoring the unprotected downstand steel beams was conservative in the previous derivations. This is supported by the large-scale tests that were conducted by BRE. These tests show that although the unprotected beams reached temperatures above 1150°C, leading to large deflections, no structural collapse occurred. The fact that such large deflections remained localised and did not lead to structural collapse brought more attention to the composite action, even when the internal secondary beams were left unprotected.

Bailey argues that for this composite system to be able to work properly in order to mobilize the membrane action, the edge beams should be designed so that no plastic hinges form in them. If such hinges form in the beams, folding mechanism, rather than membrane action, occurs. Catenary action can take place if enough support is provided. However, if plastic hinges do not form, and each slab panel withstands the loads, membrane action occurs, providing that vertical support on the perimeter of the slab is provided. Both probabilities are illustrated in Figure 35.

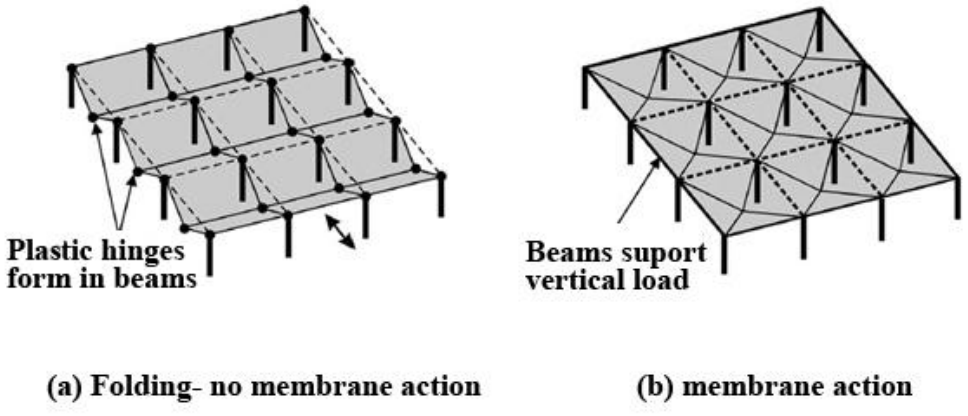

Figure 35: Comparison between folding mechanism and membrane action (Bailey 2004)

Bailey (2004) uses the same principles that were used in the previous derivations by Bailey & Moore (2000a), so that the slab is divided into panels as shown in Figure 36. On the perimeter, the primary edge beams are fire-protected in order to provide the vertical support; while the internal secondary beams were left unprotected. During fire, when membrane action is mobilized, loads are transferred from the internal unprotected beams towards the protected primary beams.

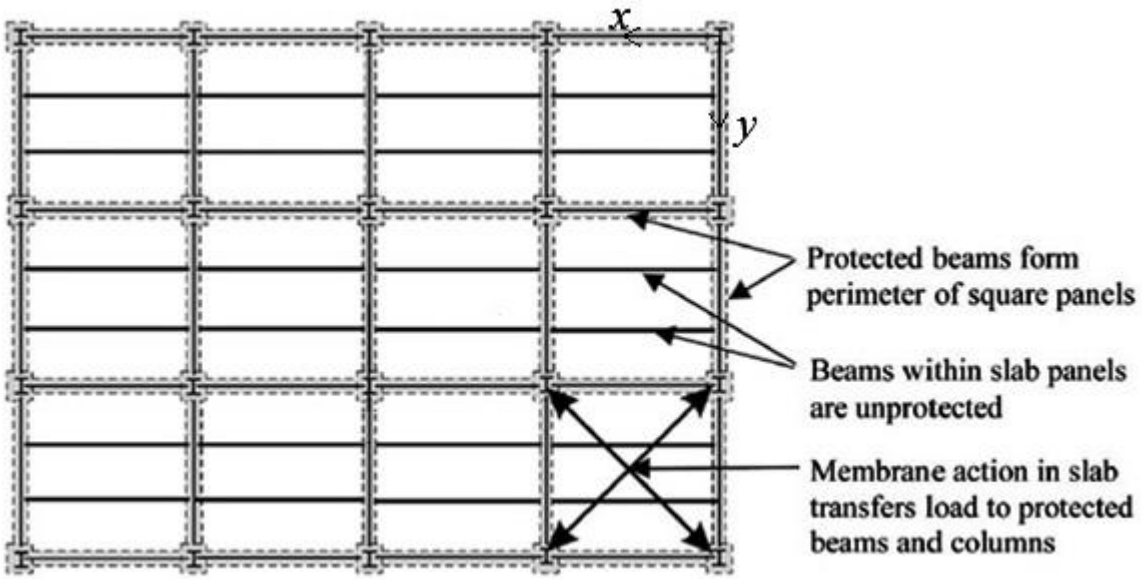

Figure 36: Mobilization of membrane action within slab panels (Bailey 2004)

Bailey (2004) argues that the vertical support, which is provided by the peripheral primary beams, is essential for the mobilization of the membrane action. This is important in case that the slab is horizontally unrestrained; therefore the required anchorage should be provided by the compressive membrane action on the perimeter of the slab, which is provided by this vertical support on the perimeter. The horizontal unrestraint of the slab panels might be neutralized when the slab is adjacent to surrounding buildings which provide the horizontal restraint. It can even be assumed that the slab is horizontally restrained since the reinforcement is continuous over the protected beams. However, Bailey argues that the large hogging moments at the peripheral supporting beams cause the reinforcement to fracture along the perimeter of the slab, thus this horizontal restraint is lost. Therefore, the conservative assumption of

the fractured reinforcement along the edges (i.e. isolated panels) is considered (Bailey 2004).

Bailey describes the load-carrying system in composite slabs under fire, considering a one-way slab with one downstand beam. As temperatures rise, the unprotected steel beam loses strength and stiffness until a plastic hinge forms in it. A fan-type yield line pattern appears and directs loads away from the centre, towards the vertically supported edges of the slab. With further temperature increase, a travelling hinge forms in the beam until it [the beam] cannot take any further loads. At this moment, the slab fully supports the loads in a typical envelope yield line pattern. As the yield line pattern forms, membrane action develops as the deflection increases further.

Bailey expressed the load carrying capacity for a slab/beam system w_p as follows:

$$w_p = e_{sys}\left[\frac{internal\ work\ done\ by\ composite\ slab\ in\ bending}{external\ work\ done\ by\ the\ floor\ system\ per\ unit\ load} + \frac{internal\ work\ done\ by\ beam(s)\ in\ bending}{external\ work\ done\ by\ the\ floor\ system\ per\ unit\ load}\right] \quad (37)$$

Where e_{sys} is the enhancement of the slab-beam system due to membrane action.

Equation 37 assumes full connection between the slab and the beam. Thus, it is assumes that all tensile forces that were mobilized by the beam are transferred to the slab. These tensile forces are balanced by the compressive membrane forces ring on the perimeter of the slab.

The enhancement factors for elements 1 and 2 due to membrane action for the slab/beam system e_{1m} and e_{2m} are given by:

$$e_{1m} = \frac{M_{1m}}{M_0\, L} = \frac{4b}{3 + g_0}\left(\frac{w}{d_1}\right)\left((1 - 2n) + \frac{n(3k + 2)}{3(1 + k)^2} - \frac{nk^3}{3(1 + k)^2}\right) \quad (38)$$

$$e_{2m} = \frac{M_{2m}}{M_0\, l + M_{fi}}\left[T_o lbw\left(\frac{2 + 3k - k^3}{6(1 + k)^2}\right) + T_b w\right] * \frac{1}{T_o d_1\left(3 + \frac{g_0}{4}\right) l + M_{fi}} \quad (39)$$

M_{fi} is the moment capacity of the steel beam at elevated temperatures.

Taking into account that a downstand steel beam exists, M_{2m} is given by:

$$M_{2m} = T_o lbw\left(\frac{2+3k-k^3}{6(1+k)^2}\right) + T_b w \tag{40}$$

T_b is the tensile capacity of the steel beam at elevated temperatures.

The enhancement factors for elements 1 and 2 due to flexural behaviour for the slab/beam system e_{1b} and e_{2b} are given by:

$$e_{1b} = \frac{M}{M_0 L} = 2n\left[1 + \frac{\alpha b}{2}(k-1) - \frac{\beta b^2}{3}(k^2-k+1) + (1-2n)(1-\alpha b-\beta b^2)\right] \tag{41}$$

$$e_{2b} = \frac{M}{M_0 l} = 1 + \frac{\alpha b K}{2}(k-1) - \frac{\beta b^2 K}{3}(k^2-k+1) \tag{42}$$

As it was considered by Bailey, recalling Equations 34 to 36, the enhancement factors for elements 1 and 2 due to bending and membrane action are given by:

$$e_1 = e_{1m} + e_{1b}$$

$$e_2 = e_{2m} + e_{2b}$$

The total averaging enhancement factor e_{sys}, for both slab elements 1 and 2, is given by:

$$e_{sys} = e_1 - \frac{e_1 - e_2}{1+2a^2}$$

The catenary capacity of the unprotected steel beam is taken into account by Bailey (2004) , and no longer ignored as previously done. The membrane action becomes related to the deflected slab shape which is defined by the continuously-changing yield-line pattern.

The benefits and shortcomings of the Bailey-BRE method can be summarised as follows:

Benefits:

- It is the first method to address composite slabs including the slab/beam system.
- The failure mode which is adopted in this method correlates to the test observations (i.e. the BRE ambient-temperature test).

Shortcomings:

- Inherited from Hayes' model, the equilibrium of the slab is assumed as the equilibrium of a deep beam. This is illogical.
- Like Hayes, two incompatible enhancement components (i.e. bending and membrane actions) are illogically added to give a single enhancement factor.
- The equilibrium of the method is based on a linear distribution of tension force along the diagonal yield-lines, similar to Hayes' method. However, even when Bailey & Toh (2007) presented a more realistic in-plane stress distribution, this did not result in a tangible change (Burgess et al. 2012).
- The averaging enhancement factor equation, which combines the enhancements from slab elements 1 and 2, ignores the effect of the vertical shear force. This leads to an incorrect prediction of the total enhancement.
- The method cannot predict reinforcement fracture. Therefore it is necessary to set a conservative deflection limit.
- The deflection limit set by Bailey is given as a combination of two incompatible components (i.e. thermal bowing of the slab and deflection of the slab). This is illogical. Mechanics-wise, the first component is based on a simply supported beam, while the second component is based on a beam which is fixed at both its ends. These components are simply added in the method, with no rational justification of such an illogical process.
- The method does not take the reinforcement ductility into account, although the reinforcement ductility is key as the bars fracture.
- Checks by Abu & Burgess (2010) show that the Bailey-BRE method is conservative when low reinforcement ratio is used. However, a marginal reinforcement ratio increase leads to a large enhancement and the method then overestimates the slab's load-carrying capacity.

- The loss of vertical support of the primary beams is ignored. The vertical support of the primary beams should be taken into account to avoid unrealistic enhancements.

Bailey corrected the mode of failure that Hayes used in his model. A more realistic in-plane stress distribution was presented by Bailey & Toh (2007). However, the shortcomings still exist and it was necessary to established a new method in order to address the limitations of the Bailey-BRE method and keep the predicted enhancement reasonable. The method that was established by Burgess et al. (2014), in addition to this study, considered a similar equilibrium assumptions to the Bailey-BRE method, but with different kinematic assumptions, as is further discussed in Sections 5.3 and 6.3.

3.5 The necessity of a new alternative simplified method

The existing simplified method which was presented by Bailey & Moore (2000 a&b) is widely used in the UK in practical structural fire engineering design. In Europe, the project FRACOF (Vassart & Zhao 2011) extended this method resulting in a design guide similar to the one used in the United Kingdom. However, the existing simplified method has shortcomings which lead to inaccurate results that differ from the slabs' behaviour in reality.

Firstly, the existing method assumes that the vertical support along the edges of the slab, which is provided by the fire-protected primary beams, is ideal without reduction in fire conditions. Bailey (2004) argues that if the peripheral protected beams are designed so that no plastic hinges form in them, then membrane action can occur. This assumes that this vertical support can be maintained, ignoring the fact that when the temperature of the protected steel beams reaches the beams limit temperature, these beams start to lose capacity and deflect under the effect of the imposed loads. This leads to probable folding mechanism which decreases the mobilization of tensile membrane action. Thus, assuming that the vertical support remains ideal at all times in fire conditions is invalid. Having the vertical support condition partially lost transfers the slab’s two-way bending, which is a one of the essential requirements for the mobilization of tensile membrane action, to one-way bending mechanism. This means that the slab fails in sagging without effectively mobilizing tensile membrane action (Burgess et al. 2012). Ignoring this fact leads to unrealistically optimistic designs.

Secondly, the capacity enhancement in the existing method is calculated due to two independent components: 1. bending enhancement; 2. tensile membrane action enhancement. These two enhancements are then irrationally merged into a single enhancement factor by simply adding them together, without justifying the rationality behind this process. The capacity enhancement of the slab cannot be merely the sum of two independent components in the way it is presented in the Bailey-BRE method.

Thirdly, Abu & Burgess (2010) show by, comparing to finite-element analysis, that the Bailey-BRE method leads to over-conservative designs when lower reinforcement size is used. On the other hand, the method leads to unrealistically significant enhancement by a marginal increase of the reinforcement ratio. Burgess et al. (2012) present a more detailed study, which was conducted using finite-element analysis using Vulcan software, on the effect of reinforcement ratio on composite slabs behaviour in fire. The authors show that even after the developed method which was presented by Bailey & Toh (2007), a marginal increase in the reinforcement ratio leads to an optimistic yield-line capacity enhancement. Compared to the finite-element results, the simplified method was found to be conservative when using A142 and A193 meshes, but unconservative when using larger mesh sizes. Burgess et al. (2012) argue that this disproportionate increase of the calculated capacity when using large mesh sizes is due to ignoring the stability loss of the protected beams. Therefore, this unconservative design is intuitively seen in slabs with large spans, since such large slabs require larger mesh sizes.

Fourthly, the Bailey-BRE method cannot predict the real deflection at which reinforcement fracture or concrete crushing actually occurs (Bailey & Toh 2007). Therefore the method considers a deflection limit w_{lim} in order to avoid integrity failure. This limit is given by:

$$w_{lim} = \frac{\alpha_T (T_{bot} - T_{top}) l^2}{19.2 d_1} + \sqrt{\left(\frac{0.5 f_y}{E}\right) \frac{3L^2}{8}} \tag{43}$$

α_T is the coefficient of thermal expansion of concrete
T_{top} is the temperature at the slab bottom surface
T_{bot} is the temperature at the slab top surface
E is the elastic modulus of the reinforcement

The first term of Equation 43 represents the thermal bowing of the slab, where a linear temperature gradient is assumed across the slab's depth, assuming that the slab is heated from its bottom surface. The second term of the equation represents the resulted deflection of the slab when applying a 50% reinforcement mechanical strain at ambient temperature (20ºC) along the longer span *L*. These two components of deflection are irrationally summed, ignoring the fact that they represent two incompatible components of deflection.

Furthermore, the second component of the Equation 43 uses an elastic modulus of reinforcement to calculate the mechanical strain. Using the elastic modulus results in conservative elastic deflection limits that the slab can definitely go beyond in fire conditions when tensile membrane action is being mobilized.

All these factors lead to inaccuracies in various cases, leading to conservative or optimistic designs.

Burgess et al. (2013) present an alternative simplified method of tensile membrane action of thin concrete flat slabs, which is based on the yield-line theory. It uses the same yield-line pattern which is used by Bailey & Moore (2000a), however, with different kinematic assumptions. This alternative simplified method shows that the Bailey-BRE method can lead to over-estimated enhancement. Burgess et al. (2014) presents a re-examination of the mechanics of tensile membrane action of thin-flat concrete slabs at large deflections. The analysis of the re-examination starts from the initial yield-line capacity, allowing monitoring the changes in the stress patterns along the yield-lines. It also monitors the formation of cracks over the slab, up to the loss of the slab's load capacity. The alternative simplified method and the re-examination of tensile membrane action accounts for flat slabs enhancements at ambient temperature.

This thesis presents an extension of the alternative simplified method and the re-examination of the mechanics of TMA, in order to include composite slabs in fire. Based on the yield-line theory, this study considers the equilibrium of the forces over the slab, in order to work out the internal work dissipated by the slab at large deflections and high temperatures.

4 The Theory and Principles Behind this Study

4.1 Assumptions

The new mechanics of tensile membrane action of composite slabs is based on the yield line theory, starting from small-deflection analysis, followed by large-deflection plastic analysis. This is justified since weakly-reinforced slabs, such as composite slabs, do not show tension stiffening; hence such slabs crack along the yield-lines after the latter formed. Since it is highly unlikely that the yield-line pattern changes after it formed, the large-deflection analysis can be safely implemented following the small-deflection analysis. In other words, the formation of the yield-line pattern marks the end of the small-deflection phase, establishing for the large-deflection phase if any further deflection is experienced.

The slab which is considered in this study is a rectangular composite slab with an aspect ratio *r*, vertically supported along its four edges by fire-protected primary beams. Within the slab, a single secondary beam exists along the long span of the slab. This single secondary beam was left unprotected. The slab is reinforced by isotropic reinforcement in the *x* and *y* directions. Both reinforcement layers of the mesh are assumed to be at the mid-depth of the slab. The slab is considered isolated, although the mechanism is not limited to this condition. The mesh reinforcement bars are assumed to be welded, forming anchorage points for the reinforcement. The slab is vertically loaded over its surface by a uniform load which remained constant during the analysis. As it is usually considered in the case of composite slabs in fire conditions, the metal deck is not included in the calculations since the steam which is usually released at high temperatures pushes the deck to detach from the bottom surface of the slab.

Since concrete has a low thermal conductivity, the reinforcement is considered well insulated within the concrete and remained at relatively cool temperatures. Therefore, it is assumed that only the secondary unprotected steel beam is considerably affected by the temperature increase. Therefore, the overall loss of the load capacity is due to the capacity degradation of the unprotected steel beam.

4.2 Methodology

Two main stages are distinguished in the study. The first stage is the small-deflection analysis at which the optimum yield-line capacity of the slab is calculated at high temperature, based on the plastic energy theory. As temperatures increase, the changing yield-line capacity is continuously compared to the applied load at every temperature increment. This temperature increase reduces the strength capacity of the unprotected secondary downstand beam, leading to the degradation of the overall load capacity of the slab. Once the small-deflection load-carrying capacity of the slab degrades to the applied load, the yield-line pattern forms. The small-deflection analysis phase ends here.

In the next stage, large-deflection analysis is conducted, using the optimum yield-line intersection point distance resulted from the small-deflection analysis. An iteration of two intersected loops of deflection and temperature is conducted in the large-deflection analysis, coded in Matlab. This iteration is deflection-controlled, at which deflection is increased by constant increments, allowing tensile membrane action, therefore more capacity, to be mobilized at elevated temperatures. As the deflection increases, yield-lines starts to crack through distinguishable phases, leaving the reinforcement across the cracks in pure tension. When an actual crack width reaches the crack limit-width, the reinforcement across this crack fractures, transferring the analysis to a new phase within the large-deflection stage. In the Matlab code, the slab's load capacity is continuously compared to the applied load at the end of every deflection loop. These intersected loops (i.e. deflection and temperature) continue mobilizing TMA until no further enhancement is possible. At this point, the slab is considered structurally failed. This process gives the enhancement in terms of the calculated temperature.

It was observed in previous tests on loaded thin-concrete slabs that after the initial yield-line pattern, failure is likely to occur by the formation of a full-depth crack. This crack penetrated the slab across its short span at the middle of the central yield-line (Burgess et al. 2014). However, the initial failure mechanism, which is called mechanism-b in this study, represents the optimum yield-line pattern at which cracks open along the yield lines and the slab might fail even before the formation of the full-depth crack perpendicularly to the central yield line. This optimum pattern is shown in Figure 37.

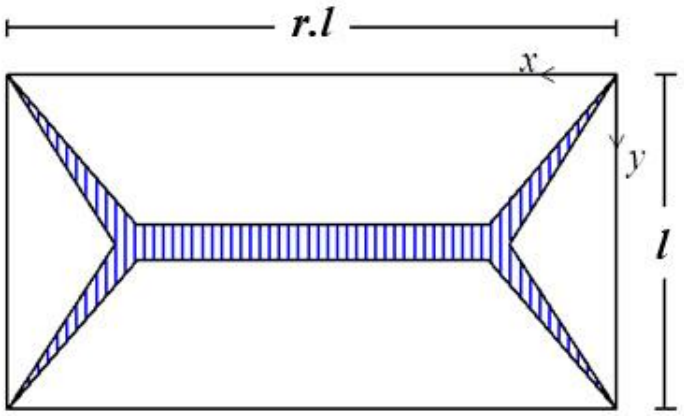

Figure 37: Mechanism-b which results from the cracking of the optimum yield-line pattern

r is the aspect ratio of the slab.

This study focuses on mechanism-b. Therefore, the mechanics of this pattern is studied through different phases; starting from the optimum yield-line mechanism until failure at large deflections.

4.3 Temperature-based enhancement

The enhancement due to tensile membrane action, TMA, is usually presented in terms of the load-carrying capacity as shown by Bailey (2003) and Burgess et al. (2013). The concept of enhancement is simply defined as the ratio of the load capacity of a slab due to TMA, to the conventional yield-line load capacity of the slab.

In this research, the load capacity of the slab is intentionally reduced within the iteration by raising the temperature until this capacity degrades to the applied load. Thus, intuitively, the ratio between the degraded load capacity of the slab to the applied load at the end of each loop reached one. Therefore, the methodology which is used in this research requires presenting the enhancement in terms of the calculated temperature at each loop. This temperature is the amount of temperature needed to degrade the load capacity of the slab to the level of the applied load at each loop. During the continuous comparison between the capacity by the applied load at each loop as the slab deflects, if the load capacity is higher than the applied load, the temperature is increased. If the slab's load capacity is lower than the applied load, the temperature is decreased until the load capacity of the slab increases and becomes equal to the applied load. This latter condition occurs at high temperatures when the strength capacity of the unprotected

beam degrades. Therefore, some reinforcement fractures, consequently degrading the slab's load capacity further, so that this capacity of the slab decreases to an extent that the slab cannot withstand the applied loads at such high temperatures and the deflection level. Therefore the temperature is decreased to get the capacity back to the applied load, marking a stage at which the slab's load capacity reduces and can no more take as high temperatures as it did in the previous stages. This temperature is the limit temperature at which the slab survives at the corresponding conditions. In the next loop, the internal deflection loop runs again and the mechanics is applied for every deflection value, looking for the limit temperature for the new slab status. Temperature affects only the unprotected steel beams as it is considered in this study. This thermal reduction of the strength occurs due to the thermal reduction factor k_y, as given in (Eurocode 3 BS EN 1993-1-2: 2005). The thermal reduction factor is shown in Figure 38.

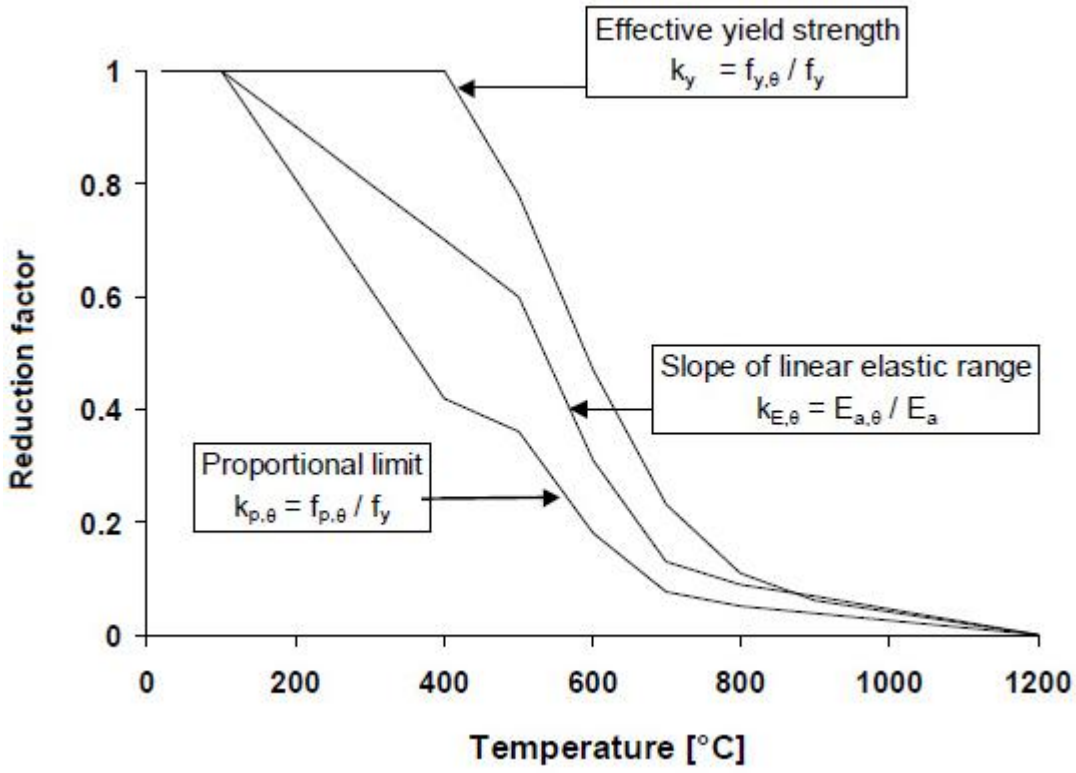

Figure 38: Steel reduction factor (BS EN 1993-1-2: 2005)

f_y is the yield stress of the steel at ambient temperature

$f_{y,\theta}$ is the effective yield strength of the steel at elevated temperatures.

$k_{p,\theta}$ is the reduction factor relative to the steel yield stress for the proportional limit.

$f_{p,\theta}$ is the proportional limit for the steel at elevated temperatures.

$k_{E,\theta}$ is the reduction factor for the slope of linear elastic range at the steel temperature.

$E_{a,\theta}$ is the slop of linear elastic range for the steel at elevated temperatures.

E_a is the modulus of elasticity of the steel for normal temperature design.

4.4 Load-carrying capacity of the slab

According to the energy theory, the load-carrying capacity of the slab P is given by:

$$P = \frac{total\ internal\ work}{external\ work\ done\ by\ loads} \tag{44}$$

4.4.1 Internal work of the slab

The internal work, or the internal energy, is the work dissipated by the components of the slab that are working in tension or compression. Reinforcement and steel beams dissipate plastic work when they are in tension, thus both of them dissipate work by the extension undergone through the deflection. Concrete, on the other hand, dissipates work when it is in compression along slab regions which are in contact.

4.4.1.1 Internal work of the reinforcement

The reinforcement which is left in tension when a crack widens, extends across the crack. The extension of the reinforcement depends on the actual crack width and the angle of rotation of the slab facets which form the crack. The internal work dissipated by the reinforcement is given by its extension multiplied by its tension force. Reinforcement bars keep on dissipating work in tension until fracture. This fracture occurs when the actual crack width reaches the limit crack width.

The limit crack width depends on the spacing of the reinforcement bars of the mesh, and the ductility of these bars. This limit is given by:

$$Limit\ crack\ width = rebars\ spacing \times ductility \tag{45}$$

It should be noted that only the reinforcement bars in tension are considered in the calculations of the internal work of the slab.

In order to accurately address the extension of the reinforcement bars across the cracks as the slab elements rotate, the bond-slip behaviour should be addressed correctly. Many studies addressed this issue for normal reinforcement bars at ambient temperatures. However, in composite slabs, the reinforcement bars usually have small diameters (6mm when using A142 mesh for example), forming merely anti-cracking mesh. This means that the bond-slip behaviour of such small-diameter reinforcement bars should be addressed for such special conditions, especially at elevated temperatures. Pull-out tests should be conducted on specimens reinforced with small-diameter bars subjected to elevated temperatures. Two tests were conducted in the Heavy Structures Lab at the University of Sheffield. These tests are presented in Appendix-3. Since the bond-slip behaviour was not among the objectives of this research, completion of the test series and addressing the bond-slip behaviour problem is a recommendation for future researches.

4.4.1.2 Internal work of the unprotected beam

The secondary downstand beam contributes to the internal work of the slab. When the slab deflects, its elements rotate about the yield-lines by rotation angles at its supporting edges. This results in the extension of the beam that spans the cracks, in a similar manner to the reinforcement bars. The extension of the steel beam, which is affected by the elevated temperatures, results in plastic work dissipation which contributes to the total internal work of the slab. The extension of the beam is illustrated in Figure 39.

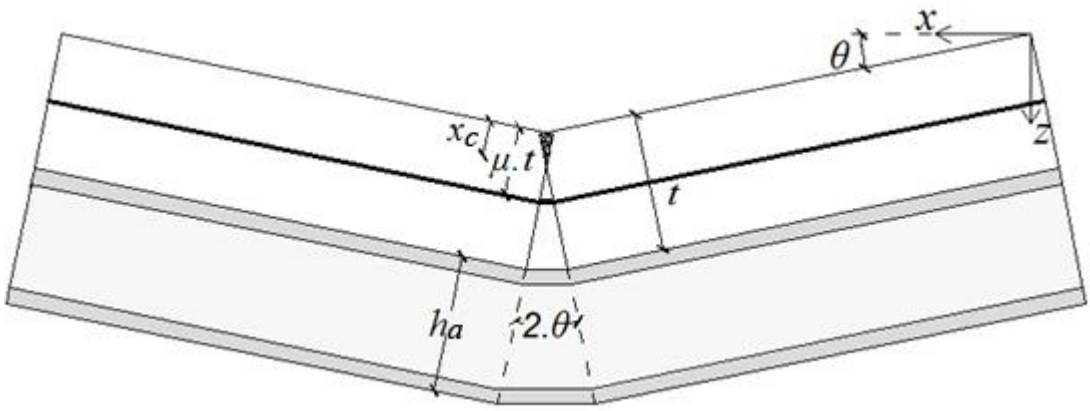

Figure 39: Extension undergone by the downstand beam

h_a is the total depth of the beam.

t is the depth of the concrete part of the slab.

x_c is the neutral axis depth.

θ is the angle of the rotation of the slab about the short span.

μ is the reinforcement depth ratio.

The tension force of the beam T_b is calculated by:

$$T_b = A.f_y.k_y \tag{46}$$

A is the cross-section area of the beam

The internal work of the beam is given by its tension force at its temperature multiplied by its extension. The extension of the beam can be calculated linearly at the mid-height of the beam, determined by the depth of the neutral axis of the slab, the angle of rotation of the slab facets, and the extension of the reinforcement.

4.4.1.3 Internal work of concrete

The contribution of concrete in plastic work dissipation is considered in this study, although it is relatively small compared to the work dissipated by the reinforcement and the steel beam. The internal work done by the concrete is related to the compression which is applied on the concrete and between the facets of the slab which are in contact. Hence, the work dissipated by concrete should be calculated as the area of concrete in compression multiplied by the corresponding compression force. Once a crack opens, the contact between the slab facets is lost. Therefore the compression force is lost and the corresponding internal work of concrete over that area is zero. The compression loss occurs abruptly along the central yield-line crack, which is met by a sudden reinforcement fracture along this line. Meanwhile, along the diagonal yield-lines the cracks open progressively, leading to progressive loss of contact between the slab elements. Therefore, the compression force retreats along these yield-lines towards the corners of the slab until it [compression force] becomes concentrated in a single point at each corner of the slab.

The slab goes through different phases during the large-deflection stage. These phases are defined by the compression stress blocks converting from thin blocks to triangular,

and then to trapezoidal; eventually putting the whole depth of the slab edges in compression. Concrete compression force is directly related to these stress-block phases which is further discussed in Section 6.3.4.

4.4.2 External work of the slab

The external work of the slab is simply calculated according to the work method, as the transverse loading on the slab multiplied by the corresponding deflection of the slab element under the loads. This is further discussed in Section 6.2.1.3.

5 An Alternative Simplified Method of the Mechanics of TMA

5.1 Kinematic mechanism

Burgess et al. (2013) presented an alternative simplified method to estimate the mechanics of tensile membrane action of thin-flat concrete floor slabs. The derivations of the alternative simplified method were presented in more details by Staikova (2014). The assumptions that were considered for this method include the following:

1. Plain flat concrete slabs are considered.
2. Analysis is based on large-deflection plastic yield-line analysis.
3. Vertical support along the primary beams is assumed.
4. The slab can be reinforced with isotropic or orthotropic reinforcement.
5. Reinforcement bars are welded at constant spacing, forming a reinforcing mesh.
6. The formulation accounts for the plasticity and fracture of reinforcement mesh.
7. The reinforcement bars contribute to the total internal work of the slab by the extension of these bars as the slab deflects.
8. Only the reinforcement in tension contributes in the slab internal work calculation.
9. The method allows for a change in stress patterns around the yield-lines. This pattern change could be monitored through the analysis.
10. The concrete in compression contributes to the internal work of the slab.

The alternative method considers a two-way spanning rectangular slab with an aspect ratio *r*. The slab is reinforced with anti-cracking reinforcement mesh, which is considered isotropic. Both layers of the mesh lie at a single layer in the mid-depth of the slab thickness.

The slab is loaded transversally until the plastic yield line pattern appears by means of cracks as shown in Figure 40.

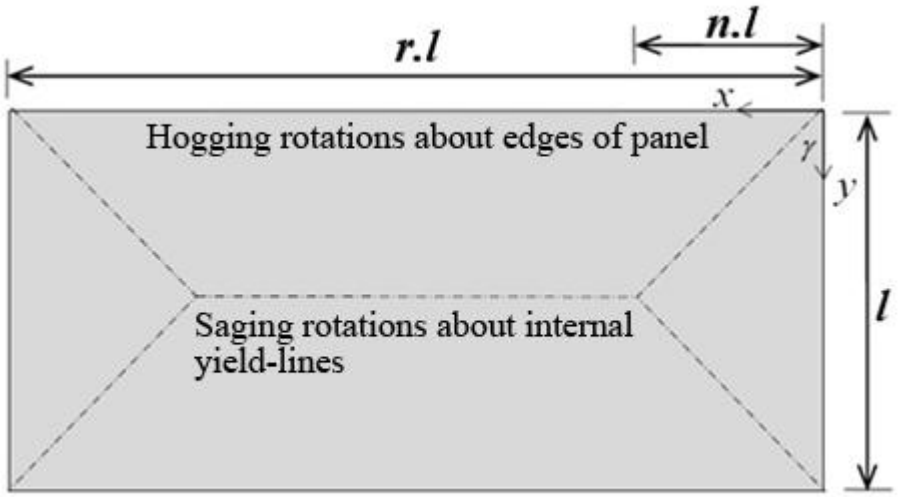

Figure 40: Small-deflection yield-line pattern (Burgess et al. 2013)

l is the short span of the slab

n is the yield-lines intersection point distance from the short edge of the slab.

r is the aspect ratio of the slab

For the lowest failure load, the optimum yield line mechanism is defined by the yield lines intersection distance parameter *n*, which is given by:

$$n = \frac{1}{2r}\left(-1 + \sqrt{1 + 3r^2}\right) \tag{47}$$

This method allows for four probable kinematically correct mechanisms. These mechanisms a, b, c and d, shown in Figure 41, are anticipated for small-deflection patterns of composite slabs (Staikova 2014).

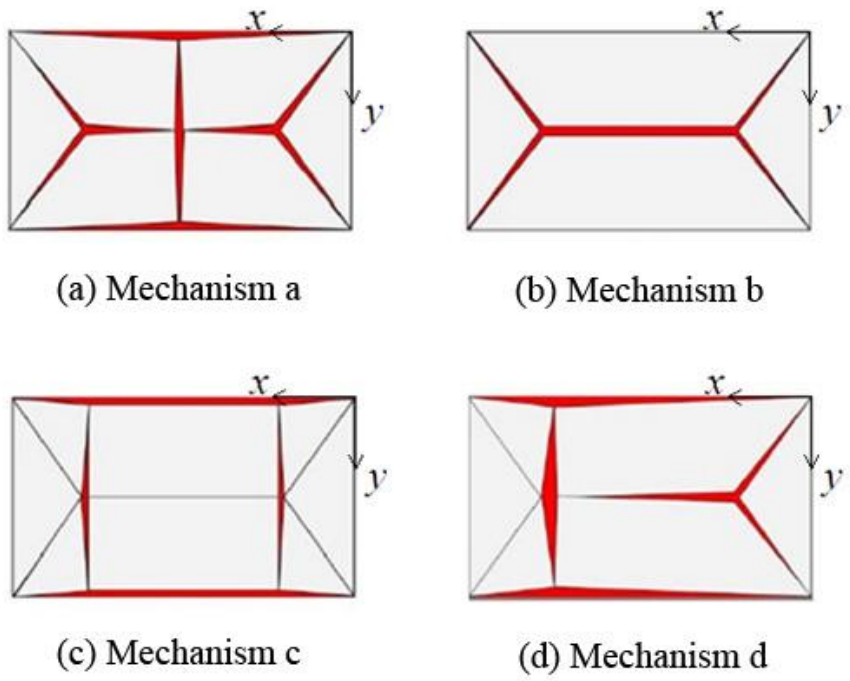

Figure 41: Probable yield-line mechanisms (Staikova 2014)

Full-depth cracks might form either in the middle of the slab across the short span or at the intersection points of the yield lines as shown in Figure 41(c). Mechanism b, shown in Figure 41(b), is the optimum yield line pattern which is expected to take place initially.

After the formation of the optimum yield line pattern, any further increase of the load on the slab results in further rotations of the slab facets about the yield lines, leading to cracks formation along the yield lines. Once cracks form, the reinforcement along these cracks starts to fracture.

For the optimum yield-line pattern of mechanism-b, according to the work method, the external work done by the loads on the slab *E* is given by:

$$E = P.l^2.\delta\left(\frac{r}{2} - \frac{n}{3}\right) \tag{48}$$

δ is the maximum deflection of the slab

The internal work of the slab I_S is calculated by multiplying the projected length of each yield line on the axis of rotation, by the plastic moment acting on it, multiplied by the angle of rotation of the corresponding slab facets. Since both the external work done and the internal work dissipated are in balance, the load-carrying capacity of the slab P can be calculated as follows:

$$P = \frac{I_S}{l^2.\delta\left(\frac{r}{2} - \frac{n}{3}\right)} \tag{49}$$

I_S is the internal work of the slab.

By dividing this load-capacity P at the current deflection by the initial yield-line load P_o, the enhancement factor e, which indicates the excess capacity that the slab can take, is given by:

$$e = \frac{P}{P_o} \tag{50}$$

P_o is the initial yield-line load capacity. It is given by:

$$P_o = \frac{6}{l^2}\left[\frac{\left(\frac{C_s}{n} + 2r.C_r\right).\overline{m_p} + 2\left(2.r + \frac{1}{n}\right).m_p}{(3.r - 2.n)}\right] \tag{51}$$

C_s is the number of continuous short edges of the slab (=0, 1 or 2)
C_r is the number of continuous long edges of the slab (=0, 1 or 2)
m_p is the sagging moment of the slab
$\overline{m_p}$ is the hogging moment of the slab

The detailed calculations are not presented in this thesis since they are presented by Staikova (2014).

5.2 Extension and failure of reinforcement bars

The behaviour of the reinforcement bars in terms of extension and failure should be addressed in order to calculate the internal work dissipated by the reinforcement.

Burgess et al. (2013) consider a concrete slab of depth *t*, reinforced with anti-cracking mesh at the mid-depth of the slab $\mu.t$. The rotation of the slab's facets leads to concrete cracking, with no opening at the beginning as illustrated in Figure 42(a), and the neutral depth shown in Figure 42(b) for that stage.

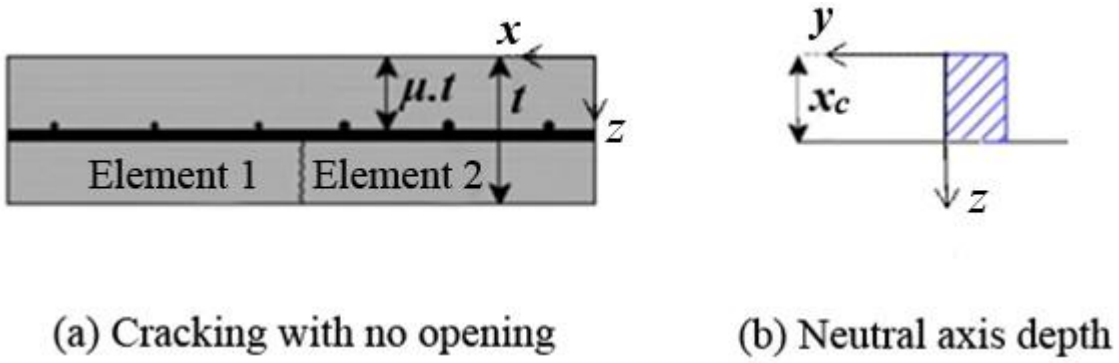

Figure 42: (a) slab cracking before opening; (b) compression stress block (Mangeon 2013)

However, for deflections beyond the small-deflection state, cracks open as the facets of the slab rotate about the yield lines. Meanwhile, the embedded reinforcement bar is stretched across the crack as shown in Figure 43(a), and the tensile force is balanced by a thin compression block in the concrete on top of the section as shown in Figure 43(b).

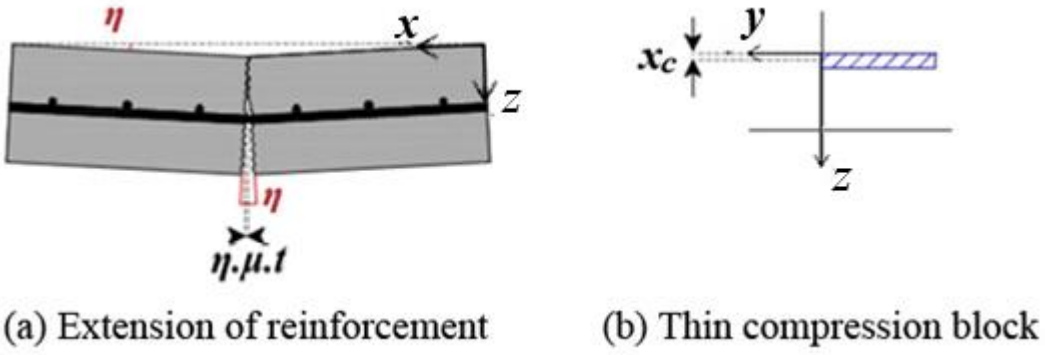

Figure 43: (a) the extension of the reinforcement bar across the crack; (b) shallow compression stress block (Mangeon 2013)

η is the angle of rotation between the slab elements across cracks.

As the crack opens further, the rotation of the slab facets increases, and the extension of the reinforcement bars increases until they fracture, as shown in Figure 44.

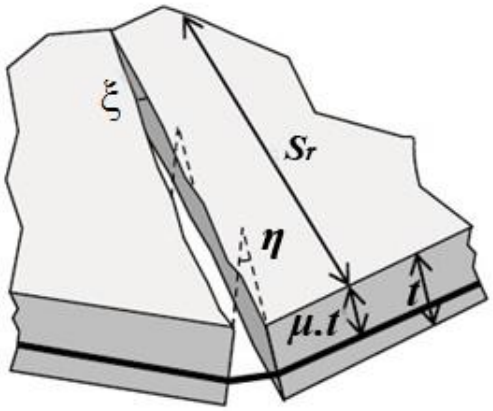

Figure 44: Reinforcement extension due to crack opening and slab facets rotation (Burgess et al. 2013)

ξ is the rotation angle between two slab elements.
S_r is the distance between the reinforcement bar in tension and the edge of the slab.

The extension of the reinforcement bar Δ is given by:

$$\Delta = \xi . S_r + \eta . \mu . t \tag{52}$$

The maximum extension of the reinforcement Δ_{Lim} is given by:

$$\Delta_{Lim} = \varepsilon_u . d \tag{53}$$

d is the space between two reinforcement bars in any direction.
ε_u is the fracture ductility strain of the reinforcement.

5.3 The re-examination of the mechanics of TMA

5.3.1 Mechanism-b geometrics

Burgess et al. (2014) presented a re-examination of the mechanics of tensile membrane action of thin flat concrete slabs at ambient temperature. The re-examination accounts for reinforcement fracture based on large-deflection plastic analysis. It assumes a changing compression stress block, which its depth is governed by the deflection. In the beginning, when the deflection is zero or negligible, a rectangular compression block is assumed over the slab, at which loads are resisted by bending mechanism. As

the deflection increases, the depth of the compression block decreases over the central region of the slab until it disappears, while it increases at the peripheral edges, forming a compression ring around the slab. The compression stress block along the compression ring converts to a triangular block as the deflection increases. With further deflections, the compression block depth increases until the whole thickness of the slab is in compression, forming a trapezoidal compression block, as shown in Figure 45. When the central region of the slab becomes in pure tension, concrete cracks and the yielded reinforcement fractures abruptly. Along the diagonal yield-lines, this occurs progressively, unzipping the reinforcement bars as compression disappears gradually. Eventually, compression is concentrated in a single point at the corner of the slab.

The transformation of the compression stress block between the phases, or cases, was studied for each phase or case. These phases were divided into different categories, at which the compression block can be either above or below the reinforcement bars, depending on the compression depth. Therefore, these bars can be intact or fractured depending on the development of the compression block depth, as shown in Figure 45. In other words, when a reinforcement bar is in pure tension, the yielded bar fractures. Stretching the bars until they yield then fracture dissipates work which contributes to the total internal work of the slab.

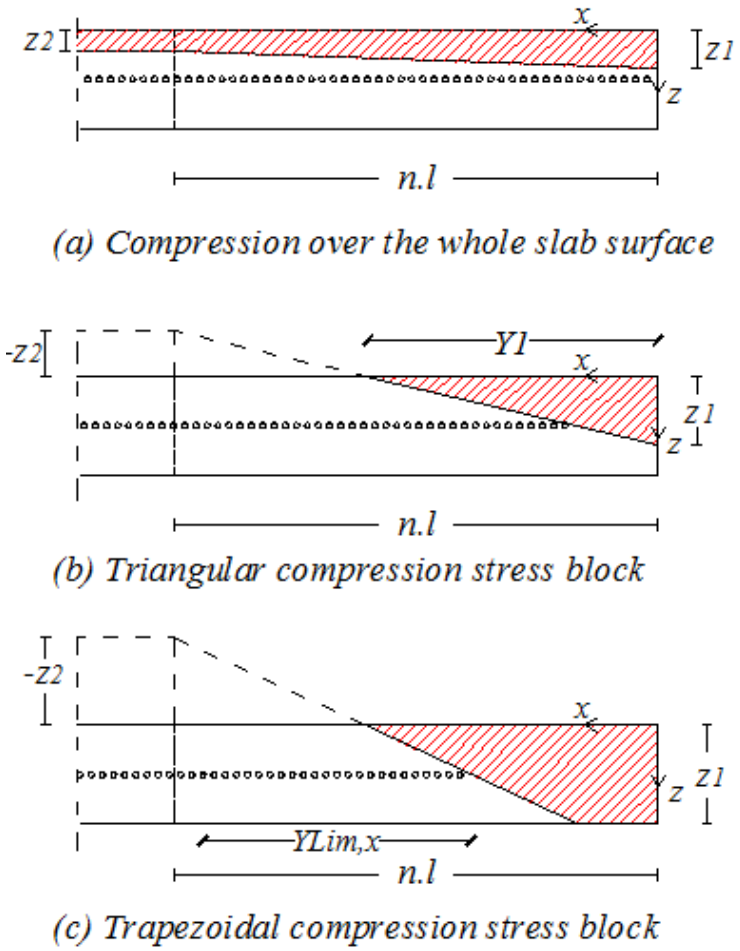

Figure 45: Compression stress block cases which vary depending on the slab's deflection

z_1 is the compression depth at the slab edge.

z_2 is the compression depth at the central region of the slab.

As the slab deflects, the slab elements rotate in particular angles of rotation, θ and ϕ, in the x and y directions as shown in Figure 46, leading to geometric changes over the slab. The slab elements move horizontally in the both main the directions x and y. These movements, Δx and Δy, govern the calculation of other important geometrics, like the compression stress block.

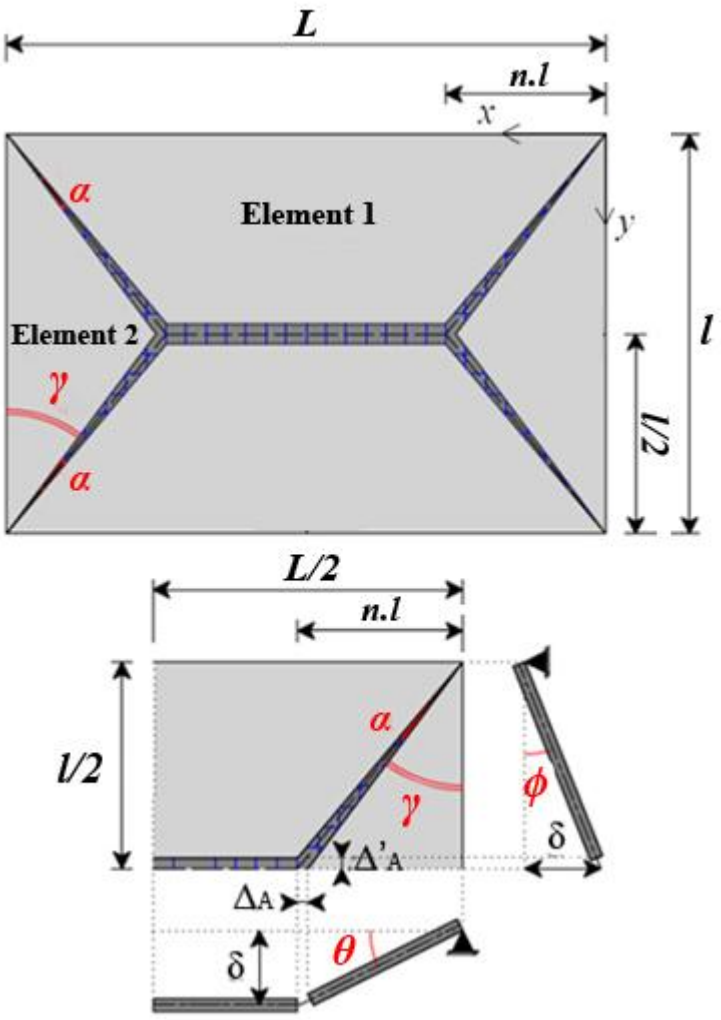

Figure 46: Failure mechanism b (Staikova 2014)

L is the larger span of the slab.

θ is the angle of rotation of the slab about the short span.

ϕ is the angle of rotation of the slab about the larger span.

γ is the angle between diagonal yield lines and the slab support.

α is the angle of the diagonal yield lines cracks.

Δ_A is the displacement in the x direction between the edges of the slab elements 1 and 2

Δ'_A is the displacement in the y direction between the edges of the slab elements 1 and 2

Figure 47 illustrates the geometrics of the slab as it deflects, including the horizontal movements and rotations of the slab elements. The rotation angles of the slab elements are calculated as follows:

$$\theta = \frac{\delta}{n.l} \tag{54}$$

$$\phi = \frac{2.\delta}{l} \tag{55}$$

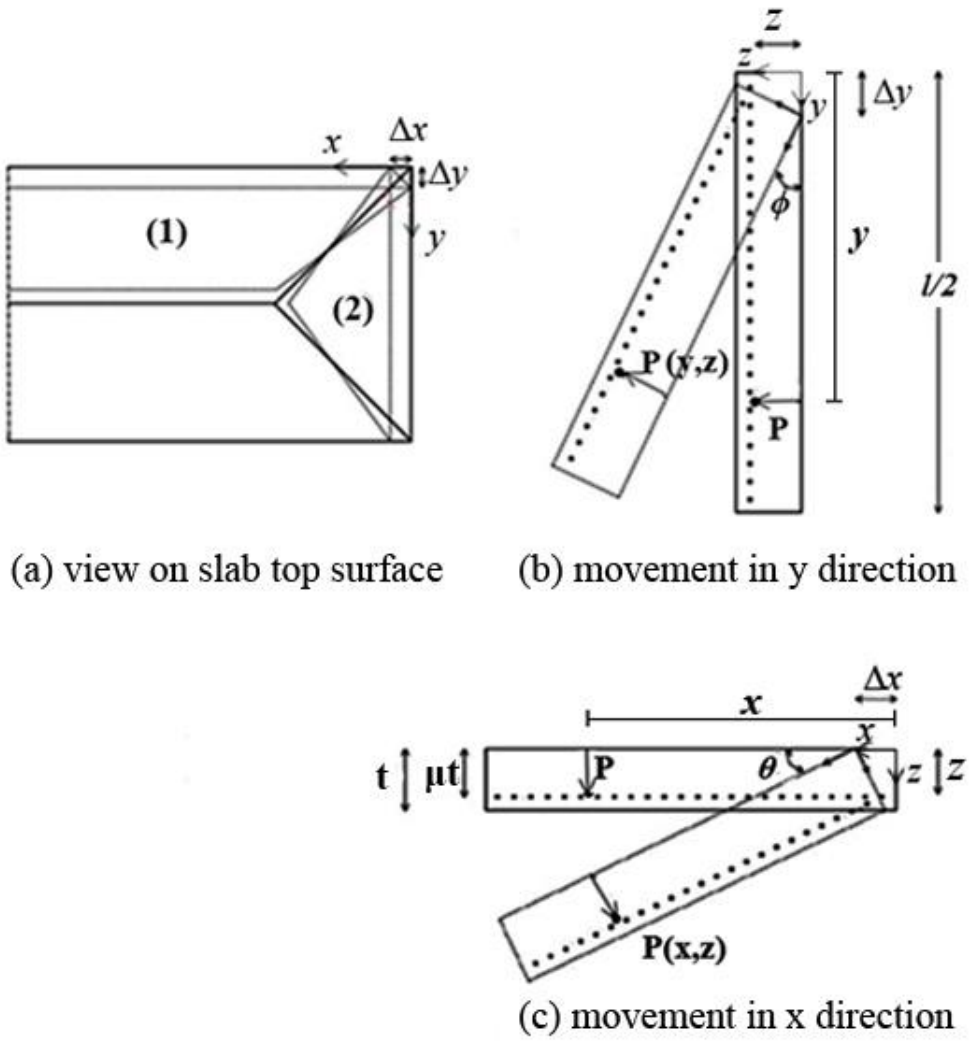

Figure 47: Movement and rotation of the slab elements (Staikova 2014)

Consider a general point P as shown in Figure 47. The movement in the *x*-direction Δx, and the *y*-direction Δy, and the rotation θ, which result from the slab deflection, lead to the movement of the point P in the *x* and *y* directions as follows:

The movement at P in the *x*-direction *u* is given by:

$$u = \Delta x - \theta . z - \frac{\theta^2 . x}{2} \tag{56}$$

x represents an arbitrary distance in the *x*-direction. For the case shown in Figure 47, *x* is the distance of the point P from the origin.

z represents a general depth of the reinforcement on *z* axis. For the case shown in Figure 47, $z=\mu t$.

Δx is the movement of the point P in the *x*-direction.

The movement at P in the *y*-direction *v* is given by:

$$v = \Delta y - \phi . z - \frac{\phi^2 . y}{2} \tag{57}$$

y represents an arbitrary distance in the *y*-direction. For the case shown in Figure 47, *y* is the distance of the point P from the origin.

Δy is the movement of the point P in the *y*-direction.

The relationship between *x* and *y* horizontal movements is given by:

$$\Delta y = 2n \, . \, \Delta x \tag{58}$$

Where: $2.n$ represents $tg(\gamma)$. The angle γ is illustrated in Figure 46. It is the angle between the diagonal yield-line α and the short-span of the slab.

The relationship between the angles of rotations of the slab elements ϕ and θ is also represented in terms of $tg(\gamma)=2n$ and given by: $\phi = 2n . \theta = 2 . \delta$

For $u = 0$, Equation 56 gives:

$$\Delta x = \theta \left(z + \frac{\theta . x}{2} \right) \tag{59}$$

The same applies to the horizontal movement in the *y*-direction Δy. However, the derivations of mechanism-b are with respect to the *x*-direction as the main direction. $tg(\gamma)$ can be used for conversion between the *x* and *y* directions when necessary.

5.3.2 Reinforcement geometrics

Only reinforcement bars in tension contribute to the calculation of the internal work of the slab. Therefore, the distances at which the reinforcement bars are intact should be worked out. Figure 48 illustrates the distances of the intact reinforcement.

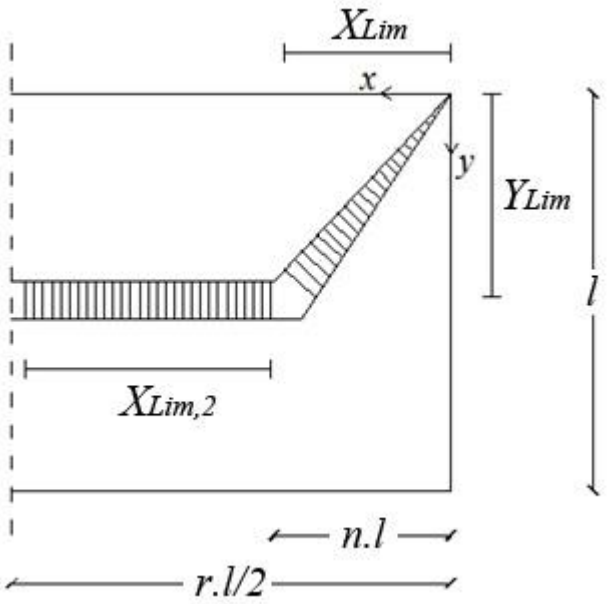

Figure 48: Distances of intact reinforcement bars in the *x* and *y* directions

X_{Lim} is the length that covers intact reinforcement bars in the *x*-direction, for *x* or *y* bars.

$X_{Lim,2}$ is the length that covers intact reinforcement bars across the central yield-line in the *x* direction.

Y_{Lim} the length that covers intact reinforcement bars in the *y*-direction, for *x* or *y* bars.

The length that covers the intact reinforcement in the *x*-direction for *x*- reinforcement bars $X_{Lim,x}$ (i.e. the distance of the working forces in the *x*-direction) is given by:

$$X_{Lim,x} = \frac{2}{\theta^2}\left(\Delta x + \Delta_{Lim,x} - \theta.\mu.t\right) \tag{60}$$

when $0 \leq X_{Lim,x} \leq n.l$

$\Delta_{Lim,x}$ is the deformation in the *x*-direction when the reinforcement bar fractures (i.e. reinforcement maximum extension in the *x*-direction). It is given by:

$$-\Delta_{Lim,x} = \Delta x - \theta.\mu.t - \frac{\theta^2.X_{Lim,x}}{2} \quad (61)$$

The deformation can be calculated similarly for the middle yield-line and the diagonal yield lines.

The distance that covers the intact reinforcement in the *y*-direction for *y*- reinforcement bars $Y_{Lim,y}$ (i.e. the distance of the working forces in the *y*-direction) is given by:

$$Y_{Lim,y} = \frac{2}{\phi^2}\left(\Delta y + \Delta_{Lim,y} - \phi.\mu.t\right) \quad (62)$$

when: $0 \leq Y_{Lim,x} \leq l/2$

$\Delta_{Lim,y}$ is the deformation in the *y*-direction when the reinforcement bar fractures (i.e. reinforcement maximum extension in the *y*-direction). It is given by:

$$-\Delta_{Lim,y} = \Delta y - \theta.\mu.t - \frac{\theta^2.Y_{Lim,y}}{2} \quad (63)$$

Since the reinforcement bars across the central yield line fracture abruptly when the yield line cracks as the slab deflects, the distance of the intact reinforcement bars in the *y*-direction across the central yield line (i.e. the distance $X_{Lim,y}$)can be either of:

- $X_{Lim,y} = l/2.(r-2n)$ when the yield-line reinforcement bars are intact.
- $X_{Lim,y} = 0$ when the yield-line reinforcement bars are all fractured.

Each working force distance (i.e. $X_{Lim,x}$ and $Y_{Lim,y}$) can be written in terms of the other direction. This is required for the methodology of the re-examination, and it is given by Burgess et al. (2014) as follows:

For *x*-reinforcement bars:

$$Y_{Lim,x} = \frac{2}{\theta^2}\left(\Delta x + \Delta_{Lim,x} - \theta.\mu.t\right).\frac{1}{2n} \quad (64)$$

$Y_{Lim,x}$ is the distance in the *y*-direction that covers the intact *x*-reinforcement bars, as shown in Figure 49.

For *y*-reinforcement bars:

$$X_{Lim,y} = \frac{2}{\emptyset^2}\left(\Delta y + \Delta_{Lim,y} - \emptyset.\mu.t\right).2n = \frac{2}{\theta^2}\left(\Delta x + \frac{\Delta_{Lim,y}}{2n} - \theta.\mu.t\right) \quad (65)$$

$X_{Lim,y}$ is the distance in the *x*-direction that covers the intact *y*-reinforcement bars, as shown in Figure 49.

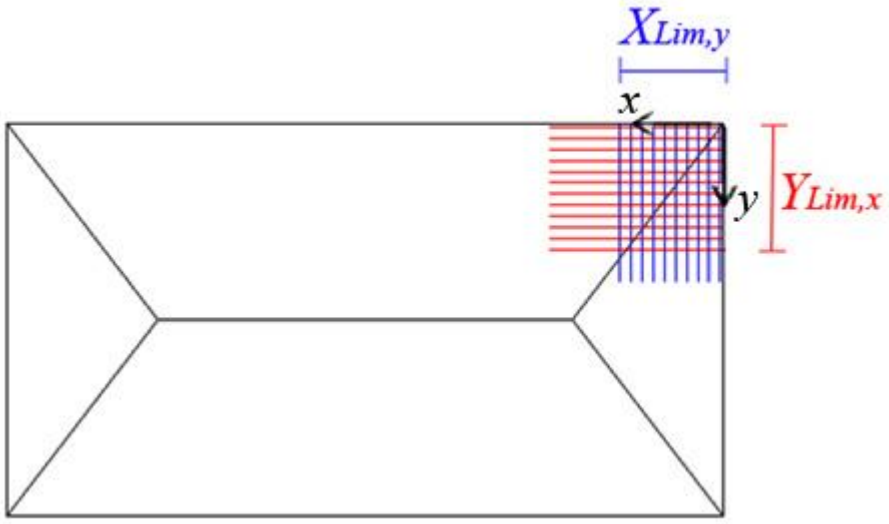

Figure 49: Illustrating the distance of intact reinforcement bars in the *x* and *y* directions

5.3.3 Concrete geometrics

The geometrics of the compression stress blocks have great influence on the calculations of the internal work of the slab. This is due to the fact that reinforcement bars which are embedded in compression blocks do not contribute to the internal work of the slab. Therefore, the geometrics of the concrete compression stress blocks need to be worked out as presented by Burgess et al. (2014).

Figure 50 shows the compression stress block of a slab at an early stage of deflection. Compression still exists over the central region of the slab, with a thickness of z_2 as shown in Figure 50. Meanwhile, the thickness of the compression block increases along the edge of the slab (i.e. z_1). Some reinforcement bars are embedded in compression in this case as illustrated in Figure 50.

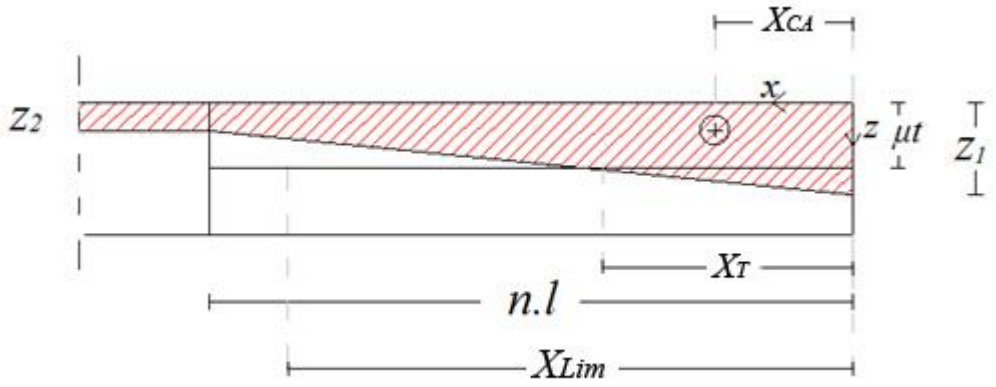

Figure 50: Cross-section of diagonal yield-line α, illustrating compression stress block

X_{CA} is the distance in the *x*-direction from the origin to the centroid of the concrete compression area.

X_T is the distance that covers the reinforcement bars in compression in the *x*-direction.

From Equation 59, at distance $x=0$, z_1 is given by:

$$z_1 = \frac{\Delta x}{\theta} \tag{66}$$

From Equation 59, at distance $x=nl$, z_2 is given by:

$$z_2 = \frac{\Delta x}{\theta} - \frac{\theta . n . l}{2} \tag{67}$$

Figure 50 shows that X_T is the length of which the reinforcement bars are embedded in compression stress block; therefore these bars do not dissipate work. X_T is given by:

$$X_T = n . l \left(\frac{z_1 - \mu . t}{z_1 - z_2}\right) = 2 \left(\frac{\Delta x}{\theta^2} - \frac{\mu . t}{\theta}\right) \tag{68}$$

The distance that covers the reinforcement bars in compression in the *y*-direction Y_T is given by the relationship between the *x* and *y* directions as follows:

$$Y_T = X_T . \frac{1}{2n} \tag{69}$$

These reinforcement bars in compression need to be subtracted from the working force distance in order to calculate the internal work of the reinforcement. This is conducted as follows:

For *x*-reinforcement bars: when $Y_{Lim,x}<0$ and $Y_T>0$:

$$\left(Y_{Lim,x} - Y_T\right) = \frac{\Delta_{Lim,x}}{n.\theta^2} \tag{70}$$

For *y*-reinforcement bars: when $X_{Lim,y}<0$ and $X_T>0$:

$$\left(X_{Lim,y} - X_T\right) = \frac{\Delta_{Lim,y}}{n.\theta^2} \tag{71}$$

5.3.4 Compression stress block development

Burgess et al. (2014) consider three phases when the slab goes through large deflections. These phases are divided into sub-phases which are called "cases"; in which the reinforcement bars, all or part of them, might be either intact or fractured, depending the reinforcement bars being below or embedded in the compression stress blocks. These phases and cases were divided as the following:

1. Phase (a): Compression block is trapezoidal. Cases within the phase are divided as:

   (a1) Cases: All of the compression is above reinforcement bars:

   - a1) All reinforcement bars are intact.
   - a1') Central yield-line reinforcement bars, in the *y*-direction, are fractured.
   - a1*) Reinforcement bars in the *x*-direction are partly fractured, while the *y*-direction bars are intact.
   - a1**) Reinforcement bars in the *y*-direction are partly fractured, the *x*-direction bars are intact.

- a1'*) Reinforcement bars in the *x*-direction are partly fractured, the *y*-direction middle yield-line are bars fractured.
  a***) Reinforcement bars in the *x* and *y* directions are partly fractured.

(a2) Cases: Some of the reinforcement bars are embedded in compression:

Similar to (a1) cases, but in (a2) cases some reinforcement bars are embedded in compression. These compressed bars should not taken into consideration in internal work calculations.

2. Phase (b): the compression block becomes triangular as the deflection increases and compression over the central region disappears (i.e. $z_2=0$). The concept is similar to phase (a), taking into consideration the different geometrics of the triangular compression block and the related geometries to this difference.

3. Phase (c): the compression block becomes trapezoidal as the deflection increases further; and the depth of compression block theoretically becomes larger than the depth of the slab, and the whole slab depth is in compression. Phase (c) has similar process and cases to phase (a), with new geometry regulations depending on the compression block geometrics.

These phases and cases were fully presented by Staikova (2014). In this study, the whole mechanism of the re-examination was developed and extended, taking into consideration the presence of a composite beam and the effects of elevated temperatures.

The benefits and shortcomings of the alternative simplified method can be summarized as follows:

Benefits:

- The method allows monitoring of the behaviour of the reinforcement fracture as the slab deflects.
- Monitoring the reinforcement fracture allows removal of the conservative and unrealistic deflection limit which was imposed by the Bailey-BRE method. This

allows the designer to decide when the analysis should be stopped, complying with the desired safety factor.

- Compared to the Bailey-BRE method, the alternative simplified method is not as conservative as the Bailey-BRE method when it is compared to Cardington tests (Burgess et al. 2012). Furthermore, it is not over-sensitive to marginal changes of reinforcement ratio, as is the Bailey-BRE method.

Shortcomings:

Since the development of the method was incomplete, the following shortcomings existed at the time of this study :

- The loss of vertical support by the primary beams was ignored.
- The detailed bond-slip behaviour between the reinforcement bars and the adjacent concrete was not addressed.
- The method addresses only flat concrete slabs before it was extended to include composite slabs in this study.

The alternative method gives reasonable results for slab load enhancement at large deflections. However, the alternative method exclusively considers plain flat slabs in ambient temperature. The method, however, is not limited to these factors (i.e. flat slab and ambient temperature). As a main aim of this study, the alternative method was extended in order to account for the composite action with unprotected internal secondary beams. In addition, the effect of elevated temperatures was addressed in the extension of the alternative method.

6 The Mechanics of Tensile Membrane Action in Composite Slabs in Fire

6.1 Rotated yield-line pattern

In this chapter, the alternative simplified method of tensile membrane action, which was developed by Burgess et al. (2013), and the re-examination of the mechanics of TMA at ambient temperature, developed by Burgess et al. (2014), are presented after they were developed and extended to include composite slabs at elevated temperatures.

As mentioned in Section 4.1, one secondary steel beam was added to the slab, attached to it by shear studs. This single secondary beam was left unprotected against fire and elevated temperatures. The composite action, which was provided by the downstand beam, changed the yield line pattern from normal pattern, aligned to the *x*-direction, to rotated yield-line pattern, aligned to the *y*-direction as illustrated in Figure 51.

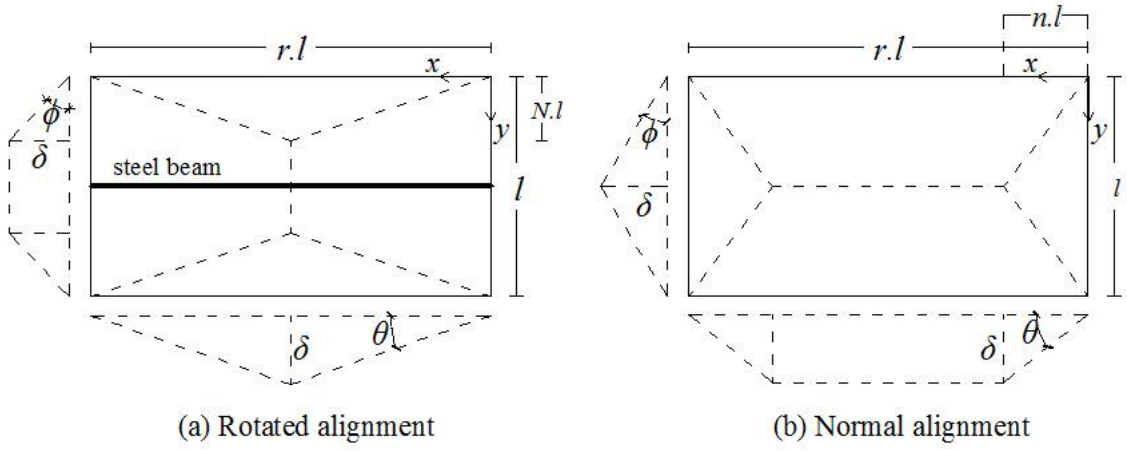

Figure 51: Comparison between normal and rotated alignments of yield line patterns

N is the yield-lines intersection point distance from the larger span of the slab.

To distinguish between the normal and rotated yield-line patterns, the optimized yield-line intersection point distance, in the presence of the steel beam, was denoted as *N* instead of *n* as it was denoted in the normal yield-line pattern.

As the slab deflects, the mechanism starts with the rotated alignment since the downstand beam is at its full strength capacity at ambient temperature in the beginning. As temperature increases, the unprotected downstand beam loses its strength progressively, leading to increase the yield-line intersection point parameter *N*, pushing the yield-lines intersection points to get closer to each other until they meet and form a cross yield-line pattern as shown in Figure 52(c). If the cross yield-line pattern forms before the slab load carrying capacity decreases to the optimum yield-line load capacity (i.e. the slab did not fail yet) the yield line pattern converts to the normal alignment after the beam lost most of its capacity and became ineffective. However, this transformation from the rotated to normal alignment is highly unlikely to occur since the load capacity of the slab degrades to the yield-line capacity when the yield-line pattern is still in rotated alignment (i.e. aligned to the *y*-direction). Repeating the analysis and trying multiple slab and beam properties showed that this transformation from the rotated to normal yield-line pattern does not practically occur with a properly designed beam. When at least one downstand steel beam exists, the optimum yield line pattern forms in rotated alignment. Nonetheless, this transformation of the alignments is worth mentioning only as a theoretical possibility. The theoretical pattern transformation is illustrated in Figure 52, starting from ambient temperatures as shown in Figure 52(a), increasing until failure as shown in Figure 52(f).

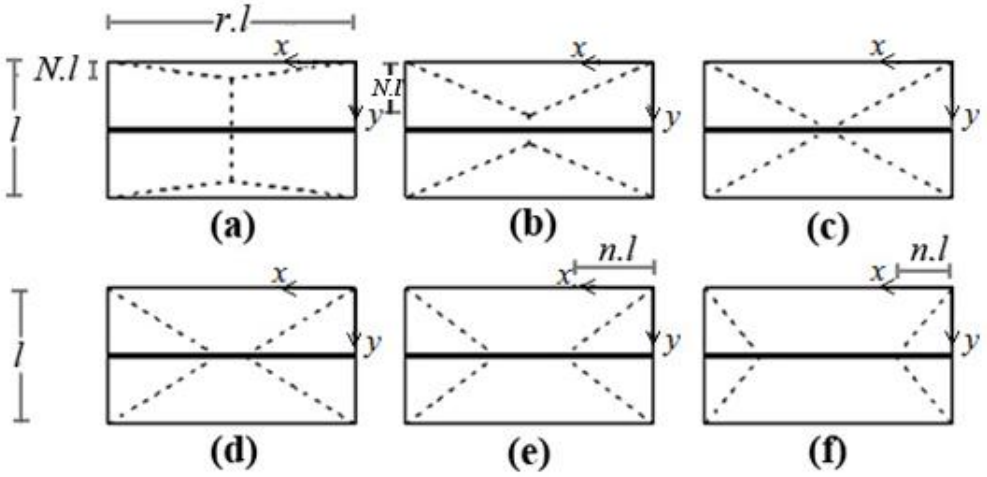

Figure 52: Changing yield-line pattern from rotated to normal alignment as temperature increases

6.2 Small-deflection analysis

6.2.1 Rotated yield-line mechanism

Figure 53 shows the rotated alignment of the yield-line pattern when the downstand beam is still at full or significant ratio of its strength capacity before reaching high temperatures. As temperatures increase, the unprotected steel beam is affected by the heat which reduces its strength capacity. This capacity degradation leads to slab deflection under the effect of the load.

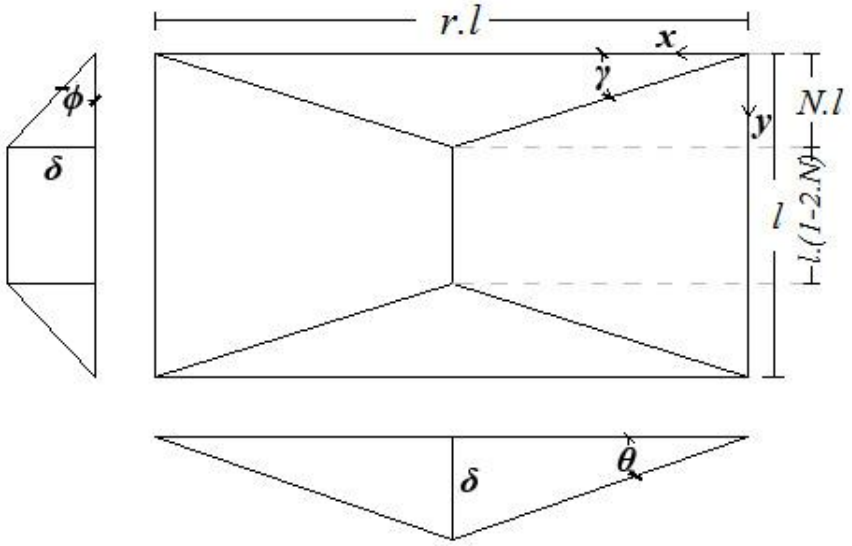

Figure 53: Rotated alignment yield-line pattern

As mentioned in Section 2.2.2, the slab elements, which are defined by the straight yield-lines, rotate as rigid bodies in two angels of rotations: θ and ϕ, in the x and y directions, respectively, resulting in a maximum deflection δ at the yield lines intersection points. These angles θ, ϕ, in addition to γ as shown in Figure 53, are calculated as follows:

$$tg(\gamma) = \frac{N.l}{\frac{r.l}{2}} = \frac{2.N}{r} \tag{72}$$

$$\phi = \frac{\delta}{N.L} \tag{73}$$

$$\theta = \frac{2.\delta}{r.l} \tag{74}$$

6.2.1.1 Internal work of the secondary beam

In order to calculate the load capacity of the slab, the internal work should be worked out. Therefore, the internal work of the steel beam should be calculated. For the small-deflection analysis, the internal work dissipated by the secondary steel beam is calculated by its moment capacity, multiplied by its angle of rotation as it deflects. The moment capacity of the composite beam is given by:

$$M_{pl} = A.f_y.(\frac{h_a}{2} + t - \frac{x_c}{2}) \tag{75}$$

M_{pl}	is the moment of resistance of the beam.
A	is the area of the beam.
f_y	is the yield stress of the steel.
h_a	is the total height of the beam.
t	is the thickness of the concrete part of the slab.
x_c	is the neutral axis distance from the top of surface of the slab.

The internal work dissipated by the single secondary beam I_B is calculated as follows:

$$I_B = 2.M_{pl}.\theta \tag{76}$$

Substituting Equation 74 into Equation 76 leads to:

$$I_B = 2.M_{pl}.\frac{2\delta}{r.l} \tag{77}$$

$$I_B = 4.M_{pl}.\frac{\delta}{r.l} \tag{78}$$

6.2.1.2 Internal work of the slab

The internal work of the flat slab without the secondary beam I_S is calculated according to the work method as presented in Section 2.3. It is given by:

$$I_S = 2.m_p.r.l.\phi + 2.m_p.l.\theta \tag{79}$$

m_p is the sagging moment the slab per unit length
l is the projected length of the yield-line on the corresponding axis of support

Consider $K=2.m_p$

By substituting the angles of rotation in Equations 73 and 74 and arranging:

$$I_S = K.r.\frac{\delta}{N} + 2.K.\frac{\delta}{r} \tag{80}$$

$$I_S = K.\delta.\left(\frac{r}{N} + \frac{2}{r}\right) \tag{81}$$

The total internal work of the slab I_{tot} is the sum of the internal work of the flat I_S slab and the internal work of the beam I_B as follows:

$$I_{tot} = I_S + I_B \tag{82}$$

Substituting Equations 78 and 81 give:

$$I_{tot} = K.\delta.\left(\frac{r}{N} + \frac{2}{r}\right) + 4.M_{pl}.\frac{\delta}{r.l} \tag{83}$$

6.2.1.3 External work done on the slab

The external work done by the load on the slab E is calculated according to the work method as follows:

$$E = 2.P.r.l.\frac{N.l}{2}.\frac{\delta}{3} + 4.P.\frac{N.l}{2} + \frac{r.l}{2}.\frac{\delta}{3} + P.r.l.l(1-2N).\frac{\delta}{2} \tag{84}$$

P is the load-carrying capacity of the slab.

Rearranging Equation 84 gives:

$$E = P.r.l^2.\delta.\left(\frac{2}{3}N + \frac{1}{2} - N\right) \tag{85}$$

$$E = P.r.l^2.\delta.\left(\frac{1}{2} - \frac{1}{3}N\right) \tag{86}$$

6.2.1.4 Slab's load capacity

According to the work method: the internal work dissipated by the slab= the external work expended by loads

By substituting Equations 78, 81 and 86 into the external work expended by loads:

$$K.\delta.\left(\frac{r}{N} + \frac{2}{r}\right) + 4.M_{pl}.\frac{\delta}{r.l} = P.r.l^2.\left(\frac{1}{2} - \frac{1}{3}N\right)\delta \tag{87}$$

By rearranging Equation 87:

$$P = \frac{\frac{K.r}{N} + \frac{2.K}{r} + \frac{4.M_{pl}}{r.l}}{\frac{1}{2}.r.l^2 - \frac{1}{3}.r.l^2.N} \tag{88}$$

In order to get the smallest yield-line load capacity (i.e. the optimum yield-line load capacity) the parameter *N* should be optimized so that it gives the minimum failure load. Taking the first derivative of *P* in Equation 88 with respect to *N*, gives:

$$\frac{dP}{dN} = \frac{\frac{-K.r}{N^2}.\left(\frac{1}{2}.r.l^2 - \frac{1}{3}.r.l^3.N\right) - \left(-\frac{1}{3}r.l^2\right).\left(\frac{K.r}{N} + \frac{2.K}{r} + \frac{4.M_{pl}}{r.l}\right)}{\left(\frac{1}{2}.r.l^2 - \frac{1}{3}.r.l^2.N\right)^2} \tag{89}$$

$\frac{dP}{dN} = 0$ When the numerator = 0. This is given by:

$$\frac{-K.r}{N^2}.\left(\frac{1}{2}.r.l^2 - \frac{1}{3}.r.l^3.N\right) - \left(-\frac{1}{3}r.l^2\right).\left(\frac{K.r}{N} + \frac{2.K}{r} + \frac{4.M_{pl}}{r.l}\right) = 0 \tag{90}$$

Rearranging Equation 90 gives:

$$-\frac{1}{2}.K.r^2.l^2.\frac{1}{N^2}+\frac{2}{3}.K.r^2.l^2.\frac{1}{N}+\frac{2}{3}.K.l^2+\frac{4}{3}.M_{pl}.l=0 \quad (91)$$

$$\left(\frac{2}{3}K.l^2+\frac{4}{3}.M_{pl}.l\right).N^2+\frac{2}{3}.K.r^2.l^2.N+\left(-\frac{1}{2}.K.r^2.l^2\right)=0 \quad (92)$$

By solving Equation 92, the solution for *N* which gives the smaller value for *P* is given by:

$$N=\frac{-\frac{2}{3}K.r^2.l^2+\sqrt{\left(\frac{2}{3}K.r^2.l^2\right)^2-4.\left(\frac{2}{3}.K.l^2+\frac{4}{3}.M_{pl}.l\right).\left(-\frac{1}{2}.K.r^2.l^2\right)}}{2.\left(\frac{2}{3}K.l^2+\frac{4}{3}.M_{pl}.l\right)} \quad (93)$$

The other solutions for *N* from Equation 92 and from the denominator of Equation 89 give either too large values of *N* or negative values. Therefore, Equation 93 represents the ideal solution for the optimized yield-line capacity *P*.

6.2.2 Normal yield-line mechanism

The transformation from the initial rotated yield-line pattern, aligned to the *y*-direction to the normal yield-line pattern, aligned to the *x*-direction, was found to be merely theoretical hypothesis when a downstand steel beam exists. However, the derivation of the normal yield-line mechanism which proved this is presented in this section only for the small-deflection analysis part of this study. Figure 54 shows the normal yield-line pattern in the presence of the downstand steel beam.

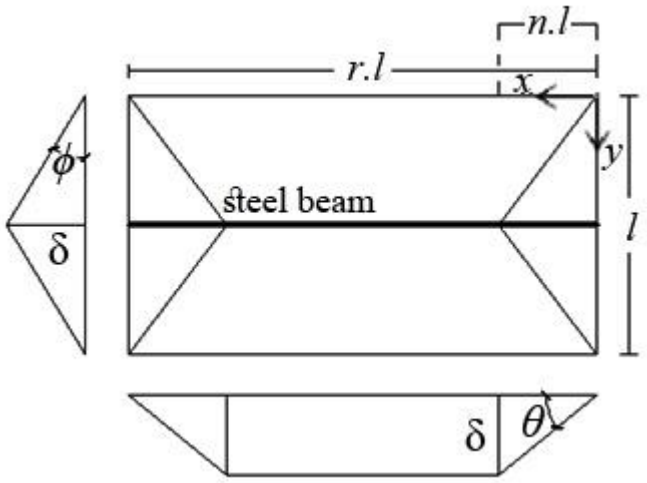

Figure 54: Normal alignment yield-line pattern

The internal work of the slab I_S is given by:

$$I_S = 2.m_p.r.l.\phi + 2.m_p.l.\theta = K.r.l.\frac{2.\delta}{l} + K.l.\frac{\delta}{n.l} \tag{94}$$

$$I_S = 2.K.r.\delta + \frac{K}{n}.\delta \tag{95}$$

The internal work of the beam I_B is given by:

$$I_B = 2.M_{pl}.\theta = 2.M_{pl}.\frac{\delta}{n.l} \tag{96}$$

The external work done by the loads on the slab E is given by:

$$E = 2.P.l.\frac{n.l}{2}.\frac{\delta}{3} + 4.P.\frac{n.l}{2}.\frac{l}{2}.\frac{\delta}{3} + P.l.(r-2n).l.\frac{\delta}{2} \tag{97}$$

Rearranging Equation 97 gives:

$$E = \frac{2}{3}.P.n.l^2.\delta + \frac{1}{2}.P.l^2.(r-2n).\delta \tag{98}$$

According to the energy method: the internal energy dissipated by the slab = the external work done by loads. Therefore:

$$2.K.r + \frac{K}{n} + \frac{2.M_{pl}}{n.l} = \frac{2}{3}.P.n.l^2 + \frac{1}{2}.P.l^2.(r - 2n) \quad (99)$$

Rearranging Equation 99 to make *P* the subject gives:

$$P = \frac{2.K.r.n + K + \frac{2.M_{pl}}{l}}{\frac{2}{3}.n^2.l^2 + \frac{1}{2}.n.l^2.r - n^2.l^2} \quad (100)$$

In order to get the optimum yield-line load capacity, the parameter *n* should be optimized so that it gives the minimum *P*. Similarly to the rotated yield-line mechanism, the numerator of $\frac{dp}{dn}$ was found to give the ideal value of *n* for the optimum yield-line load capacity as follows:

$$\frac{dP}{dn} = \frac{2.K.r.\left(\frac{2}{3}.n^2.l^2 + \frac{1}{2}.n.r.l^2 - n^2.l^2\right) - \left(\frac{4}{3},l^2.n + \frac{1}{2}.r.l^2 - 2.n.l^2\right).\left(2.K.r.n + K + \frac{2M_{pl}}{l}\right)}{\left[\frac{2}{3}.n^2.l^2 + \frac{1}{2}.n.l^2.r - n^2.l^2\right]^2} \quad (101)$$

$\frac{dP}{dn} = 0$ when the numerator = 0 as follows:

$$2.K.r.\left(\frac{2}{3}.n^2.l^2 + \frac{1}{2}.n.r.l^2 - n^2.l^2\right) - \left(\frac{4}{3},l^2.n + \frac{1}{2}.r.l^2 - 2.n.l^2\right).\left(2.K.r.n + K + \frac{2M_{pl}}{l}\right) = 0 \quad (102)$$

Rearranging Equation 102 gives:

$$\frac{2}{3}.K.r.l^2.n^2 + \left(\frac{2}{3}.K.l^2 + \frac{4}{3}M_{pl}.l\right).n + \left(-\frac{1}{2}.K.r.l^2 - M_{pl}.r.l\right) = 0 \quad (103)$$

The solution that gives the minimum value of the load P is given by:

$$n = \frac{-\left(\frac{2}{3}.K.l^2 + \frac{4}{3}M_{pl}.l\right) + \sqrt{\left(\frac{2}{3}.K.l^2 + \frac{4}{3}M_{pl}.l\right)^2 - 4.\left(\frac{2}{3}.K.r.l^2\right).\left(-\frac{1}{2}.K.r.l^2 - M_{pl}.r.l\right)}}{2.\left(\frac{2}{3}.K.r.l^2\right)} \quad (104)$$

6.2.3 Failure of the slab

Consider the uniformly applied load on the slab P_a. As temperatures increase, the slab load capacity P decreases progressively until P=P_a. At this point, the yield lines form over the slab and the yield-line pattern is fixed (i.e. highly unlikely to change later). At this point, the slab is considered failed according to conventional design methods, including the yield-line theory. The yield-lines form as plastic hinge lines. The corresponding load-carrying capacity of the slab at this point is referred to as the failure load. However, as this study takes the membrane action into account, it was considered that this failure load is no more than the yield-line load (i.e. the load at which the yield-lines form over the slab). Actually, the slab does not really fail, but it moves from the small-deflection phase to the large-deflection phase as the slab deflects further. This allows the mobilization of tensile membrane action which provides further capacity with more deflection and further work dissipation, until the real failure occurs in the end. The large-deflection phase is discussed in Section 6.3.

6.2.4 Critical temperature

In order to calculate the temperature which is required for the yield-line load to decrease until it is equal to the applied load, an iteration should be conducted starting from the rotated alignment until the slab loses its load-carrying capacity and fail, whether this failure occurs during the rotated or normal alignment phase eventually. It was found that the transformation from the rotated to normal alignment does not happen. However, this was conducted here for checking purpose. The iteration increased the temperature gradually and therefore reduced the capacity of the downstand steel beam. To simulate the decrease of the beam strength, the moment resistance capacity of the unprotected downstand beams M_{pl} was multiplied by a reduction factor k_y, as discussed in Section

4.2. At ambient temperatures, $k_y = 1$, which means that the secondary unprotected beam retains its full strength capacity so far. At elevated temperatures, k_y decreases, therefore the load capacity of the steel beam decreases too.

The initial value of k_y was considered 1.0 in the beginning of the analysis (i.e. the temperature was still below or equal 400ºC). In the beginning of the iteration, an initial temperature of 400ºC was considered as a starting temperature; and with every loop, the temperature increased by a small increment. A temperature of 400ºC was chosen as a start instead of 20ºC only for programming issues, with no difference in the results since the reduction factor has a constant value of 1 between 20ºC and 400ºC. The corresponding reduction factor k_y was, then, calculated from Table 3.1 in EN 1993-1-2: 2005, depending on the steel temperature.

The iteration continued until the continuously-decreasing load capacity of the slab P dropped to the level of the applied load P_a. This whole process was carried out using Microsoft Excel Visual Basic (VBA). The programming code is presented in Appendix-2, in addition to the coding methodology.

6.3 Large-deflection analysis - compression stress block method

The mechanics of the compression stress block method was derived in order to work out the geometrics, rotations and movements of the slab elements as the slab deflects beyond the level of the yield-line mechanism. These geometrics, rotations and movements govern the forces and stress blocks over the slab which are required to calculate the slab's plastic load capacity P at large deflections. This capacity P is required to determine the critical temperature of the slab for every large deflection level until failure. The forces on the slab are: concrete compression forces, and tension forces of both the reinforcement and the unprotected downstand steel beam. Before working out the equilibrium of the forces on the composite slab, the geometric arrangements should be worked out.

6.3.1 General geometrics

Consider an arbitrary point P' on the slab. As the slab deflects, the slab elements rotate as shown in Figure 55. In addition to the rotation, the slab elements experience horizontal movements in the *x* and *y* directions.

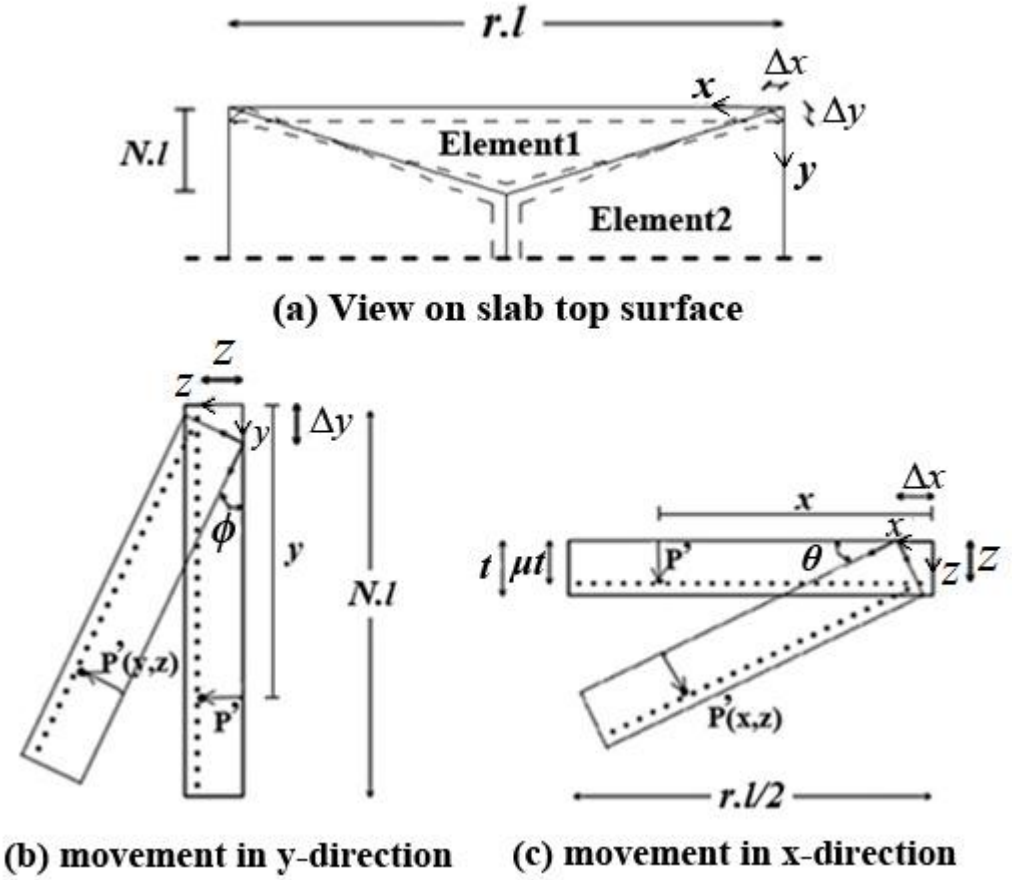

Figure 55: Slab element rotation and movement

The movements and rotations of the slab elements 1 and 2, in the *x* and *y* directions, result in crushing the concrete at the corners of the slab as shown in Figure 56 . These crushing corners give compressive forces which contribute to the internal work dissipated by the slab as it deflects. At a late stage of deflections, the compression forces are confined at these corners of the slab.

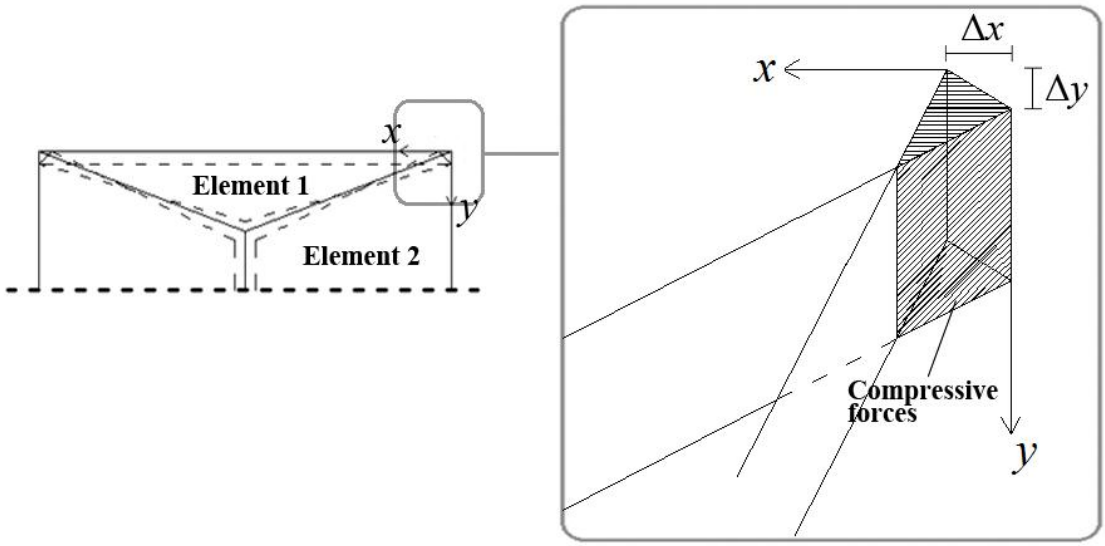

(a) Top view of the slab **(b) Crushing slab conrers**

Figure 56: Crushing concrete at the corners of the slab at large deflections

From the geometry of the deflecting slab shown in Figure 55, the movement of the point P' or any point in the *y*-direction *v*, is calculated as follows:

$$v = \Delta y - \phi . z - \frac{\phi^2 . y}{2} \tag{105}$$

The term *y* represents an arbitrary distance in the *y*-direction. For the case which is shown in Figure 55, *y* is the distance of the point P' from the origin.

From the geometry of the deflecting slab shown in Figure 55, the movement of the point P' or any point in the *x*-direction *u*, is calculated as follows:

$$u = \Delta x - \theta . z - \frac{\theta^2 . x}{2} \tag{106}$$

The term *x* represents an arbitrary distance in the *x*-direction. For the case which is shown in Figure 55, *x* is the distance of the point P' from the origin.

For v=0:

$$\Delta y = \phi . z + \phi^2 \frac{y}{2} = 0 \tag{107}$$

Rearranging Equation 107 gives:

$$\Delta y = \phi\left(z + \frac{\phi.y}{2}\right) \tag{108}$$

From Equation 108, when y=0, the compression block depth z_1 is given by:

$$z_1 = \frac{\Delta y}{\phi} \tag{109}$$

From Equation 108, when $y=N.l$, the compression block depth z_2 is given by:

$$z_2 = \frac{\Delta y}{\phi} - \frac{\phi.N.l}{2} \tag{110}$$

The compression block depths z_1 and z_2 are illustrated in Figure 57.

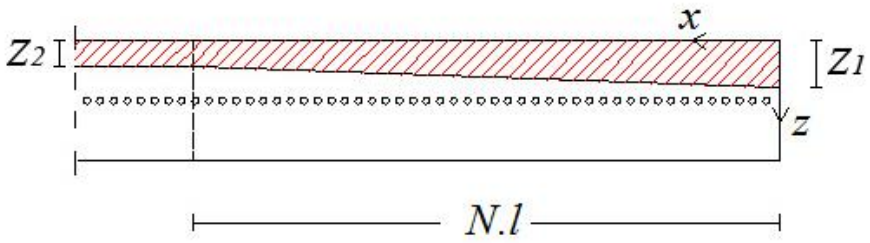

Figure 57: Compression block depths z_1 and z_2 along diagonal yield-line

The distances of the intact reinforcement forces in the x and y directions $X_{Lim,x}$ and $Y_{Lim,y}$ are illustrated in Figure 58, and given by:

$$X_{Lim,x} = \frac{2}{\theta^2}(\Delta x + \Delta_{Limx} - \theta.\mu.t) \text{ When } 0 \le X_{Lim,x} \le \frac{r.l}{2} \tag{111}$$

$$Y_{Lim,y} = \frac{2}{\emptyset^2}\left(\Delta y + \Delta_{Limy} - \emptyset.\mu.t\right) \text{ When } 0 \le Y_{Lim,y} \le N.l \tag{112}$$

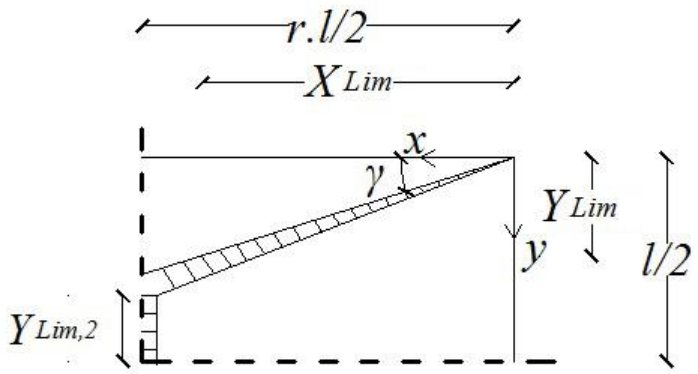

Figure 58: Distances where reinforcement bars are intact

$Y_{Lim,2}$ is the distance that covers the intact reinforcement across the central yield-line crack in the *y*-direction.

From Figure 58:

$$tg(\gamma) = \frac{N.l}{r.l/2} = \frac{2N}{r} \tag{113}$$

The distances of the reinforcement forces in the *x* and *y* directions $Y_{Lim,x}$ and $X_{Lim,y}$ can be calculated and written with respect of the other direction, using $tg(\gamma)$ as follows:

$$tg(\gamma) = \frac{Y_{Lim,x}}{X_{Lim,x}} = \frac{2N}{r} \tag{114}$$

$$tg(\gamma) = \frac{Y_{Lim,y}}{X_{Lim,y}} = \frac{2N}{r} \tag{115}$$

$$Y_{Lim,x} = \frac{2}{\phi^2}\left(\Delta y + \frac{\Delta_{Limx}}{\frac{2N}{r}} - \phi.\mu.t\right) \tag{116}$$

From Figure 58:

$$tg(\gamma) = \frac{Y_{Lim,y}}{X_{Lim,y}} \tag{117}$$

Equation 117 gives:

$$X_{Lim,y} = \frac{Y_{Lim,y}}{tg(\gamma)} \tag{118}$$

Substituting Equations 112 and 117 into 118 gives:

$$X_{Lim,y} = \frac{2}{\phi^2}\left(\Delta y + \Delta_{Limy} - \phi.\mu.t\right).\frac{r}{2.N} \tag{119}$$

Rearranging gives:

$$X_{Lim,y} = \frac{r}{N.\phi^2}\left(\Delta y + \Delta_{Limy} - \phi.\mu.t\right) \tag{120}$$

Equations 116 and 120 give the distances that cover the intact reinforcement bars in the *x* and *y* directions with respect to the other direction.

6.3.2 Geometrics of mechanism-b

As the slab deflects beyond the formation of the optimum yield-line pattern, the yield-lines start to crack, leaving the reinforcement in pure tension, therefore, to fracture after it yielded. This process occurs in different phases as the deflection increases. Each phase is distinguished by the shape that the compression stress block takes. The process is similar to what was explained in Section 5.3, but the geometrics are different. Therefore, it is presented in this chapter with the new mechanism and geometrics behind it . Phase (a), for example, is the first phase that the slab goes through, at which the compression stress block is nearly rectangular, spread over the whole region of the slab, converting to trapezoid at the peripheral edge along the supporting beams. Phase (b) witnesses the disappearance of the compression from the central region of the slab, and the conversion of the compression block to triangular shape at the perimeter of the slab, or what is called the compression ring.

Each of phases (a) and (b) was, in turn, divided into different cases, representing the different scenario paths that these phases might go through. For example, Phase (b) contains different cases, like: case (b1), case (b1') and case (b1*). These scenario paths, or cases, depend on the fracture sequence of the reinforcement bars. Across a particular yield-line, reinforcement bars might fracture in the *x*-direction first, then the bars in the

y-direction follow; or the opposite scenario might occur. This is further discussed in Section 6.3.7 when the equilibrium of these cases is presented.

6.3.2.1 Initial Phase (a)

In the initial large-deflection phase, compression exists over the whole area of the slab. The slab resists the loads in bending. As it is illustrated in Figure 59, the upper level of central region of the slab is still in compression with a compression block depth of z_2. At the perimeter of the slab, the compression thickness increases gradually towards the supporting edges, reaching its maximum z_1. The reinforcement bars can be either below the compression block (i.e. case a1) or embedded in the compression block (i.e. case a2). It is important that this is determined, since reinforcement bars which are embedded in compression do not contribute to the internal work of the slab. Therefore, when the compression block is below the reinforcement bars (i.e. the distance that covers the reinforcement bars in compression in the *y*-direction $Y_T>0$) only the working distance over which the reinforcement bars are intact is considered (i.e. $Y_{Lim,y} - Y_T$). In order to calculate the compression force for each phase and case, the rest of the geometric parameters of the cross-section, which are shown in Figure 59, should be calculated.

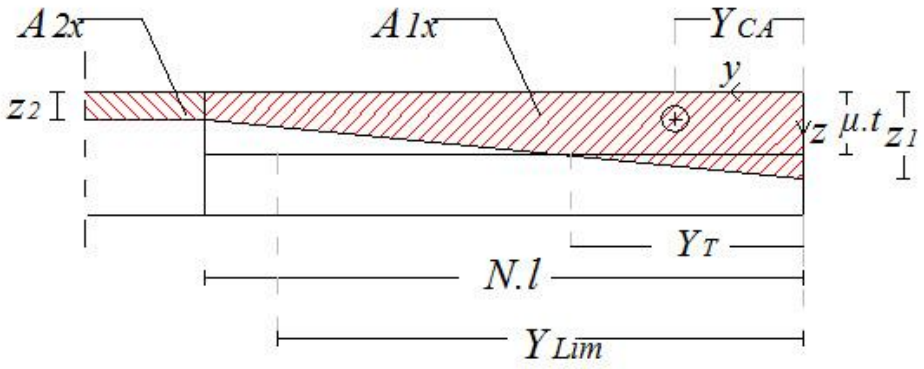

Figure 59: Compression stress block in phase (a)

A_{1x} is the compression area in the diagonal yield-lines at the edge of the slab.

A_{2x} is the compression area in the diagonal yield-lines at the central region of the slab.

Y_T is the distance that covers the reinforcement bars in compression in the *y*-direction.

The distance from the edge of the slab to the centroid of the compression stress block in the *y*-direction Y_{CA} is given by:

$$Y_{CA} = \frac{N.l\left(\frac{\Delta y}{\phi} - \frac{\phi N.l}{3}\right)}{\frac{2.\Delta y}{\phi} - \frac{\phi.N.l}{2}} \tag{121}$$

The distance of which the reinforcement bars are embedded in compression Y_T is given by:

$$Y_T = \frac{2}{\phi}\left(\frac{\Delta y}{\phi} - \mu.t\right) \tag{122}$$

This distance Y_T is zero for all (a1) cases, since these cases represent a scenario of which all reinforcement bars are below the compression stress block, as is discussed in Section 6.3.5.

The areas of the compression stress blocks at the edge and centre zones of the slab A_{1x} and A_{2x}, respectively, are given by:

$$A_{1x} = \left(\frac{2\Delta y}{\phi} - \phi\frac{N.l}{2}\right)\frac{N.l}{2} = \frac{\Delta y.N.l}{\phi} - \phi\frac{N^2.l^2}{4} \tag{123}$$

$$A_{2x} = l\left(\frac{1}{2} - N\right)\left(\frac{\Delta y}{\phi} - \phi\frac{N.l}{2}\right) \tag{124}$$

6.3.2.1.1 Case (a1): compression above all reinforcement bars

In this case, the depth of the compression stress block z_1 is smaller than the reinforcement vertical depth within the slab μt, and the compression block over the central region of the slab still exists (i.e. z_2>0). This is illustrated in Figure 60.

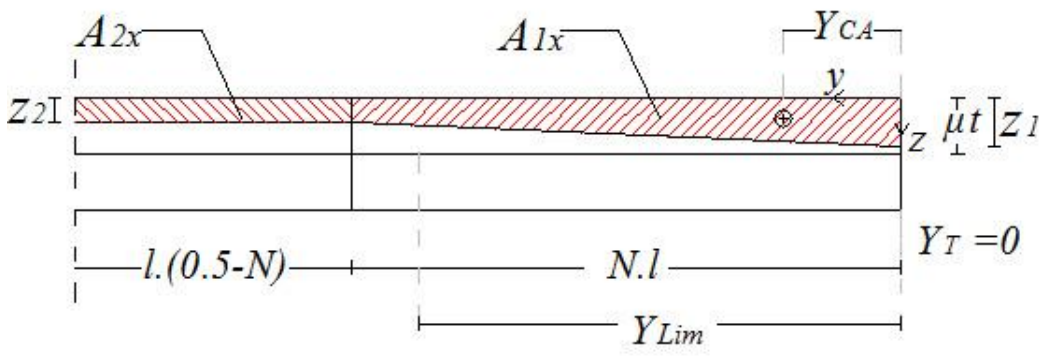

Figure 60: Case (a1) - compression above all reinforcement bars

There are two mathematical probabilities here: 1. the distance that covers the intact reinforcement bars is larger than *N.l* (in this situation this distance is taken as *N.l* as a maximum); 2. the distance that covers the intact reinforcement bars has a certain value which can be calculated. These two probabilities are interpreted as follows:

For reinforcement bars in the *x*-direction:

$$\left(Y_{Lim,x} - Y_T\right) = N.l \quad \text{when} \quad Y_{Lim,x} > N.l \tag{125}$$

$$\left(Y_{Lim,x} - Y_T\right) = \frac{r}{N.\phi^2}\left(\Delta y + \frac{\Delta_{Limx}}{\frac{2N}{r}} - \phi.\mu.t\right) \quad \text{when} \quad Y_{Lim,x} < N.l \tag{126}$$

For reinforcement bars in the *y*-direction:

$$\left(X_{Lim,y} - X_T\right) = \frac{r.l}{2} \quad \text{when} \quad X_{Lim,y} > \frac{rl}{2} \tag{127}$$

$$\left(X_{Lim,y} - X_T\right) = \frac{r}{N.\phi^2}\left(\Delta y + \Delta_{Limy} - \phi.\mu.t\right) \quad \text{when} \quad X_{Lim,y} < \frac{rl}{2} \tag{128}$$

6.3.2.1.2 Case (a2): compression below reinforcement

This case represents phase (a) when the compression stress block is below some of the reinforcement bars (i.e. some of the reinforcement bars are embedded in compression). In this case, X_T and Y_T are larger than zero and should be calculated according to

Equation 120. To calculate the distance $Y_{Lim,x}$, the relationship between the *x* and *y* directions can be used by converting between these directions in Equation 120 by using $tg(\gamma)$.

6.3.2.2 Phase (b):

As the deflection increases, the depth of the compression block z_1 increases while z_2 decreases until z_2=0, although it theoretically becomes negative as shown in Figure 61. This converts the compression stress block area to a triangular block. This scenario is represented by Phase (b) that has different geometrics from phase (a). A slab cross-section in Phase (b) is illustrated in Figure 61.

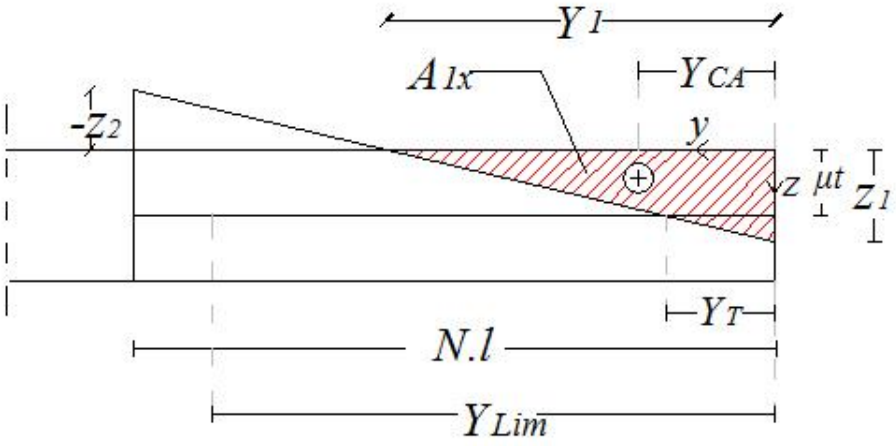

Figure 61: Phase (b) - triangular compression block

The parameters of Phase (b) can be calculated from the geometrics as shown in Figure 61 as follows:

$$Y_1 = \frac{N.l.z_1}{z_1 - z_2} = \frac{N.l.\frac{\Delta y}{\phi}}{\frac{\Delta y}{\phi} - \frac{\Delta y}{\phi} + \frac{\phi.N.l}{2}} = \frac{2\Delta y}{\phi^2} \quad (129)$$

Y_1 is the length of the triangular concrete compression block in the *y*-direction.

Since z_2 is negative here, it was not considered in the calculations. Therefore, the area of the compression block A_{1x} is given by:

$$A_{1x} = \frac{z_1 . Y_1}{2} = \frac{\frac{\Delta y}{\phi} . 2\frac{\Delta y}{\phi}}{2} = \frac{\Delta y^2}{\phi^3} \tag{130}$$

The distance of the centroid of the compression stress block in the *y*-direction from the edge of the slab Y_{CA} is given by:

$$Y_{CA} = \frac{Y_1}{3} = \frac{\Delta y}{3\phi^2} \tag{131}$$

Y_T is calculated according to Equation 122.

6.3.2.2.1 Case (b1): triangular compression above all reinforcement bars

Case (b1) represents Phase (b) when the triangular compression block is effectively above all the reinforcement bars in the slab (i.e. none of the reinforcement bars is in compression). In other words, the depth of the compression block at the edge of the slab z_1 is smaller than the depth of the reinforcement within the slab μt, and $z_2<0$, therefore Y_T and $X_T = 0$. Case (b1) is illustrated in Figure 62.

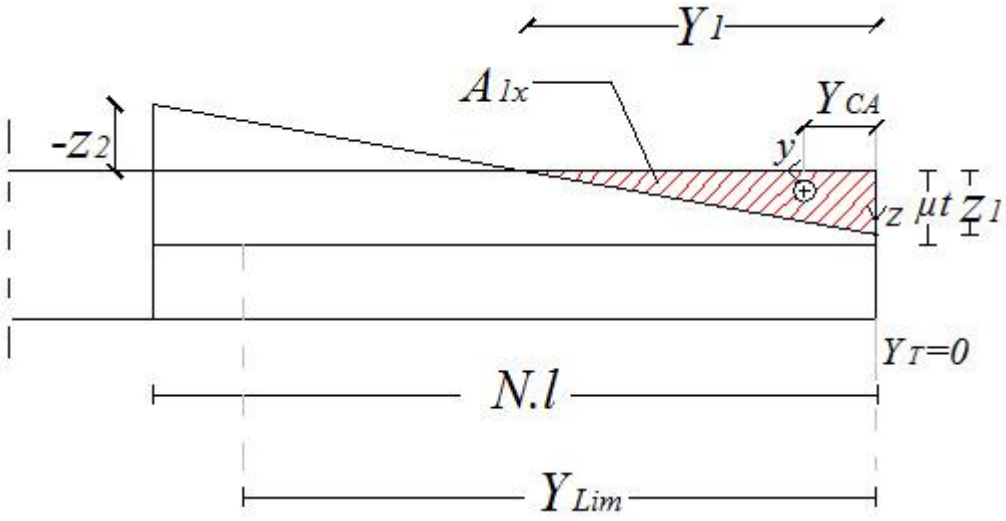

Figure 62: Case (b1) – triangular compression block above the reinforcement

Similar to Case (a1), there are two probabilities as follows:

For reinforcement bars in the *x*-direction

$$\left(Y_{Lim,x} - Y_T\right) = N.l \quad \text{when} \quad Y_{Lim,x} > N.l \tag{132}$$

$$\left(Y_{Lim,x} - Y_T\right) = \frac{2}{\phi^2}\left(\Delta y + \frac{\Delta_{Limx}}{\frac{2N}{r}} - \phi.\mu.t\right) \quad \text{when} \quad Y_{Lim,x} < N.l \tag{133}$$

For reinforcement bars in the *y*-direction

$$\left(X_{Lim,y} - X_T\right) = \frac{r.l}{2} \quad \text{when} \quad X_{Lim,y} > \frac{r.l}{2} \tag{134}$$

$$\left(X_{Lim,y} - X_T\right) = \frac{r}{N.\phi^2}\left(\Delta y + \Delta_{Limy} - \phi.\mu.t\right) \quad \text{when} \quad X_{Lim,y} < \frac{r.l}{2} \tag{135}$$

6.3.3 Forces equilibrium

The compression and tension stresses within the slab can be represented by compression and tension forces which are used to calculate the internal work of the slab. The equilibrium of these forces should be worked out in order to calculate the internal work of the slab. The forces in elements 1 and 2 of the slab are shown in Figure 63.

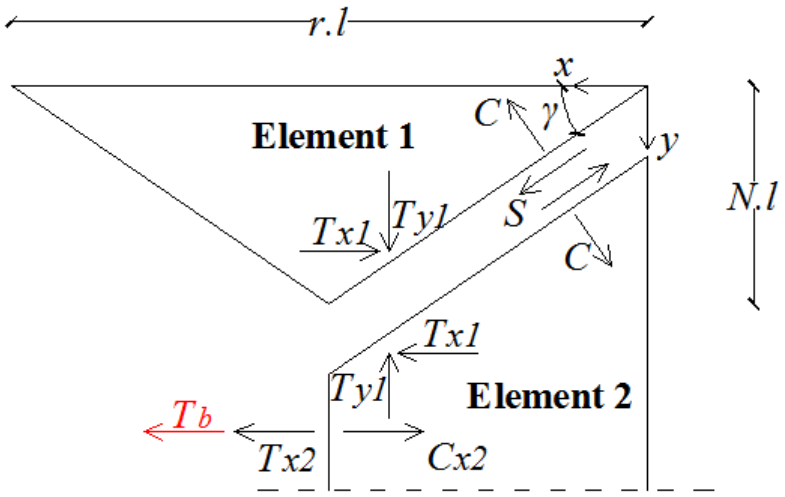

Figure 63: The forces of elements 1 and 2 of the slab

C is the concrete compression force in the diagonal yield-lines.

C_{x2} is the concrete compression force in the central yield-line.

T_{x1}, T_{x2} are the reinforcement tension forces in the *x*-direction across the diagonal and central yield-lines, respectively.

T_{y1} is the reinforcement tension force in the *y*-direction across the diagonal yield-lines.

T_b is the tension force of the steel beam.

S is the shear force between the slab elements.

γ is the angle between the diagonal yield-lines and the slab support (i.e. the *x* axis here).

Taking the equilibrium of the forces on the element 2 of the slab in the *x*-direction gives:

$$T_{x1} + T_{x2} + T_b - C_{x2} - C.sin(\gamma) - S.cos(\gamma) = 0 \quad (136)$$

By eliminating the shear force (i.e. taking the equilibrium of the slab forces perpendicularly to the direction of the shear force) gives:

$$T_{x1}.sin(\gamma) + T_{x2}.sin(\gamma) + T_b.sin(\gamma) - C_{x2}.sin(\gamma) - C + T_{y1}.cos(\gamma) = 0 \quad (137)$$

Rearranging Equation 137 gives:

$$T_{y1}.cos(\gamma) + (T_{x1} + T_{x2} + T_b).sin(\gamma) = C_{x2}.sin(\gamma) + C \quad (138)$$

Equation 138 is the general forces equilibrium equation which is used in Sections 6.3.5 to 6.3.11 to calculate the deformations of the slab including the horizontal movements Δx and Δy.

6.3.4 Forces on the slab

Each force in the slab has a certain value depending on the phase or case that the slab go through as it deflects. In this regard, what actually changes from a phase or case to another one is the distance of which reinforcement bars are intact (i.e. the number of intact reinforcement bars). The forces on the slab are given by:

$$T_{y1} = \left(X_{Lim,y} - X_T\right).f_{py} \quad (139)$$

$$T_{x1} = \left(Y_{Lim,x} - Y_T\right).f_{px} \quad (140)$$

$$T_{x2} = l.(0.5 - N).f_{px} \quad (141)$$

$$C = \frac{A_{1x}}{sin(\gamma)} f_c \tag{142}$$

$$C_{x2} = A_{2x}.f_c \tag{143}$$

f_{px} is the reinforcement yield stress in the *x*-direction.

f_{py} is the reinforcement yield stress in the *y*-direction.

6.3.5 Case (a1) equilibrium

Recalling the geometrics of case (a1), these geometrics are illustrated in Figure 64.

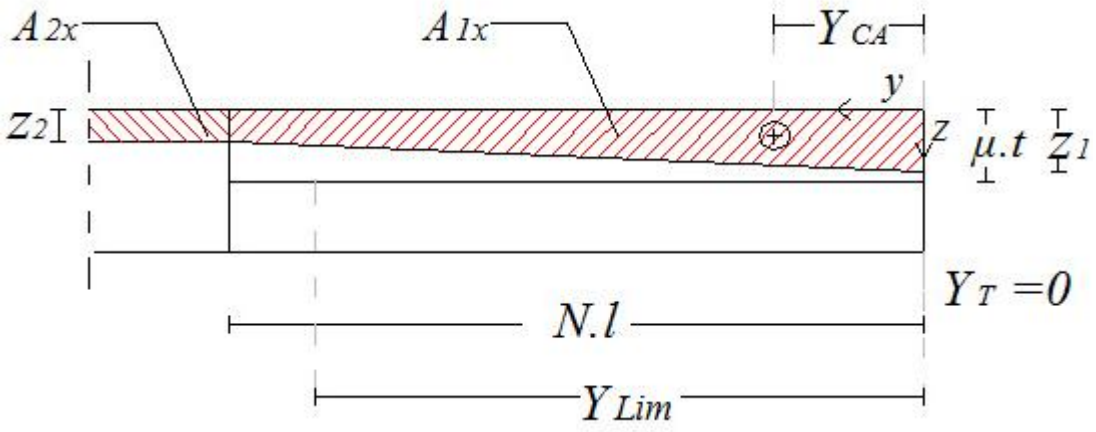

Figure 64: Geometrics of case (a1)

Case (a1) represents the case of which the compression stress block is above all reinforcement bars which are left in tension; therefore all reinforcement bars are intact. The distances that cover the intact reinforcement bars in the *x* and *y* directions, ($X_{Lim,y}$ - X_T) and ($Y_{Lim,x}$ - Y_T), respectively, are given by:

$$\left(X_{Lim,y} - X_T\right) = \frac{r.l}{2} \tag{144}$$

$$\left(Y_{Lim,x} - Y_T\right) = N.l \tag{145}$$

Substituting the forces from Equations 139 to 143, and the distance of the working forces from Equations 144 and 145 in Equation 138, gives:

$$f_{py}.\frac{r.l}{2}.cos(\gamma)+\left(f_{px}\frac{l}{2}+T_b\right).sin(\gamma)=A_{2x}.f_c.sin(\gamma)+\frac{A_{1x}}{sin(\gamma)}.f_c \quad (146)$$

Recalling the geometrics of this case from Section 6.3.2.1, and by substituting these geometries in Equation 146 gives:

$$f_{py}.\frac{r.l}{2}.cos(\gamma)+\left(f_{px}\frac{l}{2}+T_b\right).sin(\gamma) = \left(\frac{\Delta y}{\phi}-\frac{\phi.N.l}{2}\right).l.(1-2N).f_c.sin(\gamma)+\frac{N.l}{2.sin(\gamma)}\left(\frac{2\Delta y}{\phi}-\frac{\phi.N.l}{2}\right).f_c \quad (147)$$

f_c is the concrete characteristic strength.

Rearranging Equation 147 gives:

$$\frac{\Delta y}{\phi}.l.f_c.\left(sin(\gamma)-2N.sin(\gamma)+\frac{N}{sin(\gamma)}\right)+\phi.N.l.f_c\left(N.l.sin(\gamma)-\frac{l.sin(\gamma)}{2}-\frac{N.l}{4.sin(\gamma)}\right) = f_{py}.\frac{r.l}{2}.cos(\gamma)+\left(f_{px}\frac{l}{2}+T_b\right).sin(\gamma) \quad (148)$$

By dividing all terms in Equation 148 by *cos(γ)*, noting that *tg(γ)=2.N/r*:

$$\frac{\Delta y}{\phi}.l.f_c.\left(\frac{2N}{r}-\frac{4N^2}{r}+\frac{N}{sin(\gamma).cos(\gamma)}\right)+\phi.N.l.f_c\left(\frac{2N^2.l}{r}-\frac{N.l}{r}-\frac{N.l}{4.sin(\gamma).cos(\gamma)}\right) = f_{py}\frac{r.l}{2}+\frac{2N}{r}\left(f_{px}\frac{l}{2}+T_b\right) \quad (149)$$

Multiplying Equation 149 by *l* gives:

$$\frac{\Delta y}{\phi.l}.l^3.f_c.\left(\frac{2N}{r}-\frac{4N^2}{r}+\frac{N}{sin(\gamma).cos(\gamma)}\right)+\phi.N.l^3.f_c\left(\frac{2N^2}{r}-\frac{N}{r}-\frac{N}{4.sin(\gamma).cos(\gamma)}\right) = f_{py}\frac{rl^2}{2}+\frac{2N.l}{r}\left(f_{px}\frac{l}{2}+T_b\right) \quad (150)$$

Rearranging Equation 150 gives:

$$\frac{\Delta y}{l} = \frac{\phi . f_{py} \frac{r . l^2}{2} + \phi \frac{2N . l}{r} \left(f_{px} \frac{l}{2} + T_b \right) - \phi^2 . N . l^3 f_c \left(\frac{2N^2}{r} - \frac{N}{r} - \frac{N}{4 . sin(\gamma) . cos(\gamma)} \right)}{f_c . l^3 \left(\frac{2N}{r} - \frac{4N^2}{r} + \frac{N}{sin(\gamma) . cos(\gamma)} \right)} \quad (151)$$

Equation 151 represents the equilibrium for case (a1).

6.3.6 Case (b1) equilibrium

As the deflection increases, the compression stress block becomes triangular at the peripheral edge of the slab, and the central region becomes in pure tension. Case (b1) represents the case of which the all reinforcement bars in the *x* and *y* directions are still intact, with the existence of triangular compression stress block above these bars. The geometrics of case (b1) are shown in Figure 65.

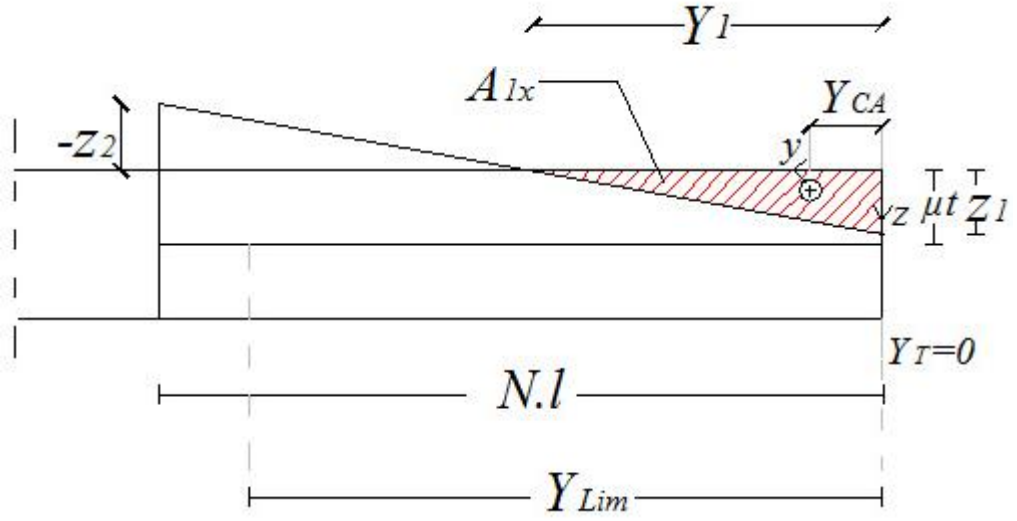

Figure 65: Geometrics of case (b1)

From the geometrics of case (b1), the distances of the intact reinforcement bars in the *x* and *y* directions, ($X_{Lim,y}$ - X_T) and ($Y_{Lim,x}$ - Y_T), respectively, are given by:

$$\left(X_{Lim,y} - X_T \right) = \frac{r . l}{2} \quad (152)$$

$$\left(Y_{Lim,x} - Y_T\right) = N.l \tag{153}$$

Since $z_2<0$, A_{2x} was not considered in this case.

Substituting the geometries of case (b1), and the distances of the intact reinforcement from Equations 152 and 153, in Equation 138 gives:

$$f_{py}.\frac{r.l}{2}.cos(\gamma) + \left(f_{px}\frac{l}{2} + T_b\right).sin(\gamma) = \frac{A_{1x}}{sin(\gamma)}.f_c \tag{154}$$

Rearranging Equation 154, following the same steps followed in case (a1), gives:

$$f_{py}.\frac{r.l^2}{2} + f_{px}.l^2\frac{N}{r} + T_b.l.\frac{2N}{r} = \frac{f_c.l^3}{\phi^3.sin(\gamma).cos(\gamma)}.\left(\frac{\Delta y}{l}\right)^2 \tag{155}$$

By making $\left(\frac{\Delta y}{l}\right)^2$ the subject:

$$\left(\frac{\Delta y}{l}\right)^2 = \frac{\phi^3.\left[f_{py}.\frac{r.l^2}{2} + f_{px}.l^2\frac{N}{r} + T_b.l.\frac{2N}{r}\right].sin(\gamma).cos(\gamma)}{f_c.l^3} \tag{156}$$

6.3.7 Case (b1') equilibrium

Case (b1') represents a scenario which descends from Phase (b), at which the reinforcement bars across the central yield-line in the *x*-direction fractured, while the reinforcement in the *y*-direction is still intact as shown in Figure 66. The fracture of the central yield-line reinforcement occurs abruptly. Hence, all the central yield-line reinforcement is either intact or fractured. This case is illustrated in Figure 66.

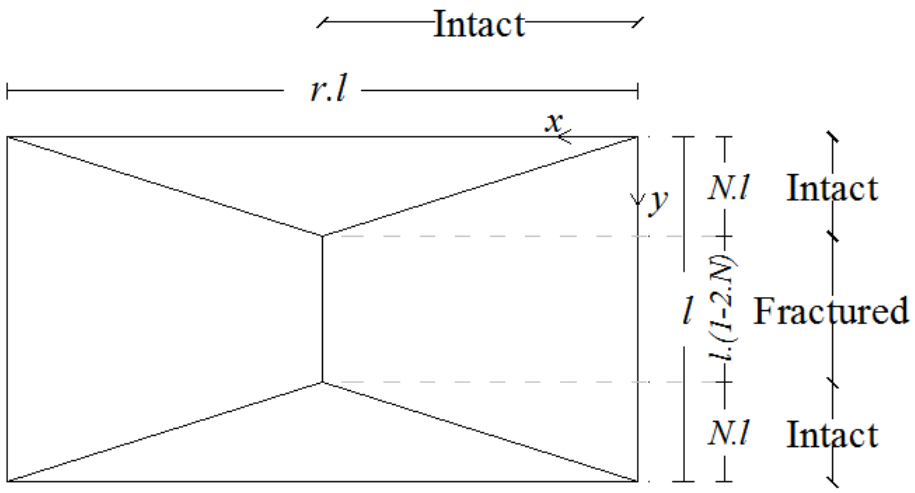

Figure 66: Distances of intact and fractured reinforcement bars in the *x* and *y* directions, representing Case (b1')

Taking the distances that cover intact reinforcement bars in the *x* and *y* directions from Equations 132 to 135, and substituting them in Equation 138 gives:

$$T_{y1}.\frac{r.l}{2}.cos(\gamma) + \left(f_{px}.N.l + T_b\right).sin(\gamma) = \frac{A_{1x}}{sin(\gamma)}.f_c \tag{157}$$

Executing similar rearranging steps as cases (a1) and (b1) cases to Equation 157 gives:

$$f_{py}\frac{r.l^2}{2} + f_{px}\frac{2.N^2.l^2}{r} + T_b.l\frac{2N}{r} = \left(\frac{\Delta y}{l}\right)^2 \frac{f_c.l^3}{\phi^3.sin(\gamma).cos(\gamma)} \tag{158}$$

By making $\left(\frac{\Delta y}{l}\right)^2$ the subject:

$$\left(\frac{\Delta y}{l}\right)^2 = \frac{\phi^3\left[f_{py}\frac{r.l^2}{2} + f_{px}\frac{2.N^2.l^2}{r} + T_b.\frac{2.N.l}{r}\right].sin(\gamma).cos(\gamma)}{f_c.l^3} \tag{159}$$

6.3.8 Case (b1*) equilibrium

In this scenario, the reinforcement bars of the diagonal yield-lines unzip in the *y*-direction (i.e. the reinforcement partly fractured) while the bars in the *x*-direction remain

intact. Therefore, by taking $Y_{Lim,x}=l/2$ (i.e. all bars are intact) and by taking the distance $X_{Lim,y}$ from Equation 135, the forces of the reinforcement for this case are given by:

$$T_{y1} = f_{py}.X_{Lim,y} = \frac{r}{N.\emptyset^2}\left(\Delta_y + \Delta_{Lim,y} - \emptyset.\mu.t\right) \tag{160}$$

$$T_{x1} + T_{x2} = f_{px}\frac{l}{2} \tag{161}$$

Substituting the forces from Equations 160 and 161 in Equation 138 gives:

$$f_{py}\frac{r}{N.\phi^2}\left(\Delta_y + \Delta_{Lim,y} - \phi.\mu.t\right).\cos(\gamma) + f_{px}\frac{l}{2}\sin(\gamma) + T_b.\sin(\gamma) = \frac{A_{1x}}{\sin(\gamma)}.f_c \tag{162}$$

Rearranging Equation 162 to make $\left(\frac{\Delta y}{l}\right)^2$ the subject gives:

$$\left(\frac{\Delta_y}{l}\right)^2.\frac{f_c.l^3}{\phi^3.\sin(\gamma).\cos(\gamma)} - \left(\frac{\Delta_y}{l}\right)\frac{f_{py}r.l^2}{N.\phi^2} - \left[\frac{f_{py}.r.l^2}{N.\phi^2}.\frac{\Delta_{Lim,y}}{l} - \frac{f_{py}.r.l^2}{N.\phi}.\mu.\frac{t}{l} + \frac{N.l^2}{r}.f_{px} + \frac{2.N}{r}.T_b\right] = 0 \tag{163}$$

6.3.9 Case (b1'*) equilibrium

In this case, the reinforcement bars in the *y*-direction across the diagonal yield-lines are partly fractured; and the reinforcement along the central yield-line in the *x*-direction fractured too.

Thus, $T_{x2}=0$; $T_{y1}=f_{py}.X_{Lim,y}$; $T_{x1}=f_{px}.N.l$

Therefore, Equation 138 becomes:

$$T_{y1}.cos(\gamma) + (T_{x1} + T_b).sin(\gamma) = C \tag{164}$$

Substituting the forces of this case in Equation 164 gives:

$$f_{py}.\frac{r}{N.\phi^2}.\left(\Delta y+\Delta_{Lim,y}-\phi.\mu.t\right).cos(\gamma)+\left(f_{px}.N.l+T_b\right).sin(\gamma)=\frac{A_{1x}}{sin(\gamma)}.f_c \quad (165)$$

Executing similar procedures conducted on case (b1*) gives the equilibrium equation of case (b1'*) as follows:

$$\left(\frac{\Delta y}{l}\right)^2.\frac{f_c.l^3}{\phi^3.sin(\gamma).cos(\gamma)}-\left(\frac{\Delta y}{l}\right).\frac{f_{py}.r.l^2}{N.\phi^2}-\frac{f_{py}.r.l^2}{N.\phi}.\left(\frac{\Delta_{Limy}}{l.\phi}-\frac{\mu.t}{l}\right)-\frac{2.N^2.l^2.f_{px}}{r}-\frac{2.N.l.T_b}{r}=0 \quad (166)$$

6.3.10 Case (b1**) equilibrium

This case represents the scenario when the reinforcement in the *y*-direction is fractured, while in the *x*-direction the reinforcement is intact.

Therefore, $T_{x2}=0$; $T_{y1}=f_{py}.r.l/2$; $T_{x1}=f_{px}.Y_{Lim,x}$

$$Y_{Lim,x}=\frac{2}{\phi^2}\left(\Delta y+\frac{\Delta_{Limx}}{\frac{2N}{r}}-\phi.\mu.t\right) \quad (167)$$

Substituting these forces and $Y_{Lim,x}$ in Equation 138 gives:

$$f_{py}.\frac{r.l}{2}.\cos(\gamma)+f_{px}\frac{2}{\phi^2}\left(\Delta y+\frac{\Delta_{Lim,x}}{\frac{2.N}{r}}-\phi.\mu.t\right).\sin(\gamma)+T_b.\sin(\gamma)=\frac{A_{1x}}{\sin(\gamma)}.f_c \quad (168)$$

Rearranging Equation 168, and making $\left(\frac{\Delta y}{l}\right)^2$ the subject gives:

$$\left(\frac{\Delta y}{l}\right)^2 . \frac{f_c . l^3}{\phi^3 . \sin(\gamma) . \cos(\gamma)} - \left(\frac{\Delta y}{l}\right) \frac{4N . l^2 f_{px}}{r . \phi^2} - \left[\frac{f_{py} . r . l^2}{2} + \frac{2 . l^2 . f_{px}}{\phi^2} . \frac{\Delta_{Lim,x}}{l} - \frac{4 . f_{px} . N . l^2}{r . \phi} . \mu . \frac{t}{l} + \frac{2N . l}{r} . T_b\right] = 0 \quad (169)$$

6.3.11 Case (b1***) equilibrium

This case represents the scenario at which the reinforcement along the central yield-line in the *x*-direction already fractured; and reinforcement along the diagonal yield-lines in the *x* and *y* directions partly fractured (i.e. unzipping). Therefore, the extent of the intact reinforcement in the *x* and *y* directions are $X_{Lim,y}$ and $Y_{Lim,x}$ respectively.

Hence, the forces of the reinforcement are given by:

$$T_{y1} = f_{py} . \frac{r}{N . \phi^2} (\Delta y + \Delta_{Lim,y} - \phi . \mu . t) \quad (170)$$

$$T_{x1} = f_{px} \frac{2}{\phi^2} \left(\Delta y + \frac{\Delta_{Lim,x}}{\frac{2 . N}{r}} - \phi . \mu . t \right) \quad (171)$$

Substituting Equations 170 and 171 in Equation 138 gives:

$$f_{py} \frac{r}{N . \phi^2} (\Delta y + \Delta_{Lim,y} - \phi . \mu . t) \cos(\gamma) + f_{px} \frac{2}{\phi^2} \left(\Delta y + \Delta_{Lim,x} \frac{r}{2 . N} - \phi . \mu . t\right) \sin(\gamma) + T_b . \sin(\gamma) = \frac{A_{1x}}{\sin(\gamma)} . f_c \quad (172)$$

Rearranging Equation 172 and making $\left(\frac{\Delta y}{l}\right)^2$ the subject gives:

$$\left(\frac{\Delta y}{l}\right)^2 . \frac{f_c . l^3}{\phi^3 . \sin(\gamma) . \cos(\gamma)} - \left(\frac{\Delta y}{l}\right) \left(\frac{f_{py} . r . l^2}{N . \phi^2} + \frac{4 . N . l . f_{px}}{r . \phi^2}\right) - \left[\frac{f_{py} . r . l^2}{N . \phi} . \left(\frac{\Delta_{Lim,y}}{l . \phi} - \frac{\mu . t}{l}\right) + \frac{4 . N . l^2 . f_{px}}{r . \phi} \left(\frac{\Delta_{Lim,x}}{l . \phi} . \frac{r}{2 . N} - \frac{\mu . t}{l}\right) + \frac{2 . N . l}{r} . T_b\right] = 0 \quad (173)$$

6.3.12 The development of the slab deformations against deflection

The phases and cases which are presented in Sections 6.3.5 to 6.3.11 give the deformations of the slab as it deflects. These deformations are the key components to monitor cracks formation and reinforcement fracture at large deflections. The equations of these deformations (i.e. Equations 151 to 173) were coded and processed in Matlab in order to conduct an iteration. In this iteration, a temperature increase was applied in order to determine the critical temperature of the slab for each deflection level (i.e. the temperature enhancement). The details and methodology of this iteration are presented in Appendix 2.

6.3.13 Crack widths

The internal work of the working forces depends on the extension of the reinforcement bars and the beam, as discussed in Sections 4.4.1.1 and 4.4.1.2. This extension is governed by the corresponding crack widths. Therefore, these crack widths should be calculated. Two distinctive crack types are apparent in mechanism-b: diagonal cracks α, and the central crack β as shown in Figure 67. The central crack β has a constant width along its length. Each diagonal crack α, however, is at its maximum width at the yield-lines intersection point, and gets narrower reaching zero-width at the corner of the slab. Therefore, when the width of α crack was used in the internal work calculations, the width was taken at the middle distance of the intact reinforcement bars row.

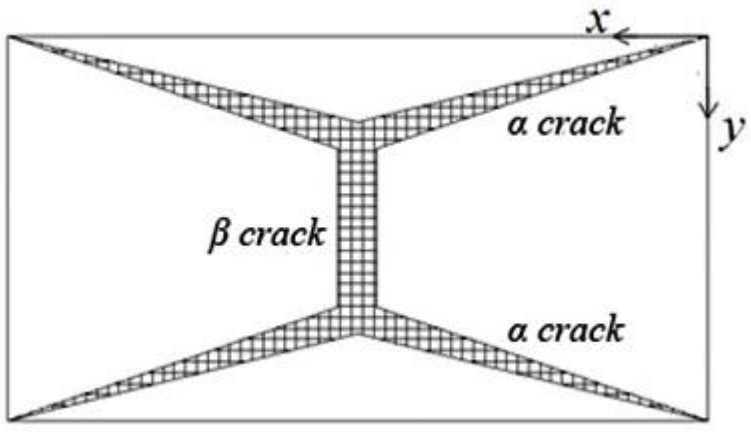

Figure 67: Crack types on the slab

7 Application of the Method

7.1 Example of composite slab in fire

The mechanism which was derived and presented in Chapter 6 was coded in Matlab in order to examine the behaviour of composite slabs at elevated temperatures, and to calculate the enhancement of the slab's load capacity at large deflections.

The slab which is used in the example is a rectangular slab (9m x 6m) with an aspect ratio $r=1.5$. The thickness of the slab $t=130mm$. The slab is reinforced by isotropic A142 mesh. The mesh consists of two layers which are welded, forming bars spacing of 200mm. Both mesh layers lie at the slab's mid-depth (i.e. $\mu.t=65mm$). Reinforcement yield stress $f_{px}= f_{py} =500N/mm^2$. Reinforcement ductility = 5%. Concrete characteristic strength $f_c=35N/mm^2$.

The secondary-unprotected downstand steel beam is UKB 406x140x39. As is mentioned in Section 4.1, one secondary beam is used. The secondary beam is aligned in the direction of the larger span of the slab. The yield stress of the beam $f_y=355N/mm^2$. The slab is loaded by uniformly distributed transverse loading with an intensity of $4kN/m^2$.

The slab-beam cross section is shown in Figure 68.

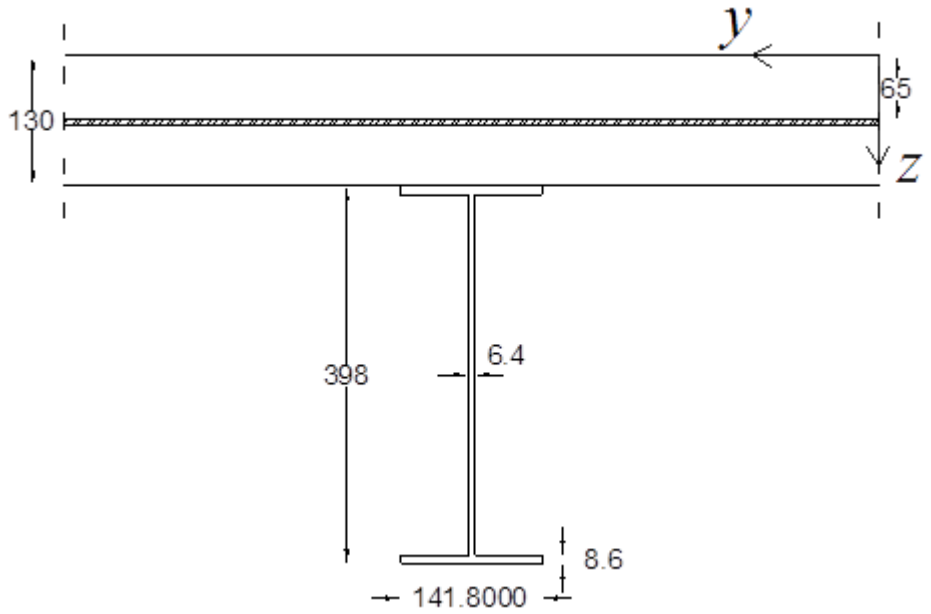

Figure 68: Slab-beam cross section; beam Section (UKB 406x140x39)

7.1.2 Small-deflection analysis results

The first phase of the analysis (i.e. the small-deflection yield-line analysis) was coded in Visual Basic on Microsoft Excel. The composite slab information, including the geometric information of the slab, the load capacity of the unprotected beam, the reinforcement and the applied transverse loading intensity, and the other characteristics of the slab as mentioned in Section 7.1, was entered to the computer program that was designed for the small-deflection analysis. Then, the program took this information from the excel sheet cells, and the small-deflection analysis was conducted. The detailed process and methodology of this program are presented in Appendix 2.

The results of the small-deflection analysis were as follows:

The optimized yield-line intersection dimension (i.e. the yield-line parameter) *N=0.4181679*.

The critical temperature of the optimum yield-line capacity T_{cr}= 762ºC.

The yield-line parameter *N* which resulted from the small-deflection analysis was used as a constant in the large-deflection analysis since the optimum yield-line pattern

formed and fixed. The resultant critical temperature T_{cr} was not used in the large-deflection analysis since the latter could start over from ambient temperature with no change in the final results. The additional computational time due to starting over from 400ºC was trivial in the large-deflection analysis.

The plan of the slab with the yield line pattern which resulted from the initial small-deflection analysis is shown in Figure 69.

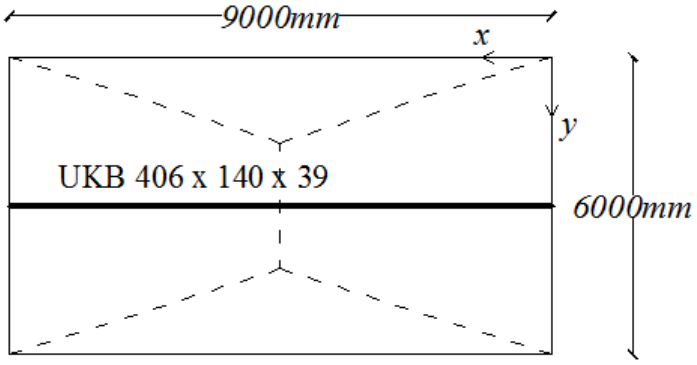

Figure 69: The optimum yield-line pattern of the initial small-deflection analysis

7.1.3 Large-deflection analysis results

The complete analysis results which were extracted from the Matlab program cannot be presented here. The Matlab results table is too large to be presented in the thesis. However, the results table is not important since these results are interpreted as figures and discussed thoroughly, as presented in this chapter. The enhancement factor and the crack widths that resulted from the large-deflection analysis are presented in Figures 70 (a) and (b), respectively.

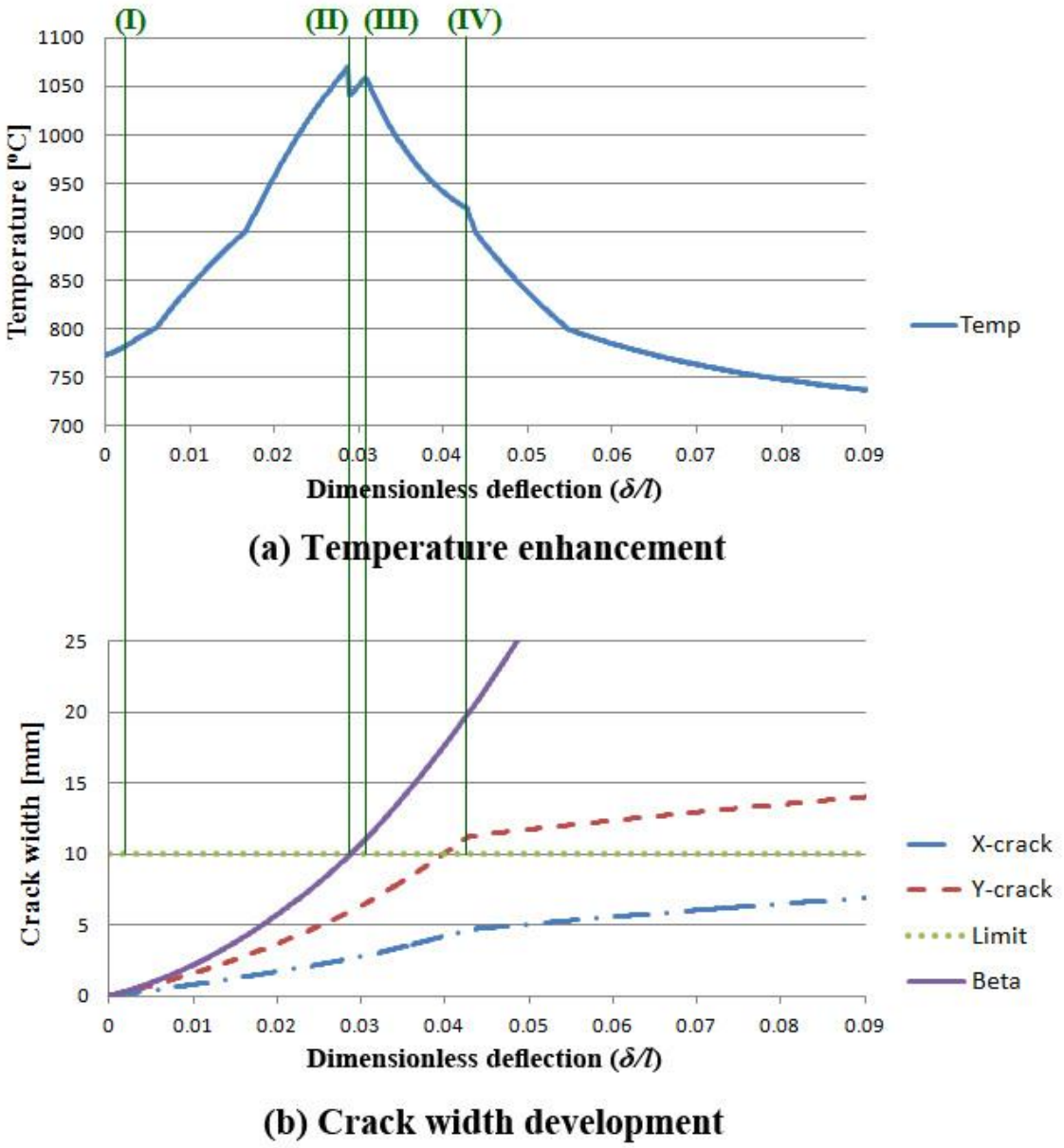

Figure 70: (a) Temperature against dimensionless deflection; (b) crack width development against deflection. Vertical lines represent transmission between two successive cases

Figure 70(a) represents the temperature enhancement against the dimensionless deflection of the slab (i.e. δ/l. Figure 70(a)) demonstrates the changing critical temperature as the deflection increases. The temperature peaks shown in Figure 70(a) mark reinforcement fracture in distinguishable phases. Each reinforcement fracture at each enhancement peak marks a case transition through the analysis. The last case transition (i.e. case b1***) is marked by the vertical line (IV) as shown in Figures 70(a) and (b).

Figure 70(b) demonstrates the development of the various crack widths against the dimensionless deflection of the slab. The horizontal dotted line represents the limit-crack width at which the corresponding reinforcement fractures.

The vertical lines (I) to (IV) that go through Figures 70(a) and (b), mark the end of a case and the start of a following one as deflection increases. The vertical line (I) marks the end of case (a1), at which all the reinforcement bars are intact, with the presence of a thin compression stress block over the whole slab, and the start of case (b1), at which the compression stress block converts to triangular along the peripheral ring of the slab and disappears from the central region, as discussed in Section 6.3.2.2. The vertical line (II) marks the abrupt fracture of the central yield line reinforcement in the *x*-direction, met by a temperature peak in Figure 70(a), which takes the analysis from case (b1) to case (b1'). The vertical line (III) marks the transition to case (b1'*), which is met by the second peak of the temperature enhancement in Figure 70(a), at which the reinforcement in the *y*-direction unzip along the diagonal yield-lines as the slab deflects. The vertical line (IV) marks the start of case (b1***), at which the reinforcement in the *x* and *y* directions fracture, unzipping the mesh together, degrading the slab's load capacity until no further enhancement is possible and the slab structurally fails.

The development of the forces on the slab facets against the deflection are shown in Figure 71. It is intuitive that the forces are affected by the temperature changes due to the tension force in the beam T_b which is affected by the temperature increase and the slab deflection. This is demonstrated by the distinguishable two peaks in the beam force T_b, shown in Figure 71, which mirror the two temperature peaks in Figure 70(a).

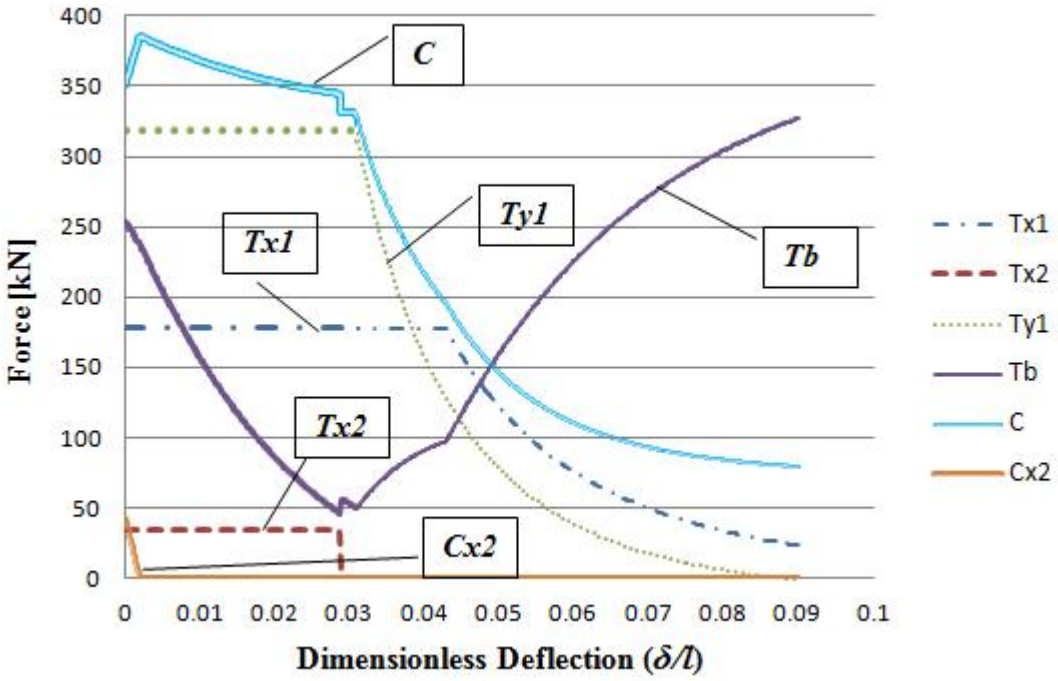

Figure 71: Internal forces on the slab facets

If it occurs that the actual maximum temperature exceeds the highest temperature enhancement at any point, then the slab fails and the printed forces in Figure 71 after the collapse point are merely theoretical. This potential theoretical part of the forces is printed in thin lines to account for this probability. On the other hand, if the actual temperature does not reach the theoretical temperature peaks, the rest of the solution scenario presented here is also theoretical and the slab survives. This also applies to the temperature enhancement and crack widths.

7.2 Comparisons against other methods

Straightforward comparisons with the original alternative simplified method and the Bailey-BRE method are not possible since the results of this study were presented as temperature enhancement rather than load capacity enhancement as in the other methods. Although enhancement in this study was related to the load capacity enhancement, since the temperature enhancement was derived from the load enhancement, the final results were interpreted differently (temperature instead of load capacity enhancement). However, behaviour-wise comparison against the alternative

simplified method and maximum temperature comparison against the Bailey-BRE method were conducted. These comparisons are presented in Sections 7.2.1 and 7.2.2.

7.2.1 Comparison against the alternative simplified method

The re-examination of the mechanics of tensile membrane action was conducted by Burgess et al. (2014) in order to re-examine the behaviour of flat concrete slabs at ambient temperature. Therefore, intuitively its results cannot be directly compared to the results of this study which addressed composite slabs at high temperatures. As is mentioned in Section 6.1, the presence of the unprotected steel beam changed the mechanism and the process of the analysis. In addition, the re-examination gives the enhancement with respect to the load capacity, while this study gives the temperature enhancement. However, the behaviour trend in both situations of a slab with and without a composite beam, at ambient or elevated temperatures, should be similar behaviour-wise. The mechanics behind both studies is the same. Therefore, a slab which mobilizes tensile membrane action at large deflections witnesses similar towards-failure phases, as is discussed in Sections 6.3.5 to 6.3.11. Hence, in spite of the different structures of flat and composite slabs, at ambient or elevated temperatures, the main behaviour trends of both the original alternative method and the extended one in this study should be alike.

The re-examination of TMA was modelled in a spreadsheet which was programmed in the University of Sheffield by Burgess et al. (2014). In this spreadsheet of the re-examination, a flat slab was considered, with no downstand beam. The analysis was conducted at ambient temperature. The parameters of the same slab which is used in the example of this study in Section 7.1 were entered to the spreadsheet. It should be noted that the optimum yield line pattern in the spreadsheet of the re-examination of TMA of flat slabs is aligned to the *x*-direction, while in the example of this study the optimum yield-line is rotated by 90^{o} (i.e. aligned in the *y*-direction) due to the presence of the downstand beam. However, the comparison was conducted only to compare the behaviour of both situations. Furthermore, in the re-examination of TMA example, which was analyzed in a spreadsheet, the enhancement was given by the ratio of the excessive load that the slab could carry when TMA was mobilized for every deflection increment of the slab, to the optimum yield-line load.

Figure 72(a) shows the results of the flat slab analysis at ambient temperature. Figure 72(b) shows the results of the slab which is presented in the original example of this study in Section 7.1, with the same dimensions and the same reinforcement and concrete configurations.

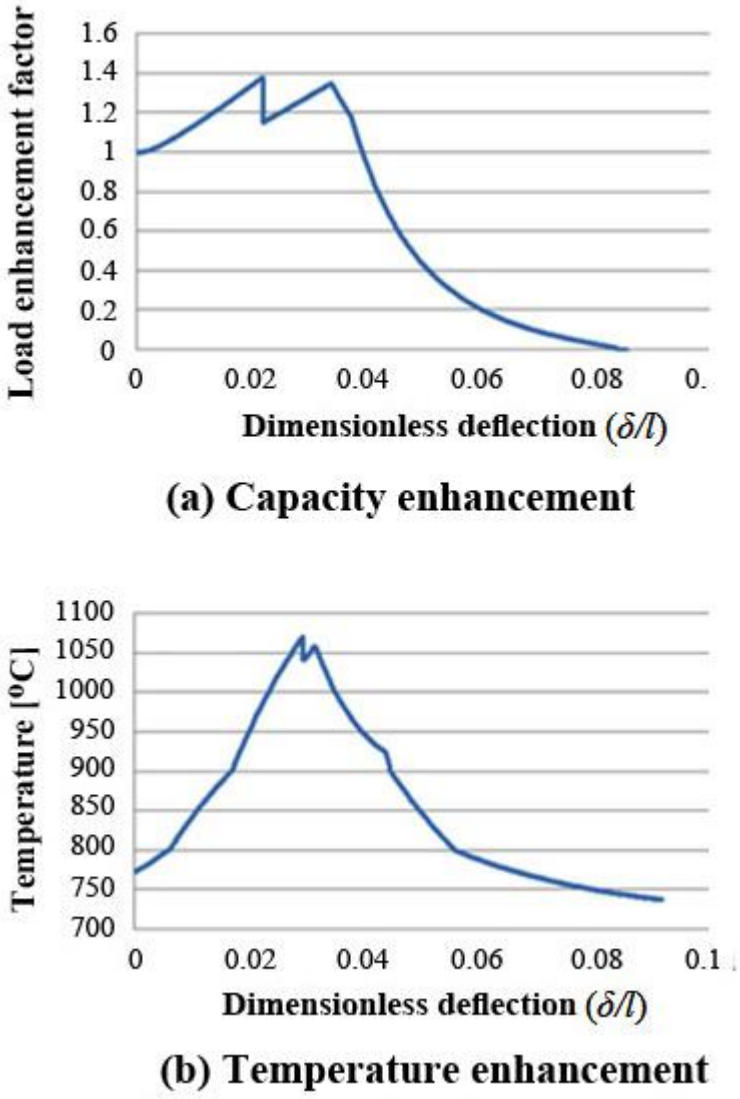

Figure 72: Comparison between the re-examination of TMA and this study, (a) no temperature and no beams; (b) with an unprotected beam in fire

Figure 72(a) presents the enhancement with respect to the load-capacity, which starts from the value 1 (i.e. the optimum yield-line capacity). Figure 72(b) presents the enhancement of the slab with respect to temperature.

The behaviour of the flat and composite slabs in Figures 72(a) and (b) is similar. Figure 72(a) shows two distinctive peaks in the enhancement factor. The first peak represents the central yield-line reinforcement fracture in the *y*-direction, perpendicular to the yield-line. The second peak represents the fracture of the diagonal yield-line reinforcement bars in the *x*-direction, unzipping the mesh. Just after the second peak, a change in the inclination of the enhancement (at the value 1.2 in Figure 72(a)) represents the fracture of the reinforcement bars in the *x* and *y*-directions, unzipping the mesh until the slab fails.

Figure 72(b) shows the same behaviour, also with two distinguishable enhancement peaks, taking into consideration the rotated yield-line pattern. The first peak in Figure 72(b) represents the abrupt fracture of the central yield-line reinforcement bars in the *x*-direction perpendicular to the yield-line. The second peak represents the fracture of reinforcement bars across the diagonal yield-lines in the *y*-direction. After the second peak, a change in the inclination of the temperature enhancement is apparent (similar to the small peak which was marked by the vertical line (IV) as shown in Figure 70(a)). This peak represents the reinforcement fracture in the *x* and *y*-direction, unzipping the mesh across the diagonal yield-lines until the slab fails. Because of the rotated yield-line pattern in the example of this study, the direction of the fracturing reinforcement bars is rotated by 90^{o} compared to the alternative simplified method, however, with the same behaviour.

As a direct comparison, the first peak in the example of this study which is shown in Figure 72(b) represents the fracture of the reinforcement in the *x*-direction across the central yield-line. In the example of the flat slab at ambient temperature shown in Figure 72(a) the first peak represents the fracture of the reinforcement in the *y*-direction across the central yield-line. The second enhancement peak shown in Figure 72(b) represents the fracture of reinforcement in the *y*-direction along the diagonal yield-lines; while the second peak in Figure 72(a) represents the fracture of the diagonal yield-lines reinforcement in the *x*-direction. Technically, the behaviour of the slab in both methods is identical but the yield-lines, therefore the cracks, are rotated as illustrated in Figure 73.

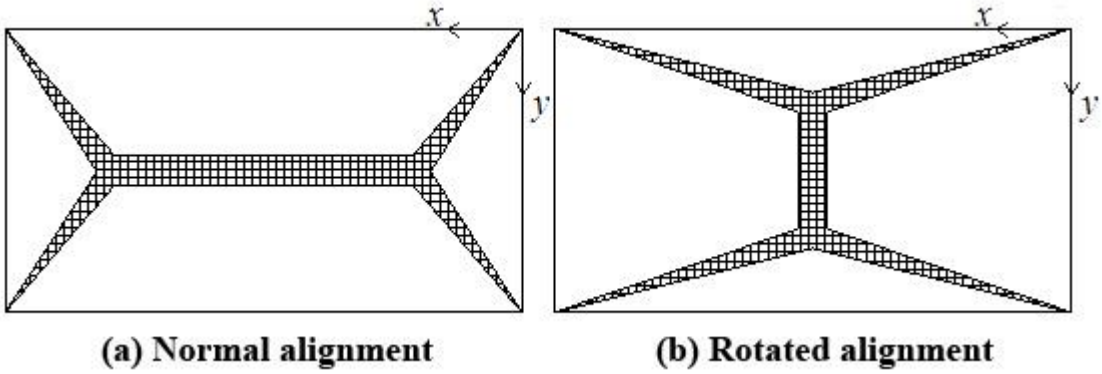

Figure 73 (a) Normal yield-line alignment; (b) Rotated yield-line alignment

7.2.2 Comparison against the Bailey-BRE method

A direct comparison against the Bailey-BRE method is not possible because this study gives the temperature enhancement of a composite slab at elevated temperatures, not the load enhancement. This is different from the Bailey-BRE method which gives the slab's load capacity enhancement. However, comparing the maximum allowed temperatures from both methods for the same slab configurations is possible. This comparison does not fully show the complete behaviour of the slab in both methods, but it shows the maximum allowed critical temperatures for both of them.

When the comparison between this study and the Bailey-BRE method was conducted, a difference between the maximum deflections corresponding to the maximum temperatures in the two methods was found. The main reason behind this was the reinforcement ductility, which can be changed in the method of this study, but cannot be changed in the Bailey-BRE method. Nonetheless, this issue was addressed by changing the ductility in the example of this study from 5 to 6 percent. This was found to make the maximum critical temperatures given by both methods occur at the same slab deflection level. Therefore, a direct temperature comparison is possible. The comparison against the Bailey-BRE method is shown in Figure 74. Note that the caption “new method” refers to this study, which is the extension of the alternative simplified method.

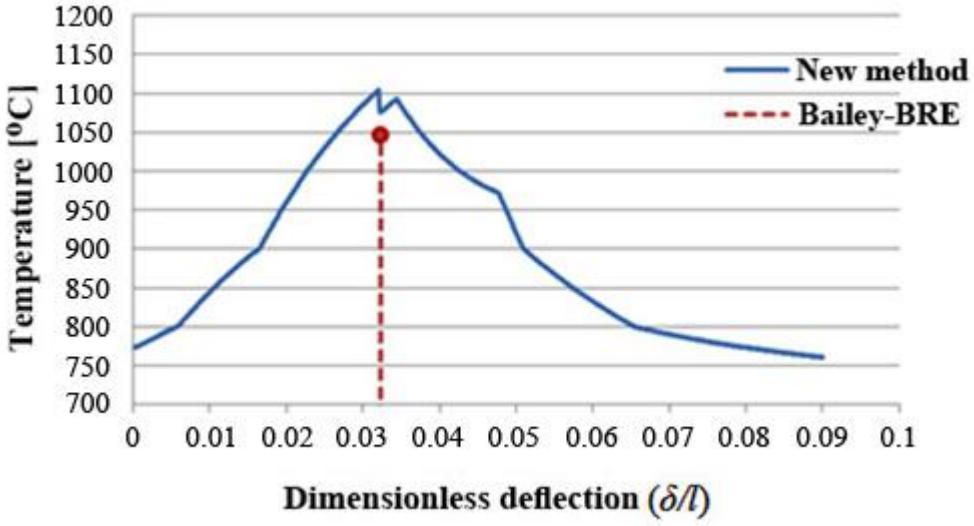

Figure 74: Comparison between the new method (this study) against the Bailey-BRE method.

Figure 74 shows the temperature enhancement, which resulted from the analysis of this study, in a continuous blue line. Although the reinforcement ductility was slightly changed, the new enhancement is almost similar to the enhancement which resulted from the example of this study in Section 7.1.3. The vertical dotted line presents the amplitude of the maximum allowed temperature by the Bailey-BRE method. The maximum temperature is marked by the circle on top of the dotted line. The Bailey-BRE analysis of this slab configuration was conducted in a spreadsheet used in the University of Sheffield.

This comparison shows that the Bailey-BRE method gives lower allowed temperature than the allowed temperature which was given by this study. While the maximum allowed temperature by this study is 1104.5ºC, the maximum allowed temperature by the Bailey-BRE method for the same configurations is 1048ºC, with a difference of 56ºC. The Bailey-BRE is slightly conservative here. This result is consistent with the results of the comparison between the alternative simplified method and the Bailey-BRE method for flat slabs, as is shown by Burgess et al. (2014).

8 Discussion and Conclusions

8.1 Discussion

This study is an extension of the alternative simplified method which handled flat concrete slabs and conducted by Burgess et al. (2013) and Burgess et al. (2014). The study was set out to investigate the effects of an unprotected steel beam on the enhancement of composite slabs in fire. The main question of this research was to examine the importance of the slab large deflection in mobilizing tensile membrane action and its effect on the enhancement factor beyond the conventional yield-line mechanism; and how does the presence of an unprotected steel beam affect the whole failure mechanism.

In order to achieve this main goal of this research, the mechanics of the original alternative simplified method had to be extended to include the influence of the unprotected steel beam on the tensile membrane action mechanism. The extended mechanics behind this study was divided into two parts: small-deflection and large deflection analyses.

In this chapter, general discussion and important points related to this research are presented. These important points include: study limitations, factors influencing the new method and recommendations for further researches.

8.1.1 Small-deflection analysis

Originally, the slab resists the transverse loading in bending. Conventional load-carrying capacity methods are used up to the point of the formation of the optimum yield-line pattern. Based on the yield-line theory and work method, this small-deflection mechanism determines the slab status at the moment of the yield-line pattern formation. The extension which is presented in this study accounts for the mechanism change which occurs by adding an unprotected secondary steel beam to the slab. This steel

beam, which is attached to the slab by shear studs, changes the yield-line pattern from the *x*-alignment to *y*-alignment, rotating the pattern by 90^o. The formation of the optimum yield-line pattern is mainly dependent on the strength capacity of the beam which is affected by elevated temperatures. The yield-line pattern forms when the beam significantly loses its capacity. The corresponding temperature is marked as the critical temperature for the small-deflection analysis. What was used from the output of the small-deflection analysis was the yield-line parameter *N*. This parameter was the main purpose of conducting the small-deflection analysis, although the core part of the study is the large-deflection analysis which is further discussed in Section 8.1.2.

8.1.2 Large-deflection analysis

The large-deflection analysis makes up the main body of this research. Following the advantages of the re-examination of the mechanics of tensile membrane action which was presented by Burgess et al. (2014), this extension inherited the same advantages from the original method. In addition to the inherited advantages, this extension accounts for the effects of elevated temperatures in the presence of the unprotected secondary steel beam. One of the advantages of this study is that it allows the cracks formation over the slab to be monitored. Furthermore, reinforcement fracture is also monitored across the corresponding cracks on the slab. This reinforcement fracture governs the enhancement through the deflection until failure. The changing stress patterns along the yield-lines are also monitored.

Through the large-deflection analysis, using the compression stress block method, the load-carrying capacity of the slab with the effect of tensile membrane was calculated at every deflection increment. The ratio of the slab's load capacity, with the effect of TMA, to the optimum yield-line capacity gives the temperature enhancement at each level of deflection. This temperature enhancement represents the excessive temperature which is allowed beyond the critical temperature given by conventional methods. Technically, it is the temperature which is required to degrade the enhanced load capacity, due to TMA, to the level of the yield-line load capacity.

As is presented in Section 7.2.1, the identical behaviour of the slab according to this study and the results presented by the original re-examination by Burgess et al. (2014), gives this study good credibility. The sequence of the different phases and cases which

the slab went through in the Matlab model, monitoring the reinforcement fracture as the deflection increased until failure, was exactly as theoretically expected according to the original alternative simplified method. These phases and cases were fully coded, but the sequence itself was only monitored and not dictated by any means.

Comparisons against the Bailey-BRE method showed that the latter is conservative, as is discussed by Burgess et al. (2014). This comparison was merely a comparison between the maximum allowed temperatures from both methods.

8.1.3 The new aspects of this study compared to Burgess et al. (2014)

This study presents an extension of the alternative simplified method proposed by Burgess et al. (2014). The same kinematics and in-plane stress distribution were considered in both models. The main differences between the models are listed as follows:

1. The proposed model of this study addressed composite slabs instead of plain flat concrete slabs as it was in the original method by Burgess et al. (2014). The extended model took into consideration the beam-slab composite action at large deflections and its effect on the tensile membrane action mechanism.
2. Due to the composite action of a single downstand beam, as assumed in this study, the rotated yield-line pattern which resulted from the strength of the beam was addressed as it led to a rotated mode of failure.
3. The proposed model of this study addressed the effect of elevated temperatures instead of ambient temperature analysis as it was in the original method proposed by Burgess et al. (2014). The effect of elevated temperature was applied to a single secondary steel beam across the larger span of the slab.

8.1.4 The key benefits of this study over the Bailey-BRE method

The extension of the alternative method, which is proposed by this study, has certain benefits over the Bailey-BRE method. Although the proposed model of this study has its own limitations, as is presented in Section 8.2, the model addressed the following limitations of the Bailey-BRE method:

1. This study takes different slab kinematic assumptions and accounts for the horizontal movements and rotations of the slab elements at large deflections; while the Bailey-BRE method inherits the same equilibrium and in-plane stress distribution from Hayes' model which leads to either conservative or optimistic results. Although Bailey & Toh (2007) corrected the in-plane stress distribution, the results of the Bailey-BRE method were not tangibly improved.
2. The proposed method in this study allows monitoring the behaviour of the slab at large deflections. This includes reinforcement fracture in tension and concrete crushing under compression. This allows the prediction of the real time history behaviour of the slab as it deflects, starting from the yield-line pattern formation until failure.
3. Since the proposed model of this study predicts the reinforcement fracture, the unrealistically safe deflection limit, as proposed by the Bailey-BRE method, is not necessary. It is up to the designer to decide on the fracture ductility of the reinforcement which leads to slab failure.
4. The proposed method accounts for the effect of the reinforcement ductility and its effect on the bars fracture across the cracks, while the Bailey-BRE method completely ignores the effects of reinforcement ductility.
5. The method implies that the compression force is confined at each corner of the slab, which complies with the true behaviour of slabs as they fail, rather than the suggested compression arch cracks at the corners as suggested by the Bailey-BRE method.

8.2 Study limitations

The alternative simplified method, presented by Burgess et al. (2014), was originally conducted to come up with a new method because of the shortcomings and limitations which are found in the Bailey-BRE method. Following the alternative simplified method, which focuses on thin-flat reinforced concrete slabs, this study aims to extend it to account for composite slabs at elevated temperatures. The results that were obtained from this research present the temperature enhancement of composite slabs beyond the conventional solutions. The results were found to be logic and give similar slab behaviour to that shown by the original simplified method. However, the main course of this alternative method does not end with this study. Limitations that are related to

original alternative simplified method, and limitations inherited from the mechanics of tensile membrane action methods still persist. Furthermore, the assumptions that are considered in this study were over-simplified in certain cases. The result of these over-simplified assumptions might slightly affect the future physical validation of the model proposed in this study. As is mentioned in Section 2.2.2, the yield-lines are assumed to be straight lines. In reality, the yield-lines, and therefore the corresponding cracks, do not form perfectly straight lines. However, the effect of this over-simplification is not significant. Moreover, as is mentioned in Section 2.2.2, the slab facets rotate as rigid bodies as the slab deflects. In practice, the deflected shape of the slab is unlikely to be a collection of perfectly flat facets. Therefore, the deflected shape of slabs in test observations is not a perfect deflection curve. Nevertheless, these over-simplified assumptions are justified since the method proposed in this study is a simplified method. However, the limitations of this study, as presented in Sections 8.2.1, 8.2.2 and 8.2.3, should be addressed in future studies in order to implement this extended method correctly and get accurate results. These limitations include: vertical support of the slab edges, isotropic reinforcement and thermal deflection.

8.2.1 Vertical support of the slab edges

This limitation, which the Bailey-BRE method is criticized for (Burgess et al. 2012), still persists in the alternative simplified method that was presented by Burgess et al. (2014) and in this study. As is mentioned in Section 3.5, ignoring the capacity degradation of the primary beams as the temperature increases might lead to the formation of plastic hinges in these beams, therefore less tensile membrane action to be mobilized. This means that the actual load enhancement factor is less than the calculated enhancement. Therefore, the results might be optimistic to some extent when the temperature exceeds the critical temperature of the primary beams. Thus, there is a probability that a folding mechanism occurs and the slab fails in catenary action rather than failing after the tensile membrane action is fully mobilized as the slab configurations allow. This depends on the fire protection of the primary beams and the actual temperature during the fire.

8.2.2 Isotropic reinforcement limitation

The reinforcement which is considered in this study is isotropic reinforcement; therefore, the neutral axis depth in the *x* and *y* directions is the same for every cross-section of the slab. However, the mechanics behind the small-deflection analysis which forms the initial part of this study is limited to isotropic reinforcement. Using orthotropic reinforcement in the small-deflection analysis leads to different neutral axis depths in the slab in the *x* and *y* directions for the same cross-section, which is intuitively irrational. Only the small-deflection analysis is limited to this, due to its equations which depend on the yield-line theory and the work method. The same problem is encountered with the Bailey-BRE method, though it has not properly addressed or corrected yet. Nonetheless, in spite of the existence of the unprotected steel beam, when using isotropic reinforcement as it is the case in this study, the effect of this limitation itself is extremely limited and leads to trivial differences in the final results (i.e. the temperature enhancement). This is completely justified since the only output parameter which was extracted from the small-deflection analysis in order to be used in the large-deflection analysis is the yield-line intersection point distance *N*. As mentioned in Section 7.1.2, the critical temperature T_{cr} which resulted from the small-deflection analysis was not used in the large-deflection analysis, as the latter started over from 400ºC. This is justified since the computational time is trivial in the large-deflection analysis. Similarly, the optimum yield-line load capacity *P* which results from the small-deflection analysis was not used in the large-deflection analysis. In the large-deflection analysis, the load capacity of the slab was calculated from scratch, using completely different equations based on the compression stress block method. This newly calculated slab's load capacity *P* was compared to the applied load on the slab P_a. Hence, the only output that was extracted from the small-deflection analysis in order to be used in the large-deflection analysis was the yield-line intersection point distance parameter *N*. In other words, the isotropic reinforcement limitation is of trivial effects.

The fact that only one unprotected secondary steel beam is used in this study makes the offset of the resultant yield-line intersection point distance *N* extremely small. Such differences in *N* values were found to be confined to the third decimal digit after comma. Applying such differences to *N* led to extremely trivial difference in the final results of the large-deflection analysis (i.e. the temperature enhancement).

8.2.3. Thermal deflection

The large-deflection analysis in this study is based on the deflection which mainly results from the degradation of the unprotected steel beam's load capacity at high temperatures. In fact, there is another factor that affects the overall slab deflection in fire, which is the thermal bowing. A slab which is affected by heat bows towards the direction of the fire. Since the slab is heated from the bottom, it bows downwards. This thermal bowing should contribute to the deflection calculations, therefore the mobilization of tensile membrane action. However, because of the low thermal conductivity of concrete and the relatively long time it needs to be heated up, the required period for the slab to bow under the effect of the heat is longer than the period at which the unprotected steel beam starts to lose strength at elevated temperatures and becomes dominant. This makes it more probable that the deflection which results from the degradation of the steel beam's capacity governs the overall deflection of the slab. The question lies in the extent of the further enhancement generated by the additional deflection from the thermal bowing; and if this additional deflection leads to further enhancement at all. This should be checked in future researches, examining the effects of the thermal deflection of slabs and its contribution to the overall enhancement.

8.3 Other factors affecting the failure mechanism

There are few factors that are believed to have a significant effect on the slab failure mechanism. These factors should be examined in order to determine the extent of their influence on tensile membrane action efficiency before the slab failure. These factors are: bond-slip behaviour, reinforcement heating effect and beam-slab detachment.

8.3.1 Bond-slip behaviour

In composite slabs in fire, two issues regarding the bond-slip behaviour between the reinforcement and concrete arise: firstly, composite slabs reinforcement is usually anti-cracking mesh, which its reinforcement is small-diameter bars, typically 6mm. This is different from the pull-out tests with normal structural reinforcement which is usually 14mm in diameter; secondly, the bond-slip behaviour of the reinforcement bars is different at elevated temperatures from what it is at ambient temperature. Therefore, in these conditions the bond behaviour between the reinforcement and concrete might not

be similar to normal situations when structural reinforcement at ambient temperature is used. Two pull-out tests, aimed at studying the bond-slip behaviour, were designed and conducted in the Heavy Structures lab at the University of Sheffield. However, since the bond behaviour was not the aim of this study, data analysis related to these tests were not completed. Nonetheless, for future researches, the design of the tests and their results are presented in Appendix 3.

8.3.2 Reinforcement heating effect

From the beginning of this study, it was assumed that the gradient heat across the slab's cross-section is ignored, as mentioned in Section 4.1, since the unprotected downstand steel beam loses its capacity far quicker than the heat is transferred across the slab's cross-section. This assumption is strongly justified before cracks form and widen. However, once the slab cracks, the reinforcement is heated up and therefore it is affected by the elevated temperatures. This should have consequences on the overall behaviour of the reinforcement. The effect of the elevated temperatures on the reinforcement depends on the vertical depth of the mesh within the slab, the width of the cracks, and the time it takes the crack to form and open as the slab deflects (i.e. the reinforcement exposure time to elevated temperatures). These factors affect the reinforcement strength and the bond-slip behaviour as well, and should be investigated in future researches.

8.3.3 Beam-slab detachment

In composite slabs, composite action is provided by connecting the downstand beams to the slab by connectors (i.e. shear studs). However, in fire conditions the unprotected steel beams are quickly heated, therefore they expand quickly. The expansion of the beam, in addition to the slab deflection as the result of the strength degradation of the beams due to the elevated temperature which in turn causes cracks to penetrate the slab, all these factors might lead to the fracture of the shear studs after they yield near the cracks. This puts the attachment between the slab and the beam in question. The detachment, if it occurs at all, and its effects should be examined in future researches.

8.4 Validation of this study by future research

The validation of this study should be conducted taking into account the limitations that are mentioned in Section 8.2 in order to correlate with the model proposed by this study.

No suitable isolated furnace tests were reported at the time of this study, except the COSSFIRE test which was conducted in 2008. However, the test was terminated early because the reinforcement bars were badly tack-welded together and broke at an early stage of the test. Therefore, for the purpose of future validation of this study, a proper slab model is presented in this section in order to be tested by future researchers.

A slab with an aspect ratio of 1.5 can be cast, with unprotected downstand steel beam attached to it with shear studs. The steel beam should be aligned to the long span of the slab. Since this study assumes full connection between the composite beam and the slab, the shear studs should be designed so that they withstand the loads with no shear fracture.

The slab should be left horizontally unrestrained, which is even easier than the other alternatives, taking into account that the slab is cast for testing in a lab. However, since vertical support was assumed with no loss along the perimeter of the slab, the slab should be supported on its four edges with strong primary beams. This should not compromise the horizontal unrestraint.

The slab should be reinforced with small reinforcement bars, forming merely anti-cracking mesh. Typically, a reinforcement bar of the mesh is 6mm in diameter. Setting the same depth of the reinforcement mesh layer for the theoretical analysis and the test is key (i.e. at the mid-depth of the slab cross-section). It is worth noting that the slab does not contain a steel deck, since the deck is assumed to have been detached from the slab due to the released steam as temperatures increase.

As the cross-section of the slab was assumed to be cool during the analysis, only the single secondary steel beam should be heated during the test in order to address this limitation of a cool slab cross-section. This leaves the reinforcement bars cool as the slab deflects and keeps the bars' ductility unchanged. The composite slab design is left to the future researcher according to the budget allowance for the test.

Uniformly distributed loads can be provided by loading the slab with sand bags evenly on its top surface. In order to allow enough temperature increase of the single unprotected steel beam, the load intensity should not be very low. In the case that the load is very low, the slab will be unrealistically safe and the slab will not fail in the proposed pattern. This means that the beam will be heated until it loses its strength capacity with a probability that the slab does not even fail with virtually zero beam capacity.

These points can be summarized as follows:

1. Perfect vertical support along the slabs four edges should be provided.
2. The slab should be horizontally unrestrained.
3. The slab is reinforced with anti-cracking mesh.
4. No steel deck is attached to the bottom surface of the slab.
5. A single unprotected steel beam should be attached along the large span of the slab, attached with strong shear studs to the slab.
6. Only the unprotected steel beam should be heated during the test. The slab should remain cool.

8.5 Final conclusions

This study presents an extension of the alternative simplified method which was originally presented in order to replace the existing method of TMA (i.e. the Bailey-BRE method) due to significant shortcomings in its assumptions and results. However, although this study itself has its own limitations, still it gives reasonable results. The importance of this study lies in that it confirms the expected insights about the behaviour of composite slabs in fire. It extends the alternative simplified method that was presented in 2014, retaining its advantages while eliminating some flaws of the Bailey-BRE method regarding the latter being either conservative or unconservative depending on the reinforcement ratios. Furthermore, this method allows monitoring the cracks formation and reinforcement fracture as deflection increases at elevated temperatures. Therefore, real-time monitoring of the slab's load capacity enhancement is possible, with no need to impose a deflection limit in the elastic range as the Bailey-BRE method is forced to do, which is intuitively conservative.

As the main purpose of this study was to examine the behaviour of the composite action effect on the enhancement factor as the slab deflects, it was found that the strength degradation of the unprotected steel beam allows further slab deflection, which in turn allows work dissipation of the reinforcement, concrete and the steel beam itself. This work dissipation allows further capacity to be mobilized by the tensile membrane action. The results of the examination of the unprotected steel beam effect agree with previous studies regarding slabs at large deflections. Therefore, the answer to one of the questions of this study, whether the large deflection of composite slabs is also beneficial as the alternative simplified method shows for flat slabs, the answer is yes. The results of this research confirm this point, providing that the tensile membrane action is allowed to be properly mobilized. Slabs at large deflections are able to withstand more loads and withstand higher temperatures than what was previously thought in the conventional methods. This is not merely a safety factor; it also has to do with the economical aspect of the structural design. Leaving the secondary beams within the slab panels unprotected against fire is beneficial structural-wise as this study shows, economically efficient and time & effort saving.

Comparisons against the Bailey-BRE method, as shown in Section 7.2.2, confirms that the latter method is conservative for lightly reinforced slabs. The maximum allowed temperature that the Bailey-BRE method gives is lower than the maximum temperature allowed by this study. This was already expected, as the other previous studies showed.

Addressing the limitations of this research should be the course of new studies in this field. Hence, the recommendations for future researches were already mentioned as the limitations of this research in Section 8.2, the other important factors to investigate in Section 8.3 and the validation model proposed for future research in Section 8.4. Some of these limitations are believed to have an important impact, such as the peripheral vertical support of the slab and the probability of folding mechanism occurrence. The other limitations might or might not have a significant influence. Therefore, they also should be examined.

Although the small-deflection analysis should be implemented carefully, limited to isotropic reinforcement, the mechanics of the large-deflection analysis can be confidently used as the basis for future researches in this field. In addition to the small-

deflection coding, the complete Matlab code is presented Appendix 2 for future modifications and development.

References

Abu, A.K. & Burgess, I.W., 2010. The effect of edge support on tensile membrane action of composite slabs in fire. In *Stability and Ductility of Steel Structures*. Rio de Janeiro: University of Canterbury. Civil and Natural Resources Engineering, pp. 21–32.

Alexander, R.S., 2002. *The World Trade Center Collapse*, Institution of Civil Engineers, Proceedings of the Insitution of Civil Engineers, Structures & Buildings 152.

ASFP, 2010. *Fire protection for structural steel in buildings* 4th ed., Bordon, Hampshire: Association for Specialist Fire Protection.

Bailey, C.G., 2003. Efficient arrangement of reinforcement for membrane behaviour of composite floor slabs in fire conditions. *Journal of Constructional Steel Research*, 59, pp.931–949. Available at: http://linkinghub.elsevier.com/retrieve/pii/S0143974X02001165 [Accessed October 3, 2014].

Bailey, C.G., 2004. Membrane action of slab/beam composite floor systems in fire. *Engineering Structures*, 26, pp.1691–1703. Available at: http://linkinghub.elsevier.com/retrieve/pii/S0141029604001853 [Accessed November 11, 2014].

Bailey, C.G., 2001. Membrane Action of Unrestrained Lightly Reinforced Concrete Slabs at Large Displacements. *Engineering Structures*, 23(5), pp.470–483. Available at: http://linkinghub.elsevier.com/retrieve/pii/S014102960000064X.

Bailey, C.G. & Moore, D.B., 2000a. The structural behaviour of steel frames with composite floors slabs subject to fire—part 1 Theory. *Struct Eng*, 78, pp.19–27.

Bailey, C.G. & Moore, D.B., 2000b. The structural behaviour of steel frames with composite floors slabs subject to fire—part 2 Design. *The Structural Engineer*, 78(11), pp.28–33.

Bailey, C.G. & Toh, W.S., 2007. Behaviour of concrete floor slabs at ambient and elevated temperatures. *Fire Safety Journal*, 42(6-7), pp.425–436.

Burgess, I.W., Dai, X. & Huang, S., 2013. An Alternative Simplified Model of Tensile Membrane Action of Slabs in Fire. In *Proceedings of International Conference Application of Structural Fire Engineering. Applications of Structural Fire Engineering conference*. Prague, Czech: CTU Publishing House.

Burgess, I.W., Huang, S. & Staikova, S., 2014. A Re-examination of the Mechanics of Tensile Membrane Action in Composite Floor Slabs in Fire. In *8th International Conference on Structures in Fire*. Shanghai, China.

Burgess, I.W., Plank, R.J. & Abu, A.K., 2012. The effect of reinforcement ratios on composite slabs in fire. *Proceedings of the ICE - Structures and Buildings*, 165(7), pp.385–398.

Chen, F.C. & El-Metwally, S.E.D., 2011. *Understanding Structural Engineering: From Theory to Practice*, Broken Sound Parkway, NW: CRC Press. Available at: https://books.google.co.uk/books?id=zRjOBQAAQBAJ&printsec=frontcover#v=onepage&q&f=false.

Corley, G., Hamburger, R. & McAllister, T., 2002. *World Trade Center Building Performance Study: Data Collection, Preliminary Observations, and Recommendations*, New York. Available at: http://www.fema.gov/pdf/library/fema403_execsum.pdf.

Eurocode 3, 2005. *BS EN 1993-1-2:2005 Eurocode 3: Design of Steel Structures*,

Fletcher, I., Borg, A., Hitchen, N. & Welch, S., 2006. Performance of Concrete in Fire: A Review of the State of the Art , With A Case Study of the Windsor Tower Fire. In *Proceedings of the 4th International Workshop in Structures in Fire*. Aveiro, Portugal, pp. 779–790.

Foster, S.J., 2006. *Tensile Membrane Action of Reinforced Concrete Slabs at Ambient and Elevated Temperatures. PhD*. University of Sheffield.

Gann, R.G., 2008. *Final Report on the Collapse of World Trade Center Building 7, Federal Building and Fire Safety Investigation of the World Trade Center Disaster (NIST NCSTAR 1A)*,

Gershon, R.R.M., Magda, L.A., Riley, H.E.M. & Sherman, M.F., 2011. The World Trade Center evacuation study: Factors associated with initiation and length of time for evacuation. *Wiley Online Library*. Available at: http://onlinelibrary.wiley.com/doi/10.1002/fam.1080/full [Accessed February 6, 2015].

Green, M., Butterworth, N., Burgess, I.W. & Plank, R., 2003. Practical case studies in performance-based structural fire engineering design. In *Designing Structures for Fire*. Baltimore: American Society of Civil Engineers (ASCE), pp. 259–269.

Gross, J.L. & McAllister, T.P., 2005. *Structural Fire Response and Probable Collapse Sequence of the World Trade Center Towers. Federal Building and Fire Safety Investigation of the World Trade Center Disaster (NIST NCSTAR 1-6)*,

Hamilton, S.R., 2011. *Performance-Based Fire Engineering for Steel Framed Structures: A Probabilistic Methodology. PhD*. Stanford University.

Hayes, B., 1968a. *A Study of the Design of Reinforced Concrete Slab Structures. PhD*. University of Manchester.

Hayes, B., 1968b. Allowing for Membrane Action in the Plastic Analysis of Rectangular Reinforced Concrete Slabs. *Magazine of Concrete Research*, 20(65), pp.205–212.

Hayes, B. & Taylor, R., 1969. Load-testing RC slabs. *Consult Eng*, 33(11), pp.46–7.

Huang, Z., Burgess, I.W. & Plank, R.J., 2001. The Influence of Tensile Membrane Action in Concrete Slabs on the Behaviour of Composite Steel-framed Buildings in Fire. In *ASCE Structures Congress*. Washington DC, pp. 1–14. Available at: http://ascelibrary.org/doi/abs/10.1061/40558%282001%2986.

Kemp, K.O., 1967. Yield of a square reinforced concrete slab on simple supports, allowing for membrane forces. *The Structural Engineer*, 45(7), pp.235–240.

Kennedy, G. & Goodchild, C.H., 2004. *Practical Yield Line Design: An introduction to the practical use of Yield Line Theory in the design of flat slabs, raft foundations and refurbishment*, Surrey, UK: The Concrete Centre. Made available on the website of the Reinforced Concrete Council.

Kirby, B.R., 1998. *THE BEHAVIOUR OF A MULTI-STOREY STEEL FRAMED BUILDING SUBJECTED TO FIRE ATTACK*, Rotherham, UK: British Steel, Swinden Technology Centre.

Lennon, T., 2014. *BRE-Cardington Steel Framed Building Fire Tests-SM*, Available at: http://data.bre.co.uk/page.jsp?id=4.

Lim, L.C.S., 2003. *Membrane Action in Fire Exposed Concrete Floor Systems*. University of Canterbury.

Mangeon, W., 2013. *Behaviour of steel and concrete composite floor slabs at elevated*

temperature. University of Sheffield - Polytech'Clermont Ferrand.

Mattock, A.H. & Kriz, L.B., 1961. Ultimate Strength of Non Rectangular Structural Concrete members. *A.C.I Journal*, 57.

Meacham, B.J. & Custer, R.L.P., 1995. Performance-Based Fire Safety Engineering: an Introduction of Basic Concepts. *Journal of Fire Protection Engineering*, 7(2), pp.35–53. Available at: http://jfe.sagepub.com/cgi/doi/10.1177/104239159500700201 [Accessed October 16, 2014].

Newman, G.M., Robinson, J.T. & Bailey, C.G., 2000. *Fire Safe Design - A New Approach to Multi-Storey Steel Framed Buildings, SCI-P288*, Ascot, Berkshire, UK: Steel Construction Institute.

NIST NCSTAR 1A, 2008. *Final Report on the Collapse of World Trade Center Building 7*, Gaithersburg, MD, USA.

Parker, D., 2005. Madrid tower designer blames missing fire protection for collapse. *New Civil Engineer*. Available at: http://www.nce.co.uk/madrid-tower-designer-blames-missing-fire-protection-for-collapse/532985.article [Accessed February 3, 2015].

Pope, R., 2006. Lessons from Madrid. *Carba Consulting Ltd*.

Purkiss, J.A., 2007. *Fire Safety Engineering - Design of Structures* 2nd ed., Oxford, UK: Elsevier Ltd.

Sawczuk, A. & Winnicki, L., 1965. Plastic Behavior of simply supported reinforced concrete plates at moderately large deflections. *International Journal of Solids and Structures*, 1, p.97 to 111.

Staikova, S., 2014. *Development of a kinematically correct simplified fire resistance design process for composite floor systems in buildings*. The University of Sheffield.

Szilard, R., 2004. *Theories and Applications of Plate Analysis: Classical, Numerical and Engineering Methods*, WILEY.

Taylor, R., 1965. A Note on a Possible Basis for a New Method of Ultimate Load Design of Reinforced Concrete Slabs. *Magazine of Concrete Research*, 17.

Vassart, O. & Zhao, B., 2011. *Fire Resistance Assessment of Partially Protected Composite Floors (FRACOF)*, The Steel Construction Institute (SCI).

Wang, Y., Burgess, I.W., Wald, F. & Gillie, M., 2012. *Performance-Based Fire Engineering of Structures*, Broken Sound Parkway, NW: CRC Press.

Wood, R.H., 1961. *Plastic and Elastic Design of Slabs and Plates*, London: Thames and Hudson.

Appendix 1

A1 Publications

The publication which is presented in this appendix was accepted in July 2015 as a proceeding for the ASFE'15 conference, Croatia.

THE MECHANICS OF TENSILE MEMBRANE ACTION IN COMPOSITE SLABS AT HIGH TEMPERATURES

A. Alskeif [a], I.W. Burgess [a], S.-S. Huang [a]

[a] Department of Civil & Structural Engineering, University of Sheffield, UK

Abstract

The mechanics of tensile membrane action of thin lightly-reinforced concrete slabs has been re-examined during the last two years. The re-examination is based on large-deflection plastic yield-line analysis, applied to flat slabs. As deflection increases beyond the optimum yield-line pattern, tensile membrane action is mobilized and further load carrying capacity is provided. This paper represents an extension of this re-examination to include composite slabs at high temperatures. As temperature increases, the unprotected downstand steel beams significantly lose capacity, allowing for further deflection until the overall capacity degrades to the applied load. Tensile membrane action then allows further increase of steel temperature until a maximum is reached.

Keywords: Tensile membrane action, composite slab, fire, Bailey-BRE method

1 INTRODUCTION

Bailey & Moore (2000a, b) presented a simplified method for the fire design of composite slabs, based on a calculation of the enhanced load capacity of the slab at large deflection due to its tensile membrane action, which was originally published by Hayes (1968). The simplified method considers that, as the unprotected downstand steel beams lose considerable strength at high temperature, the mechanism by which the slab resists the applied loads changes from bending resistance to tensile membrane action (TMA) at large deflection. TMA increases as the downstand steel beams lose strength, allowing for further deflection as temperature increases, until no further capacity can be mobilized. However, the existing simplified method is based on empirical assumptions, which are made at many stages without mentioning the effects of these assumptions. The method considers two components of load enhancement, namely bending resistance *and* membrane action, as independent of one another. These two independent components are eventually combined as one single enhancement, without justifying the rationality of such a process. Furthermore, the method is based on calculations which use different neutral axis depths in the x and y directions for the same cross-section, which is intuitively irrational. Burgess et al. (2013) presented an alternative simplified method based on the mechanics of TMA using the same yield-line pattern, which had been used by Bailey and Moore, but with different subsequent kinematic assumptions. This yield-line pattern has been observed in tests on loaded thin slabs which experience a full-depth central crack penetrating the slab perpendicular to its long span. The mechanism used in this paper is based on the equilibrium and kinematics presented by Burgess et al., extended to account for the presence of the unprotected downstand steel beams at high temperature, and their effects on the yield-line pattern and enhancement factor.

2 YIELD LINE MECHANISM AND CRACKING SYSTEM EQUILIBRIUM

As an extension of the work presented by Burgess et al. (2014), the same initial assumptions are considered in this paper. A two-way rectangular slab of aspect ratio *r* is considered. The slab is supported vertically along its four edges, and is reinforced by two layers of isotropic welded mesh, which lie at its mid-surface. The slab is considered as isolated, but is in no way limited to this, or to the assumptions mentioned above. However, due to the contribution of the downstand steel beams, the resulting yield-line pattern is rotated by 90° from that of a non-composite slab, due to the strength added in the original direction of the yield-line alignment. For the purpose of this paper, only one steel beam is considered in the study. A comparison of the usual and rotated alignments of yield-line patterns is shown in Figure 75.

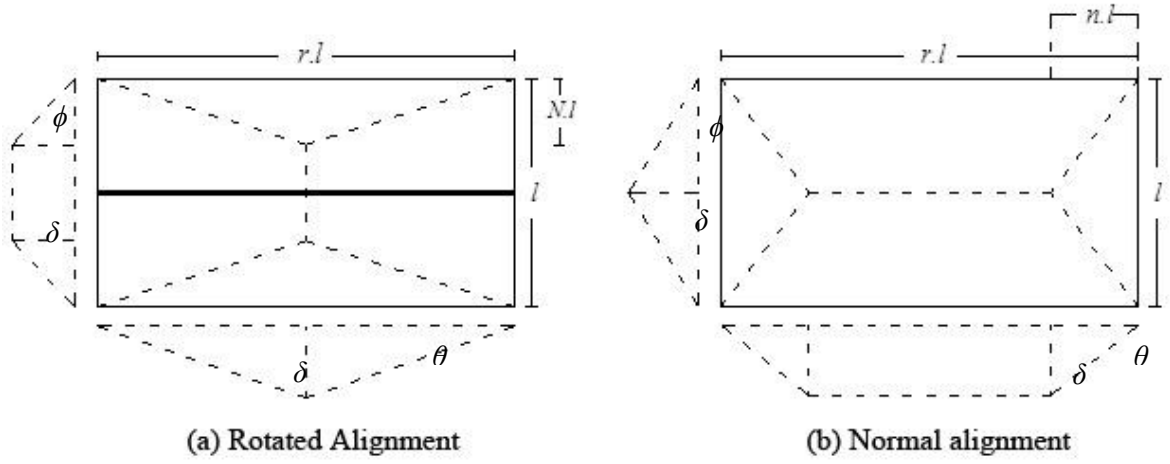

Figure 75: Rotated & normal yield-line alignments

As is the case with the normal yield-line pattern, each resulting flat facet of the slab rotates about its supporting edge by angles θ or ϕ, as shown in Figure 75. The rotation of these facets results in the same maximum deflection δ at both yield line intersection points, as shown in Figure 76.

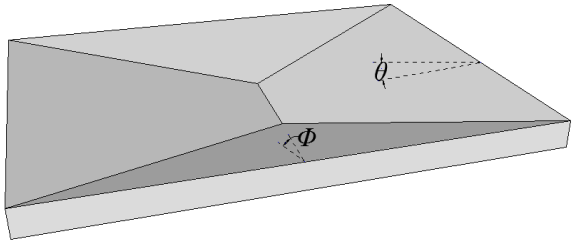

Figure 76: Rotated yield-line pattern illustrated in 3D

The optimized yield-line intersection dimension in the presence of the steel beam, which is denoted as *N* to distinguish the rotated from the normal alignment, is given as:

$$N = -\frac{2}{3}K.r^2.l^2 + \sqrt{\left(\frac{2}{3}K.r^2.l^2\right)^2 - 4.\left(\frac{2}{3}.K.l^2 + \frac{4}{3}.M_{pl}.l\right).\left(-\frac{1}{2}.K.r^2.l^2\right)}\,/2\left(\frac{2}{3}K.l^2 + \frac{4}{3}.M_{pl}.l\right) \quad (1)$$

Where K is $2*m_P$ (m_P is the sagging moment capacity of the slab), and M_{pl} is the steel beam strength capacity. r is the slab aspect ratio, and l is the slab short span. This represents the level at which the yield-line capacity is minimized. It is highly unlikely that the optimum yield-line pattern will change after the yield lines have been formed. Temperature increase allows further increase of deflection due to weakening of the steel beam, allowing further capacity to be mobilized by tensile membrane action. As the deflection increases, the compression block depth in the central region of the slab decreases until it disappears completely, when the whole central area is then in pure tension. During this retreat of compression from the central region of the slab, the stress blocks on the diagonal yield lines change from trapezoidal to triangular, and its depth at a slab corner can increase until the whole slab corner is in compression as shown in Figure 77 Concrete dissipates internal work wherever slab elements are in contact. The reinforcement dissipates internal work when it is plastically stretched under tension. The extent by which the cracks between facets of the slab widen during deflection plays a crucial role in determining the existence of both the concrete compression blocks and reinforcement tension zones.

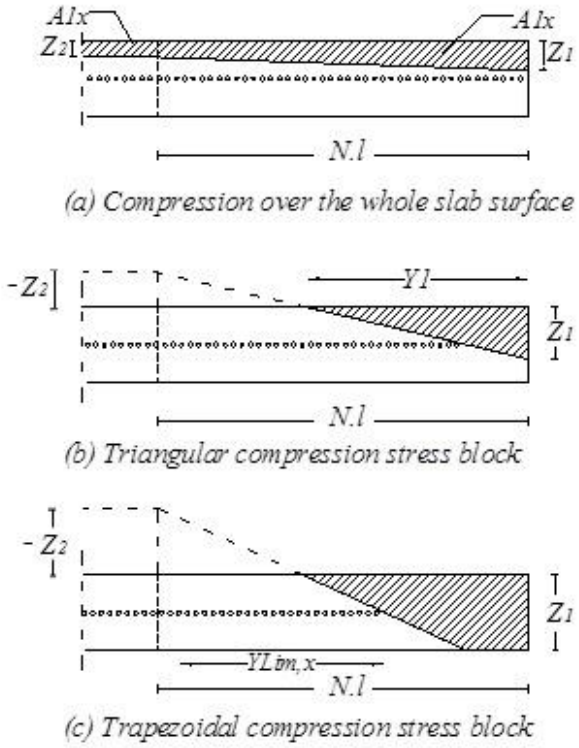

Figure 77: Compression block phases shown at the edge of the slab as deflection increases

As shown in Figure 77, it is possible for compression and tension to co-exist over a complete yield line cross-section. However, as the crack widens the compression zones move towards the corners and tension exists wherever the mesh lies below the neutral axis. Only reinforcement bars which are in tension are considered in the calculation of energy dissipation. Therefore, only those between any intersection with the neutral axis and the limiting distances $Y_{Lim,x}$ (for x-aligned bars) and $X_{Lim,y}$ (for y-aligned bars) at which the bars fracture are taken into account in calculation of load capacity. When the slab deflects, its facets rotate about the yield-lines by the rotation angles at its supporting edges. This results in the beams spanning the cracks to extend in a similar fashion to the reinforcement bars as shown in Figure 78. This extension of the

heated steel beams results in dissipation of plastic work which has to be included in the load capacity calculation.

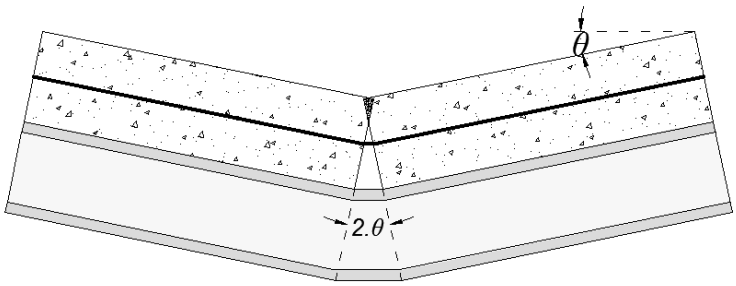

Figure 78: Extension undergone by the downstand beam, and reinforcement

Due to the compression stress blocks in the concrete, and the extensions of the reinforcement and the steel beams, in-plane equilibrium of the slab facets must exist under the compression and tension forces crossing the yield lines. The forces involved in this equilibrium are shown in Figure 79. Tx1 and T_{x2} represent reinforcement tension forces on Elements 1 and 2 respectively in the x-direction. T_{y1} is the reinforcement tension force in the y-direction. T_b is the tension force generated by the extension of the downstand beam. C & C_{x2} are the resultant concrete compression forces and S represents the resultant shear force between facets on a diagonal yield line. When the central yield line opens as the slabs facets lose contact, C_{x2} disappears abruptly, leaving only the pure reinforcement tensile force across this yield line. Along the diagonal yield-lines, this complete separation does not occur, but it develops progressively, starting from the intersection point of the yield-lines, towards the corner of the slab, effectively "unzipping" the mesh.

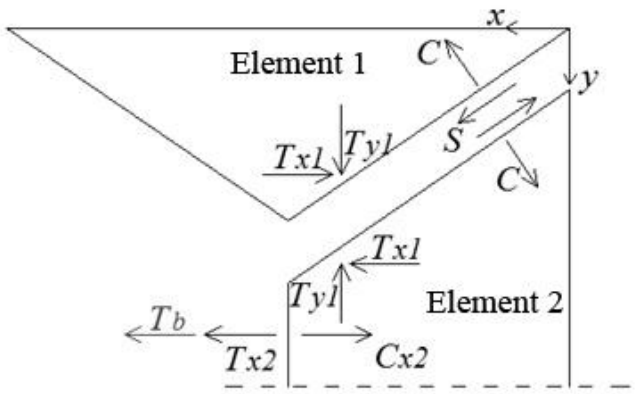

Figure 79: Force equilibrium on the slab elements

Eliminating the shear force S, the equilibrium state can be expressed by the equation:

$$T_{y1}.Cos(\gamma) + (T_{x1} + T_{x2} + T_b).Sin(\gamma) = C_{x2}.Sin(\gamma) + C \qquad (2)$$

In which the forces are given by:

$$T_{y1} = \left(X_{Lim,y} - X_T\right).f_{py} \qquad (3)$$
$$T_{x1} = \left(Y_{Lim,x} - Y_T\right).f_{px} \qquad (4)$$
$$T_{x2} = l.(1 - 2.N).f_{px} \qquad (5)$$

$$C = A_{1x}.f_c/Sin(\gamma) \quad (6)$$
$$C_{x2} = A_{2x}.f_c \quad (7)$$

The terms ($X_{Lim,y}$-X_T), and ($Y_{Lim,x}$-Y_T) are the distances over which the reinforcement bars are still intact and generating their full yield strength. f_{px} *and* f_{py} are reinforcement forces in both directions. A_{1x} and A_{2x} are the compression block areas, as illustrated in Figure 77.

3 KINEMATICS OF THE SOLUTION

The forces, which were calculated above, are substituted into the equilibrium equation and expressed as a function of the horizontal movement in the *y*-direction Δy as shown in Figure 80. Y is taken as the major direction in the calculations since it is the direction of the obtained rotated yield-line pattern. This horizontal movement Δ*y* changes as deflection increases. A program has been coded in Matlab to conduct a deflection-controlled iteration. At each deflection level, the temperature is increased, until the slab capacity has degraded to the level of the applied load. This allows further deflection until a maximum load capacity is reached and the slab is considered to have structurally failed.

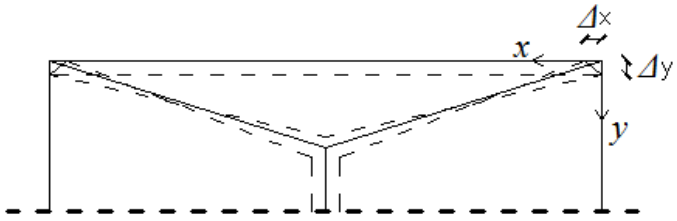

Figure 80: Horizontal movements seen from the top surface of the slab

The calculated forces and geometry allow the calculation of the internal energy dissipated within the slab, which allows the calculation of the load capacity of the slab *P*. The internal plastic work of the reinforcement is expressed using the plastic stretch of the bars across the widening crack width between the slab elements. As for concrete areas which are still in contact, the internal energy is expressed in terms of the compression forces between the overlapped elements. The loss of potential energy of the transverse loading on the surface of the slab *P* is calculated similarly to the optimal small-deflection yield-line mechanism, and is given as:

$$E = P.r.l^2\delta.\left(\frac{1}{2} - \frac{1}{3}N\right) \quad (8)$$

Where: *E* is the external work done by loads; δ is the maximum deflection of slab elements. According to plastic energy theory, external work done = internal energy dissipated. This gives the load capacity of the slab as:

$$P = I_s/\left[r.l^2\delta.\left(\frac{1}{2} - \frac{1}{3}N\right)\right] \quad (9)$$

Where: I_s is the internal work of the slab. The iteration increases the temperature of the unprotected steel beams until this calculated load capacity *P* has reduced to the applied load. Then the deflection loop is repeated. This iteration continues until no further increase is possible. The enhancement is taken in terms of the temperature calculated at the end of every internal loop.

4 APPLICATION OF THE METHOD

A composite slab will be considered in order to demonstrate the application of the newly extended method. The slab used in the Matlab model is 9m by 6m with an aspect ratio *r=1.5*; thickness *t=130mm*; reinforced by isotropic A142 mesh (142mm^2/m in both directions) located at the slab mid-depth; The mesh bar spacing is 200mm. Reinforcement ductility=5%; Yield stress of reinforcement $f_{p,x,y}$*=500MPa*; Beam section (UKB 406x140x39); Yield stress of the steel beam f_y*=355MPa*; Concrete characteristic strength f_c*=35MPa*. Uniformly distributed transverse loading on the slab= 4kN/m^2. The result of the analysis is shown in Figure 81.

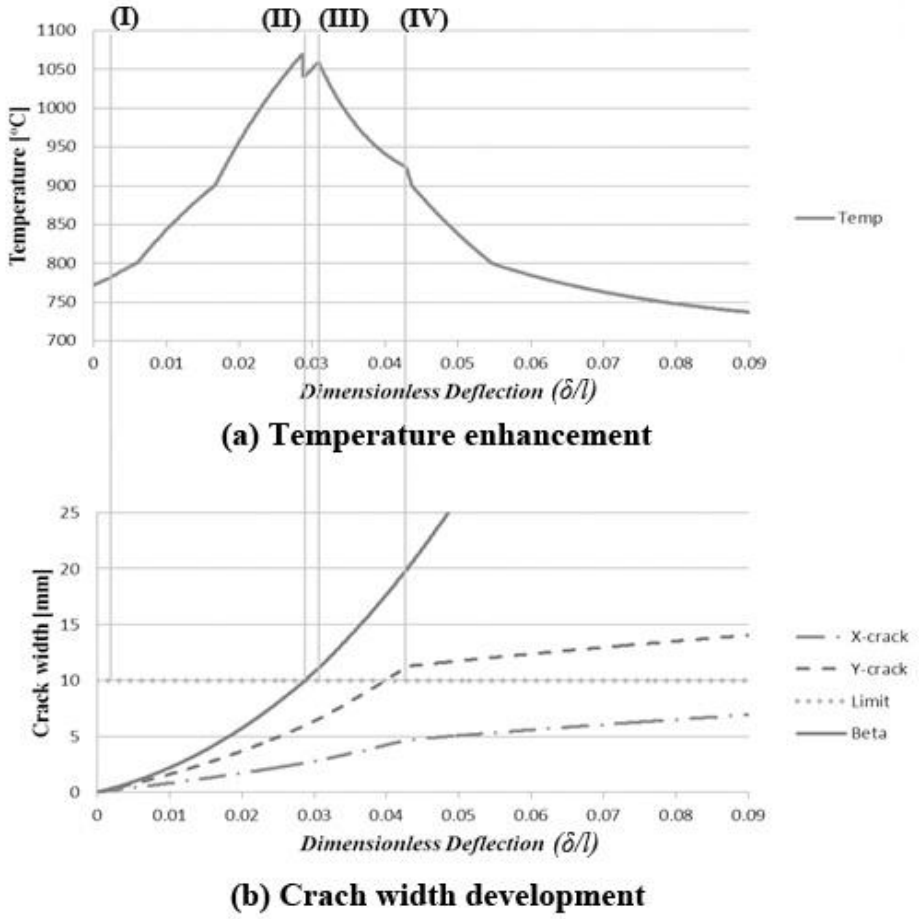

Figure 81: (a) represents temperature against deflection; (b) represents crack width development against deflection. The vertical lines (I) to (IV) define phase changes through the process

Figure 81(a) shows the enhancement in terms of temperature against normalized deflection. Figure 81(b) shows the development of the crack widths of the diagonal yield-lines in the *x* and *y* directions. It also monitors the development of the central yield-line crack width β. The limit crack width, demonstrated by a horizontal line, represents the limit at which reinforcement fractures. The vertical line (I) in Figure 81(b) represents the end of the first phase at which the compression stress block becomes triangular on the diagonal yield lines of the slab, while compression disappears from the central yield line. The end of second phase witnesses the fracture of the mid yield-line bars, coinciding with a temperature decrease which gives the first peak shown in Figure 81(a). The final two phases account for the unzipping of the bars in the *y*-direction and then *x* and *y*, respectively. However, if it happens that the slab cools down before any of the temperature enhancement peaks, shown in Figure 81(a), has been reached, the slab will survive with its current reinforcement and crack status, and the rest of the chart will simply be theoretical in this case. If, on the other hand, the temperature happens to rise higher than the

temperature enhancement peak for the same slab configurations, the slab fails due to excessive temperature and the rest of the enhancement chart does not apply any more. Similarly, the slab forces, shown in Figure 82, which have been illustrated in thinner lines after the second peak, account for the theoretical course of action which might change in case the factual fire scenario differs from the theoretical one.

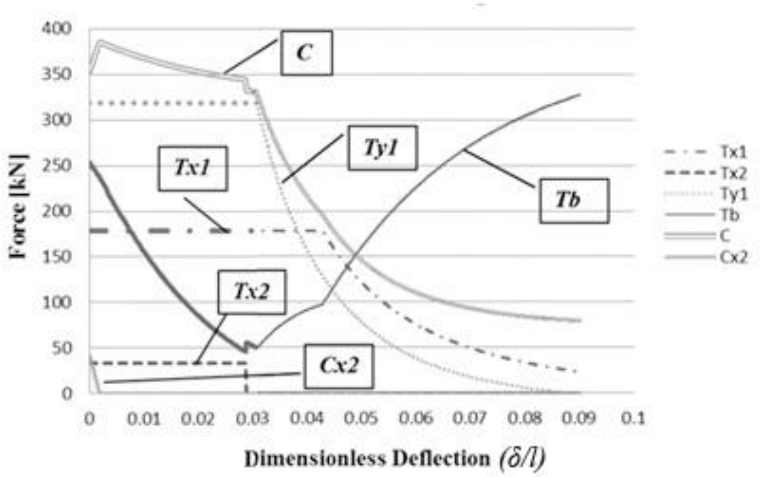

Figure 82: Internal forces on the slab facets

5 CONCLUSIONS

This paper has demonstrated an extension of the alternative simplified method which accounts for composite slabs with unprotected downstand steel beams at high temperature. The analysis conducted in this study is based on plastic yield-line mechanism at large deflection. The temperature is assumed only to affect the unprotected steel beams since concrete has low thermal conductivity, which causes the unprotected steel beams to heat faster, leaving the reinforcement at a relatively cool temperature. Temperature increase controls the enhancement, accounting for the reinforcement fracture that occurs when the slab experiences large deflections, as the unprotected steel beams lose capacity. The enhancement depends on the temperature to which the slab is subjected, and different fire scenarios will affect the actual enhancement.

REFERENCES

Bailey, C.G. & Moore, D.B., 2000. The structural behaviour of steel frames with composite floors slabs subject to fire—part 1 Theory. Struct Eng, 78, pp.19–27.

Burgess, I.., Huang, S. & Staikova, S., 2014. A re-examination of the mechanics of tensile membrane action in composite floor slabs in fire. In 8th International Conference on Structures in Fire. Shanghai, China.

Burgess, I.W., Dai, X. & Huang, S., 2013. An alternative simplified model of tensile membrane action of slabs in fire. ASFE 2013, Prague.

Hayes, B., 1968. Allowing for Membrane Action in the Plastic Analysis of Rectangular Reinforced Concrete Slabs. Magazine of Concrete Research, 20(65), pp.205–212.

Appendix 2

A2 Code Scripts and Coding Methodology

A2.1 Introduction

The analysis of this study comprises two distinguishable parts: small-deflection and large-deflection analyses. In this appendix, the methodology of the coding of both parts of the analysis is presented with the full code scripts attached in the end of each analysis part.

The first part of this study (i.e. the small-deflection analysis) was coded in Microsoft Excel- Visual Basic macro in order to determine the characteristics of the optimum yield-line pattern of the composite slab at elevated temperatures.

The second part of the analysis (i.e. the large-deflection analysis) which forms the core of this study, was coded in Matlab in order to conduct the controlled-deflection iteration of the composite slab at elevated temperatures until failure.

A2.2 Coding methodology

A2.2.1 Small-deflection coding

The derivations of the small-deflection analysis were fully presented in Chapter 6. The equations that resulted from these derivations were coded in Microsoft Excel- Visual Basic macro. The slab parameters should be entered in details; for example, the slab dimensions, reinforcement diameter and the vertical depth of the mesh within the slab, the yield stress of reinforcement and concrete, the applied load and the strength capacity of the unprotected secondary steel beam. These parameters were entered in the

spreadsheet and then imported by the visual basic code when the Run macro button was clicked.

The equations of the optimized yield-line intersection point distances n and N were coded in order to calculate the initial yield-line load capacity P at ambient temperature. The analysis started from 400ºC, rather than 20ºC since the Eurocodes define the reduction factor of the yield strength of the steel k_y as constant and equals one, when the temperature is less than or equals 400ºC (Eurocode 3 BS EN 1993-1-2: 2005). Hence, it is a waste of time to raise the temperature in small increments from 20ºC to 400ºC, as this makes a noticeable difference in computational time of this program. Calculations were done to determine if the yield-line pattern was aligned to the x or y-direction, so that the analysis was conducted according to the detected mechanism. Although the yield-line pattern was theoretically rotated (aligned to the y-direction) in the presence of a downstand secondary steel beam, both alignments were derived and coded to double check this issue. It was found later that when at least one steel beam existed, the initial and the optimum yield-line patterns (when the pattern forms) were rotated by 90^o. This check, however, was conducted in order to be certain that the large-deflection analysis was conducted on correct basis.

Once the yield-line load capacity was calculated at the current temperature, it was compared to the applied load on the slab. If the load capacity is higher than the applied load, the temperature is increased by a small increment and the reduction factor of the yield strength k_y is calculated according the newly increased temperature in a new loop. The steel strength reduction factor k_y was calculated according to the Eurocode 3. It decreased as the temperature increased. Since heating across the cross-section of the slab was not considered in this study, only the strength capacity of the steel beam was reduced by the steel reduction factor as the temperature increased. In the new loop, the parameters (i.e. the yield-line parameter N and load capacity P) were calculated again in the light of the new increased temperature. The new yield-line capacity P was compared again to the applied load P_a. Temperature was increased, decreasing the capacity of the unprotected steel beam until the yield-line capacity degraded to the level of the applied load (i.e. $P=P_a$). At this point, the final temperature, which led to the reduction of the yield-line capacity to the level of the applied load, was called the critical temperature T_{cr}. The corresponding yield-line intersection distance N defines the optimum yield-line pattern. After this point it is highly unlikely that the already formed yield-line pattern

changes. The yield lines rather crack if further deflection is experienced beyond the point of their formation.

A2.2.2 Small-deflection analysis coding flowchart

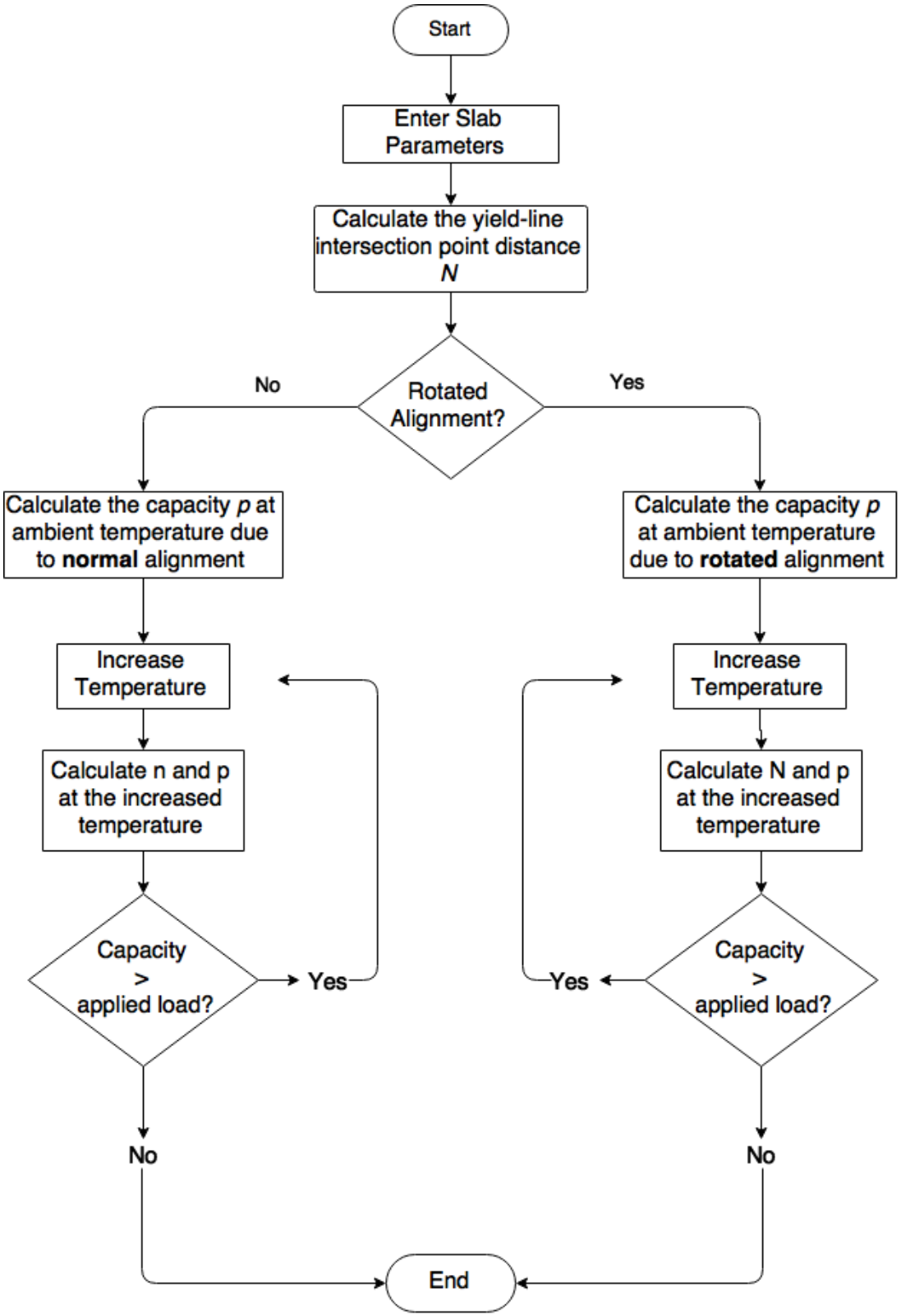

A2.2.3 Small-deflection analysis code script – Visual Basic

```
Sub complete()
'Defining the parameters
Dim ti     'initial T
Dim tj     'next step T
Dim ky      'reduction factor Ky
Dim deltat     'Delta T
Dim deltap      'P - pa
Dim Ddeltap, Dd     'For deltap refine process
Dim nj        'new n
Dim Sj, acj, bj, n, k, e, r, m, mp, l, p, pa, Mky, pre

'MAIN PARAMETERS
pa:
mp = Range("g1")
l = Range("g2")
k = (2 * Range("G1"))
r = Range("b2")
m = Range("b4")
Range("h18") = "" 'reset
tj = 400     'starting from 400 doesn't affect initial steps

pre = Range("c22") 'precision of temperature increment increase
If pre < 0.01 Or pre > 5 Then
Range("c22") = 0.5
pre = Range("c22")
End If

Rotated:
'start with Rotated alignment since the slab contains steel beams - highly likely to be
rotated-aligned
Range("d19") = "N"      'Telling the user that the process is currently at Rotated
Alignment
ky = 1  'for initial step
m = m * ky
Mky = m

a = (2 * k * l ^ 2 / 3) + (4 * m * l / 3)
b = 2 * k * r ^ 2 * l ^ 2 / 3
c = -0.5 * k * r ^ 2 * l ^ 2
n = (-b + Sqr((b ^ 2) - 4 * a * c)) / (2 * a)
'Range("a12") = "N="     'Telling the user that the process is currently at Rotated
Alignment
If n > 0.5 Then GoTo Normal
p = ((k * r / n) + (2 * k / r) + (4 * m / (r * l))) / (0.5 * r * l ^ 2 - r * l ^ 2 * n /
3)


pa = Application.InputBox(Prompt:="Enter Applied Load Value; or enter 0 to exit",
Title:="Pa", Type:=1)
If pa = False Then
MsgBox ("You entered 0 value. Application will end")
End
End If
If pa > p Then
MsgBox ("Applied Loads cannot be bigger than slab's capacity at ambient temperature")
GoTo pa
End If

Range("b18") = pa

Do
tj = tj + pre     'Start increasing temperature gradually
If tj > 1200 Then
MsgBox ("Applied Load is too small to cause collapse")
tj = 400
GoTo pa
End If
```

```
' Calculating corresponding Ky for the new tj temperature
If 20 < tj And tj < 400 Then
ky = 1

ElseIf 400 <= tj And tj < 500 Then
ky = 1 - 0.22 * (tj - 400) / 100
ElseIf 500 <= tj And tj < 600 Then
ky = 0.78 - 0.31 * (tj - 500) / 100
ElseIf 600 <= tj And tj < 700 Then
ky = 0.47 - 0.24 * (tj - 600) / 100
ElseIf 700 <= tj And tj < 800 Then
ky = 0.23 - 0.12 * (tj - 700) / 100
ElseIf 800 <= tj And tj < 900 Then
ky = 0.11 - 0.05 * (tj - 800) / 100
ElseIf 900 <= tj And tj < 1000 Then
ky = 0.06 - 0.02 * (tj - 900) / 100
ElseIf 1000 <= tj And tj < 1100 Then
ky = 0.04 - 0.02 * (tj - 1000) / 100
ElseIf 1100 <= tj And tj < 1200 Then
ky = 0.02 - 0.02 * (tj - 1100) / 100
ElseIf 1200 <= tj Then
ky = 0
End If
'########################################
Mky = Mky * ky         'Reduced moment strength

Range("a20") = tj
a = (2 * k * l ^ 2 / 3) + (4 * Mky * l / 3)     'new a
n = (-b + Sqr((b ^ 2) - 4 * a * c)) / (2 * a)
If n > 0.5 Then GoTo Normal
p = ((k * r / n) + (2 * k / r) + (4 * Mky / (r * l))) / (0.5 * r * l ^ 2 - r * l ^ 2 * n
/ 3)

If p > pa Then
Mky = m
Else
Range("a20") = tj
Range("b20") = p
Range("c20") = p - pa
Range("d20") = n
End
End If
Loop

'#####################################################################
Normal: 'Normal Allignment
' Increasing Temperature gradually
Range("d19") = "n"    'to tell that the process is at normal alignment
'MAIN PARAMETERS
pa_n:
Mky = m

a = (2 * k * r * l ^ 2 / 3)
b = (2 * k * l ^ 2 / 3) + (4 * m * l / 3)
c = -0.5 * k * r * l ^ 2 - m * r * l
n = (-b + Sqr((b ^ 2) - 4 * a * c)) / (2 * a)
p = (2 * k * r * n + k + 2 * m / l) / ((2 * n ^ 2 * l ^ 2 / 3) + 0.5 * n * l ^ 2 * r - n
^ 2 * l ^ 2)
Range("h18") = p

Do
tj = tj + pre     'Start increasing temperature gradually
If tj > 1200 Then
MsgBox ("Applied Load is too small")
tj = 400
End
End If

' Calculating corresponding Ky for the new tj temperature
If 20 < tj And tj < 400 Then
ky = 1
```

```
ElseIf 400 <= tj And tj < 500 Then
ky = 1 - 0.22 * (tj - 400) / 100
ElseIf 500 <= tj And tj < 600 Then
ky = 0.78 - 0.31 * (tj - 500) / 100
ElseIf 600 <= tj And tj < 700 Then
ky = 0.47 - 0.24 * (tj - 600) / 100
ElseIf 700 <= tj And tj < 800 Then
ky = 0.23 - 0.12 * (tj - 700) / 100
ElseIf 800 <= tj And tj < 900 Then
ky = 0.11 - 0.05 * (tj - 800) / 100
ElseIf 900 <= tj And tj < 1000 Then
ky = 0.06 - 0.02 * (tj - 900) / 100
ElseIf 1000 <= tj And tj < 1100 Then
ky = 0.04 - 0.02 * (tj - 1000) / 100
ElseIf 1100 <= tj And tj < 1200 Then
ky = 0.02 - 0.02 * (tj - 1100) / 100
ElseIf 1200 <= tj Then
ky = 0
End If
Mky = Mky * ky          'Reduced moment strength
Range("a20") = tj
'New parameters
b = (2 * k * l ^ 2 / 3) + (4 * Mky * l / 3)
c = -0.5 * k * r * l ^ 2 - Mky * r * l
n = (-b + Sqr((b ^ 2) - 4 * a * c)) / (2 * a)
p = (2 * k * r * n + k + 2 * Mky / l) / ((2 * n ^ 2 * l ^ 2 / 3) + 0.5 * n * l ^ 2 * r -
n ^ 2 * l ^ 2)
If p > pa Then
Mky = m
Else
Range("a20") = tj
Range("b20") = p
Range("c20") = p - pa
Range("d20") = n
End
End If
Loop

End Sub
```

A2.2.4 Large-deflection coding

A2.2.4.1 Geometrics of the deflected slab

The large-deflection analysis was coded in Matlab in order to conduct a deflection-controlled iteration of two intersected loops: deflection and temperature. As explained in Chapter 4, in the large-deflection analysis deflection was increased in increments beyond the optimum yield-line pattern until the load capacity of the slab degraded to the level of the applied load, then the temperature was increased to reduce the capacity strength of the unprotected secondary downstand steel beam, allowing further deflection and therefore the mobilization of tensile membrane action. In conventional methods, the optimum yield-line capacity is considered as the failure load of the slab. But as a main goal of this study, the composite slab was allowed to deflect further, allowing further load-capacity beyond the limit of conventional load limit.

The yield-line intersection point distance N was the only parameter that was imported from the small-deflection analysis output in order to be used in the large-deflection analysis. The optimum yield-line capacity that resulted from the small-deflection analysis was not used in this part; and the critical temperature of the optimum yield-line pattern was not used here either. The large-deflection analysis started over from 400ºC since the computational time of this stage of analysis is trivial and not noticeable.

The detailed specifications of the composite slabs should be entered to the Matlab program, such as: the beam cross-section height, the area and the yield stress of the beam; the dimensions of the slab, reinforcement details such as the diameter of the bars that form the mesh, the vertical depth of the mesh within the slab, spacing of the bars and the ductility and yield stress of the reinforcement. Furthermore, the characteristic strength of concrete should be entered. The yield-line intersection point distance N should be entered as it resulted from the previous small-deflection analysis. The transversely applied load which should definitely be the same.

The iteration started by the calculation of the rotation angles of the slab elements (i.e. θ and ϕ) and the movement components that result from these rotations, as mathematically explained in Section 6.3. These values, and the rest of the calculations,

were calculated for every single increment of the increasing deflection. The equations of each case scenario were coded in order to calculate the horizontal movement in the main direction Δy, which resulted from the increasing deflection of the slab. The limit crack was calculated at the beginning as explained in Chapter 4, depending on the reinforcement bars ductility and spacing.

A2.2.4.2 Checking flags

It was mentioned in Chapter 8 that the sequence which the cases follow as the slab deflects, was monitored and not dictated by any means. All cases were fully coded, but the sequence of these cases was monitored through checking flags that determine which of the cases was active at each moment through the analysis phase. These flags are sets of IF conditional statements. Based on the results of these statements, the flags were given certain values (1 or 0, or even other values as required); digitally simulating True or False output. Depending on the results of these conditional statements (1 or 0 for example), the required actions and considerations can be taken later in the code.

After the horizontal movement of every single scenario case was calculated, a set of flag checks was conducted to check whether this case was, or was not, valid at every moment of the analysis (i.e. currently active for the current deflection phase). These flags are:

- Compression above the reinforcement bars:
  It is valid (therefore its flag =1) as long as $\Delta y < \phi.\mu.t$. Hence, it [compression] exists as long as the horizontal movement in the *y*-direction is smaller than the distance that results from the rotation ϕ. If not, the flag value is zero.
- Compression in the central yield-line:
  It is valid (i.e. its flag given a value of 2 to distinguish it from the previous flag) as long as the horizontal displacement in the *y*-direction Δy is smaller than the increasing distance resulted from the rotation of the slab element $\phi^2.N.l/2$.
- Middle yield-line reinforcement unbroken in the *x*-direction:
  It is true (hence its flag = 4) if the limit crack width is bigger than double the current crack width at the corresponding point of the yield-line. The limit crack is compared to double the value of the existing crack because the central yield-

line consists of a crack width that comes from the rotation from both the slab elements from both sides of the horizontal axis of the slab.

- Diagonal yield-line reinforcement in the *x*-direction unbroken:
  True (hence the flag is given a value 8) when the limit crack width is bigger than the calculated existing crack widths in the *x*-direction.
- Diagonal yield-line reinforcement in the *y*-direction unbroken:
  True (hence the flag is given a value 16) when the limit crack width is bigger than the calculated existing crack widths in the *y*-direction.
- Case Flag:
  This flag is the sum of all the previous flags. This flag is used to check if a particular case is valid (currently in action) or not. Each case scenario has a particular configuration of intact and fractured reinforcement in order to be activated or not. For example, case (b1') at which the compression stress block is triangular and the reinforcement of the central yield-line fractured, this case is activated when only the flag of the unbroken middle yield-line reinforcement is zero (i.e. false). Therefore, if the case flag of case (b1')= 1+2+0+8+16=27, then case(b1') is currently valid and the slab is going through this case scenario at the moment. These summed numbers are the values of the all the flags, respectively. Other cases have other values in order to be valid. For example, scenario case (b1***) represents a slab with its middle yield-line reinforcement had already fractured, and its reinforcement along the diagonal yield-lines are being fractured (unzipping) in the *x* and *y* directions. Thus, for the validation flag of case (b1***) to be true, the corresponding case flag should equal 1+2+0+0+0=3.

- Validation Flag
  A particular scenario case is currently valid if the case flag takes its corresponding value. Taking the two examples which were mentioned in the case flag explanation, if the case flag occurs to equal 27, then the current case in action is certainly case (b1'), and the validation flag of this case is given the value 1, pointing out that this case is true currently. Otherwise, for other values of the case flag, the validation flag of case (b1') is zero, i.e. false. If the case flag occurs to equal 3, then the slab is going through case (b1***), and its validation flag equals 1, otherwise the validation flag equals 0 and this case is not currently

active. Duplication of active cases is not possible, and if it occurs it points out to coding or calculation error. This did not occur during this study, but if it does in any future researches, checks and corrections must be done.

According to this set of the flags for each case, monitoring the sequence of the cases that the slab went through is possible for every deflection level. Depending on the activated flags of each case, therefore the current scenario case of the analysis, the geometric parameters of the slab were calculated; like: z_1 and z_2 (i.e. the depth of the compression at the edge of the slab and at the intersection point of the yield-lines, respectively), the area of concrete compression stress blocks.

A2.2.4.3 Yield-lines crack widths

The crack widths across the yield-lines on the slab were calculated by the geometric changes as the slab deflects. These changes comprise the slab elements rotations and the horizontal movements of the elements Δx and Δy. The crack width of the central yield-line is constant, according to the yield-line theory. However, since the crack width of the diagonal yield-line has variable width, changing from its maximum at the intersection points of the yield lines and getting narrower and closing at the corners of the slab, the width of a diagonal yield line was taken at the middle of the distance which covers the intact-working reinforcement bars. This is important for the calculations of the internal work.

A2.2.4.4 Internal work

The internal work is the force multiplied by the corresponding deformation. This applied to the internal work dissipated by the concrete, reinforcement bars and the downstand steel beam.

A2.2.4.4.1 Reinforcement

The internal work of the reinforcement is the reinforcement force multiplied by the corresponding deformation. Reinforcement deformation is the extension of the reinforcement across the cracks, as explained in Chapter 5. Therefore, it is taken as the corresponding crack width, unless this crack width exceeds the limit-crack width, so

that the corresponding reinforcement bar is then considered fractured and technically out of service.

A2.2.4.4.2 The downstand steel beam

The internal work dissipated by the beam is the extension undergone by the beam under the deflection, multiplied by the tension force of the beam. This was explained in Chapter 4.

A2.2.4.4.3 Concrete

The internal work of concrete is the area of the compression stress block multiplied by the corresponding compression force. The internal work is dissipated where compression exists; therefore, it disappears when a crack opens and the slab facets widen.

A2.2.4.5 Load-capacity of the slab

Once the total internal work of the slab is calculated, the external work done by the transverse loads on the slab is worked out as the follows:

$$P = \frac{total\ internal\ work}{\delta . r . l^2 * \left(\frac{1}{2} - \frac{N}{3}\right)} \quad \text{(A.2.1)}$$

The term $\delta . r . l^2 * \left(\frac{1}{2} - \frac{N}{3}\right)$ represents the external work done by the load, divided on *p*, as derived in Section 6.2.1, Equation 73.

A2.2.4.6 Temperature enhancement

Once the slab's load capacity *P* is calculated for every deflection increment, it is compared to the applied load on the slab P_a.

If $P > P_a$, then the temperature is increased by a small-constant increment and a new loop calculates the load capacity of the slab after the strength of the unprotected steel

beam is degraded by the newly increased temperature. If the load capacity of the slab is still higher when they are compared again, the temperature is further increased, and so on. This is repeated until the load capacity of the slab degrades and equals the applied load of the slab (i.e. $P=P_a$). At this point, the temperature, which caused the load capacity of the slab degradation to the level of the applied load, is saved as the limit temperature of the current deflection level. Then, deflection is increased further, and more tensile membrane action is mobilized, allowing more strength and therefore more temperature increase. Meanwhile, the reinforcement fractures, marking temperature enhancement peaks as presented in Chapter 7, Figure 70; or even temperature enhancement degradation until no further strength can be mobilized, and the slab fails.

When $P<P_a$, and this happens once a certain set of reinforcement fractures at high temperature, the temperature is decreased until the load capacity of the slab meets the applied load, and so on. The results of these conditional statements are presented as the temperature enhancement which was presented in Chapter 7.

$P<P_a$ (i.e. the load capacity of the slab is lower than the applied load) occurs when reinforcement fractures at high temperature as the slab deflects. This tells that the slab became weaker after some of the reinforcement fractured; therefore the slab cannot withstand the applied loads at such an elevated temperature and the corresponding deflection level. The temperature is therefore reduced, so that the load capacity of the slab increases and meets the applied load level again. This temperature reduction gives the maximum temperature that the slab can withstand at the current temperature and deflection level. It should be noted that this situation (i.e. $P<P_a$) is not allowed to happen at the start of the analysis, as this is considered as an input error at which the program user entered a higher applied load than the slab can initially withstand. The program asks the user to re-enter the applied load properly so that it is within the slab's strength capacity. This error should not occur anyway, since the slab survived the applied load in the small-deflection analysis in the first place.

The detailed results of the Matlab code cannot be presented in details in this thesis. The output table is 900 x 98 lines and columns. Nonetheless, the output presentation is by no means necessary.

A2.2.5 Large-deflection analysis coding flowchart

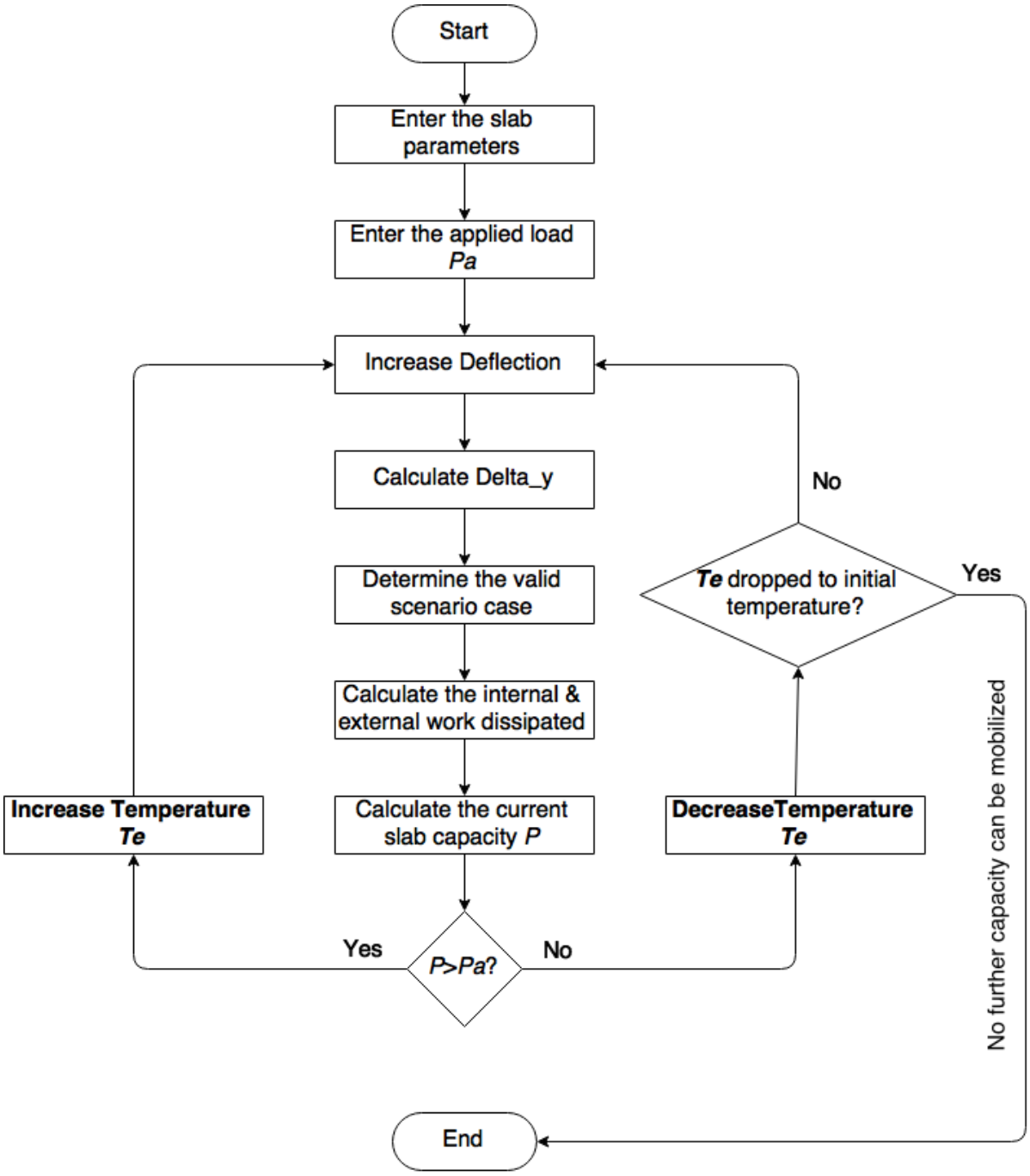

A2.2.6 Large-deflection code - Matlab

```
clear all
pa= 0.004; %0.01; %'APPLIED LOAD';
&&&&&&&&&&&&&&&&&&&&&&&&&&&&&&&&&&&&&&&&&&&&&&&&&&&&&&&&&&&&&&&&&&&&&&&&&&&&&&
&&&&&
N=0.41800;
A=4970; 'steel beam area
ha=398; 'steel beam height';

r=1.5;
l=6000;

'mm2/m , reinforcement area';
As=141.4;
sp=200; %rebar spacing
duc=5; %percent; %Ductility of rebars
fy=355; beam'
tj=400; 'initial temperature'

[p]=capacity(j); 'only to establish the load capacity empty matrix before it
is calculated.

'MPa , rebar strength';
fs=500 ;
fpx=As*fs/1000;
fpy=fpx;
mu=0.5;
t=130;
tau=t/l;
fc=35;
crk=sp*duc/100; %Crack width at yield line
dlimy=crk/l; %dlimy/l
dlimx=dlimy; %dlimy/l
'dlimx & y are dimensionless ( /l)';

gam=acos(1/(1+4*N^2)^0.5);

hc=t; 'concrete slab thickness';

ky=1;


if pa>p(1)      %This is to terminate the code if applied load is larger than
the capacity of the slab from the beginning
     warndlg('Applied Load > Slab Capacity. Change Applied Load Value','Code
Terminated')
     break
end

mainstep=0.5; %temperature raise step


for i=1:900

    tt=0 %to measure the internal loop steps
    step=mainstep;
    % tj=tj+step; stopped for now
     %p(i)=1.1*pa;

     if i==287
         tete=1
     end
```

```
     while pa;

    'Calculate the corresponding ky';
    if 20 < tj & tj < 400 ;
        ky = 1;
        elseif 400 <= tj & tj < 500 ;
        ky = 1 - 0.22 * (tj - 400) / 100;
        elseif  500 <= tj & tj < 600 ;
        ky = 0.78 - 0.31 * (tj - 500) / 100;
        elseif  600 <= tj & tj < 700 ;
        ky = 0.47 - 0.24 * (tj - 600) / 100;
        elseif  700 <= tj & tj < 800 ;
        ky = 0.23 - 0.12 * (tj - 700) / 100;
        elseif  800 <= tj & tj < 900 ;
        ky = 0.11 - 0.05 * (tj - 800) / 100;
        elseif  900 <= tj & tj < 1000 ;
        ky = 0.06 - 0.02 * (tj - 900) / 100;
        elseif  1000 <= tj & tj < 1100 ;
        ky = 0.04 - 0.02 * (tj - 1000) / 100;
        elseif  1100 <= tj & tj < 1200 ;
        ky = 0.02 - 0.02 * (tj - 1100) / 100;
        elseif  1200 <= tj
        ky = 0;
    end

%other cases include phi so they were put inside the loop

    ' ----------------------------------------------------------------Note-
1';
    if i==1
        delta(i)=0.000001;
    else
        delta(i)=0+(i/10000);
    end

    theta(i)=asin(2*delta(i)/r);
    phi(i)=asin(delta(i)/N);
    %phi(i)=asin(2*delta(i)); OLD
    delta_ry(i)=phi(i)*mu*tau;
    delta_cy(i)=phi(i)^2*0.5*N;



    'Case a1 parameters ===========';
    AB=0.5*r*l^2*fpy;
    AC=2*N*(l/r)*(fpx*0.5*l+0.5*A*ky*fy); '0.5*A*ky because half of the beam
is taken - half a beam included in the considered quarter section of the slab
';
    AD=N*l^3*fc*((-N/r)+2*(N^2/r)-(N/(4*sin(gam)*cos(gam)))) ;
    AE=fc*l^3*(2*(N/r)-4*(N^2/r)+N/(sin(gam)*cos(gam))) ;

    'Case b1 parameters ===========';
    b1a=fpy*0.5*r*l^2+fpx*l^2*N/r+(0.5*A*ky*fy)*l*2*N/r;
    b1b=sin(gam)*cos(gam);
    b1c=fc*l^3;

    'Case b1p (b1 prime) parameters ===========';
    b1pa=(0.5*fpy*r*l^2)+(fpx*2*N^2*l^2/r)+(0.5*A*ky*fy*l*2*N/r);
    b1pb=b1b;
    b1pc=b1c;

    'Case b1t (b1* star) parameters ===========';
    b1ta(i)=fc*l^3/(phi(i)^3*sin(gam)*cos(gam));
```

```
    b1tb(i)=-fpy*r*l^2/(N*phi(i)^2);
    b1tc(i)=-((fpy*r*l^2*dlimy/(N*phi(i)^2))-
(fpy*r*l^2*mu*tau/(N*phi(i)))+(N*l^2*fpx/r)+(2*N*l*0.5*A*ky*fy/r));

    'Case b1pt (b1 prime-star) parameters ==========';
    b1pta(i)=fc*l^3/(phi(i)^3*sin(gam)*cos(gam));
    b1ptb(i)=-fpy*r*l^2/(N*phi(i)^2);
    b1ptc(i)=-(dlimy*(fpy*r*l^2/(N*phi(i)^2))-
(mu*tau*fpy*r*l^2/(N*phi(i)))+(2*N^2*l^2*fpx/r)+(2*N*l*0.5*A*ky*fy/r));

    'Case b1tt (b1 prime-Double star) parameters ==========';
    b1tta(i)= fc*l^3/(phi(i)^3*sin(gam)*cos(gam));
    b1ttb(i)= -4*N*l^2*fpx/(r*phi(i)^2);
    b1ttc(i)= -(((fpy*0.5*r*l^2)+2*l^2*fpx*dlimx/(phi(i)^2))-
(4*fpx*N*l^2*mu*tau/(r*phi(i)))+2*N*l*0.5*A*ky*fy/r);

    'Case b1tr (b1 Triple-star) parameters ==========';
    b1tra(i)= fc*l^3/(phi(i)^3*sin(gam)*cos(gam));
    b1trb(i)= -((fpy*r*l^2/(N*phi(i)^2))+(4*fpx*N*l^2/(r*phi(i)^2)));
    b1trc(i)= -(fpy*r*l^2*(((dlimy/phi(i))-
mu*tau)/(N*phi(i)))+(4*N*l^2*fpx*((dlimx*r/(phi(i)*2*N))-
mu*tau)/(r*phi(i)))+(2*N*l*0.5*A*ky*fy/r));

    'Case b2 parameters ================================';
    b2a(i)=fc*l^3/(phi(i)^3*sin(gam)*cos(gam));
    b2b(i)=(fpy*r*l^2/(N*phi(i)^2))+(4*fpx*N*l^2/(r*phi(i)^2));
    b2c(i)=-
(fpy*0.5*r*l^2+fpy*r*l^2*mu*tau/(N*phi(i))+(fpx*N*l^2/r)+(4*fpx*N*l^2*mu*tau/(
r*phi(i)))+2*N*l*0.5*A*ky*fy/r);

    %----------- Delta_y for each case-------------

    deltay_a1(i)=((phi(i)*AB)+(phi(i)*AC)-(phi(i)^2*AD))/AE; 'Delta y/l - case
a1 --------------';

    if delta(i)==0.0274
        aaa=1;
    end
    'checkings for a1 case';

     'rebars checks';
    'compr above rebar';
    if deltay_a1(i)<delta_ry(i);
        abva1(i)=1;
    else;
        abva1(i)=0;
    end;

    'compr in mid y-l';
    if deltay_a1(i)>delta_cy(i);
        mid_yla1(i)=2;
    else;
        mid_yla1(i)=0;
    end;

    'mid y-l x rebars unbroken'; '2*--- because movement occurs on two sides';
    if dlimx>(2*((2*N)/r)^+1*(delta_ry(i)+delta_cy(i)-deltay_a1(i)));
'1/tan(gam) because here it is about x and y rebars on x and y directions';
        miduna1(i)=4;
    else;
        miduna1(i)=0;
    end
```

```
    'diagonal-x y-l unbroken - CHECK tg RELATION - last update against
normal';
    if dlimx>((2*N)/r)^1*(delta_ry(i)+delta_cy(i)-deltay_a1(i));
        diag_xa1(i)=8;
    else;
        diag_xa1(i)=0;
    end;

    'diag-y y-l unbroken';
    if dlimy>(delta_ry(i)+delta_cy(i)-deltay_a1(i));
        diag_ya1(i)=16;
    else;
        diag_ya1(i)=0;
    end;

    a1flag(i)=abva1(i)+mid_yla1(i)+miduna1(i)+diag_xa1(i)+diag_ya1(i);

    'validate a1 flags';
    if a1flag(i)>30;
        valid_a1(i)=1;
    else;
        valid_a1(i)=0;
    end

    use_a1(i)=deltay_a1(i)*valid_a1(i); 'Usable a1 cases (only a1 so far) -
refere to BP45'; 'TO BE EXTENDED FOR OTHER a1s';

    deltay_b1(i)=sqrt((b1a*phi(i)^3*b1b)/b1c); 'Delta y/l - case b1----------
-------------------------';

    'Checkings for b1 case';
    'rebars checks';
    'compr above rebar';
    if deltay_b1(i)<delta_ry(i);
        abvb1(i)=1;
    else;
        abvb1(i)=0;
    end;

     'compr in mid y-l';
    if deltay_b1(i)<delta_cy(i);
        mid_ylb1(i)=2;
    else;
        mid_ylb1(i)=0;
    end;

    'mid y-l unbroken'; '';
    if dlimx>(2*((2*N)/r)^1*(delta_ry(i)+delta_cy(i)-deltay_b1(i))); '2*---
because movement occurs on two sides'; '1/tan(gam) because here it is about x
and y rebars on x and y directions';
        midunb1(i)=4;
    else;
        midunb1(i)=0;
    end

    'diagonal-x y-l unbroken - CHECK tg RELATION';
    if dlimx>((2*N)/r)^1*(delta_ry(i)+delta_cy(i)-deltay_b1(i));
        diag_xb1(i)=8;
    else;
        diag_xb1(i)=0;
    end;

    'diag-y y-l unbroken';
    if dlimy>(delta_ry(i)+delta_cy(i)-deltay_b1(i));
```

```
        diag_yb1(i)=16;
    else;
        diag_yb1(i)=0;
    end;
    b1flag(i)=abvb1(i)+mid_ylb1(i)+midunb1(i)+diag_xb1(i)+diag_yb1(i);

    'validate b1 flags';
    if b1flag(i)==31;
        valid_b1(i)=1;
    else;
        valid_b1(i)=0;
    end


    deltay_b1p(i)=sqrt(b1pa*b1pb*phi(i)^3/b1pc); 'Delta y/l - case b1 prime---
-----------------------------------';

    'Checkings for b1 case';
    'rebars checks';
    'compr above rebar';
    if deltay_b1p(i)<delta_ry(i);
        abvb1p(i)=1;
    else;
        abvb1p(i)=0;
    end;

    'compr in mid y-l';
    if deltay_b1p(i)<delta_cy(i);
        mid_ylb1p(i)=2;
    else;
        mid_ylb1p(i)=0;
    end;

    'mid y-l unbroken';
    if dlimx>(2*((2*N)/r)^1*(delta_ry(i)+delta_cy(i)-deltay_b1(i))); because
here it is about x and y rebars on x and y directions';
        midunb1p(i)=4;
    else;
        midunb1p(i)=0;
    end

    'diagonal-x y-l unbroken';
    if dlimx>((2*N)/r)^1*(delta_ry(i)+delta_cy(i)-deltay_b1p(i));
        diag_xb1p(i)=8;
    else;
        diag_xb1p(i)=0;
    end;

     'diag-y y-l unbroken';
    if dlimy>(delta_ry(i)+delta_cy(i)-deltay_b1p(i));
        diag_yb1p(i)=16;
    else;
        diag_yb1p(i)=0;
    end;

     b1pflag(i)=abvb1p(i)+mid_ylb1p(i)+midunb1p(i)+diag_xb1p(i)+diag_yb1p(i);

     'validate b1p flags';
    if b1pflag(i)==27;
        valid_b1p(i)=1;
    else;
        valid_b1p(i)=0;
    end
```

```
    deltay_b1t(i)=(-b1tb(i)+sqrt((b1tb(i)^2-4*b1ta(i)*b1tc(i))))/(2*b1ta(i));
'Delta y/l - case b1 star ----------------------------';

     'Checkings for b1* case';
    'rebars checks';
    'compr above rebar';
    if deltay_b1t(i)<delta_ry(i);
        abvb1t(i)=1;
    else;
        abvb1t(i)=0;
    end;

     'compr in mid y-l';
    if deltay_b1t(i)<delta_cy(i);
        mid_ylb1t(i)=2;
    else;
        mid_ylb1t(i)=0;
    end;

    'mid y-l unbroken';
    if dlimx>(2*((2*N)/r)^1*(delta_ry(i)+delta_cy(i)-deltay_b1t(i)));
midunb1t(i)=4;
    else;
        midunb1t(i)=0;
    end

     'diagonal-x y-l unbroken';
    if dlimx>((2*N)/r)^1*(delta_ry(i)+delta_cy(i)-deltay_b1t(i));
        diag_xb1t(i)=8;
    else;
        diag_xb1t(i)=0;
    end;

      'diag-y y-l unbroken';
    if dlimy>(delta_ry(i)+delta_cy(i)-deltay_b1t(i));
        diag_yb1t(i)=16;
    else;
        diag_yb1t(i)=0;
    end;

     b1tflag(i)=abvb1t(i)+mid_ylb1t(i)+midunb1t(i)+diag_xb1t(i)+diag_yb1t(i);

      'validate b1t flags';
    if b1tflag(i)==15;
        valid_b1t(i)=1;
    else;
        valid_b1t(i)=0;
    end

    deltay_b1pt(i)=(-b1ptb(i)+sqrt((b1ptb(i)^2-
4*b1pta(i)*b1ptc(i))))/(2*b1pta(i));  'Delta y/l - case b1 prime-star --------
----------------------------';

    'Checkings for b1 prime-star case';
    'rebars checks';
    'compr above rebar';
    if deltay_b1pt(i)<delta_ry(i);
        abvb1pt(i)=1;
    else;
        abvb1pt(i)=0;
    end;

    'compr in mid y-l';
    if deltay_b1pt(i)<delta_cy(i);
```

```
        mid_ylb1pt(i)=2;
    else;
        mid_ylb1pt(i)=0;
    end;

    'mid y-l unbroken';
    if dlimx>(2*((2*N)/r)^1*(delta_ry(i)+delta_cy(i)-deltay_b1pt(i)));
        midunb1pt(i)=4;
    else;
        midunb1pt(i)=0;
    end

      'diagonal-x y-l unbroken';
    if dlimx>((2*N)/r)^1*(delta_ry(i)+delta_cy(i)-deltay_b1pt(i));
        diag_xb1pt(i)=8;
    else;
        diag_xb1pt(i)=0;
    end;


     'diag-y y-l unbroken';
    if dlimy>(delta_ry(i)+delta_cy(i)-deltay_b1pt(i));
        diag_yb1pt(i)=16;
    else;
        diag_yb1pt(i)=0;
    end;


b1ptflag(i)=abvb1pt(i)+mid_ylb1pt(i)+midunb1pt(i)+diag_xb1pt(i)+diag_yb1pt(i);

     'validate b1pt flags';
    if b1ptflag(i)==11;
        valid_b1pt(i)=1;
    else;
        valid_b1pt(i)=0;
    end


    deltay_b1tt(i)=(-b1ttb(i)+sqrt((b1ttb(i)^2-
4*b1tta(i)*b1ttc(i))))/(2*b1tta(i));   'Delta y/l - case b1-Double Star ------
--------------------------------';

    'Checkings for b1 Double-star case';
    'rebars checks';
    'compr above rebar';
    if deltay_b1tt(i)<delta_ry(i);
        abvb1tt(i)=1;
    else;
        abvb1tt(i)=0;
    end;

    'compr in mid y-l';
    if deltay_b1tt(i)<delta_cy(i);
        mid_ylb1tt(i)=2;
    else;
        mid_ylb1tt(i)=0;
    end;

     'mid y-l unbroken';
    if dlimx>(2*((2*N)/r)^1*(delta_ry(i)+delta_cy(i)-deltay_b1tt(i)));
midunb1tt(i)=4;
    else;
        midunb1tt(i)=0;
    end
```

```
      'diagonal-x y-l unbroken';
    if dlimx>(((2*N)/r)^1)*(delta_ry(i)+delta_cy(i)-deltay_b1tt(i));
        diag_xb1tt(i)=8;
    else;
        diag_xb1tt(i)=0;
    end;

     'diag-y y-l unbroken';
     aatt(i)=(delta_ry(i)+delta_cy(i)-deltay_b1tt(i));
    if dlimy>(delta_ry(i)+delta_cy(i)-deltay_b1tt(i));
        diag_yb1tt(i)=16;
    else;
        diag_yb1tt(i)=0;
    end;


b1ttflag(i)=abvb1tt(i)+mid_ylb1tt(i)+midunb1tt(i)+diag_xb1tt(i)+diag_yb1tt(i);

     'validate b1tt flags';
    if b1ttflag(i)==19;
        valid_b1tt(i)=1;
    else;
        valid_b1tt(i)=0;
    end


     deltay_b1tr(i)=(-b1trb(i)+sqrt((b1trb(i)^2-
4*b1tra(i)*b1trc(i))))/(2*b1tra(i));   'Delta y/l - case b1-Triple Star ------
--------------------------------';

      'Checkings for b1 Triple-star case';
    'rebars checks';
    'compr above rebar';
    if deltay_b1tr(i)<delta_ry(i);
        abvb1tr(i)=1;
    else;
        abvb1tr(i)=0;
    end;

        'compr in mid y-l';
    if deltay_b1tr(i)<delta_cy(i);
        mid_ylb1tr(i)=2;
    else;
        mid_ylb1tr(i)=0;
    end;

        'mid y-l unbroken';
    if dlimx>(2*((2*N)/r)^1*(delta_ry(i)+delta_cy(i)-deltay_b1tr(i)));
midunb1tr(i)=4;
    else;
        midunb1tr(i)=0;
    end

       'diagonal-x y-l unbroken';
    if dlimx>((2*N)/r)^1*(delta_ry(i)+delta_cy(i)-deltay_b1tr(i));
        diag_xb1tr(i)=8;
    else;
        diag_xb1tr(i)=0;
    end;

     'diag-y y-l unbroken';
    if dlimy>(delta_ry(i)+delta_cy(i)-deltay_b1tr(i));
        diag_yb1tr(i)=16;
```

```
    else;
        diag_yb1tr(i)=0;
    end;


b1trflag(i)=abvb1tr(i)+mid_ylb1tr(i)+midunb1tr(i)+diag_xb1tr(i)+diag_yb1tr(i);

     'validate b1tr flags';
    if b1trflag(i)==3;
        valid_b1tr(i)=1;
    else;
        valid_b1tr(i)=0;
    end

    deltay_b2(i)=(-b2b(i)+sqrt((b2b(i)^2-4*b2a(i)*b2c(i))))/(2*b2a(i));
'Delta y/l - case b2 ----------------------------------------';

    'Checkings for b2 case';
    'rebars checks';
    'compr BELOW rebar';
    if deltay_b2(i)>delta_ry(i);
        belb2(i)=1;
    else;
        belb2(i)=0;
    end;

    'compr in mid y-l';
    if deltay_b2(i)<delta_cy(i);
        mid_ylb2(i)=2;
    else;
        mid_ylb2(i)=0;
    end;

     'mid y-l unbroken';
    if dlimx>(2*((2*N)/r)^1*(delta_ry(i)+delta_cy(i)-deltay_b2(i)));
midunb2(i)=4;
    else;
        midunb2(i)=0;
    end

     'diagonal-x y-l unbroken';
    if dlimx>((2*N)/r)^1*(delta_ry(i)+delta_cy(i)-deltay_b2(i));
        diag_xb2(i)=8;
    else;
        diag_xb2(i)=0;
    end;

    'diag-y y-l unbroken';
    if dlimy>(delta_ry(i)+delta_cy(i)-deltay_b2(i));
        diag_yb2(i)=16;
    else;
        diag_yb2(i)=0;
    end;

    'comp abv bottom';
    if deltay_b2(i)<phi(i)*tau
        abvb2(i)=32;
    else
        abvb2(i)=0;
    end


b2flag(i)=belb2(i)+mid_ylb2(i)+midunb2(i)+diag_xb2(i)+diag_yb2(i)+abvb2(i);
```

```
      'validate b2 flags';
    if b2flag(i)==63;
        valid_b2(i)=1;
    else;
        valid_b2(i)=0;
    end



use_b1(i)=deltay_b1(i)*valid_b1(i)+deltay_b1p(i)*valid_b1p(i)+deltay_b1t(i)*va
lid_b1t(i)+deltay_b1pt(i)*valid_b1pt(i)+deltay_b1tt(i)*valid_b1tt(i)+deltay_b1
tr(i)*valid_b1tr(i); 'Usable ALL b1 cases (combination)'

    'case a1 flag - ALL a1 CASES';
    ca_a1f(i)=a1flag(i)*valid_a1(i); 'All a1 cases';

    'case b1 flag - ALL b1 CASES (b1 & b1 prime)';

ca_b1f(i)=b1flag(i)*valid_b1(i)+b1pflag(i)*valid_b1p(i)+b1tflag(i)*valid_b1t(i
)+b1ptflag(i)*valid_b1pt(i)+b1ttflag(i)*valid_b1tt(i)+b1trflag(i)*valid_b1tr(i
); 'All b1 cases';



    'CASE FLAG'; 'MT';    if ca_a1f(i)>0;
        flag(i)=1;
    elseif ca_b1f(i)>0;
        flag(i)=3;
    else;
        flag(i)=0;
    end


    if flag(i)==1 'in case a1';
        z1(i)=(use_a1(i))/phi(i); 'z1/l';
        z2(i)=((use_a1(i))/phi(i))-0.5*N*phi(i); 'z2/l';

    elseif flag(i)==3 'in case b1';
        z1(i)=(use_b1(i))/phi(i); 'z1/l';
        z2(i)=0;

    else
        z1(i)=0;
        z2(i)=0;

    end


    if flag(i)==1
        A1x(i)=(z1(i)+z2(i))*0.5*N; 'A1x/l^2';
        A2x(i)=(0.5-N)*z2(i); 'A2x/l^2';
    elseif flag(i)==3
        A1x(i)=use_b1(i)^2/phi(i)^3; 'A1x/l^2';
        A2x(i)=0; 'A2x/l^2';
    end

     'FINAL DELTA_Y/L';
    if flag(i)==1 'case a1';
        use_dy(i)= use_a1(i);
    elseif flag(i)==3 'cases b1 (All b1 cases)';
        use_dy(i)=use_b1(i);
    else;
        error_cases_finished=1;
```

```
        break
    end

    'Final Delta Y after having multiplied by l';
    dyl(i)= use_dy(i)*l;


    'FORCES';
    C(i)=A1x(i)*fc*l^2/sin(gam);
    Cx2(i)=A2x(i)*fc*l^2;

    if (2/phi(i)^2)*(use_dy(i)+(dlimx/(2*N/r))-phi(i)*mu*tau)> N;
        ylim(i)=N;
    'ylim/l';

    else;
        ylim(i)=(2/phi(i)^2)*(use_dy(i)+(dlimx/(2*N/r))-phi(i)*mu*tau);

    end;

    if flag(i)>0 & flag(i)<2; 'case a1 & b1 Cases';
        YT(i)=0;
    elseif flag(i) >2 & flag(i)<4; 'b1 CASES';
        YT(i)=0;
    else
        YT(i)=0;
    end

    Tx1(i)=(ylim(i)-YT(i))*fpx*l;

    if (r/(N*phi(i)^2))*(use_dy(i)+dlimy-phi(i)*mu*tau)>0.5*r;
        xlim(i)=0.5*r;
         'xlim/l';
    else;
        xlim(i)=(r/(N*phi(i)^2))*(use_dy(i)+dlimy-phi(i)*mu*tau);
    end

     if flag(i)>0 & flag(i)<2; 'case a1';
         XT(i)=0;
     elseif flag(i)>2 & flag(i)<4 'b1 CASES';
         XT(i)=0;
     else
         XT(i)=0;
     end


    miduna1s(i)=miduna1(i)*valid_a1(i); 'Middle y-l x-rebar intact for a1
cases
midunb1s(i)=midunb1(i)*valid_b1(i)+midunb1p(i)*valid_b1p(i)+midunb1t(i)*valid_
b1t(i)+midunb1pt(i)*valid_b1pt(i)+midunb1tt(i)*valid_b1tt(i)+midunb1tr(i)*vali
d_b1tr(i); 'Middle y-l x-rebar intact for ALL b1 CASES (b1 & b1 prime)' ;

    'Eventual middle y-l x-rebar intact'; 'account for a1 &b1 &b1 prime';
         Mid_yl(i)= (miduna1s(i)+midunb1s(i))/4;

        'for cases a1 & b1';
    Ty1(i)=(xlim(i)-XT(i))*fpx*l;

    'Flags check for the mid y-l unbroken';

    Tx2(i)=l*(0.5-N)*fpx*Mid_yl(i); 'Tx2 exists as long Mid_yl, the eventual
Mid yl rebars, is unbroken';
    'CASES';
```

```
    Tb(i)=nu*A*ky*fy;


   Z1(i)=z1(i)*l;
   Z2(i)=z2(i)*l;

   if flag(i)==1; 'Y_ca1/l case a1';
    Y_ca1(i)=N^2*(z1(i)+2*z2(i))/(6*A1x(i));  %A1x is actually A1x/l^2
   elseif flag(i)==3 'case b1 & b1 prime';
       Y_ca1(i)= (2/3)*use_dy(i)/phi(i)^2;

   else
       Y_ca1(i)= 0; 'CASE NOT FOUND YET. WILL WORK ON IT LATER';
   end
    Z_ca(i)=0.5*(Z1(i)*(1-Y_ca1(i))+Z2(i)*Y_ca1(i));
    dy_ca(i)=dyl(i)-phi(i)*Z_ca(i)-0.5*(phi(i)^2)*Y_ca1(i)*l; 'alpha';
    dely(i)=-(dyl(i)-phi(i)*mu*(tau*l)-0.5*phi(i)^2*0.5*l*(ylim(i)+YT(i)));
'alpha';
    dx_ca(i)= dy_ca(i)*2*N/r; 'alpha';
    delx(i)=-(dyl(i)*(2*N)/r-phi(i)*mu*(tau*l)*2*N/r-
0.5*(phi(i)*2*N/r)^2*0.5*l*(ylim(i)+YT(i))); 'alpha';    dcx2(i)=dyl(i)*2*N/r-
phi(i)*(2*N)/r*Z2(i)/2-0.5*(phi(i)*2*N/r)^2*0.5*r*l; 'Beta'
dsx2(i)= -(dyl(i)*2*N/r-phi(i)*(2*N/r)*mu*(tau*l)-0.5*(phi(i)*2*N/r)^2*r*l/2);
' Beta';


    xc(i)=dyl(i)/theta(i);
    x(i)=(mu*t-xc(i))*cos(phi(i)*2*N/r); 'geometry parameter';
    L(i)=(hc-xc(i)+0.5*ha)*cos(phi(i)*2*N/r); 'geometry parameter';

    if xc(i)==0
        error_xc=1;
    end

    dbeam(i)=dely(i)*L(i)/x(i); 'Delta Beam';
'>>>>>>>>>>>>>>>>>>>>>>>>>>>>>>>>>>>>>>>>>>>>>>>>>>>>>>>>>>>>>>>>>>>';

    'INTERNAL WORK';
    iwC(i)=4*(C(i)*sin(gam)*dx_ca(i)+C(i)*cos(gam)*dy_ca(i)); 'force c1';
    iwTx1(i)=4*Tx1(i)*delx(i); 'force Tx1';
    iwTy1(i)=4*Ty1(i)*dely(i); 'force Ty1';
    iwTx2(i)=4*Tx2(i)*dsx2(i); 'force Ty2';
    iwCx2(i)=4*Cx2(i)*dcx2(i); 'force Cx2';
    iwb(i)=dbeam(i)*A*fy*ky; 'Beams';
    totiw(i)=iwC(i)+iwTx1(i)+iwTy1(i)+iwTx2(i)+iwCx2(i)+iwb(i); 'Total
Internal work';

    'External Work P';
    delta_A(i)=delta(i)*l; 'delta_A';
    EWP(i)=delta_A(i)*r*l^2*(0.5-N/3); 'the external work p';

    'Capacity';
    p(i)=totiw(i)/EWP(i);

    'Enhancement'; %This is only load capacity enhancement. It is a flat line
equals one
    e(i)=p(i)/pa;

    pi=p(i);


    if p(i)>pa
        step=mainstep
            tj=tj+step;
```

```
    elseif p(i)<pa
        step=mainstep*0.5;
            tj=tj-step;
    end

    pp=abs(pa-p(i)); %to measure how much p is away from pa
    tt=tt+1 %to measure how many internal steps within "while" loop

   k(i)=ky;
   cep=0.003; %Circle of Error Probable for how much p should be close to pa
   pcep=cep*pa;
    if abs(pa-p(i))<=cep*pa
    Temp(i)=tj;

        break
    end

    %This is to avoid big shift differences.
if tt>1000
    tata=1;
end

    if tt>5000
        Temp(i)=tj;
        %tt_break=tt_break+1;
        tete=1
        break
    end

    if tj>1199
        break
    elseif tj<400
        error_Temp=1;
        break
    end

     end

      if error_cases_finished==1
         break
      end

   if tj>1199

        break
         elseif tj<400
        error_Temp=2;
         break
    end
   sss=1+1;

end

if error_cases_finished==1
     warndlg('Programmed cases finished','Code Terminated')
     break
end

%Final Matrix
z_mat=[delta' phi' delta_ry' delta_cy' deltay_a1' abva1' mid_yla1' miduna1'
diag_xa1' diag_ya1' a1flag' valid_a1' z1' z2' A1x' A2x' ...
    use_a1'  deltay_b1' abvb1'  mid_ylb1' midunb1' diag_xb1' diag_yb1' b1flag'
valid_b1' deltay_b1p' abvb1p' mid_ylb1p' midunb1p' ...
```

```
    diag_xb1p' diag_yb1p' b1pflag' valid_b1p' deltay_b1t' abvb1t' mid_ylb1t'
midunb1t' diag_xb1t' diag_yb1t' b1tflag' valid_b1t' ...
    deltay_b1pt' abvb1pt' mid_ylb1pt' midunb1pt' diag_xb1pt' diag_yb1pt'
b1ptflag' valid_b1pt' deltay_b1tt' abvb1tt' mid_ylb1tt' ...
    midunb1tt' diag_xb1tt' diag_yb1tt' b1ttflag' valid_b1tt' deltay_b1tr'
abvb1tr' mid_ylb1tr' midunb1tr' diag_xb1tr' diag_yb1tr' b1trflag' valid_b1tr'
flag' ...
    C' Cx2' xlim' ylim' XT' YT' Tx1' Ty1' Tx2' Tb' use_dy' dyl' Y_ca1' Z_ca'
dx_ca' dy_ca' delx' ...
    dely' dcx2' dsx2' iwC' iwTx1' iwTy1' iwTx2' iwCx2' iwb' totiw' delta_A'
EWP' p' Temp' e'];
```

Appendix 3

A3 Pull Out Test of Small-Diameter Reinforcement

A3.1 The purpose of the test

Plenty of pull-out tests were conducted to study the bond-slip behaviour of reinforced concrete elements in structures. However, almost all of these tests studied the behaviour of bars that far exceed the diameters used in composite slabs. The reinforcement used in composite slabs is anti-cracking mesh, which is usually 6mm in diameter. Thus, the bond behaviour of such small diameter bars differ than normal ones with diameter of 14mm or larger.

The other important factor which is important to examine is the bond-slip behaviour at elevated temperatures. In fire, slabs are subjected to high temperatures. When the slab cracks and these cracks widen to certain extent, the temperature affects the reinforcement bars. At such high temperatures, bond behaviour is not supposed to be the same as it is at ambient temperature.

In order to study the bond-slip behaviour of small-diameter reinforcement, a new pull out test should be conducted. Such a test aims to examine the bond behaviour of a cylindrical concrete specimen, reinforced with a single reinforcement bar of a diameter of 6mm, subjected to high temperature. Applying pull-out forces from both sides until the fracture of the bar is a proper method to simulate the tension force on the bar.

A3.2 Test specimens

Since the used reinforcement bar is small in diameter (6mm), the important aspect of the test is to observe if such a reinforcement bar fractures in a brittle manner, or if it pulls out smoothly. For this purpose, two types of failure should be considered:

- The concrete cracks before the reinforcement bar fractures. The bar is then in pure tension.
- The reinforcement bar fractures while it is still embedded in concrete before the latter cracks.

Therefore, two specimens should be tested in order to simulate both the types. Specimens should comprise the following:

1. A Specimen with a split in the middle which simulates cracked concrete and an exposed reinforcement bar.
2. A Normal specimen at which the reinforcement is embedded in concrete; with a notch in the middle of the specimen in order to control the failure mode. In this case, concrete should fracture at the notch.

Figure 83 shows both types of specimens; Specimen (a) with a notch, and specimen (b) with a split in the middle.

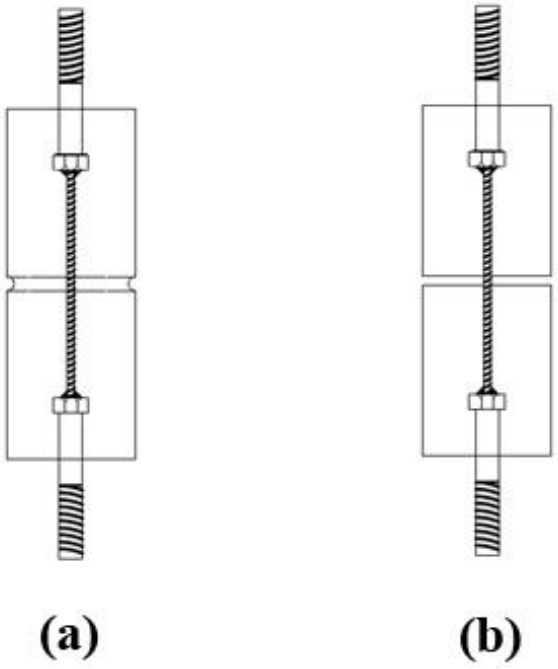

Figure 83: (a) Specimen with notch; (b) Specimen with a split in the middle

Both specimens are cylindrical with a reinforcement bar which has a diameter of 6mm. The rebar (in both specimens) is welded from both sides to M20 bolts as shown in Figure 84. These bolts are used to anchor the specimens to the pull out test machine in order to apply the pull-out forces.

A3.3 Specimens design

It is important that the specimens fail at the middle of their cylindrical body, not at the area of their bases. In other words, the specimens should not fail around the bolts washers where the concrete cross-section is smaller than the rest of the specimen's body. Failure should be due to slip after the bond was lost and the concrete cracked in case of specimen (a). Hence, the specimens should fail in the middle, away from their bases. To prevent an unwanted failure mode, some calculations should be done in order to make sure that the test goes as planned, allowing the desired observation.

The reinforcement bars that are used in this test have a yield strength of 460MPa. Since the design is aimed to study the actual behaviour for scientific purposes (not commercial design), the actual yield strength, rather than the factored strength, should be considered. This is estimated by 1.3 times the commercially declared strength (460MPa), as it is recommended by technicians.

A3.3.1 Specimen specifications

Figure 84 shows the dimensions of the specimen before customizing it with a notch or a split in the middle.

Rebar diameter: 6mm. Specimen diameter: 100mm (cylindrical). Bolts used: M20

Rebar cross section area

$$A_s = \frac{\pi . 6^2}{4} = 28.3mm^2$$

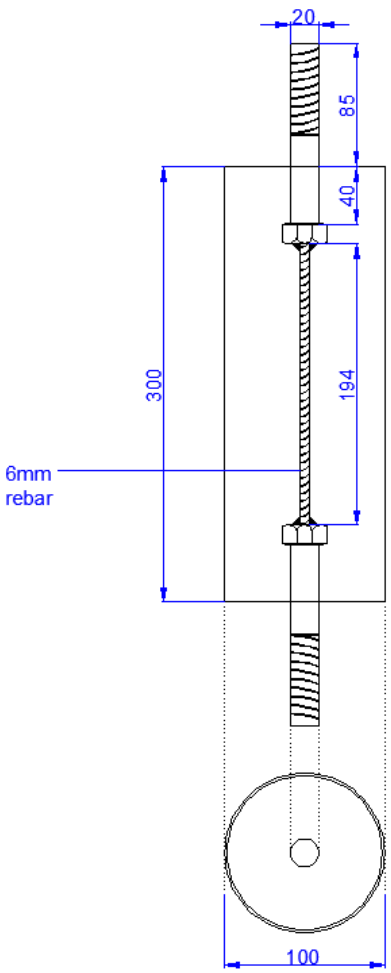

Figure 84: Specimen dimensions

Maximum force the bar can take:

$$F = f_p . A_s = 1.3 * 460 * 28.3 \approx 17000N$$

Concrete Tensile Strength:

According to EN 1992-1-1

$$f_{ctm}(t_i) = [\beta_{cc(t)}]^{\alpha_i} * f_{ctm}$$

$$f_{ctm} = 0.3 * f_c^{\frac{2}{3}} \approx 2.9MPa$$

Where: f_{ctm} is the mean axial tensile strength of concrete

$t_i < 28$ days → $\alpha_i=1$

$t_i \geq 28$ days → $\alpha_i=2/3$

$$\beta_{cc}(t_i) = e^{s_s.\left[1-\left(\frac{28}{t_i}\right)^{0.5}\right]} = 0.778$$

$$\rightarrow f_{ctm}(t_i) = 0.778 * 2.9 = 2.25MPa$$

Notch Design (The Second Specimen)

The notch around the specimen is intended to guarantee the failure of the specimen occurs at the middle of the specimen's body, rather than breaking around the bolts washer. A cross-section area reduction of 36mm leaves the specimen with a diameter of 65mm at the notch.

Concrete cross-section area at the notch:

$$A_{nc} = \frac{\pi.65^2}{4} - 28.3 = 3290mm$$

Where: 65 is the radios of the concrete at the notch

28 is the area of the 6mm-reinforcement bar

Notch breaks at a force of:

$$\frac{F}{3290} = 7419N$$

The stress of the bar at this point = 7419/28.3=262.2MPa

Concrete Tensile Strength around the Bolt

The area of the bolts head occupies space within the specimen. This means that the net concrete cross-section around the bolt's head is smaller than the rest of the specimen. Concrete tensile strength at that area should be checked in order to prevent tensile failure near the bolt's head. Figure 85 shows this area around the bolt's head.

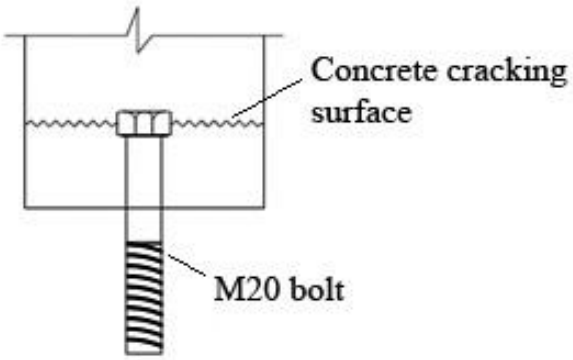

Figure 85: The base of the specimen with the net concrete area around the bolt's head

Concrete area around the bolt:

$$A_c = \frac{\pi.100^2}{4} - \frac{\pi.30^2}{4} = 7147mm^2$$

Maximum force applied = 7419MPa

$$\frac{7419}{7147} = 1.03MPa < 2.25MPa$$

Since the maximum stress at this area is smaller than the concrete mean tensile strength, the concrete does not fail in tension around the bolt's head.

Bolt embedded length (h):

When the tension force is applied, the bolts tend to pull out of the concrete, tending to pull concrete cone out of the specimen. The concrete cone cracks in an angle of 45^o as Figure 86 shows.

To prevent the formation of pull-out cones at each end of the specimen, a minimum embedded length of the bolt should be satisfied.

The force which is needed to pull out the bolt is equal to the concrete tensile strength multiplied by the lateral surface area of the pull-out cone L_a.

$$f = f_{ctm} * L_a$$

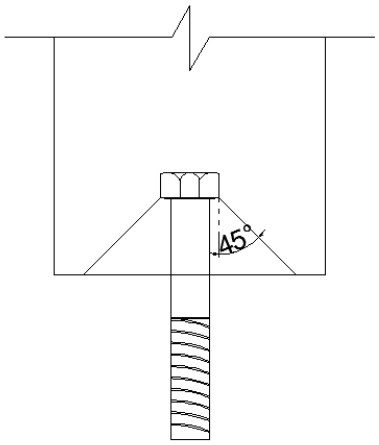

Figure 86: Concrete pull-out cone in 45° angle

Lateral surface area of the concrete frustum:

$$L_a = \pi.(r1 + r2) * \sqrt{(r1 - r2)^2 + (h_e)^2}$$

Where: r_1 and r_2 are the small and big bases of the frustum, respectively

h_e is the height of the frustum

$F=17000=2.25 \,.\, L_a$

$\rightarrow La=7522mm$

This is the minimum lateral surface area of the frustum necessary to keep the bolt embedded in the concrete.

To make sure the bolt will not be pulled out, h is taken 40mm.

A3.4 Loading rate

The tension-loading rate which is applied to the specimens is calculated by the following equation, as suggested by many other pull-out tests:

$$V_p = 0.56\,.\,(d_s)^2$$

Where, d_s is the diameter of the reinforcement bar.

$V_p = 0.56*6^2 = 20\ N/sec$

A3.5 Tests results

A3.5.1 First specimen – with the split

The first specimen is the one which has a split in the middle. This split simulates a crack that widened, leaving the reinforcement bar to be exposed to elevated temperatures. The result of the first specimen tests is shown in Figure 87.

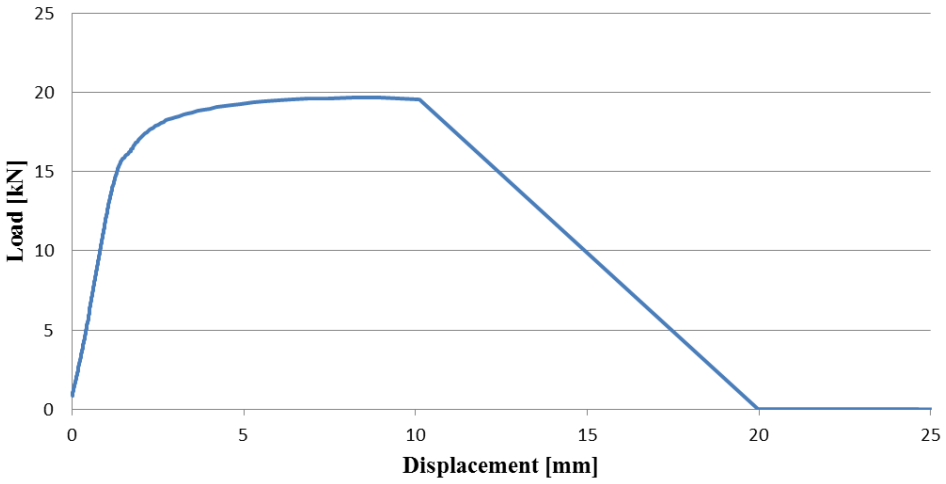

Figure 87: Load vs. displacement for the first specimen, with split

The first specimen went slightly higher in resistance than it was expected. This is mainly because of the extra safety factor of the reinforcement bar which took a larger load than what was believed to be the unfactored strength.

A3.5.2 Second specimen – with the notch

Unfortunately, the second specimen test did not go as planned. The base of the specimen broke before reaching the failure load in a brittle manner. Load vs. displacement data of the second specimen is presented in Figure 88. The base of the

specimen broke due to rebar-bolt detachment, although the same base design was used in the first specimen, which took even a higher load than what was expected. Therefore, the reason for this base failure is due to flawed welding between the reinforcement bar and the bolt. This flaw welding caused the detachment in a brittle manner.

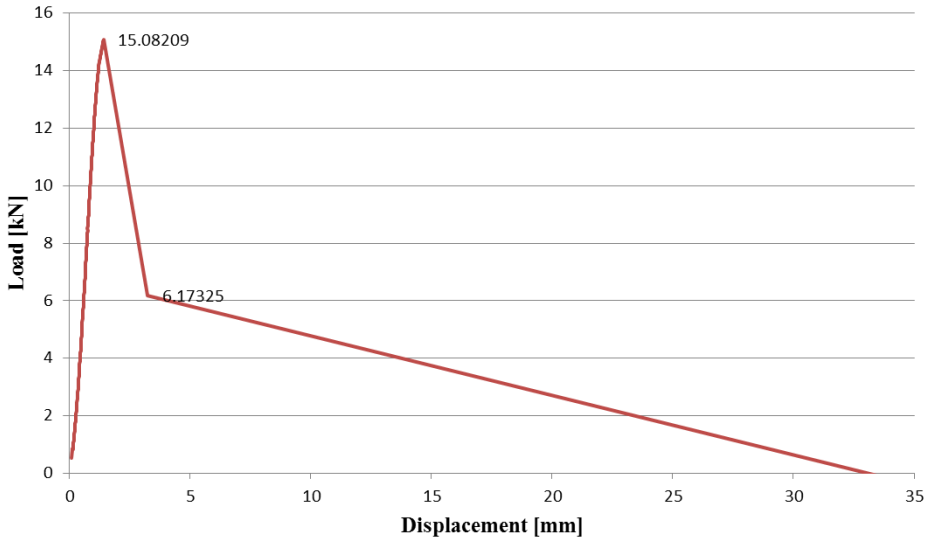

Figure 88: Load vs. displacement of the second specimen showing an abrupt breaking of the specimen

Since the bond-slip behaviour issue was not an objective of this study, information and specimen design procedures was presented in this appendix, so that the future researchers can re-do the test and conduct data analysis properly.

Images of the second specimen after failure are presented in Figures 89 and 90.

Figure 89: The second specimen after the test failed, showing the broken base

Figure 90: Rebar-bolt weld detachment that occurred during testing the second specimen